

Surface Spectroscopic Investigation of Rare Earth Minerals Flotation

Jianlan Cui
M. E. (CAS)
B. Sc. (SYS)

School of Natural Sciences
Griffith Sciences
Griffith University

Submitted in fulfilment of the requirements of the degree of
Doctor of Philosophy

August 2015

Abstract

This thesis describes fundamental studies of the surface interactions between rare earths and the collector hydroxamate to obtain a mechanistic understanding of the flotation process. A model and systematic investigation has been undertaken in order to ascertain the flotation mechanism and optimise flotation response and selectivity. Major constituent components (rare earth oxides, minerals and gangue minerals) in the flotation system were fully characterized individually prior to the interaction investigations. Six rare earth hydroxamate model compounds have been synthesized to characterize the surface chemical bonding. A model mineral thin film was also synthesized and investigated with the hydroxamate collector.

For the vibrational characterization of the rare earth oxides, this thesis has adopted multiple radiation sources (wavelengths of 325 nm, 442 nm, 514 nm and 632.8 nm) scanning Raman shifts from 100 cm^{-1} – 5000 cm^{-1} . It has been demonstrated that each individual rare earth oxide has similar, but distinct vibrational and electronic properties including Raman and fluorescence spectra. Nd, Er and Ho can be identified through their fluorescence emissions that do not overlap the Raman spectra. It is possible to develop a fast detection technique for these rare earths using their fluorescence emissions spectra in mineral processing. The characterization of natural mineral bastnaesite and monazite demonstrated that the ore exhibits localized enrichment zones of the rare earths of sizes from $1\text{ }\mu\text{m}$ - $5\text{ }\mu\text{m}$. The results from atomic force microscopy and magnetic atomic force microscopy have confirmed the enrichment zones are smaller than the present grinding sizes for flotation. It would be of interest to re-examine the grinding sizes in practice in order to maximise the liberation of minerals.

Six model rare earth hydroxamate compounds (Nd, Ce, Er, Ho, Gd and Dy) were synthesized for the measurement of their spectral properties. The functional groups

C=O, N-O and C-N have been identified as being as bound to the coordination centre in the complex formation. These functional groups were used as indicators for the formation of hydroxamate complexes at the surface of the natural minerals. A cerium carbonate thin film was synthesized on calcite as a model bastnaesite mineral surface, in order to investigate the surface interaction with hydroxamate. The film was found to comprise particles and the sizes were consistent with the natural bastnaesite and monazite (from 1 - 3 μm in diameter). The AFM-Raman results revealed that hydroxamate was selective for cerium over gangue calcium.

Six rare earth oxides (La_2O_3 , CeO_2 , Nd_2O_3 , Er_2O_3 , Yb_2O_3 and Tm_2O_3) were selected for surface interaction investigations with hydroxamate. La_2O_3 exhibited the strongest interaction to hydroxamate, followed by CeO_2 , Tm_2O_3 and Yb_2O_3 . Nd_2O_3 exhibited only weak interaction with hydroxamate while no adsorption was observed for Er_2O_3 with hydroxamate under any of the conditions investigated. The selectivity of hydroxamate for rare earth oxides determined in this investigation is not consistent with the reported stability constants of the corresponding rare earth hydroxamate complexes. To achieve boarder selectivity for the rare earths during flotation, a combination of collectors would be required.

For the natural minerals (bastnaesite and monazite) interaction with hydroxamate produced localization adsorption on the surface for both samples. Bastnaesite exhibited a better coverage to hydroxamate compared to monazite. This difference should allow the separation of bastnaesite from monazite during flotation where both minerals are present. The adsorption investigation of a gangue mineral sample that comprises four different components has confirmed that hydroxamate is selective to bastnaesite over monazite. No chemisorption evidence was observed for the gangue mineral (calcite) when it was conditioned for the same length of time as rare earth minerals.

Declaration

This work has not previously been submitted for a degree or diploma at any university. To the best of my knowledge and belief, the thesis contains no material previously published or written by another person except where due reference is made in the thesis itself.

Jianlan Cui

Acknowledgements

It has been an amazing journey in the last four years of accomplishing this thesis. It is certainly impossible to finish it without many people's generous help. The differences in culture, language, or even the academic environment between the East and West have definitely added lots of challenges/fun into this journey.

I would like to express the deepest appreciation to my principal supervisor Professor Gregory Hope for his understanding, wisdom, patience and encouragement that have helped and inspired me to complete this thesis. His vast knowledge and experiences have provided a strong and clear guidance for my PhD research. His advice is always useful and has saved me from being lost in the darkness of confusion and frustration. Another thing I must mention is that the way he deals with the cultural differences involving every aspect of the daily life. I always feel I am being respected. I am very grateful and feel lucky working with him.

I would also like to thank my co-supervisor Professor Debra Bernhardt, who constantly assisted me on my research journey and encouraged me to join the Student Committee board. This has helped me fit in with my new environment much quicker, which was definitely beneficial for my PhD research. In addition, I would like to thank Professor Alan Buckley who provided insight and expertise in the X-ray photoelectron spectroscopy that greatly assisted this research. I would also like to mention Dr. Gretel Heber who has provided valuable contributions for this thesis. I always received inspiration from the discussion with her and her comments have greatly improved the manuscript.

I wish to express my gratitude to the members of the spectroscopic research team. Specifically, they are Dr. Kym Watling and Dr. Apisit Numprasanthai as well as my

fellow postgraduate student Kun Zhang. I am also grateful to all the academic and technical staff from Griffith University School of Science and Queensland Micro- and Nanotechnology Centre who have provided generous supports to this program. Particularly, I would like to thank Professor Igor Agranovski and Ali Al Ibrahim who provided instrumental and technical support for the scanning electronic microscopy/energy-dispersive x-ray spectroscopy instrument. Also, I would like to thank Alan White as well as Sarah Brookes from the teaching lab for their constant support for multiple experiments.

I have been awarded two scholarships, the Griffith University Postgraduate Research Scholarship and the Tuition Fee Scholarship. I wish to take this opportunity to thank Griffith University for providing this financial assistance. The Australian National Fabrication Facility (ANFF) and Griffith University Postgraduate Funding are acknowledged for the support for the three papers published.

I would like to acknowledge with gratitude the support and love from Elizabeth Hope and all the members from the Hope family who always treated me with love and kindness. Their generous and unstinting support helped me survive all the stress and never give up. I would also like to express my appreciation to my parents, Yantian Cui and Lifang Lao; my brother Jianfei Cui; my husband's parents Bruch Milne and Jean Milne, and all my friends for their unconditional support to make this thesis possible.

A special thanks to my beloved husband Richard Milne. Thank you for all the sacrifices you have made for me, working hard to support me. Those hugs and little comforts have kept me going and helped me maintain a positive attitude to finalise this thesis.

This thesis is dedicated to the memory of my grandmother Li Xinglian.

Publications

1. Cui J. and Hope G. A., 2015, Raman and Fluorescence Spectroscopy of CeO_2 , Er_2O_3 , Nd_2O_3 , Tm_2O_3 , Yb_2O_3 , La_2O_3 , and Tb_4O_7 , *Journal of Spectroscopy*, 2015, 1-8.
2. Cui J. and Hope G. A., 2013, A surface investigation of rare earths mineral by atomic force microscopy and atomic force microscopy tandem confocal Raman spectroscopy, In *Chemeca 2013: Challenging Tomorrow*. Barton, ACT: Engineers Australia, 9781922107077, 222-226.
3. Cui J., Hope G. A. and Buckley A. N., 2012, Spectroscopic investigation of the interaction of hydroxamate with bastnaesite (cerium) and rare earth oxides, *Minerals Engineering*, 36-38, 91-99.

Table of Contents

ABSTRACT.....	iii
DECLARATION.....	vi
ACKNOWLEDGEMENTS.....	viii
PUBLICATIONS.....	xii
TABLE OF CONTENTS.....	xiv
LIST OF ABBREVIATION.....	xx
LIST OF FIGURES.....	xxiv
LIST OF TABLES.....	xxxii
LIST OF DIAGRAMS.....	xxxiii
 Chapter 1 Introduction	 1
1.1 Preamble	2
1.2 Aims and objectives of this study	4
1.3 Structure of this thesis	5
References	6
 Chapter 2 Literature Review	 8
2.1 Rare earth elements and minerals	9
2.2 Distribution, history and process development of REs	18
2.2.1 Chinese RE deposits	22

2.3 Flotation reagents and interaction on mineral surface	30
2.4 Environmental concern	36
2.5 Future trends	40
References	41
Chapter 3 Experimental and Instrumental	51
3.1 Preamble	52
3.2 Material and experimental methods	53
3.2.1 Chemicals	53
3.2.2 Characterization of rare earth oxides and rare earth minerals	53
3.2.3 Synthesis of the REE compounds with hydroxamate	54
3.2.4 Synthesis of cerium hydroxamate	54
3.2.5 Synthesis of Ce carbonate on calcite and adsorption study with hydroxamate	54
3.2.6 Adsorption studies between hydroxamate and REOs	55
3.2.7 Adsorption studies between hydroxamate and RE minerals	55
3.3 Technical and instrumental	57
3.3.1 Raman spectroscopy	60
3.3.2 Infrared spectroscopy (IR)	65
3.3.3 Atomic force microscopy and atomic force microscopy tandem confocal Raman spectroscopy	67
3.3.4. X-ray photoelectron spectroscopy	71
3.3.5 Scanning electron microscopy	74
References	78
Chapter 4 Characterization of rare earth oxides, rare earth minerals and gangue mineral	82

4.1 Preamble	83
4.2 Characterization of rare earth oxides	85
4.2.1 Cerium oxides (CeO_2)	85
4.2.2 Erbium oxides (Er_2O_3)	90
4.2.3 Neodymium oxides (Nd_2O_3)	93
4.2.4 Thulium oxide (Tm_2O_3)	98
4.2.5 Ytterbium oxide (Yb_2O_3)	100
4.2.6 Lanthanum oxide (La_2O_3)	102
4.2.7 Terbium oxide (Tb_4O_7)	104
4.3 Characterization of rare earth minerals	106
4.3.1 Bastnaesite crystal	106
4.3.2 Monazite	124
4.4 Gangue minerals investigation	134
4.4.1 Investigation by SEM-EDX and XPS	134
4.4.2 Investigation by vibrational spectroscopy	140
Conclusion and future work	143
References	144
Chapter 5 model systems investigation for rare earth hydroxamate compounds and bastnaesite (Ce)	149
5.1 Preamble	150
5.2 Synthesis and characterization of REE hydroxamate compounds	151
5.2.1 Neodymium hydroxamate	151
5.2.2 Cerium hydroxamate	157
5.2.3 Other RE hydroxamate compounds (Ho, Gd, Dy and Er)	164
5.3 Model system investigation for bastnaesite (Ce)	169

5.3.1 Preparation and characterization of cerium carbonate thin film on calcite	169
5.3.2 Absorption study for cerium carbonate thin film on calcite with hydroxamate	179
Conclusion	182
References	183
Chapter 6 Interfacial interaction studies using <i>in-situ</i> and <i>ex-situ</i> techniques – rare earth oxides, rare earth minerals and gangue minerals	185
6.1 Preamble	186
6.2 Adsorption studies between REO and potassium hydrogen n-octanohydroxamate	187
6.2.1 Conditioned cerium oxide	187
6.2.2 Conditioned neodymium oxide	188
6.2.3 Conditioned erbium oxide	194
6.2.4 Conditioned thulium oxide	197
6.2.5 Conditioned ytterbium oxide	199
6.2.6 Conditioned lanthanum oxide	201
6.2.7 Summary and discussion for the adsorption studies for REOs	204
6.3 Adsorption studies between RE minerals and hydroxamate	205
6.3.1 Bastnaesite conditioned with hydroxamate	205
6.3.2 Monazite crystal conditioned with hydroxamate	211
6.4 Gangue minerals	215
6.4.1 Gangue mineral conditioned in hydroxamate	215
Conclusion	221

References	222
Chapter 7 Conclusion	223
7.1 Summary of results	224
7.2 Characterization of REO, RE minerals and gangue minerals	224
7.3 Model RE-hydroxamate compounds	225
7.4 Model system for surface interaction of RE minerals	225
7.5 Adsorption study on the REO surface	226
7.6 Adsorption study on the surface of RE minerals	226
7.7 Adsorption study on the surface of a gangue mineral specimen	227
7.8 Future work	228
7.9 Concluding remarks	229
References	230

List of Abbreviations

Å	Angstrom/s
AFM	atomic force microscopy
AR	analytical reagent
ATR	attenuated total reflection
CCD	charge-coupled device
cm	centimetre
d	day
ΔG°	free energy change
DDI	doubly de-ionized
DTGS	deuterium triglycine sulfate
EDX	energy dispersive X-ray
E_b	binding energy
E_{kin}	kinetic energy
eV	electron volt
FT	Fourier-transfer
γ	gamma
Gy	gray
h	hour
inorg.	inorganic
IR	infrared
K	Kelvin

keV	kiloelectron volt
kHz	kilohertz
km	kilometre
kV	kilovolt
liq.	liquid
LREO	light rare earth ores
M	molar ($\text{moles} \cdot \text{L}^{-1}$)
m	metre
μA	microampere
min	minute
mm	millimetre
mbar	millibar
μm	micron (10^{-6} m)
μg	microgram (10^{-6} g)
mg	milligram (10^{-3} g)
Mt	megatonne
mSv	millisievert
mW	milliwatt
ng	nanogram (10^{-9} g)
nm	nanometre (10^{-9} m)
NIR	near infrared

v	stretching vibration
N·m ⁻¹	newton metre
N/A	not available
HREEs	heavy rare earth elements
HREO	heavy rare earth ores
IUPAC	International Union of Pure and Applied Chemistry
OHA	n-octanohydroxamate
org.	organic
OT	oxidation percentage
Pa	Pascal
pm	picometers (10 ⁻¹² m)
RE	rare earth
REEs	rare earth elements
REOs	rare earth oxides
SEM	scanning electron microscope
S/N	signal to noise
t	tonne
UV	ultraviolet
V	volt
V/V	volume per unit volume
Φ _{sp}	work function

XPS	X-ray photoelectron spectroscopy
w/w	weight per unit weight
XRD	X-ray diffraction

List of Figures

Fig 2.1 Productive or potentially productive REE bearing deposits in North America (Figure sourced from Castor, 2008)	19
Fig. 2.2 Locations of four major plants for rare earth extraction in China: 1. Bayan Obo; 2. Weishan; 3. Maoniuping; 4. Longnan	20
Fig. 2.3 Structure of H_{205} molecule	33
Fig. 3.1 Energy levels of Rayleigh scattering and Raman scattering	62
Fig. 3.2 Schematics for atomic force microscope operation for scanning	68
Fig. 3.3 Diagram for AFM-Raman operation for surface scanning	70
Fig. 3.4 Schematic illustration of the XPS spectrometer	72
Fig. 3.5 Typical signals generated when the specimen is struck by the electrons	75
Fig. 4.1 Raman bands for CeO_2 with (a) 442 nm excitation (b) 514 nm excitation and (c) 633 nm excitation	86
Fig. 4.2 Emission spectra for CeO_2 with (a) 442 nm excitation (b) 514 nm excitation and (c) 633 nm excitation. The emission lines observed are from the Raman band at 465 cm^{-1} shift	87
Fig. 4.3 Spectra obtained from Er_2O_3 using (a) 442 nm excitation (b) 514 nm excitation and (c) 633 nm excitation, presented as Raman shifts	90
Fig. 4.4 Emission spectra from Er_2O_3 using (a) 633 nm excitation (b) 514 nm excitation and (c) 442 nm excitation.	91
Fig. 4.5 Fluorescence emission spectra for Er_2O_3 with (a) 442 nm excitation (b) 514 nm excitation and (c) 633 nm excitation in the range of (1) 640 nm – 700 nm (2) 530 nm – 580 nm. The emission lines exhibit good agreement in emission positions for different excitation wavelengths.	92

Fig. 4.6 Energy level for Er(III), data sourced from Wu et al. (Wu et al., 2013)	93
Fig. 4.7 Energy level diagram of Nd(III) (Borrero-Gonzalez and Nunes, 2012)	94
Fig. 4.8 Fluorescence emissions for Nd ₂ O ₃ by using (a) 442 nm (b) 514 nm and (c) 633 nm excitations	95
Fig. 4.9 Raman spectra for Nd ₂ O ₃ by using (a) 442 nm (b) 514 nm and (c) 633 nm excitations	97
Fig. 4.10 Raman spectra for Tm ₂ O ₃ with (a) 442 nm excitation (b) 514 nm excitation and (c) 633 nm excitation	98
Fig. 4.11 Fluorescence emission spectra for Tm ₂ O ₃ with (a) 442 nm excitation (b) 514 nm excitation and (c) 633 nm excitation. Raman bands, being Raman shifts appear at different wavelengths in the emission spectra	99
Fig. 4.12 Raman spectra for Yb ₂ O ₃ with (a) 442 nm excitation (b) 514 nm excitation and (c) 633 nm excitation	100
Fig. 4.13 Emissions spectra for Yb ₂ O ₃ with (a) 442 nm excitation (b) 514 nm excitation and (c) 633 nm excitation. The 514 nm (blue) and 633 nm (red) spectra range from 650 nm to 700 nm is shown on the top right corner	101
Fig. 4.14 Raman spectra for La ₂ O ₃ with (a) 442 nm excitation (b) 514 nm excitation and (c) 633 nm excitation. The spectra ranges from 200 nm to 750 cm ⁻¹ are shown on the small figure. From top to bottom: 442 nm excitation, 514 nm excitation and 633 nm excitation	102
Fig. 4.15 Emission spectra for La ₂ O ₃ with (a) 442 nm excitation (b) 514 nm excitation and (c) 633 nm excitation	103

Fig. 4.16 Images for Tb ₄ O ₇ (a) before investigation using Raman spectroscopy; (b) after investigation using Raman spectroscopy. Excitation: 442 nm laser, exposure time: 10s.	104
Fig. 4.17 Raman spectra on the same spot for Tb ₄ O ₇ (a) primary spectrum and (b) consecutive spectrum (excitation wavelength was 442 nm)	105
Fig. 4.18 Photoelectron spectra from an unconditioned bastnaesite surface: (a) La 3 <i>d</i> ; (b) Ce 3 <i>d</i> ; (c) Nd 3 <i>d</i> ; (d) Nd, Ce and La 4 <i>d</i>	107
Fig. 4.19 Electron micrograph of a carbon sputtered bastnaesite crystal from Pakistan. Scanning area is 200 $\mu\text{m} \times 200 \mu\text{m}$	109
Fig. 4.20 SEM mapping on L α 1 signal on single element of a bastnaesite crystal sample from Pakistan. The colour shades stand for different concentration of the corresponding elements	111
Fig. 4.21 Raman spectra of bastnaesite by using excitations of (a) 514 nm (b) 442 nm and (c) 633 nm	112
Fig. 4.22 Emission spectra of bastnaesite by using excitations of (a) 442 nm (b) 514 nm and (c) 633 nm	113
Fig. 4.23 Energy level diagram for Pr(III), data sourced from Zhou et. al. (Zhou et al., 2012)	114
Fig. 4.24 AFM image of bastnaesite sized 5 $\mu\text{m} \times 5 \mu\text{m}$	116
Fig. 4.25 AFM and AFM-Raman images for bastnaesite: (a), (c): Surface image, 60 $\mu\text{m} \times 60 \mu\text{m}$ and 20 $\mu\text{m} \times 20 \mu\text{m}$, respectively; (b), (d): AFM-Raman image with a static scan centred at 1094.5 cm^{-1} , scan area: 60 $\mu\text{m} \times 60 \mu\text{m}$ and 20 $\mu\text{m} \times 20 \mu\text{m}$, respectively. Both of the AFM and AFM-Raman images have shown that the REs are enriched in regions. The enriched area dimensions are less than 10 $\mu\text{m} \times 10 \mu\text{m}$	118
Fig. 4.26 Topography AFM image of magnetite sized 60 $\mu\text{m} \times 60 \mu\text{m}$	120

Fig. 4.27 Magnetic AFM image of magnetite corresponding to the same area as Fig. 4.26. The colour range indicates the magnetic signal strength	120
Fig. 4.28 (a) topography and (b) magnetic AFM images of bastnaesite, $30\ \mu\text{m} \times 30\ \mu\text{m}$; (c) topography and (d) magnetic AFM images of bastnaesite, $3\ \mu\text{m} \times 3\ \mu\text{m}$	123
Fig. 4.29 Electron micrograph of a carbon sputtered monazite crystal	125
Fig. 4.30 SEM mapping on $L\alpha_1$ signal on single element of a monazite crystal sample	127
Fig. 4.31 Raman spectra of monazite using excitation sources of (a) 633 nm (b) 514 nm and (c) 442 nm, showing the wavelength dependence of the fluorescence emission	128
Fig. 4.32 Emission spectra from monazite with excitation by (a) 442 nm (b) 514 nm and (c) 633 nm	130
Fig. 4.33 AFM image of monazite ($35\ \mu\text{m} \times 35\ \mu\text{m}$ scan)	131
Fig. 4.34 AFM image of monazite ($10\ \mu\text{m} \times 10\ \mu\text{m}$ scan)	131
Fig. 4.35 (a) Topographic and (b) magnetic AFM images of monazite $30\ \mu\text{m} \times 30\ \mu\text{m}$	133
Fig. 4.36 SEM image for a bastnaesite ore specimen; (a) scanning size at $3\ \text{mm} \times 3\ \text{mm}$; (b) a $80\ \mu\text{m} \times 30\ \mu\text{m}$ crystal containing REE; (c) $10\ \mu\text{m} \times 10\ \mu\text{m}$ image for the crystal shown in (b)	135
Fig. 4.37 Elemental mapping for the area where REs were present in a bastnaesite ore specimen; Collection time: 15 min.	138
Fig. 4.38 Raman spectra of bastnaesite ore with different locations (a, b, c and d) on the surface using 633 nm of excitation	140
Fig. 4.39 Raman spectra of bastnaesite ore with different locations (a, b, c and d) on the surface using 442 nm of excitation	142

Fig. 5.1 N 1s spectra from Nd hydroxamate obtained at different stages in the spectral suite: (a) at the outset; (b) mid-suite; (c) at the end.	152
Fig. 5.2 Vibrational spectra of: (a) FT-IR of neodymium hydroxamate, (b) Raman spectra of n-octanohydroxamic acid, (c) neodymium hydroxamate and (d) Nd ₂ O ₃	155
Fig. 5.3 Emission spectra of: (a) neodymium hydroxamate and (b) Nd ₂ O ₃ . The fluorescence peaks observed for the neodymium oxide differ in intensity and energy from those for the neodymium hydroxamate	157
Fig. 5.4 Vibrational spectra of: (a) FT-IR of cerium hydroxamate, (b) Ce(NO ₃) ₃ •6H ₂ O, (c) cerium hydroxamate and (d) Raman spectra of n-octanohydroxamic acid	160
Fig. 5.5 Raman spectra of: (a) Ce(NO ₃) ₃ •6H ₂ O (b) cerium hydroxamate and (c) n-octanohydroxamic acid, in the range of 800 cm ⁻¹ to 1700 cm ⁻¹	161
Fig. 5.6 Raman spectra of: (a) Ce(IV) hydroxamate prepared from cerium ammonium nitrate (b) Ce(III) hydroxamate prepared from Ce(NO ₃) ₃ •6H ₂ O in the range of 800 cm ⁻¹ to 1700 cm ⁻¹	162
Fig. 5.7 Raman spectra in the range of 800 cm ⁻¹ to 1700 cm ⁻¹ for: (a) Ce (III) hydroxamate and (b) Ce (III) hydroxamate exposed to air for 4 d	163
Fig. 5.8 Emission spectra of: (a) holmium hydroxamate and (b) neodymium hydroxamate	165
Fig. 5.9 Raman spectra from hydroxamates of Er, Gd, Dy, Ho and Nd, from top to bottom	166
Fig. 5.10 FT-IR spectra from hydroxamates of Nd, Gd, Dy, Ho and Er from top to bottom	168
Fig. 5.11 Image for synthesized cerium carbonate on calcite	170
Fig. 5.12 Raman spectra for (a) synthesized cerium carbonate thin film and (b) calcite in different ranges	171

Fig. 5.13 Raman spectra for different spots of synthesized cerium carbonate thin film (a and b) and calcite (c). Spectrum a was collected near the edge of the thin film. Spectrum b was collected in the middle area of the sample	172
Fig. 5.14 Raman mapping over the edge of synthesized cerium carbonate thin film and calcite using 633 nm laser. The Raman bands at 1079 cm^{-1} and 1086 cm^{-1} were used for fitting where red represents cerium carbonate and green represents calcite. The microscopy image is shown in the background. $25\text{ }\mu\text{m} \times 20\text{ }\mu\text{m}$	174
Fig. 5.15 (a) AFM image for the cerium carbonate thin film on calcite and (b) AFM magnetic scan for the corresponding area; Scan size: $50\text{ }\mu\text{m} \times 50\text{ }\mu\text{m}$	176
Fig. 5.16 (a) AFM image for cerium carbonate thin film on calcite and (b) AFM magnetic scan for the corresponding area; Scan size: $15\text{ }\mu\text{m} \times 15\text{ }\mu\text{m}$. Cerium carbonate formed triangle shaped particles sized from $0.5\text{ }\mu\text{m} \times 0.5\text{ }\mu\text{m} \times 0.5\text{ }\mu\text{m}$ to $1\text{ }\mu\text{m} \times 1\text{ }\mu\text{m} \times 1\text{ }\mu\text{m}$ on calcite	177
Fig. 5.17 Raman spectra of conditioned cerium carbonate thin film with $\text{KH}(\text{OHA})_2$, (a)-(d): 72 h, 24 h, 5 h, 1 h; (e): calcite conditioned with $\text{KH}(\text{OHA})_2$ for 72	180
Fig. 6.1 Raman spectra of (a) conditioned CeO_2 with $\text{KH}(\text{OHA})_2$ for 18 h (b) conditioned CeO_2 with $\text{KH}(\text{OHA})_2$ for 1 h (c) CeO_2 (d) $\text{KH}(\text{OHA})_2$	188
Fig. 6.2 Raman spectra of (a) conditioned Nd_2O_3 with $\text{KH}(\text{OHA})_2$ in water for 48 h (b) conditioned Nd_2O_3 with $\text{KH}(\text{OHA})_2$ in water for 18 h (c) conditioned Nd_2O_3 with $\text{KH}(\text{OHA})_2$ in water for 5 h; (d) Nd_2O_3 ; (e) $\text{KH}(\text{OHA})_2$	189
Fig. 6.3 Fluorescent spectra in the range of 860 nm – 940 nm for (a) conditioned Nd_2O_3 with for $\text{KH}(\text{OHA})_2$ in water for 48 h (b) conditioned Nd_2O_3 with $\text{KH}(\text{OHA})_2$ in water for 18 h (c) conditioned Nd_2O_3 with $\text{KH}(\text{OHA})_2$ in water for 5 h; (d) Nd_2O_3	190

Fig. 6.4 Raman spectra of (a) conditioned Nd_2O_3 with $\text{KH}(\text{OHA})_2$ in 1:1 ethanol and water for 48 h (b) conditioned Nd_2O_3 with $\text{KH}(\text{OHA})_2$ in 1:1 ethanol and water for 18 h (c) conditioned Nd_2O_3 with $\text{KH}(\text{OHA})_2$ in 1:1 ethanol and water for 5 h; (d) Nd_2O_3 ; (e) $\text{KH}(\text{OHA})_2$	192
Fig. 6.5 Fluorescent spectra in the range of 875 nm – 905 nm for (a) conditioned Nd_2O_3 with $\text{KH}(\text{OHA})_2$ in 1:1 ethanol and water for 48 h; (b) conditioned Nd_2O_3 with $\text{KH}(\text{OHA})_2$ in 1:1 ethanol and water for 18 h; (c) conditioned Nd_2O_3 with $\text{KH}(\text{OHA})_2$ in 1:1 ethanol and water for 5 h; (d) Nd_2O_3	193
Fig. 6.6 Raman spectra of (a) conditioned Er_2O_3 with $\text{KH}(\text{OHA})_2$ for 18 h; (b) conditioned Er_2O_3 with $\text{KH}(\text{OHA})_2$ for 5 h; (c) conditioned Er_2O_3 with $\text{KH}(\text{OHA})_2$ for 1 h; (d) Er_2O_3 ; (e) $\text{KH}(\text{OHA})_2$	195
Fig. 6.7 Fluorescent emission spectra of (a) conditioned Er_2O_3 with $\text{KH}(\text{OHA})_2$ for 18 h; (b) conditioned Er_2O_3 with $\text{KH}(\text{OHA})_2$ for 5 h; (c) conditioned Er_2O_3 with $\text{KH}(\text{OHA})_2$ for 1 h; (d) Er_2O_3	196
Fig. 6.8 Raman spectra of (a) conditioned Tm_2O_3 with $\text{KH}(\text{OHA})_2$ for 18 h; (b) conditioned Tm_2O_3 with $\text{KH}(\text{OHA})_2$ for 5 h; (c) conditioned Tm_2O_3 with $\text{KH}(\text{OHA})_2$ for 1 h; (d) Tm_2O_3 ; (e) $\text{KH}(\text{OHA})_2$	198
Fig. 6.9 Raman spectra of (a) conditioned Yb_2O_3 with $\text{KH}(\text{OHA})_2$ for 18 h; (b) conditioned Yb_2O_3 with $\text{KH}(\text{OHA})_2$ for 5 h; (c) conditioned Yb_2O_3 with $\text{KH}(\text{OHA})_2$ for 1 h; (d) Yb_2O_3 ; (e) $\text{KH}(\text{OHA})_2$	200
Fig. 6.10 Raman spectra of (a) conditioned La_2O_3 with $\text{KH}(\text{OHA})_2$ for 18 h; (b) conditioned La_2O_3 with $\text{KH}(\text{OHA})_2$ for 5 h; (c) conditioned La_2O_3 with $\text{KH}(\text{OHA})_2$ for 1 h; (d) La_2O_3 ; (e) $\text{KH}(\text{OHA})_2$	202
Fig. 6.11 Raman spectra for (a) bastnaesite crystal (b) $\text{KH}(\text{OHA})_2$ (c) treated bastnaesite crystal. The bastnaesite crystal sourced from Pakistan	207

Fig. 6.12 AFM and AFM-Raman images for conditioned bastnaesite: (a) surface image of bastnaesite, $100 \times 100 \mu\text{m}$; (b), (c), (d): AFM-Raman images on the same area with static scans centred at 1093.5 cm^{-1} , 985 cm^{-1} and 3169 cm^{-1} , respectively	210
Fig. 6.13 Raman spectra for (a) $\text{KH}(\text{OHA})_2$; (b) $\text{KH}(\text{OHA})_2$ treated monazite crystal for 48 h; (c) $\text{KH}(\text{OHA})_2$ treated monazite crystal for 2 h and (d) monazite crystal	212
Fig. 6.14 Emission spectra for (a) $\text{KH}(\text{OHA})_2$ treated monazite crystal for 2 h (b) $\text{KH}(\text{OHA})_2$ treated monazite crystal for 48 h (c) monazite crystal. No significant shifts were observed in both treated samples compared to the untreated monazite spectrum	214
Fig. 6.15 Raman spectra for (a) $\text{KH}(\text{OHA})_2$ (b) $\text{KH}(\text{OHA})_2$ treated bastnaesite ore at location A and (c) bastnaesite ore at the same location.	217
Fig. 6.16 Raman spectra for (a) $\text{KH}(\text{OHA})_2$ (b) $\text{KH}(\text{OHA})_2$ treated bastnaesite ore at location B and (c) bastnaesite ore at the same location. No significant change was observed with the conditioned sample spectrum compared to the spectrum of the same location	218
Fig. 6.17 Raman spectra for (a) $\text{KH}(\text{OHA})_2$ treated bastnaesite ore at location C (b) $\text{KH}(\text{OHA})_2$ and (c) bastnaesite ore at the same location.	218
Fig. 6.18 Raman spectra for (a) $\text{KH}(\text{OHA})_2$ treated bastnaesite ore at location D (b) $\text{KH}(\text{OHA})_2$ and (c) bastnaesite ore at the same location.	219

List of Tables

Table 2.1 List of the rare earth elements and their electronic configurations, physical and chemical properties and applications	11
Table 2.2 Major economic or potential economic RE minerals	14
Table 2.3 Verified reserves of the world's REO, by country	21
Table 2.4 Distribution of rare earths and Ce in different phases of the Longnan deposit (%)	27
Table 2.5 Hydroxamate collectors used in China's rare earth plants	31
Table 2.6 Performance of H ₂₀₅ with different RE ores	34
Table 2.7 ThO ₂ in bastnaesite and monazite from Bayan Obo ore (%)	37
Table 3.1 Analytical techniques summary	58
Table 3.2 Energy band range in infrared radiation	66
Table 4.1 Band positions and corresponding Raman modes for REOs	88
Table 5.1 Vibrational band positions for REE hydroxamates, and n-octanohydroxamic acid	167

List of diagrams

Diagram 2.1 Flow chart for processing of REs used in Bayan Obo plant (Data sourced from Yu, 2001).	23
Diagram 2.2 Extraction process of REO from Longnan Jiangxi ore	28

CHAPTER 1

INTRODUCTION

1.1 Preamble

The flotation of rare earth (RE) minerals is important for the economic recovery of rare earth metals from their ores. This thesis describes the fundamental investigation of bastnaesite and monazite surfaces and their interactions with flotation reagents. The rare earths include the f-block elements and they are classified by International Union of Pure and Applied Chemistry (IUPAC) as scandium, yttrium and the lanthanoids (Connelly et al., 2005). The first RE mineral, ytterbite was discovered in 1787, and yttrium was isolated (as the oxide) from this mineral in 1794. An excellent history of the discovery of the rare earths has been presented by Gschneidner (Gschneidner Jr. and Capelle, 1987).

The entire RE family was not characterized until the 20th century. They have received special attention due to their unique properties that have been applied in the new technologies in recent years (Castor and Hedrick, 2006). Their properties have been harnessed for high-tech and green technology applications, falling into more than 15 categories (Tatsuo, 2011). Magnets and catalysts are the most popular research areas, with over 10,000 papers published between 2005 and 2008 according to Adachi et al. More than 20 research areas related to REs have been investigated (Adachi et al., 2010). For example, the development of RE super magnets and rechargeable batteries has facilitated the development of the vehicle industry, while RE phosphors and capacitors are critical to the electronics industry (Adachi et al., 2010). Nevertheless, particular rare earth elements (REEs) are required to fulfil different industrial needs and the abundance of individual REE varies. Neodymium and dysprosium are widely used in magnetic materials and have been in short supply (Dent, 2012). Terbium, europium, and yttrium also are at the risk of supply disruption (de Boer and Lammertsma, 2013). All these

factors have affected the rare earths market, and are driving research to develop more efficient processing techniques for the concentration and separation of the RE minerals.

Commercial supplies of individual REs emerged in the 1940s. However, costs were high as the ores are generally dispersed and seldom form easily exploitable ore deposits. The largest RE source has been largely derived from iron ore tailings at Bayan Obo, China. The minerals currently mined are limited to bastnaesite and monazite with minor loparite, xenotime and laterite (Castor and Hedrick, 2006). Flotation has been adapted widely in the commercial recovery of RE minerals. Limited fundamental research has been conducted into the interaction of reagents with RE mineral surfaces, and the mechanism of the process is not fully understood (Castor and Hedrick, 2006; Yu, 2001). According to a report that gave the statistical data sourced from the American Chemical Society from 2005 to 2008, among the thousands of papers published on REs, no study has been presented on processing research. Fundamental research is limited to Ruderman-Kittel-Kasuya-Yoshida interaction studies, Kondo effect and organometallics (Adachi et al., 2010). Pradip and Fuerstenau reported on the selectivity of hydroxamate during the RE flotation in 1984 and again published research on the interaction between fatty acid collector and Mountain Pass RE ore in 2013 (Pradip and Fuerstenau, 1983; Pradip and Fuerstenau, 2013). The authors recently presented a paper on a synthesized cerium fluocarbonate sample (Pradip et al., 2013). Systematic studies on RE flotation are urgently required; the research presented in this thesis is directed towards filling that gap. Flotation is the key step in the industrial production of RE materials; understanding the mechanisms and processes of RE flotation will facilitate improvement in flotation recovery and more efficient production of REs for their numerous applications.

1.2 Aims and objectives of this study

The aim of this study is to determine the mechanism of RE flotation, including the physical and chemical properties of the RE minerals, their surfaces and the interactions between flotation reagents and the minerals surface.

Specifically, the objectives were to:

- a. Characterize the surface properties of rare earth oxides (REOs), rare earth minerals and gangue minerals.
- b. Determine the functional groups involved in complex formation of RE-hydroxamate model compounds.
- c. Determine the mechanisms of physical and chemical absorption using a synthesized model mineral and hydroxamate flotation reagent.
- d. Determine the mechanisms of multilayer adsorption via a systematic study of hydroxamate with RE mineral surfaces (oxide powder and minerals).

1.3 Structure of this thesis

This thesis is divided into 7 chapters. The first chapter provides a blueprint of this research including a brief introduction and aims of the study.

Chapter 2 presents the background information on REs and flotation technology. Previous fundamental studies on REs and minerals are reviewed. In addition, a literature review on the distribution, history and processing development of REs is given, including an introduction to REs mining and processing in China.

Chapter 3 is devoted to the research methods and techniques used in this investigation. A description of the principles of each instrument used for this study is given. In addition, instrumental and experimental details are provided.

Chapter 4 presents the surface characterization undertaken for REOs, REs and gangue minerals using X-ray photoelectron spectroscopy (XPS), Raman spectroscopy, Atomic force microscopy (AFM), Atomic force microscopy tandem Raman (AFM-Raman) and Scanning electron microscope - energy dispersive X-ray (SEM - EDX).

Chapter 5 is devoted to a model system investigations, with the synthesis and investigation of a range of model RE hydroxamate compounds. A model thin film of Ce carbonate on calcite is also synthesized and investigated by AFM and AFM-Raman.

Chapter 6 details the investigation of the physical and chemical absorption between REOs, RE minerals, gangue minerals and the flotation reagent hydroxamate.

Chapter 7 summarises the results of the experiments and presents the major conclusions of the thesis. It discusses the implications of the results for the current and future research on REs flotation.

References

- Adachi G.-Y., Imanaka N. and Tamura S., 2010, Research trends in rare earths: A preliminary analysis, *Journal of Rare Earths*, 28, 843-846.
- Castor S. B. and Hedrick J. B., 2006, Rare earth elements, Society for Mining, Metallurgy and Exploration, Littleton, Colorado, 773-774.
- Connelly N. G., Damhus T., Hartshorn R. M. and Hutton A. T., 2005, Nomenclature of inorganic chemistry IUPAC recommendations 2005, Cambridge: RSC, 0-85404-438-8.
- Cschneider Jr. K. A. and Capelle J., 1987, 1787-1987 Two hundred years of rare earths, North Holland: Rare-earth Information Center, Iowa State University. Ames. Iowa. USA, North-Holland -Amsterdam.The Netherland, IS-RIC 10.
- De Boer M. A. and Lammertsma K., 2013, Scarcity of Rare Earth Elements, *ChemSusChem*, 6, 2045-2055.
- Dent P. C., 2012, Rare earth elements and permanent magnets (invited), *Journal of Applied Physics*, 111, 07A721.
- Pradip and Fuerstenau D. W., 1983, The adsorption of hydroxamate on semi-soluble minerals, part I: adsorption on barite, calcite and bastnaesite, *Colloids Surfaces*, 8, 103–119.
- Pradip and Fuerstenau D. W., 2013, Design and development of novel flotation reagents for the beneficiation of Mountain Pass rare-earth ore, *Minerals & Metallurgical Processing*, 30, 1-9.
- Pradip, Li C. C. H. and Fuerstenau D. W., 2013, The synthesis and characterization of rare-earth fluocarbonates, *KONA Powder and Particle* 30, 193-200.

- Tatsuo O., 2011, Rare earth resources and related industries in Japan, Journal of the Mining and Materials Processing Institute of Japan, 127, 549-557.
- Yu Y., 2001, Dressing technology of REO ore and its development in China, Journal of China University of Mining & Technology, 534-542 (中国矿业大学学报).

CHAPTER 2

LITERATURE REVIEW

2.1 Rare earth elements and minerals

Rare earth elements are traditionally classified by their atomic weights into light (atomic number 21 and 57 to 63) and heavy (atomic number 64 to 71) REEs, except for Y (atomic number 89), which is considered as a heavy rare earth element due to its similarity in properties with the heavy REEs. The electron configurations for the REEs are different from most other elements in the periodic table. The electrons fill in the inner incomplete $4f$ subshell as the charge of the nucleus increases (Table 2.1). The $4f$ orbital is well shielded by the $5s5p$ and the electrons in the $4f$ barely contribute to the valency forces (Spedding, 1971). This has resulted in most REEs occurring in the +3 oxidation state in their natural compounds, excepting europium, which has a valence of +2, and cerium, which has +2 and +4 states. Divalent RE compounds have been prepared under specific conditions (Kulyukhin, 1998) (Table 2.1). Valence fluctuation has been observed in alloys formed by REs and other transition metals. Mixed valences were reported in Ce, Sm, Yb, Tb and Eu in their alloy and oxide compounds (Adroja, 1991; Imanaka et al., 2004; Paramanik et al., 2013), two different $4f$ valence states were observed with X-ray absorption spectroscopy (Paramanik et al., 2013). A considerable amount of study has been devoted to this phenomenon (Adroja, 1991; Wertheim, 1979). A general agreement for the explanation is that the splitting of $4f$ state and the $4f$ - $5d$ exchange interaction has resulted in the mixed valence. However, no single theory has provided a satisfactory explanation (Adroja, 1991; Kotani et al., 2009).

REs have strong coordination tendency towards many ligands also due to the configuration of the $4f$ shell. The coordination numbers are from 6 to 10. Light REEs generally have larger coordination numbers while heavy REEs tend to have smaller coordination numbers, primarily attributed to the differences in atomic radius (Kanazawa and Kamitani, 2006). Additional electrons for the elements following

lanthanum primarily fill in the 4*f* subshell and these electrons cannot counterbalance the increase of the nuclear charge and this has resulted into sizes decrease (well known as the lanthanide contraction) (Table 2.1). Numerous papers have been published on rare earth compounds with different ligands (Deun et al., 2004; Feng and Fernando, 1960; Wenzel et al., 1985).

The REE metals exhibit a silver, silvery-white, or grey appearance and have a high electrical conductivity. The elements differ slightly in compound solubility and complex formation. The rare earth metals have been widely used in high-tech manufacturing, such as the magnet, rechargeable battery, phosphor and catalyst industries. Almost every REE has been studied and has found an application area. Reviews have listed the use of the REEs in more than 15 categories, including polishing, glass, luminescence, magnet etc. (Tatsuo, 2011, Adachi et al., 2010). The high demand from high-tech industries for REEs has led to supply shortages for some REEs (de Boer and Lammertsma, 2013; Dent, 2012).

Table 2.1 summarize the electronic configurations, physical and chemical properties and applications of the rare earth elements.

Table 2.1 List of the rare earth elements and their electron configurations, physical and chemical properties and applications

NAME	SYMBOL	ATOMIC NUMBER	ELECTRONIC CONFIGURATIONS	ATOMIC RADIUS (pm)	BOILING POINT (K)	OXIDATION STATE	APPLICATIONS
Scandium	Sc	21	$3d^1 4s^2$	162	3104	+3	Metallurgy
Yttrium	Y	39	$4d^1 5s^2$	180	3611	+3	Ceramics, Metallurgy, Phosphors and Others
Lanthanum	La	57	$5d^1 6s^2$	187	3730	+3	Battery alloys, Catalyst
Lanthanide elements	Cerium	58	$4f^2 5d^0 6s^2$	182	3699	+2,+3,+4	Catalyst, Ceramics, Glass, Polishing, Phosphors
	Praseodymium	59	$4f^3 5d^0 6s^2$	182	3785	+3	Magnets
	Neodymium	60	$4f^4 5d^0 6s^2$	181	3341	+2,+3	Magnets and Others
	Promethium	61	$4f^5 5d^0 6s^2$	181	~3000	+3	N/A
	Samarium	62	$4f^6 5d^0 6s^2$	180	2064	+2,+3	Magnets

Europium	Eu	63	$4f^7 5d^0 6s^2$	204	1870	+2,+3	Phosphors
Gadolinium	Gd	64	$4f^7 5d^1 6s^2$	179	3539	+3	Phosphors
Terbium	Tb	65	$4f^9 5d^0 6s^2$	178	3396	+3,+4	Phosphors and Others
Dysprosium	Dy	66	$4f^{10} 5d^0 6s^2$	177	2835	+3	Magnets
Holmium	Ho	67	$4f^{11} 5d^0 6s^2$	176	2968	+3	N/A
Erbium	Er	68	$4f^{12} 5d^0 6s^2$	175	3136	+3	Lasers and Others
Thulium	Tm	69	$4f^{13} 5d^0 6s^2$	174	2220	+2,+3	N/A
Ytterbium	Yb	70	$4f^{14} 5d^0 6s^2$	193	1466	+2,+3	N/A
Lutetium	Lu	71	$4f^{14} 5d^1 6s^2$	174	3668	+3	N/A

Data sourced from Zepf, 2013, Kulyukhin, 1998 and Spedding, 1971.

REEs are rarely found concentrated in exploitable ore deposits. Although over 200 minerals have been reported contain REEs, the major ore sources are limited to bastnaesite, monazite and xenotime, due to the commercial difficulty of extraction (Jordens et al., 2013). Table 2.2 lists the major economic or potential economic RE bearing minerals, however, no clear classifications have been defined for RE minerals (Tatsuo, 2011). The flotation reagent, hydroxamate, reacts as a ligand to selectively collect the target RE minerals. Chelate reagents have shown superiority over traditional uni/bidentate collectors, such as fatty acid and amines (Pradip and Fuerstenau, 2013).

In this thesis, the RE minerals are grouped based on the chemical nature of the host, namely carbonate, phosphate, oxide and silicate bearing minerals (Table 2.2). There are a few halide bearing RE minerals, however, they are not currently considered as commercially exploitable (Castor and Hedrick, 2006).

Table 2.2 Major economic or potential economic RE minerals

CHEMICAL UNIT	MINERAL NAME	CHEMICAL FORMULA
Carbonate	Ancylite (La)	$\text{Sr}(\text{La},\text{Ce})(\text{CO}_3)_2\text{OH}\cdot\text{H}_2\text{O}$
	Bastnaesite (Ce)	$(\text{Ce},\text{La})(\text{CO}_3)\text{F}$
	Bastnaesite (La)	$(\text{La},\text{Ce})(\text{CO}_3)\text{F}$
	Bastnaesite (Y)	$\text{Y}(\text{CO}_3)\text{F}$
	Parisite (Ce)	$\text{Ca}(\text{Ce},\text{La})_2(\text{CO}_3)_3\text{F}_2$
	Parisite (Nd)	$\text{Ca}(\text{Nd},\text{Ce})_2(\text{CO}_3)_3\text{F}_2$
	Synchysite (Ce)	$\text{Ca}(\text{Ce},\text{La})(\text{CO}_3)_2\text{F}$
	Synchysite (Nd)	$\text{Ca}(\text{Nd},\text{La})(\text{CO}_3)_2\text{F}$
	Synchysite (Y)	$\text{Ca}(\text{Y},\text{Ce})(\text{CO}_3)_2\text{F}$
Phosphate	Britholite (Ce)	$(\text{Ce},\text{Ca})_5(\text{SiO}_4,\text{PO}_4)_3(\text{OH},\text{F})$
	Britholite (Y)	$(\text{Y},\text{Ca})_5(\text{SiO}_4,\text{PO}_4)_3(\text{OH},\text{F})$
	Churchite (Y)	$\text{YPO}_4\cdot\text{H}_2\text{O}$
	Florencite (Ce)	$\text{CeAl}_3(\text{PO}_4)_2(\text{OH})_6$
	Florencite (La)	$(\text{La},\text{Ce})\text{Al}_3(\text{PO}_4)_2(\text{OH})_6$
	Florencite (Nd)	$(\text{Nd},\text{Ce})\text{Al}_3(\text{PO}_4)_2(\text{OH})_6$
	Monazite (Ce)	$(\text{Ce},\text{La},\text{Nd},\text{Th})\text{PO}_4$
	Monazite (La)	$(\text{La},\text{Ce},\text{Nd},\text{Th})\text{PO}_4$
	Monazite (Nd)	$(\text{Nd},\text{Ce},\text{La},\text{Th})\text{PO}_4$

Xenotime (Y)		YPO ₄
Oxide	Anatase	(Ti,REE)O ₂
	Brannerite	(U,Ca,Y,Ce)(Ti,Fe) ₂ O ₆
	Cerianite (Ce)	(Ce ⁴⁺ ,Th)O ₂
	Euxenite (Y)	(Y,Ca,Ce,U,Th)(Nb,Ta,Ti) ₂ O ₆
	Fergusonite (Ce)	(Ce,La,Y)NbO ₄
	Fergusonite (Nd)	(Nd,Ce)(Nb,Ti)O ₄
	Fergusonite (Y)	YNbO ₄
	Loparite (Ce)	(Ce,Na,Ca)(Ti,Nb)O ₃
	Samarskite	(REE,Fe ²⁺ ,Fe ³⁺ ,U,Th,Ca)(Nb,Ta,Ti)O ₄
Silicate	Allanite (Ce)	(Ce,Ca,Y) ₂ (Al,Fe ²⁺ ,Fe ³⁺) ₃ (SiO ₄) ₃ (OH)
	Allanite (Y)	(Y,Ce,Ca) ₂ (Al,Fe ³⁺) ₃ (SiO ₄) ₃ (OH)
	Eudialyte	Na ₄ (Ca,Ce) ₂ (Fe ²⁺ ,Mn ²⁺ ,Y)ZrSi ₈ O ₂₂ (OH,Cl) ₂
	Gadolinite (Ce)	(Ce,La,Nd,Y) ₂ Fe ²⁺ Be ₂ Si ₂ O ₁₀
	Kainosite (Y)	Ca ₂ (Y,Ce) ₂ Si ₄ O ₁₂ (CO ₃)·H ₂ O
	Thalenite (Y)	Y ₃ Si ₃ O ₁₀ (F,OH)

Data sourced from Castor and Hedrick, 2006; Jordens, 2012 and Tatsuo, 2011;

The carbonate group of RE minerals supplies more than 70% of the world's rare earths (Frost et al., 2013). Bastnaesite is the most important mineral from this group and it has become the dominant mineral source for REEs since the 1960s (Jordens et al., 2013). The mineral name bastnaesite is used synonymously with bastnäesite in the literature. It is a fluorocarbonate mineral that contains a mix of rare earth elements and yttrium with a hexagonal crystal structure. The general chemical formula for the crystal is $(\text{REE})(\text{CO}_3)\text{F}$ (Table 2.2). The most common bastnaesite is rich in Ce and La, and is referred to as bastnaesite (Ce) (Farmer, 1974; Frost and Dickfos, 2007). Characterization of bastnaesite by Raman and infrared spectroscopies has been published (Cui et al., 2012; Frost and Dickfos, 2007). The vibrational bands reported in both studies are consistent with a 2 cm^{-1} of difference for the $\nu_3 (\text{CO}_3)^{2-}$ asymmetric stretching mode in the Raman spectra. All bastnaesite minerals are paramagnetic with a REO content range from 70-74% in weight. Some of them contain ThO_2 and UO_2 (Jordens et al., 2013).

Monazite and similar rare earth element phosphates are also important source minerals. Monazite RE ore has a rare earth content of approximately of 70% with a general chemical formula of $(\text{REE})\text{PO}_4$ (Jordens et al., 2013) (Table 2.2). The mineral crystal is a RE orthophosphates, crystallizes in a monoclinic system belonging to the C_{2h}^5 space group (Silva et al., 2006). Monazite and similar RE phosphates also contain regulatory amounts of uranium and thorium (Clavier et al., 2011). Monazite can be found in placer deposits due to its high density, the most common form is as a black sand. In a review paper, Jordens et al. reported monazite is primarily separated by a high-capacity gravity method from its gangue minerals followed by additional gravity, magnetic, electrostatic steps and occasionally flotation (Jordens et al., 2013). When particle size is less than $100\text{ }\mu\text{m}$, gravity separation is not efficient and flotation has

provided an alternative for concentration of the fine particles of monazite (Cheng et al., 1993). The collector used was the oleate. Flotation using hydroxamate as collector of monazite has not been reported in literature.

Heavy rare earth ores (HREOs) are less common, and the main source is xenotime, which is an yttrium containing phosphate mineral. It normally occurs in conjunction with monazite but is much less abundant (Hetherington et al., 2008). Xenotime has a model formula of YPO_4 , in which the yttrium is tetrahedrally coordinated by phosphorous. The substitution of other members of the REE for yttrium in xenotime occurs, favouring the slightly smaller heavy rare earth elements (HREEs) (Hetherington et al., 2008). Generally xenotime has a REO content of 52%-67% and has been extracted from the ore using magnetic and flotation methods. The beneficiation of xenotime has not been widely reported (Jordens et al., 2013). Laterites normally also are considered to be an important deposit for heavy rare earths, though only two deposits are mined and both of them are in South China (Castor and Hedrick, 2006). Other rare earth oxide ore sources include sorosilicate, allanite, and fluorapatite. They occur on a small scale with unique operations, and access to detailed process information is limited (Jordens et al., 2013).

2.2 Distribution, history and process development of REs

Until 1990s the main suppliers for REs were Mountain Pass, USA (light rare earth ore, LREO) and Australia (HREO). China began to supply rare earth raw materials at about this time (Castor and Hedrick, 2006). In North America, 27 locations have been reported as productive or potentially productive REE bearing deposits (Fig 2. 1). Mountain Pass was effectively the only deposit being mined and had supplied most REs to the world (Castor, 2008). Mountain Pass is a carbonate deposit, and contains about 10% - 15% bastnaesite, 65% calcite/dolomite, and 20% -25% barite. The ratio of bastnaesite to monazite is 10 to 1. Although nine other RE minerals have been discovered at Mountain Pass, bastnaesite was the only type of mineral being processed. The ore has an 8.9% of REO content, based on a 5% cut-off grade (Castor, 2008). The detailed processing method was introduced by Castor (Castor and Hedrick, 2006). Before 2001, the feed was being screened, crushed, then processed by flotation which generated a 60% of REO raw material.



Fig 2.1 Productive or potentially productive REE bearing deposits in North America (Figure sourced from Castor, 2008).

The major REs source in Australia is Mount Weld, Western Australia. Full scale production commenced in 2013 (Jordens et al., 2013). This deposit contains mainly monazite, cheralite, cerianite, florencite and small amount of rhabdophane (Chan, 1992). Jordens reported two flotation schemes have been proposed. One was using single fatty acid as collector while the other one employed blended collector emulsions of fatty acid. No more data was available on what has been adopted and the performance is under review (Jordens et al., 2013).

Since the 1980s, over 1000 rare earth containing ore bodies have been discovered in China (Zhou and Han, 2010). Only a few of these are economically exploitable. There are four principal operating plants that play significant roles in supplying REs. The largest is Bayan Obo, Inner Mongolia, followed by Weishan (Shandong province), Maoniuping (Sichuan province) and Longnan (Jiangxi province) (Fig.2.2).



Fig. 2.2 Locations of four major plants for rare earth extraction in China: 1. Bayan Obo; 2. Weishan; 3. Maoniuping; 4. Longnan.

Bayan Obo and Weishan are both located in northern China, while Maoniuping is in central China and Longnan is located in the south. They represent over 95% of total rare earth reserves in China (Yu, 2001) and over 40% of the world's reserves (United

State Geological Survey, 2012; Zhou and Han, 2010). Table 2.3 lists the world's verified reserves of REO by country.

Table 2.3 Verified reserves of the world's REO, by country

COUNTRY	VERIFIED RESERVES (REO, MILLION TON)
China	52
Commonwealth of Independent States	19
United States	13
Australia	1.6
India	3.1
Brazil	0.048
Malaysia	0.03
Others	22
In Total	110.8

Data for China sourced from Zhou et al., 2010, while data for the other countries sourced from United State Geological Survey, 2012.

China has the dominant ore reserve, with the Commonwealth of Independent States second and the United States ranking third. REO reserves are quite widely distributed with 20% of the reserves coming from countries all over the world. In contrast to this distribution of ore bodies, Castor reports that only nine mines in six countries (four in China) were operating in 2006 (Castor and Hedrick, 2006). The United State Geological Survey published a report in 2012 that showed the trend to reopening and developing

rare earth mines has dramatically increased since 2011. The report listed geographically diverse continuing assessments of RE prospects (United State Geological Survey, 2012). Nevertheless, China is still the major supplier and the principal mine sites are still dominating the RE international market, with recent pricing falls making development uneconomic.

2.2.1 Chinese RE deposits

a. Bayan Obo deposit

The Bayan Obo deposit was discovered in the 1920s by Russian geologists when the region was under Soviet control (Castor and Hedrick, 2006). It also has been reported that the first RE mineral from this deposit was discovered by Dr. Ding Daoheng (Wu et al., 1996; Yu, 2001). It is an iron-REE-niobium deposit that was first mined in 1950s and has become the major world supplier of REOs. The Main and East ore bodies are the two largest, containing an average 5.5% of REOs (Castor and Hedrick, 2006; Yu, 2001). Over 170 different minerals have been found, with 15 of them containing REs. The main minerals are bastnaesite and monazite in ratios of 7:3 to 6:4 (Yu, 2001). There have been many studies reporting the geochemistry and mineralogy for this deposit (Castor and Hedrick, 2006; Chao et al., 1992; Xu et al., 2010; Yu, 2001; Yuan et al., 1992). The results are consistent except the genesis of this ore has not been agreed upon (Yuan et al., 1992).

The complicated composition of Bayan Obo ore led to over 20 unsuccessful proposals for processing being investigated, and it was not until 1990 that an optimised process was established. Yu reported that by 2001, the Bayan Obo plant had set up eight processing methods for their different types of ores, among which five are for oxidized ore and three for primary ore (Yu, 2001). Only one processing method has been

presented in detail while the others are under review (Zhao et al., 2012). The major processing stream is based on the recovery of the RE minerals from the iron ore tailings (Zhao et al., 2012). A Bayan Obo processing flow chart is presented as Diagram 2.1.

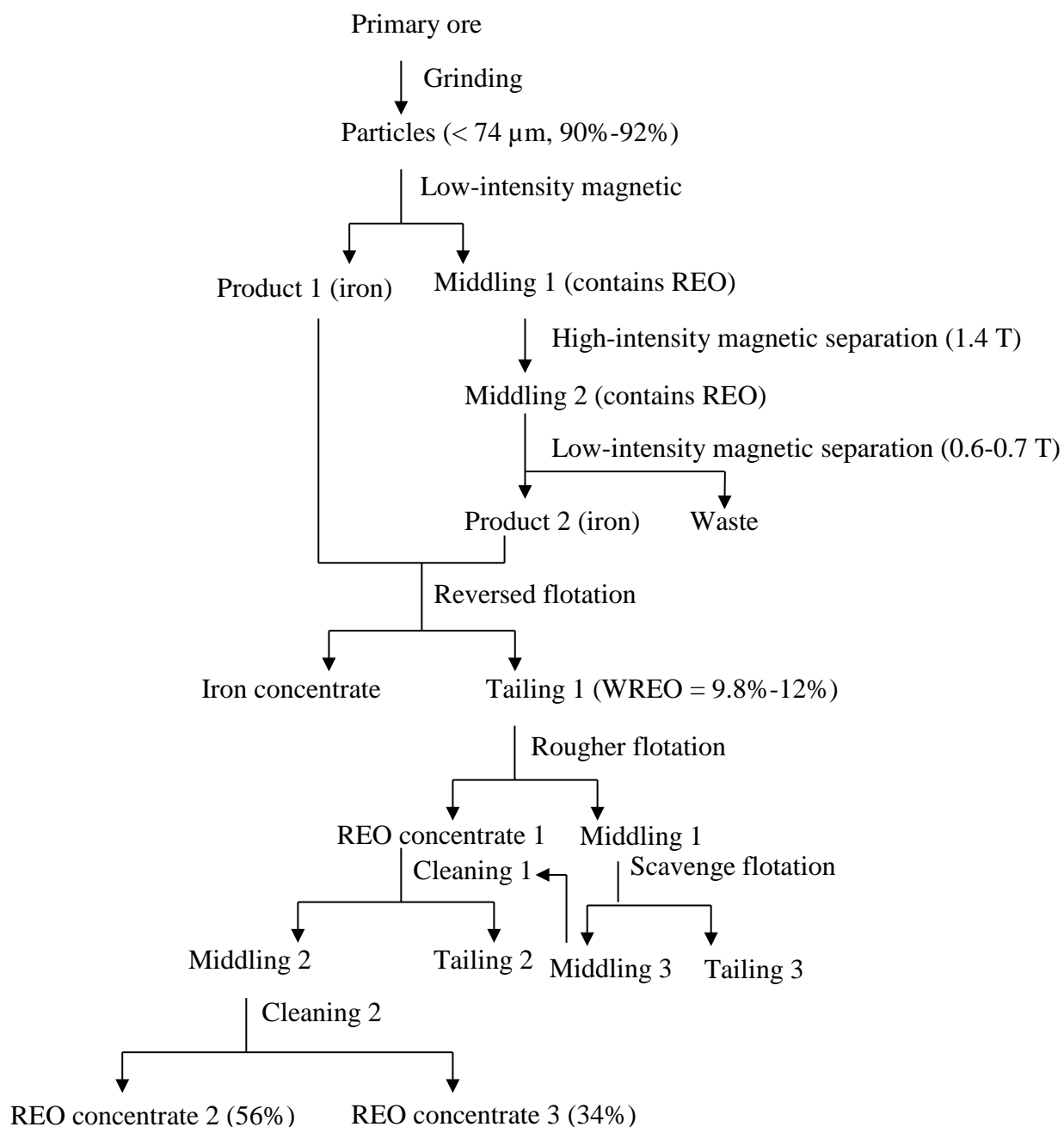


Diagram 2.1 Flow chart for processing of REs used in Bayan Obo plant (Data sourced from Yu, 2001).

In this process, the primary ore is treated in a magnetic separator with low-intensity. The tailing from this stage was further treated with a two-step magnetic separation. This concentrate, together with the middling generated in the first separation, is sent for reversed flotation, generating an iron concentrate, and the tailing from the process is the REs processor feed. The tailing normally contains 9.8% -12% by weight of REO. A three-step processing system is adopted for the REs concentration including a rougher flotation, scavenger flotation and two cleaning steps. After the cleanings, a REO grade of 56% in the concentrate and 34% in the secondary cleaner concentrate are achieved. The overall recovery from the primary ore averages 18.6%.

b. Weishan, Shandong deposit

Limited papers have been published for the Weishan Shandong deposit. The ore was discovered in 1958 by the Jinnan Geological Survey. It was not investigated comprehensively until 1970 and the first processing plant was established in 1982. The deposit is situated at Tanghu Village, Weishan Country and has 2.5 million ton (Mt) reserves within a 0.85 km² area (Yu, 2001). A schematic geological map was published by Wu (Wu et al., 1996). It is a bastnaesite - barite - carbonate vein hosted by quartz syenites and nordmarkites with a fine dissemination of REs minerals of 40-500 µm (Wu et al., 1996; Yu, 2001). The average grade of the RE deposit is 1.6% as reported by Wu, while Yu reported the grade as 3.1%.

The processing plant was relatively small, and production ceased in 2008, though the deposit represents 7% of the REO reserves of China (Zhou and Han, 2010). The Weishan deposit was mined as an open pit until 1986, when underground mining commenced as the ore grade had reduced from 5%-10% to 3%-4%. The ore was ground to < 74 µm (65%-75% of the feed) before flotation. A combination of a hydroxamate collector (code name L102, C₆H₄OHCONHOH), a depressor of sodium silicate and a

frother (Code name L102, chemical structure unknown) at a pH of 8-8.5 was used as the optimized flotation regime. Processing yielded a concentrate of > 60% REO at 60%-70% of recovery and a secondary concentrate of 32% with 10%-15% of recovery.

c. Maoniuping, Sichuan deposit

Maoniuping in Sichuan province became the most important mine recovering REs from vein deposits after Weishan was shut down. Some studies described it as a carbonatite deposit, similar to Mountain Pass in USA though this is not fully accepted (Castor and Hedrick, 2006; Huang et al., 2006; Xu et al., 2003). It located in the Mianning Country, Maoniuping Area and was discovered in 1985 during a geological survey that was searching for zinc-lead ores. The deposit has reserves of 214 Mt of REO (average grade 3.7%) and produced 0.15-0.2 Mt in 2005 (Shi, 2005). The REs ore consists mainly of coarse-grained bastnaesite with minor chevkinite, xenotime, britholite, allanite and monazite (Castor and Hedrick, 2006; Xu et al., 2008). The minerals are recovered in two size fractions; greater than 1.0 mm in diameter and as a fine sludge. 80% (by volume) of the particles are less than 44 μm (Yu, 2001).

In common with many Chinese mining ventures, there were over 100 RE processing plants in the early 1990s, with most of them being very small and inefficient. The majority were shut down by the government in 1995 leaving 39 operating. Gravity concentration is the primary beneficiation technique removing the slimes from the ore. Subsequent stages are either magnetic or flotation concentration depends on the minerals. In plants where gravity concentration only is practised, the ore is ground to <74 μm (62% of the feed), then is processed using a hydraulic classifier into 4 grades. The four grades are then concentrated by jigging tables. The final products yield 30%, 50% and 60% grades of REO concentrate with an overall recovery of 75%. Magnetic concentration had been used in plants prior to general adoption of the gravity process,

whereas now the combination of gravity and froth flotation is the preferred concentration process (Li and Zeng, 2000; Xiong and Ma, 2003; Yu, 2001). In this method, 80% of the feed is ground to $< 74 \mu\text{m}$ followed by gravity concentration, to generate a rough concentrate of 30% REO. This product provided feed for the froth flotation cells at pH 8-9. A hydroxamate collector (code name L102, $\text{C}_6\text{H}_4\text{OHCONHOH}$) is used as collector while sodium silicate is adopted as depressor during the flotation. This gave a 62-70% (of REO) concentrate with a recovery of 80%-85% (Li and Zeng, 2000).

d. The Longnan Jiangxi deposit

Longnan Jiangxi deposit is a lateritic deposit of an REE-bearing ionic absorption clay. Although lateritic deposits for REs have been discovered in many places around the world, Longnan currently is the only mine producing significant REO (Castor and Hedrick, 2006), it is an important supplier of heavy rare earths. This deposit was discovered in 1969 and subsequently, a wide range of lateritic deposits in Southern China were identified. The production from Southern China exceeded Bayan Obo to become the biggest producer in 2007. Longnan is the largest lateritic REs deposit that has been discovered. It has 1 Mt of verified REO reserves and produced 35,000 t of REO in 2006 (Huang et al., 2006; Yu, 2001). The mineral types are nerchinskite (25%-50%), illite (5%-20%), kaolinite (5%-10%) and montmorillonite ($<1\%$), these contain an average of 0.05%-0.3% REO. 50% of the REE content occurs in particles bigger than 0.78 mm (Chi and Tian, 2007) and the REEs are predominately in an ionic form. They are insoluble in water or ethanol, but can release RE ions into strong electrolyte solutions through ion exchange (Yu, 2001). Around 80% of the REEs content is ion exchangeable, 5% exist as a colloidal sediment, 13% is in a mineral form and only 0.01% is directly aqueous soluble (Chi and Tian, 2007). Most of the cerium is located in the

colloidal sediment and minerals. Table 2.4 compares the distribution for Ce and other REEs.

Table 2.4 Distribution of rare earths and Ce in different phases of the Longnan deposit (%)

	Ce	OTHER RARE EARTHS
Ion form	0.057	0.006
Hydrate (ion-exchangeable)	0.085	80.62
Colloidal sediment	21.06	5.30
Mineral (REO)	21.00	13.36

Data sourced from Chi and Tian, 2007.

It is a different ore type compared to bastnaesite or monazite hosted RE ores, the traditional processing methods are ineffective for this deposit. Processing has developed to include three principal stages, which are used to extract the REEs from the clay using an ion exchange process. In the 1960s, the raw material was simply poured in a pool (10-20 m³) reaching about 1.5 m in height and soaked in high concentration of sodium chloride (no data is available for the concentration of sodium chloride and the length of the soaking time). The leachate was filtered and collected from the bottom of the pool, and precipitated using saturated oxalate solution. After drying, calcining, washing and re-fired, a > 90% REO product was obtained (Diagram 2.2).

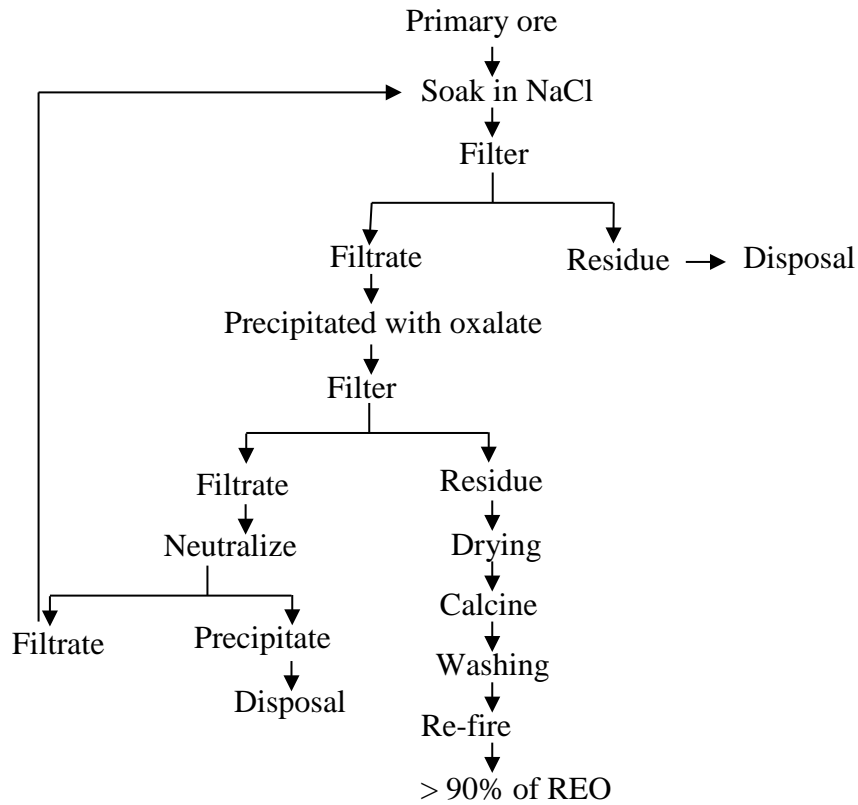


Diagram 2.2 Extraction process of REO from Longnan Jiangxi ore.

The method required large amounts of sodium chloride resulting in contamination problems for the REO product (sodium co-precipitation) and environmental concern (the residue causes land salinization). Sodium chloride was replaced by ammonium sulphate in the 1970s. Dump leaching instead of pool leaching has also been reported for this ore (Chi and Tian, 2007). Both extraction methods significantly deteriorate the surrounding environment. It has been reported that producing 1 t of REO required 200-800 m² of surface area to be stripped with a corresponding 800-1000 m³ of residue needing disposal. In the 1980s, in-situ leaching was proposed and had been adopted by about 50% of mills by 2000 (Huang et al., 2006; Yu, 2001). Injection wells are used to inject the leaching solution into the ore body to exchange with the REEs ions. The arrangement involved gravity flow of the leachate from the injection wells on the high side of the deposit with a liquid extract being collected at the bottom of the deposit, it is

generally used for hillside mineral locations (Chi and Tian, 2007). The long-term impact of this technique on the environment should be considerable and *in-situ* leaching requires further investigation.

2.3 Flotation reagents and interaction on mineral surface

Flotation is the most widely utilized separation and concentration process for REE deposits. It has greatly improved the performance of the recovery process of minerals from gangue, especially for low-grade feed, which made it possible to extract valuable metals from the once non-commercial ore. Flotation involves complex physico-chemical interactions between flotation reagents and the mineral surface and the process is not fully understood. The key mechanism is to attach valuable minerals to air bubbles and this requires a hydrophobic surface mineral surface (Wills, 2006). For RE minerals, the surface is not naturally hydrophobic and does not attach to the air bubbles without surface modification. A collector is designed to render the mineral surface water-repellent by absorption and interaction on the surface. The general approach used to concentrate bastnaesite mineral has been flotation with one of n-octanohydroxamate, an aromatic hydroxamate, or a fatty acid collector. These processes often used in conjunction with other separation techniques (Pavez et al., 1996; Sawaji et al., 1992; Zheng and Lin, 1994).

China's processing plants, the biggest REs producer, have been developing collectors for over 50 years, and several collectors have been synthesized and tested in the REE flotation process. Fatty acids were the first type of collector utilized in the REEs plants in the 1960s. Other collectors included oleic acid, oxidized paraffin soap and phthalic acid. Fatty acids collectors possess a non-polar group and a polar group. The polar end of the collectors adsorbs on the mineral particles while the non-polar ends orientates towards the solution, and resulted into a hydrophobic surface of the mineral. Luo (Luo et al., 2002) reported that, on a laboratory scale, using oleic acid or oxidized paraffin can yield a 40% of REO concentrate with 55%-75% of recovery from a 7%-9% feed. However, Yu (Yu, 2001) reported they only achieved 20% of REO concentrate

when using fatty acid as a collector in a Bayan Obo mill. This increased to 30% if a shaking table was utilized in a further refinement of the process. Phthalic acid has been reported as a selective collector for the separation of bastnaesite from monazite, it produced a 70.1% concentrate with a 64.98% of recovery from 5.3% feed in a laboratory trial (Ore sourced from Weishan, Shandong) (Luo et al., 2002).

Fatty acid was the dominant collector in China for about 10 years, before hydroxamate collectors began to be developed, due to the poor selectivity and efficiency of fatty acids. The hydroxamates are a chelating reagent that can form a five-membered ring structure with metal cations. The collector structure and activity can be modified through different R groups connecting to the carboxyl (Table 2.5).

Table 2.5 Hydroxamate collectors used in China's rare earth plants

TYPE/NAME	CHEMICAL FORMULA
Alkyl hydroxamic acid (C ₅ -C ₉)	RCONHOH
Naphthenic hydroxamic acid	C _n H _{2n-1} CONHOH
Phenyl hydroxamic acid	C ₆ H ₅ CONHOH
Salicylhydroxamic acid	C ₆ H ₄ OHCONHOH
H ₂₀₅	RCONHOH (structure see Fig. 2)
H ₃₁₆	N/A (modified from H ₂₀₅)
LF-8	N/A
XQ ₁₀₇	N/A

Several studies have been published on hydroxamate collectors covering the chemical and physical properties, absorption mechanism with metal, and performance in

flotation processing (Assis et al., 1996; Che et al., 2004; Higgins et al., 2006; Hope et al., 2010; Liu et al., 2006; Luo et al., 2002). Pradip and Fuerstenau investigated the flotation of bastnaesite from Mountain Pass using both fatty acid and alkyl hydroxamate collectors (Fuerstenau and Pradip, 1984; Pradip and Fuerstenau, 1983, 1991). The authors concluded that n-octanohydroxamate (OHA) was a more selective flotation reagent than the fatty acid collector. The laboratory investigation of hydroxamate flotation of RE minerals generally has been limited to n-octanohydroxamate (Pavez et al., 1996; Perereia and Peres, 1997; Pradip, 1988) and naphthalenic hydroxamate collectors (Cheng et al., 2007; Ren et al., 1997; Xu et al., 2002). Xu et al. (2002) used 1-hydroxy-2-naphthylhydroxamic acid and obtained a 37% REO concentrate from an 11% feed with an 80% recovery. Ren et al. (1997) reported the use of a similar hydroxylated naphthalene hydroxamic acid (claiming superior collection properties) for the flotation of bastnaesite ore.

The first type of hydroxamate used at China's REs ore processing plant was alkyl hydroxamic acid. It was utilized in Bayan Obo mill in 1975 and yielded a 67.8% of REO with 66.8% of recovery from a 35.8% of secondary concentrate. However the industrial production quality of the collector was not consistent and application required heavy dosing during flotation which had a significant impact on the processing cost. Naphthenic hydroxamic acid was subsequently produced and it had replaced alkyl hydroxamic acid from 1979-1985 (Yu, 2001). Luo (Luo et al., 2002) reported that with naphthenic hydroxamic acid, a 60.1% of REO product was produced from a 23% feed with 65.2% recovery in the Bayan Obo plant. Phenyl hydroxamic acid and salicylhydroxamic acid were also reported being used in this stage but with a similar performance as naphthenic hydroxamic acid (Luo et al., 2002). In 1985, the Baotou

Rare Earth Institute synthesized a new hydroxamate collector with a code name H₂₀₅ (Fig. 2.3).

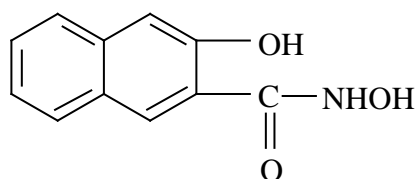


Fig. 2.3 Structure of H₂₀₅ molecule

Subsequently, this reagent has been widely utilized in many rare earths processing plants and several papers have reported on its performance (Che et al., 2004; Meng, 1994; Ren and Lu, 1997; Zeng and Li, 1994). The results obtained varied, with a produced REO concentrate from 24.4% to 65.4% and a recovery from 51.4% to 88.0% depending on the grade of the feed and ore type. Table 2.6 summarizes the performance of H₂₀₅ reported by different authors.

Table 2.6 Performance of H₂₀₅ with different RE ores

MINERALS OR ORES	GRADE OF FEED (%)	GRADE OF REO CONCENTRATE (%)	RECOVERY (%)	TRIAL SCALES	DATA SOURCES
Bastnaesite	3.8	24.4	79.6	Laboratory	Zeng and Li, 1994.
Bastnaesite	4.4	34.7	80.5	Laboratory	Zeng and Li, 1994.
Bastnaesite	5.4	45.0	81.2	Laboratory	Zeng and Li, 1994.
Bastnaesite	6.2	44.0	80.9	Laboratory	Zeng and Li, 1994.
Bastnaesite	9.5	52.7	71.6	Laboratory	Zeng and Li, 1994.
Bastnaesite	10.4	50.3	82.9	Laboratory	Zeng and Li, 1994.
Banyan Obo ore	8.1	42.6	60.1	Industry	Luo et al., 2002.
Banyan Obo ore	12.6	62.4	51.4	Industry	Luo et al., 2002.
Maoniuping ore	9.6	65.4	88.0	Industry	Luo et al., 2002.
Banyan Obo ore	NA	67.4	84.0	Laboratory	Meng, 1994.
Banyan Obo ore	NA	62.3	74.8	Industry	Meng, 1994.
Maoniuping ore	4.1	66.7	71.4	Laboratory	Meng, 1994.
Weishan ore	7.6	47.2	80.3	Laboratory	Meng, 1994.
Monazite	30.7	61.0	68.6	Laboratory	Che et al., 2004.
Banyan Obo ore	NA	53.1	67.1	Laboratory	Li et al., 2007.

NA: Not available

Though H₂₀₅ greatly improved the efficiency of the flotation, there were still some problems affecting the processing, for example, the addition of substantial quantities of

alcohol and aqueous ammonia is required when using H₂₀₅ in order to improve solubility (Yu, 2001). From 1992 to 1994, another reagent H₃₁₆ was introduced, but the structure of H₃₁₆ has not been published to date. Yu (Yu, 2001) reported that H₃₁₆ was a modified form of H₂₀₅ that did not require aqueous ammonia when being used. Ren reported H₃₁₆ had a similar performance to H₂₀₅ (Ren et al., 1995) but less depressant was needed (about 26.0 kg of Na₂SiO₃ less when producing one ton of REO concentrate). More recently, new collectors have been reported (code names LF-8 and XQ107, Table 2.3), however, their structures and performances are under review, with the only publicly available information being that they are all hydroxamate compounds (Cai et al., 2009; Zhao et al., 2000).

The utilization of combined flotation reagents has also been studied. Lan reported that through the combined use of phthalic acid and paraffin as collectors they could improve the selection for bastnaesite and monazite (Lan et al., 1983). Ren has studied the interactions between the depressants and the collectors by building a regression mathematical model. He concluded that the yield of REO was the same with a range of combinations of depressants and collectors. The optimised combination was the minimum cost of the reagents (Ren and Lu, 1997). It was also indicated that when replacing the powerful and selective reagent proportionally with a weak reagent one could yield the same result, but with a significant reduction in cost (Ren and Lu, 1997).

2.4 Environmental concern

After over 50 years of producing REs, environmental contamination and the ecological damage have attracted significant concern in the last few years. These environmental problems include radioactive pollution, water and dust pollution, soil loss and salinization, natural vegetation destruction, etc. Consequently, it was reported that the wellbeing of the animals and people who live around the Bayan Obo mine site has been threatened (Chen et al., 2002; Gao and Zhou, 2011).

Many RE ores contain natural radioactive material, mainly Th, along with minor amounts of radium (Ra). This type of contamination needs to be carefully monitored and managed. Typical monazite contains 4% to 10% of ThO_2 while bastnaesite contains much lower thorium contents. Mountain Pass ore was reported to comprise of 0.1% of ThO_2 in the bastnaesite mineral (Castor and Hedrick, 2006) and Bayan Obo has an average of 0.04% in the primary ore (Bai et al., 2004). The REO concentrate from Bayan Obo contain 0.02% to 1.68% and 0.11% to 1.67% of ThO_2 in bastnaesite and monazite respectively (Table 2.7).

Table 2.7 ThO₂ in bastnaesite and monazite from Bayan Obo ore (%)

SAMPLE NUMBER	BASTNAESITE	MONAZITE
1	0.46	0.7
2	0.11	0.26
3	0.58	0.19
4	0.20	0.23
5	0.32	0.38
6	0.18	0.11
7	0.02	0.17
8	0.52	0.42
9	1.68	1.67
10	—	0.23
11	—	0.77

Data sources from Luo et al., 2010.

At the Bayan Obo mine, the mine tailings were transported and deposited in the biggest tailings dam yet built in China. The dam is about 11 km², 1.1 km in depth and was sealed with water on the top surface. It was reported the dam had stored about 1.8 billion tonne of tailings, containing 80.6% of the Th from the ore (Luo et al., 2010). However, this tailings dam did not have a well-designed containment structure and leaching of the contaminants into the ecosystem has resulted. In addition, because it is located in an arid to semiarid area, the water seal recedes in winter, and this leads to radioactive dust contamination. This dust, carrying Th, migrates and spreads through

the surrounding district. Samples collected from Bayan Obo area showed that ^{232}Th in soil specimens was 1.7 times higher than uncontaminated background, while grass samples and sheep bone specimens were 32 and 1.18 times higher than their control groups, respectively (Zhang et al., 2001). Bai (Bai et al., 2004) reported that the average γ radiation dose in the tailing dam is $100.7 \times 10^{-8} \text{ Gy} \cdot \text{h}^{-1}$ and the highest dose recorded outside the dam is $87.4 \times 10^{-8} \text{ Gy} \cdot \text{h}^{-1}$, which is 9 times higher than the background value. γ radiation can be recorded up to 2 km from the dam. A study indicated that the residents living in Bayan Obo area received 2.96 mSv a year of radiation which is 32.2% higher than the average group (Wang et al., 2009). Unexpected death of livestock and fish have also been reported which may due to the radioactive contamination (Gao and Zhou, 2011). For humans, the death rate due to lung cancer dramatically increased in the processing workers, attributed to the dust pollution (Chen et al., 2002).

Water pollution by radiation was also reported. There have been 32 monitor points spread around the tailing dam, and these showed that the total specific activity in the underground water is 0.9-6.7 higher than background (Bai et al., 2004). However, of much more concern, is that the underground water is permeating at a rate of 300 m per year towards to the Huang River which is only 10 km away and no mitigation strategies have been implemented as yet (Gao and Zhou, 2011).

Apart from the radioactive pollution, soil salinization and natural vegetation destruction are the other major environmental concerns in the mining and processing of rare earths. This problem was most significant for the South China rare earth mines. As mentioned above, large amount of rocks were stripped off before being processed for the lateritic type deposit and this has inevitably destroyed the ecosystem. Even though *in-situ* leaching has been adopted in recent years, the high volumes of leaching solutions have had a negative impact on the environment. The extract solution contains 3% of

ammonia sulphate and the leaching time can take up to 150-400 d, which had caused soil salinization and landslides (Tang et al., 2000). In addition, the residue of the RE ions in the leachate has poisoned the water and the concentration was recorded as 1000 times higher than freshwater (Zhu et al., 2002). This section has only reviewed two major REs mines regarding their environmental issues as no more data are available for others. Waste gas and water from the metallurgical process also have greatly affected the natural environment (Lin, 1995, 2008).

2.5 Future trends

The demand of REO is expected to increase as the high-tech industry grows. China effectively became the monopoly supplier due to its competitive pricing, low labour expense and relatively loose environmental permits (Castor and Hedrick, 2006). However, China has moved to minimise wasteful processing and environmental damage by closing a number of poorly operated facilities. Several papers have been published on improving the performance of processing, for example, applying the fractional extraction theory to improve the efficiency, also new flotation reagents have been developed (Li et al., 2012; Li et al., 2007; Xu et al., 2002). Nevertheless, the environmental issue has been still the biggest concern raised in recent years. Several studies have been conducted investigating the actual effect on environment and organisms by the mining and processing (Chen et al., 2002; Chi and Tian, 2007; Gao and Zhou, 2011). A proposal was submitted to the Chinese government in 2005 appealing for improvement in the efficiency of production and protection of the environment (Xu et al., 2005). That proposal suggested the development of the feasibility for recovering thorium and its use as a nuclear fuel. It also advised that the mining companies gradually reduce mining on the Main and East deposits of Bayan Obo and stop mining in 2012. Thereafter, they would concentrate REO from the tailing stockpiles. Similar proposals have been mentioned in several papers (Chen et al., 2002; Gao and Zhou, 2011; Jia et al., 2011).

Exploitation and development for the potential RE deposits and the existing mine plants require innovative, efficient and environmentally acceptable processing technologies. Before applying to an industrial scale, fundamental research is essential to identify the interactions and mechanism in the system. Therefore, the research described in this thesis was undertaken with the aim of facilitating these requirements.

References

- Adroja D. T., 1991, Valence fluctuation and heavy fermion behaviour in rare earth and actinide based compounds, *Journal of Magnetism and Magnetic Materials*, 100, 126-138.
- Arinicheva Y., Bukaemskiy A., Neumeier S., Modolo G. and Bosbach D., 2013, Studies on thermal and mechanical properties of monazite-type ceramics for the conditioning of minor actinides, *Progress in Nuclear Energy*.
- Assis S. M., Montenegro L. C. M. and Peres A. E. C., 1996, Utilisation of hydroxamates in minerals froth flotation, *Minerals Engineering*, 9, 103-114.
- Bai L. N., Sui W. L. and Lin Z., 2004, Study of the environmental impact by the radiation generates during the rare earth and iron production in Bayan Obo ore, *Chinese Rare Earth*, 25, 75-77 (稀土).
- Brandt F., Neumeier S., Schuppik T., Arinicheva Y., Bukaemskiy A., Modolo G. and Bosbach D., 2014, Conditioning of minor actinides in lanthanum monazite ceramics: A surrogate study with Europium, *Progress in Nuclear Energy*, 72, 140-143.
- Cai Z. L., Cao M. L., Che L. P., Yu Y. F. and Hu H. Y., 2009, Study on the beneficiation process for recovering rare-earth from the LIMS tailing of HIMS rougher concentrate after magnetizing roasting in Baogang Concentrator, *Metal Mine* 7, 154-157 (金属矿山).
- Castor S. B., 2008, Rare Earth Deposits of North America, *Resource Geology*, 58, 337-347.

- Castor S. B. and Hedrick J. B., 2006, Rare earth elements, 7th edition, Kogel J. E., Trivedi N. C., Barker J. M. and Krukowski S. T.: Society for Mining, Metallurgy and Exploration, Colorado Industrial Minerals & Rocks, Littleton, 773-774.
- Chan T. N., 1992, A new beneficiation process for the treatment of supergene monazite ore, In: Rare Earths: Extraction, Preparation and Applications: TMS and AusIMM, San Diego 77-94.
- Chao E. C. T., Back J. M. and Minkin J. A., 1992, Host-rock controlled epigenetic, hydrothermal metasomatic origin of the Bayan Obo REE-Fe-Nb ore deposit, Inner Mongolia, P.R.C, Applied Geochemistry 7, 443-457.
- Che L. P., Yu Y. F., Pang J. X., Yuan J. Z. and Wang X. T., 2004, Synthesis, properties and role mechanism of hydroxamic acid collectors of RE mineral flotation, Chinese Rare Earth, 25, 74-83 (稀土).
- Chen X. A., Han X. M., Cheng Y. E., Feng Z. L., Feng G. D., Bao X. C., Zhang J. J., Dong Y. F., Ma L. F., Zhang G. Q. and Wu C. R., 2002, Study of the health effects exposure to thorium dusts of the miners in China, Chinese Journal of Radiological Health, 11, 6-8 (中国辐射卫生).
- Cheng J., Hou Y. and Che L., 2007, Flotation separation on rare earth minerals and gangues, Journal of Rare Earth, 25, 62-66.
- Cheng T.-W., Holtham P. N. and Tran T., 1993, Froth flotation of monazite and xenotime, Minerals Engineering, 6, 341-351.
- Chi R. A. and Tian J., 2007, Review of weathed crust rare ore, Journal of the Chinese Rare Earth Society, 25, 641-650 (中国稀土学报).
- Clavier N., Podor R. and Dacheux N., 2011, Crystal chemistry of the monazite structure, Journal of the European Ceramic Society, 31, 941-976.

- Crozier R. D., 1992, Flotation: theory, reagents and ore testing, 1th Edition, Pergamon Press, England, UK, 2-3.
- Cui J., Hope G. A. and Buckley A. N., 2012, Spectroscopic investigation of the interaction of hydroxamate with bastnaesite (cerium) and rare earth oxides, Minerals Engineering, 36-38, 91-99.
- De Boer M. A. and Lammertsma K., 2013, Scarcity of Rare Earth Elements, ChemSusChem, 2045-2055.
- Dent P. C., 2012, Rare earth elements and permanent magnets (invited), Journal of Applied Physics, 111, 721.
- Deun R. V., Fias P., Nockemann A., Schepers P., Parac-Vogt T. N., Hecke K. V., Meervelt L. V. and Binnemans K., 2004, Rare-earth quinolinates: Infrared-emitting molecular materials with a rich structural chemistry, Inorganic Chemistry, 43, 8461-8469.
- Editorial, 2011, The new oil?, Nature Photonics, 5, 1-1.
- Farmer V. C., 1974, The Infrared Spectra of Minerals, Mineralogical Society Monograph 4: Mineralogical Society, London, 227-285.
- Feng P. K. and Fernando Q., 1960, Chelates of 4-hydroxybenzothiazole with the rare earths, Analytica Chimica Acta, 24, 548-554.
- Frost R. L. and Dickfos M. J., 2007, Raman spectroscopy of halogen containing carbonates, Journal of Raman Spectroscopy, 38, 1516-1522.
- Frost R. L., López A., Scholz R., Xi Y. and Belotti F. M., 2013, Infrared and Raman spectroscopic characterization of the carbonate mineral huanghoite – And in comparison with selected rare earth carbonates, Journal of Molecular Structure, 1051, 221-225.

- Fuerstenau D. W. and Pradip, 1984, Mineral flotation with hydroxamate collectors, Reagents in the Minerals Industry, Jones M. J. and Oblatt R.: Institute of mining and metallurgy, London, 61–168.
- Gao Z. Q. and Zhou Q., X., 2011, Contamination from rare earth ore strip mining and its impacts on resources and eco-environment, Chinese Journal of Ecology, 30, 2915-2922 (生态学杂志).
- Hetherington C., Jercinovic M., Williams M. and Mahan K., 2008, Understanding geologic processes with xenotime: Composition, chronology, and a protocol for electron probe microanalysis, Chemical Geology, 254, 133-147.
- Heuser J., Bukaemskiy A. A., Neumeier S., Neumann A. and Bosbach D., 2014, Raman and infrared spectroscopy of monazite-type ceramics used for nuclear waste conditioning, Progress in Nuclear Energy, 72, 149-155.
- Higgins F. S., Magliocco L. G. and Colthup N. B., 2006, Infrared and raman spectroscopy study of alkyl hydroxamic acid and alkyl hydroxamate isomers, Applied Spectroscopy, 60, 279-287.
- Hope G. A., Woods R., Buckley A. N., White J. M. and Mclean J., 2010, Spectroscopic characterisation of n-octanohydroxamic acid and potassium hydrogen n-octanohydroxamate, Inorganica Chimica Acta, 363, 935-943.
- Huang X. W., Li H. W., Xue X. X. and Zhang G. C., 2006, Development status and research progress in rare earth hydrometallurgy in China, Journal of the Chinese Rare Earth Society, 24, 129-133 (中国稀土学报).
- Imanaka N., Masui T. and Kim Y. W., 2004, First electrochemical growth of $\text{Tb}_{16}\text{O}_{30}$ single crystal, Journal of Solid State Chemistry, 177, 3839-3842.

- Jia Y. Z., Zhou Y. H. and Lv P., 2011, Comprehensive improvement program for the environment of Shangdalahai and Xiadalahai village in Baotou Kundoulum district boerhantu town, Northern Environment, 23, 69-71 (北方环境).
- Jordens A., Cheng Y. P. and Waters K. E., 2013, A review of the beneficiation of rare earth element bearing minerals, Minerals Engineering, 41, 97-114.
- Kanazawa Y. and Kamitani M., 2006, Rare earth minerals and resources in the world, Journal of Alloys and Compounds, 408-412, 1339-1343.
- Kotani A., Matsuda Y. H. and Nojiri H., 2009, Theoretical and experimental study of high-magnetic-field XMCD spectra at the L_{2,3} absorption edges of mixed-valence rare-earth compounds, Journal of Physics: Conference Series, 190, 012013.
- Kulyukhin S. A., 1998, Complex formation of divalent lanthanides and actinides, Journal of Alloys and Compounds, 271-273, 168-171.
- Lan Y. C., Xu X. F., Huang F. L. and Zhao Q. H., 1983, Flotation study with phthalic acid for concentrate bastnaesite from Weishan Shandong, Chinese Rare Earth, 4, 27-29 (稀土).
- Li F. and Zeng X., 2000, Flotation research for fine particles rare earth minerals, Journal of Shanghai Second Polytechnic University, 2, 1-7.
- Li M., Liu Z. G., Wang M. T., Gao K., Zhang D. L. and Hu Y. H., 2012, The application of fractional extraction theory in the rare earth mineral processing of Baiyunebo tailing, Journal of Inner Mongolia University of Science and Technology, 31, 4-8 (内蒙古科技大学学报).

- Li Y., Zuo J. C. and Liu Y. H., 2007, Application and research of hydroxamic acid as collectors on flotation of rare earth ores, *Non-Ferrous Mining and Metallurgy*, 23, 30-33 (有色矿冶).
- Lin H. C., 1995, Treatment of waste water in rare earth production, *Industrial Water Treatment*, 15, 1-3 (工业水处理).
- Lin H. C., 2008, Treatment of waste gases in rare earth production, *Shanghai Nonferrous Metals*, 29, 84-87 (上海有色金属).
- Liu W. G., Wang B. Y., Dai S. J., Ma A. X. and Wei D. Z., 2006, Current application and development prospect of hydroxamic acid in flotation, *Non-Ferrous Mining and Metallurgy*, 22, 25-27 (有色矿冶).
- Luo J. J., Ren J., Tang F. Q. and Zhou G. Y., 2002, Development on flotation reagents of rare earth minerals in China., *Journal of the Chinese Rare Earth Society*, 20, 385-391 (中国稀土学报).
- Luo M. B., Guo G. L., Guo G. L. and Liu C. Z., 2010, Occurrence state of thorium in baotou rare earth concentrate, *Chinese Journal of Rare Metals*, 34, 471-474 (稀有金属).
- Meng Y., 1994, Application of hydroxamate on the flotation of rare earth, *Chinese Rare Earth*, 15, 68-71 (稀土).
- Paramanik U. B., Anupama, Burkhard U., Prasad R., Geibel C. and Hossain Z., 2013, Valence fluctuation in $\text{CeMo}_2\text{Si}_2\text{C}$, *Journal of Alloys and Compounds*, 13, 1-18.
- Pavez O., Brandao P. R. G. and Peres A. E. C., 1996, Technical note adsorption of oleate and octyl-hydroxamate on to rare-earths mienrals, *Minerals Engineering*, 9, 357-366.

- Perereia C. A. and Peres A. E. C., 1997, Flotation concentration of a xenotime preconcentrate, *Minerals Engineering*, 10, 1291–1295.
- Pradip, 1988, Applications of chelating agents in mineral processing, *Minerals and Metallurgical Processing*, 5, 80–89.
- Pradip D. W. and Fuerstenau, 1983, The adsorption of hydroxamate on semi-soluble minerals, part I: adsorption on barite, calcite and bastnaesite, *Colloids Surfaces* 8, 103–119.
- Pradip D. W. and Fuerstenau, 1991, The role of inorganic and organic reagents in the flotation separation of rare-earth ores, *International Journal of Mineral Processing*, 32, 1-22.
- Pradip and Fuerstenau D. W., 2013, Design and development of novel flotation reagents for the beneficiation of Mountain Pass rare-earth ore, *Minerals and metallurgical processing*, 30, 1-10.
- Ren J., Huang L. X., Huang C. X., Liu Y., Zhang W., Zhao J. C., Tian J. D., Zhao Q. H. and Song C. Q., 1995, Industrial productive test on separation the rare earth concentrate by a new type of collector-H316, *Chinese Rare Earth*, 16, 14-18 (稀土).
- Ren J., Lu S., Song S. and Niu J., 1997, A new collector for rare earth mineral flotation, *Minerals Engineering*, 10, 1395–1404.
- Ren J. and Lu S. C., 1997, Interaction and correlation of reagents in flotation system of rare-earth mineral, *Journal of University of Science and Technology Beijing*, 19, 429-433 (北京科技大学学报).
- Sawaji D., Yamashita H. and Maekawa T., 1992, Flotation of rare-earth ions with octadecyliminobismethylenebisphosphonic acid, *Analytical Sciences*, 8, 247-250.

- Shi Y., 2005, A review on rare-earth industry and chemical product (part 1), Shanghai Chemical Industry, 30, 32-34 (上海化工).
- Spedding F. H., 1971, The rare earths, historical introduction to the rare earths, Spedding F. H. and Daane, A. H., Robert E. Krieger Publishing Co. Inc., New York, 1-3.
- Survey U. S. G., 2012, Rare earths, Minerals and commodity summaries, 128-129.
- Tang X. Z., Li M. N. and Y. Y., 2000, Stope slide in *in-situ* leaching of ionic type rare-earth ore and its countermeasures, Metal Mine, 289, 5-8.
- Tatsuo O., 2011, Rare earth resources and related industries in Japan, Journal of MMIJ, 127, 549-557.
- Wang X. Q., Guo C. X., Bai L. N., Cai Y. M., Liu Y. X. and D. T., 2009, Radiothorium contamination tendency and control measure for Baotou steel factory tailing dam, Radiation Protection, 4, 270-274.
- Wenzel T. J., Willams E. J., Haltiwangers R. C. and Sievers R. E., 1985, Studies of metal chelates with the novel ligand 2,2,7-trimethyl-3,5-octanedione, Polyhedron, 4, 369-378.
- Wertheim G. K., 1979, The intermedia valence state in rare earth compounds, bulk and surface manifestations, Journal of Electron Spectroscopy and Related Phenomena, 15, 5-14.
- Wills B. A., 2006, Wills' Mineral Processing Technology, 7th Edition, Elsevier Ltd, Oxford, UK, 267-277.
- Wu C., Yuan Z. and Bai G., 1996, Mineralogical Society, Rare earth deposits in China, Rare Earth Minerals: Chemistry, Origin, and Ore Deposit, Jones A. P., Wall F. and Villiams C. T.: Chapman and Hall, London, 281-310.

- Xiong S. and Ma C., 2003, Experimental research on flotation separation of a bastnaesite-type rare-earths ore, *Multipurpose Utilization of Mineral Resources*, 3, 8-12.
- Xu C., Campbell I. H., Kynicky J., Allen C. M., Chen Y., Huang Z. and Qi L., 2008, Comparison of the Daluxiang and Maoniuping carbonatitic REE deposits with Bayan Obo REE deposit, China, *Lithos*, 106, 12-24.
- Xu C., Huang Z. L., Liu C. Q., Qi L. and Li W. B., 2003, Geochemistry of carbonatites in Maoniuping REE deposit, Sichuan Province, China, *Science in China (Series D)*, 46, 246-256.
- Xu C., Wang L., Song W. and Wu M., 2010, Carbonatites in China: A review for genesis and mineralization, *Geoscience Frontiers*, 1, 105-114.
- Xu G. X., Shi C. X., Wang D. Z., Zhao Z. X., Wang Z. D., He Z. M., Wang N. Y., Fang S. X., Guo M. S., Oouyang Y., Fei W. Y., Liu Y. F., Yang Y. C., Li D. Y., Tang X. Y. and Gu Z. M., 2005, Urgent appeal for protecting the thorium and rare earth resources and protection of Huang River and Baotou from radioactive contamination, *Chinese Academy of Science Member & Academic Divisions*, 20, 448-450 (院士与学部).
- Xu J., Xu X. and Wang J., 2002, Synthesis of 1-hydroxy-2-naphthyl hydroxamic acid and application to collecting rare earth minerals, *Nonferrous Metals* 54, 72 - 73 (有色金属).
- Yu Y., 2001, Dressing technology of REO ore and its development in China, *Journal of China University of Mining & Technology*, 30, 534-542 (中国矿业大学学报).

- Yuan Z. X., Bai G., Wu C. Y., Zhang Z. Q. and Ye X. J., 1992, Geological features and genesis of the Bayan Obo REE ore deposit, Inner Mongolia, China, *Applied Geochemistry*, 7, 429-442.
- Zeng X. L. and Li J. F., 1994, A new collector for flotation of bastnaesite (一种氟碳铈镧矿选择性捕收剂), Google Patents, CN1090226A.
- Zepf V., 2013, Rare earth elements: A new approach to the nexus of supply, demand and use: exemplified along the use of neodymium in permanent magnets, Doctoral, the University of Augsburg, Germany.
- Zhang L. C., Bai L. N. and Wang L. X., 2001, Environmental pollution and prevention of radioactive solid waste in Bayan OBo mine, Inner Mongolia Environmental Protection, 13, 39-40 (内蒙古环境保护).
- Zhao C. H., Chen H. C. and Yue X. C., 2000, Application of LF-8 and LF-6 collectors in rare earth beneficiation, *Chinese Rare Earth*, 21, 1-3 (稀土).
- Zhao R. C., Zhang B. W., Bulinchake and Zhang Y., 2012, Experimental study on recovering rare-earth from the tailing, *Journal of Inner Mongolia University of Science and Technology*, 31, 9-13 (内蒙古科技大学学报).
- Zheng X. P. and Lin H. K., 1994, Mineralogy and flotation of rare-earth-bearing barium fluorophlogopite, *Minerals Engineering*, 7, 1475-1503.
- Zhou X. and Han X., 2010, Status and development of rare earths industry in China (Part One), *Chinese Rare Earth*, 31, 96-101, (稀土).
- Zhu J. H., Yuan Z. K., Wang X. Y. and Yan S. M., 2002, Investigation on the contents of rare earth elements in environment of rare earth ore area in Jiangxi, *Journal of Environment and Health*, 19, 443-444 (环境与健康杂志).

CHAPTER 3

EXPERIMENTAL AND INSTRUMENTAL

3.1 Preamble

Spectroscopic techniques are powerful tools that can be used to investigate the properties of molecules and surfaces *in situ* and *ex situ*. Infrared and Raman spectroscopy, atomic force microscopy and atomic force microscopy tandem confocal Raman spectroscopy have been utilized in this investigation because of their ability to obtain structural and bonding information, such that the mechanisms of interaction between the reagents and the target surface *in situ* can be determined. AFM-Raman provides *in-situ* imaging and chemical groups characterization information. It is especially useful for identification of the absorption location on the surface. *Ex-situ* techniques including scanning electron microscopy - energy-dispersive X-ray spectroscopy and X-ray photoelectron spectroscopy were also used for providing information on elemental analysis and element oxidation states.

This chapter is divided into two major sections. The first part provides details of materials and experimental methods, including the preparation of all the solutions and chemicals required and synthesis of the RE compounds. The second gives a technical and instrumental introduction, related critical review and detailed instrumental information.

3.2 Material and experimental methods

3.2.1 Chemicals

Solutions were prepared using Analytical Reagent (AR)-grade chemicals and doubly de-ionized (DDI) water.

Cerium oxide (CeO_2), neodymium oxide (Nd_2O_3), dysprosium oxide (Dy_2O_3), gadolinium oxide (Gd_2O_3), holmium oxide (Ho_2O_3), erbium oxide (Er_2O_3), thulium oxide (Tm_2O_3), ytterbium oxide (Yb_2O_3), lanthanum oxide (La_2O_3), terbium oxide (Tb_4O_7) and $\text{Ce}(\text{NO}_3)_3 \cdot 6\text{H}_2\text{O}$ were purchased from Sigma-Aldrich. The n-octanohydroxamic acid was obtained by neutralising an alkaline (KOH) solution of potassium hydrogen n-octanohydroxamate (supplied by Axis House) with sulfuric acid. The precipitated hydroxamic acid was filtered, washed with DDI water and dried in air. The sample was then recrystallised from methanol and dried in air before use. Calcite, bastnaesite crystals (sourced from Pakistan), bastnaesite and monazite ore (sourced from Mountain Pass in the USA) were purchased from BK Minerals (Brisbane, Australia).

3.2.2 Characterization of rare earth oxides and rare earth minerals

The REO samples were investigated as supplied in powder form. The samples were placed on a glass microscope slide and compacted to generate a flat surface for Raman investigation. For investigation of the bastnaesite crystals and minerals, samples were sliced using a diamond wafering saw lubricated with water and then surface ground (silicon carbide paper to 400 grade) to produce a flat sample. The monazite specimen was cleaved into small pieces and examined without further processing in order to minimize exposure to radiation. SEM-EDX characterization utilized carbon sputter coating of the samples prior to investigation.

3.2.3 Synthesis of the REE compounds with hydroxamate

REE hydroxamates were prepared after the method used by Feng and Fernando for preparing 4-hydroxybenzothiazole complexes of rare earths (Feng and Fernando, 1960). REOs were dissolved in approximately 30 mL of 70% nitric acid, with heating as required; n-octanohydroxamic acid was dissolved in ethanol and then added to the rare earth nitrate solution at a ratio of 3:1. The reaction solvent consisted of 50/50 water and ethanol. Ammonia (25%) was added dropwise until the first permanent precipitate was observed, then 3-4 drops more of ammonia solution were added. The pH was measured at this point. The hydroxamate rare earth metal complexes (Nd, Er, Dy, Gd, and Ho) except Ce hydroxamate, were synthesized in this manner.

3.2.4 Synthesis of cerium hydroxamate

$\text{Ce}(\text{NO}_3)_3 \cdot 6\text{H}_2\text{O}$ in water was mixed with hydroxamate in ethanol (the mole ratio for $\text{Ce}(\text{NO}_3)_3 \cdot 6\text{H}_2\text{O}$ to hydroxamate was 1:3). A white precipitate was observed immediately without pH adjustment. The product was vacuum dried for 48 h in a desiccator before being investigated. A gradual colour change from white to reddish-brown was observed after the sample was exposed to air for 2 h. This colour change effect was observed immediately if the sample was vacuum filtered in air. The oxidized samples were also characterized using Raman spectroscopy and XPS.

3.2.5 Synthesis of Ce carbonate on calcite and adsorption study with hydroxamate

Optical calcite was cleaved into flat crystals. An inert substrate (a glass slide) was used as a reference deposition surface. The synthesis method reported by Unuma was extended to a reaction time of 12 weeks due to different substrates were used in this

thesis (Unuma et al., 2003). The calcite crystal and glass slide were immersed in 100 mL solution of $\text{Ce}(\text{NO}_3)_3$ ($0.01 \text{ mol}\cdot\text{L}^{-1}$), KClO_3 ($0.05 \text{ mol}\cdot\text{L}^{-1}$) and KCl ($0.1 \text{ mol}\cdot\text{L}^{-1}$) for the 12 weeks at room temperature in air.

For the adsorption study, the sample was conditioned in saturated potassium hydrogen n-octanohydroxamate ($\sim 0.02 \text{ mol}\cdot\text{L}^{-1}$) in water for 72 h. The sample was taken out to examine at various conditioning times. Prior to each examination, the sample was washed 3 times with water, and blotted dry with filter paper before further investigation.

3.2.6 Adsorption studies between hydroxamate and REOs

The REO adsorption samples were prepared by adding to 30 mL of saturated potassium hydrogen n-octanohydroxamate in water ($0.02 \text{ mol}\cdot\text{L}^{-1}$, pH ~ 9.6) and conditioned for up to 18 h. Samples were removed for examination at various conditioning times. The sampled solid was collected by filtering, washed 3 times with DDI water, and then dried under vacuum prior to investigation.

Nd_2O_3 was selected as the model compound for solvent dependence investigation because neodymium oxide has the strongest fluorescence emissions accessible for observation in a spectral region that does not overlap the Raman bands. 0.5 g of Nd_2O_3 was added to 30 mL of potassium hydrogen n-octanohydroxamate ($0.02 \text{ mol}\cdot\text{L}^{-1}$ in 1:1 of ethanol: water (V/V)) at pH 9.6 (KOH) and conditioned for 18 h. The solid was collected by filtering, washed 3 times with water, and then dried under vacuum before further investigation.

3.2.7 Adsorption studies between hydroxamate and RE minerals

The bastnaesite and monazite samples were treated in saturated potassium hydrogen n-octanohydroxamate in water ($0.02 \text{ mol}\cdot\text{L}^{-1}$, pH ~ 9.6) and conditioned for various

times before investigation. Following conditioning, the sample was washed three times with DDI water and dried in air prior to characterization.

3.3 Technical and instrumental

Vibrational techniques (Raman and infrared spectroscopy), AFM, AFM-Raman, XPS and SEM-EDX were utilized in this investigation. Summaries of capacities and limitations of the instruments are given in Table 3.1. Further information can be found in the references and is also discussed in each instrumental section.

Table 3.1 Analytical techniques summary

ANALYTICAL TECHNIQUE	GERNERAL USES	SIGNAL DETECTED	SAMPLES	LATERAL RESOLUTION	DEPTH RESOLUTION	DETECTION LIMITS	LIMITATION	REFERENCES
Raman	Identification of compounds (org. and inorg.), bonding characterization, structural elucidation	Raman scattering	Solid, liq. gas	1 μm	5 nm to 1 μm	0.1 wt%	Weak effect, fluorescence can be a problem; Photodecomp.; Radiation absorption	(Sherman, 1997; Skoog et al., 2007; Stiles et al., 2008)
Infrared	Similar to Raman, structural elucidation and compound identification	IR absorbance	Solid, liq. gas	-	-	Routine is 2 wt%, 0.01 wt% for most favourable con. and special tech.	Possible interference from background solvent/matrix, Compound must be IR active	(Sherman, 1997; Skoog et al., 2007)
XPS	Surface elemental identification; Valence states, bonding information	Photoelectrons	Solid	~ 300 μm (non-imaging)	< 10 nm	0.3%	UHV required; Possible sample decomposition; Special preparation for non-conducting samples	(Nefedov, 1988; Sherman, 1997; Skoog et al., 2007; van der Heide, 2011)

ANALYTICAL TECHNIQUE	GERNERAL USES	SIGNAL DETECTED	SAMPLES	LATERAL RESOLUTION	DEPTH RESOLUTION	DETECTION LIMITS	LIMITATION	REFERENCES
SEM-EDX	Topographical image; Qualitative elemental information	Secondary and backscattered electrons; X-ray	Solid	1 μm (BSE); < 5 nm (SE)	1 μm (BSE); < 5 nm (SE) < 5 μm (X-ray)	0.1 - 1%	Similar to XPS: UHV required, sample decomposition, special treatment for non- conductive samples	(Sherman, 1997; Skoog et al., 2007; Stokes, 2009)
AFM	Topographic profiling; Surface forces;	Deflection of laser beam	Solid, liquid	< 10 nm	-	-	Smooth surface required (height variation less than 1 μm)	(Eaton and West, 2010; Sherman, 1997)
AFM-Raman	Topographic profiling coupled with composition information	Deflection of laser beam Raman scattering	Solid, liquid	1.5 μm	5 nm to 1 μm (for Raman)	0.1 wt% (for Raman)	Complicated operation; Smooth surface required (height variation less than 1 μm)	(Eaton and West, 2010; Sherman, 1997; Skoog et al., 2007)

BSE - backscattered electrons

SE - Secondary electrons

3.3.1 Raman spectroscopy

3.3.1a Basic theory

Raman scattering was firstly observed and reported by Raman and Krishnan, and Landsberg and Mandel'stamm, almost simultaneously in 1928 (Miranowicz and Kielich, 1994). A great number of papers have been published on Raman spectroscopy, comprising theoretical and applied experimental investigations. The Raman spectrum can provide vibrational, rotational and other low frequency information of a molecule following excitation by a laser beam. For crystal samples, the radiation electric field interacts with two different types of phonon modes including longitudinal and transverse modes in the crystals. These phonon modes consist of large number of vibrations of similar energy corresponding to different bands (lattice modes) shown in the Raman spectra.

To generate a Raman spectrum, a momentary distortion of the electrons in the bonding of the molecule is essential. The classic theory considers that if a molecule possesses anisotropic polarizability and is illuminated by a laser beam, the electron distribution would be distorted and a dipole moment is thus induced. The energy of the laser beam is given by: (Skoog et al., 2007)

$$E = E_o \cos (2\pi v_{ex}t) \quad 3-1$$

where E_o is the amplitude of the wave and v_{ex} is the frequency of the laser. The dipole moment is given by (Skoog et al., 2007)

$$m = \alpha E = \alpha E_o \cos(2\pi v_{ex}t) \quad 3-2$$

where α is the polarizability of the bond, it is a function of the distance between nuclei according to the equation (Skoog et al., 2007),

$$\alpha = \alpha_o + (r - r_{eq})\left(\frac{\partial \alpha}{\partial r}\right) \quad 3-3$$

$$r - r_{eq} = r_m \cos(2\pi\nu_v t) \quad 3-4$$

where α_o is the polarizability of the bond at the equilibrium distance r_{eq} and r is the internuclear separation at any distance. r_m is the maximum internuclear separation compared to the equilibrium status. ν_v is the frequency of the vibration. Substitute Equation 3-3, 3-4 into Equation 3-2 gives (Skoog et al., 2007),

$$m = \alpha_o E_0 \cos(2\pi\nu_{ex} t) + E_0 r_m \left(\frac{\partial \alpha}{\partial r}\right) \cos(2\pi\nu_v t) \cos(2\pi\nu_{ex} t) \quad 3-5$$

$$\begin{aligned} m = & \alpha_o E_0 \cos(2\pi\nu_{ex} t) \\ & + \frac{E_0}{2} r_m \left(\frac{\partial \alpha}{\partial r}\right) \cos[2\pi(\nu_{ex} - \nu_v)t] \\ & + \frac{E_0}{2} r_m \left(\frac{\partial \alpha}{\partial r}\right) \cos[2\pi(\nu_{ex} + \nu_v)t] \end{aligned} \quad 3-6$$

This equation is illustrated in Fig. 3.1. The first term in Equation 3-6 represents (elastic) Rayleigh scattering (blue arrows), in which the scattered frequency is the same as the incident radiation. A small proportion of the scattering light comprises a different wavelength to the incident light. There are two contributing types of this inelastic scattering, both are Raman scattering. One has a lower frequency (orange arrow on the left) compared to the incident light (black arrow on the left) while the other is higher (orange arrow on the right compared to black arrow on the right). They are the Stokes and anti-Stokes components, which are expressed by the second and third term in

equation 3-6. According to a Boltzmann distribution, at room temperature, the ground state is far more populated than excited states, hence the Stokes scatter is more intense than the anti-Stokes scatter. For this reason Stokes lines are more often used in structural studies. The differences in the frequency between the incident radiation and the Raman scattering (the Raman shift) corresponds to the frequency of the vibrational transition (Skoog et al., 2007).

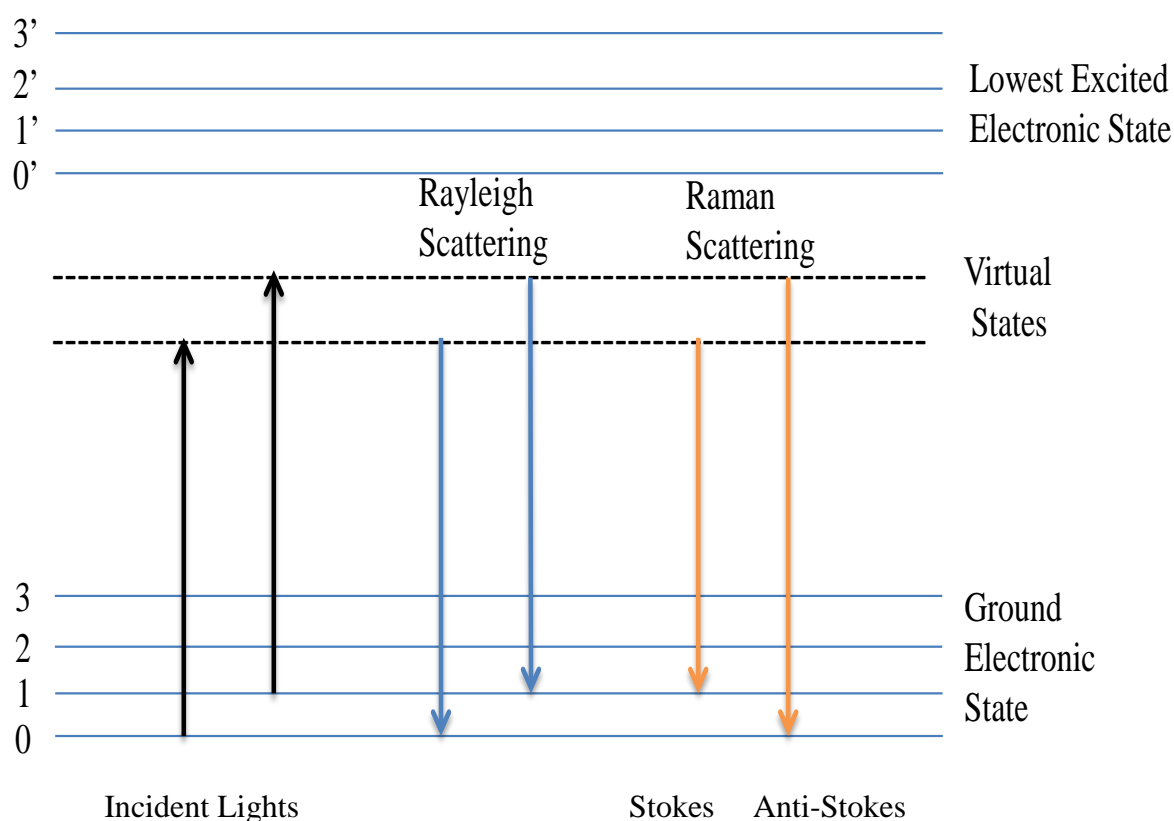


Fig. 3.1 Energy levels of Rayleigh scattering and Raman scattering.

The technique is generally non-destructive and can be utilized *in-situ* for aqueous and air studies. Solid, liquid and gas samples can be analysed. No complicated sample preparation is required. A normal sample size of 10 mg can be utilized (but can be as low as 10 ng to 50 ng depending on the optical configuration) to give a satisfactory spectrum (Sherman, 1997). The analysis time takes less than three minutes for one scan.

Longer analysis time is needed when more scanning cycles are required to give a higher signal-noise (S/N) spectrum.

3.3.1b Instrumentation

Sophisticated instrumentation for Raman spectroscopy is required to produce sufficient intensity with high signal-to-noise ratio. In modern Raman spectroscopy, instrumentation consists of a radiation source (laser), a sample illumination system, a spectrometer and a highly sensitive charge-coupled device (CCD) camera chip. A Laser is highly monochromatic, polarisable and can be focused on a very small area. The most common laser sources include Argon ion, Krypton ion, Hg/Cd, Helium-neon, Diode, and Nd-YAG. The wavelengths vary from UV through to NIR. Argon, Krypton and Hg/Cd ions generate short wavelengths of radiation, which can provide much higher energy compared to other sources. Helium-neon, Diode and Nd-YAG sources lasers generate longer wavelengths of radiation, which are suitable for samples that may decompose with short wavelengths of radiation (Skoog et al., 2007). Under certain circumstance, there is a need to utilize multiple wavelengths due to fluorescence and absorption of incident radiation or Raman-scattered radiation with coloured samples.

In the sample illumination system, a specimen is placed onto the stage of a microscope and illuminated with visible light to select an area for sampling and for adjustment of focus. The excitation laser was then switched to the surface of the sample. This illumination system has greatly improved the accuracy of focus, although adjustments need to be made for long and short wavelengths. For the spectrometer, notch filters combined with a high-performance grating monochromators are used for eliminating the Rayleigh scattering in most modern Raman instruments. Cooled charge-coupled devices for signal detection are well developed and have become commonly

used. It allows the incoming light photons to be converted to electrical signals in the device, which can then be amplified and processed into images.

3.3.1c RE minerals research by using Raman spectroscopy and instrumental details in this study

The RRUFFTM project is an open database available for the Raman spectra with many mineral types. The Renishaw database is another useful database of Raman spectra. For typical REs minerals, such as bastnaesite, monazite, xenotime and phosphate, a number of spectra from different sources can be acquired from these databases. The assignments of typical bands have also been reported. Frost has studied a broad range of carbonate and phosphate group RE minerals including kamotoite-(Y), bastnaesite, parasite, northupite and churchite-(Y) using Raman spectroscopy (Frost et al., 2013; Frost and Palmer, 2011; Frost et al., 2009; Frost et al., 2006). However, due to the nature of variation in minerals, such as impurities, particle size and variations in ion substitution, there is a need for systematic investigation to be undertaken. For example, the characterization of the physical and chemical properties for the common constituent components of the RE minerals, needs to be investigated.

In this study, the Raman spectra were recorded on a Renishaw inVia spectrometer using varied excitation wavelengths. 633 nm wavelength of excitation was generated from a HeNe source and the argon ion source produced the 514 nm excitation. 442 nm and 325 nm wavelengths of excitation were generated from a HeCd source. Samples were mounted on a digitally controlled stage. Raman spectra were calibrated using the 520 cm⁻¹ silicon band. The scanning range chosen varied depending on the laser source used and the spectral region of interest. The scattered light was analysed using a single pass high throughput grating spectrometer and detected with a Peltier-cooled CCD

giving a spectral resolution of 2 cm^{-1} . Spectral manipulation such as baseline adjustment, smoothing and normalisation were performed with the Wire 3.3 software (Renishaw, UK).

3.3.2 Infrared spectroscopy (IR)

3.3.2a Introduction

Infrared spectroscopy is a well-established technique that provides information from vibration or rotation transitions with different energy states in molecules. In this thesis, infrared spectroscopy refers to absorption FTIR spectra. It utilizes an infrared source to radiate the sample. To absorb IR, a molecule must undergo a net change in dipole moment and established a field when the radiation was directed on the sample surface. The established field can interact with the electric field of the radiation. When the natural vibrational frequency matches the radiation frequency, absorption occurs (Skoog et al., 2007). Table 3.2 lists three different ranges of IR source and their applications. Mid IR is the most commonly used radiation source. Its frequencies match most of the fundamental molecular vibrational frequencies from stretching, bending, wagging and scissoring.

A variety of samples can be measured by IR, including solid, liquid and gas. For a solid specimen, typical sample preparation is grinding (5-10%) with KBr, and pressing to produce a homogeneous solid plate before measurement. The thickness of the plate normally is less than 3 mm.

Table 3.2 Energy band range in infrared radiation

	NEAR IR	MID IR	FAR IR
WAVENUMBER (cm^{-1})	13,000-4000	4000-200	200-10
WAVELENGTH (μm)	0.78-2.5	2.5-50	50-1000
APPLICATION	Overtone and combination bands of fundamental molecular vibrations	Fundamental molecular vibrations	Molecular (gas) rotation

3.3.2b Instrument

A Fourier transform infrared (FT-IR) spectrometer has an interferometer instead of the monochromator utilized in a dispersive IR. The interferometer divides the beam into two paths, one reaches a fixed mirror and the other passes through a moving mirror, and the interferometer recombines them before it reaches the sample. The distance of the moving mirror changes of an interval of $\lambda/4$, which generates a constructive and destructive interference of light in a sinusoidal manner. When absorption occurs, it reduces the amplitude of the sinusoidal wave. This summed signal is received by the detector over the whole IR region and processed by a mathematical operation known as Fourier Transform to yield an IR spectrum. The transform is a pure mathematic process, and the simplest description is that it transforms wave into line by changing the units of the x axis. Full details for the mathematic process were introduced by Morse and Feshbach (Morse and Feshbach, 1953).

Attenuated total reflection (ATR) infrared spectrometry is a technique that is used to investigate the FTIR properties of surfaces of material that cannot be examined in the

traditional way. Examples are, films, polymers, powder and aqueous solutions. The sample is placed closely to a crystal that has very high refractive index (diamond is commonly used); the crystal completely reflected the light from the radiation and generates an evanescent wave to interact with the sample. Most samples require little or no preparation. Detailed descriptions for the spectrometer can be referred to Handbook of Instrumental Techniques for Analytical Chemistry (Sherman, 1997).

3.3.2c Flotation surface research for RE minerals using FT-IR spectroscopy and instrumental details in this study

Characterization of major RE minerals (bastnaesite, monazite and xenotime) using IR spectroscopy have been widely reported. Spectral data are available from the RRUFFTM database. For mineral researches, very limited studies have been conducted using single FT-IR technique. Characterizations for the RE minerals were usually combining with Raman, X-ray diffraction (XRD) and XPS.

In this thesis, FT-IR spectra were recorded using a Thermo Nicolet Nexus FT-IR spectrometer equipped with EverGlo IR source optics providing a stabilised signal and 0.5 cm^{-1} resolution. The spectrometer had a DTGS detector with KBr window and Ge on KBr beamsplitter. FT-IR spectra were acquired in the range of $500 - 4000\text{ cm}^{-1}$.

3.3.3 Atomic force microscopy and atomic force microscopy tandem confocal Raman spectroscopy

3.3.3a Introduction

Atomic force microscopy is an imaging technique that works differently from a traditional microscope. It generates surface image by using a tip to interact with the surface instead of focusing light or electrons on the surface. The sample topography and

properties of the surface can be measured under ambient laboratory conditions. Conductive and non-conductive samples are both suitable for study. The resolution can be at the nano scale (Eaton and West, 2010). The core technique uses a cantilever with an attached sharp tip to scan the surface of the sample (Fig. 3.2). A laser beam is applied on the cantilever. When the tip interacts with the surface, the force causes minute reflection from the laser. This signal is transferred to a photodiode and processed by the computer, thus the topography of the surface can be obtained.

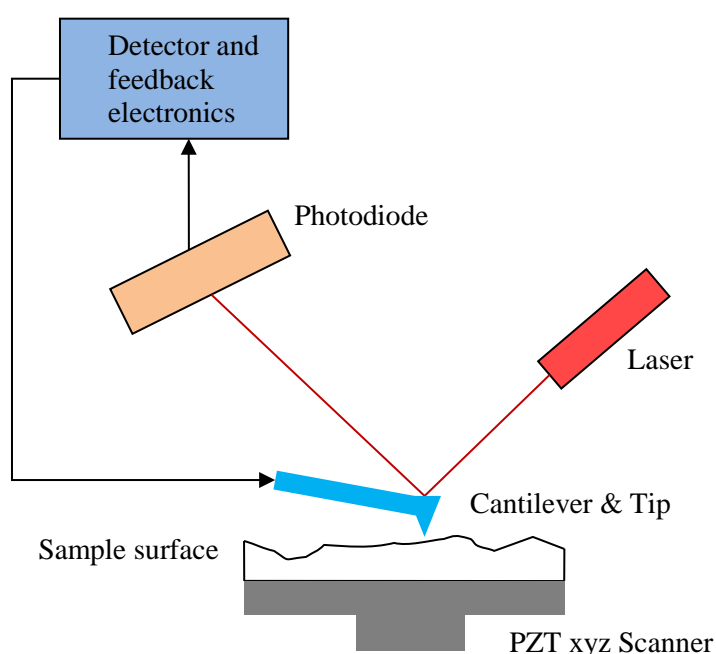


Fig. 3.2 Schematics for atomic force microscope operation for scanning.

Tips are critical for the AFM technique. Typical tip material is single crystal silicon; it is either grown or mounted on the lever. Standard sizes are 6 nm to 10 nm. A super sharp tip is also available which can be down to 1 nm. Some commercial tips are coated with Au, PtIr, TiN or CoCr to suit different needs. There are two types of operation modes for AFM, contact and semi-contact mode. With the contact mode, the tip touches the surface during scanning. This mode has a disadvantage that it requires a

near perfectly flat and smooth surface to avoid tip or sample damaged. In semi-contact mode, the cantilever is oscillated within specific frequencies, in which the signal amplitude is monitored. This can prevent the damage to the greatest extent for both the tip and the sample surface. However, using contact mode is still the preferred method for many researchers as semi-contact mode is much more difficult to obtain satisfactory results (Eaton and West, 2010). It has been a challenge to avoid contamination or interference using AFM when the operation is under ambient laboratory environment.

When the AFM instrument is coupled with a confocal Raman spectroscopy, the Raman active chemical groups on the surface can be identified simultaneously as the surface topography is measured. In the confocal AFM-Raman mode, the AFM probe is placed within the incoming laser beam with nm precision (Fig. 3.3). The Raman scattering and the reflection laser signal from the tip were collected through different pathways. With the sample scanner moves in the X and Y direction, the topographic and the vibrational signal can be simultaneously obtained. A tip that attached to the cantilever with a special angle is required when conducting AFM-Raman (Fig. 3.3). It allows two lasers with the same wavelengths from the AFM and Raman equipment focus on the same location of the surface and two different signals were received by the detectors at the same time. By using AFM-Raman, it not only improves the resolution of the image but also gives the Raman derived spectral absorption information corresponding to the topography. Specifically, when mapping an area of a sample, traditional Raman is usually focused on a particular level while the AFM-Raman can follow the topography of the specimen continuously, thus to give a stronger, more accurate and detailed signal.

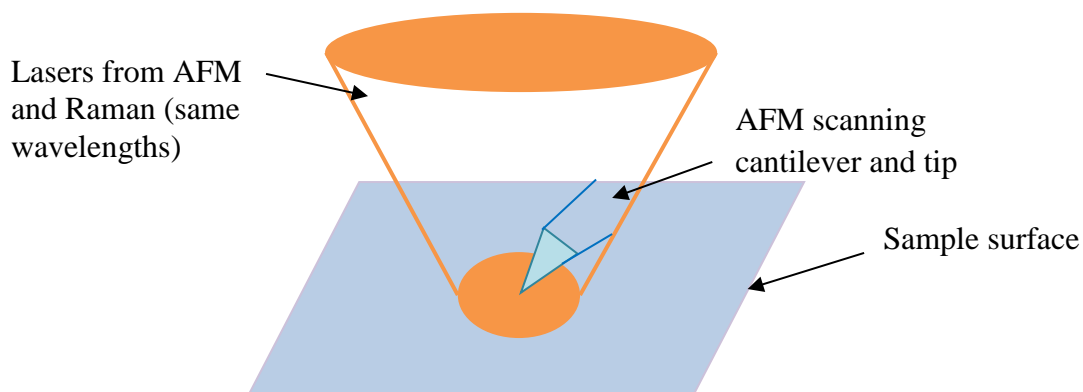


Fig. 3.3 Diagram for AFM-Raman operation for surface scanning.

3.3.3b Flotation surface research for RE minerals by using AFM and AFM-Raman and instrumental details in this study

No previous publications have been found reporting AFM or AFM-Raman on the minerals investigated in this thesis. In this study, AFM and AFM-Raman measurements were performed using a NT-MDT Integra spectra system. The investigated areas of the sample were selected using an optical microscope (100× objective) that coupled with live video camera output. All the measurements were carried out under ambient laboratory environment with semi-contact mode. The scanning probe was a Si cantilever (VIT_P series, from NT-MDT), with a thickness of 5 μm , which had a resonant frequency of 200-400 kHz and a force constant of 25-95 N/m. The AFM images were processed and analysed with Image Analysis (NT-MDT, 2007). Before scanning, an AFM reflection laser signal of near 10 was adopted while feedback gain was adjusted to 1 and the setpoint was set to half of the feedback value.

3.3.4. X-ray photoelectron spectroscopy

3.3.4a Introduction

The discovery of photoelectric effect by using X-rays in the 1940s is the original concept for XPS (Sherman, 1997). It is applicable to all elements except hydrogen. The required amount for a specimen generally ranges from 10 mg - 100 mg or 0.2 mm × 0.2 mm to 1 cm × 1 cm. The minimum mass can be analysed is 0.1 mg (Nefedov, 1988). It provides information that can be used to identify different elements and their oxidation states at the specimen surface. A reliable result can be achieved only if the sample is stable enough under the X-ray examination. The escaped depth of an ejected electron is usually less than 5 nm, thus for bulk interpretation it is required that the surface of the sample is representative of the bulk of the substance. In many cases, XPS is useful for surface absorption study due to its sensitivity, even monoatomic layers can be detected (Cui et al., 2012).

The technique is based on an electron being ejected from an atom when the specimen is irradiated by a known energy photon ($h\nu$) and that the binding energy (E_b) of the electron in the substance can be calculated by the formula:

$$h\nu = E_b + E_{kin} \quad 3-7$$

where E_{kin} is the kinetic energy of the ejected electron being detected. In practice, a work function Φ_{sp} of the spectrometer has to be calculated due to some photoelectrons absorbed by the instrument detector. The equation thus should be:

$$h\nu = E_b + E_{kin} + \Phi_{sp} \quad 3-8$$

This work function is a constant that depends on the spectrometer and material. Thus, the E_b value is,

$$E_b = h\nu - E_{\text{kin}} - \Phi_{\text{sp}}$$

3-9

The binding energy E_b measured corresponds to the different elements present in the top 10 nm of the sample. In addition, the emissions from the Auger electrons also constitute peaks in the spectrum.

3.3.4b Instrumentation

The XPS spectrometer consists of four major parts: the X-ray source, sample, energy analyser and detector (Fig. 3.4). The spectrometer operates at ultra-high vacuum conditions, pressure from $10^{-4} - 10^{-9}$ Pa depending on the type of the instrument. It is also critical that the system is shielded from the geomagnetic field.

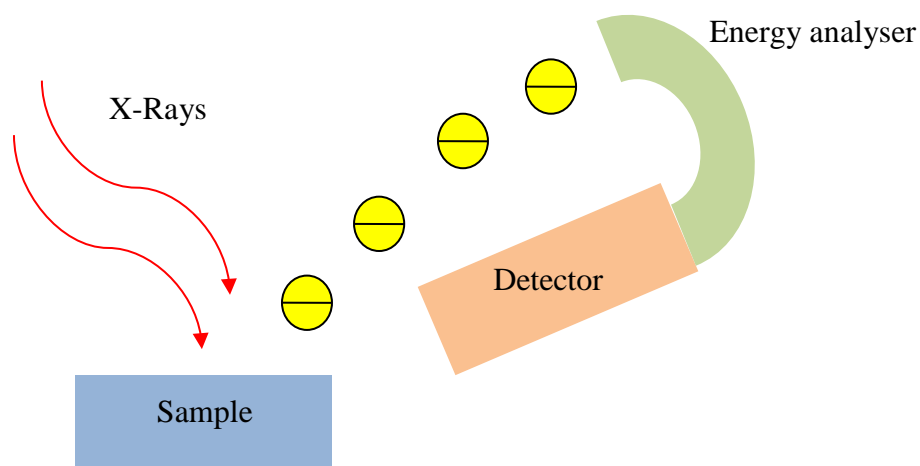


Fig. 3.4 Schematic illustration of the XPS spectrometer.

3.3.4c RE minerals research by using XPS and instrumental details in this study

XPS has been adopted by many researchers for minerals studies. A number of papers have been published on characterization and absorption studies related to the flotation process. Most of them are concentrating on copper, iron, zinc and gold sulfide minerals (Biesinger et al., 2007; Ikumapayi et al., 2012; Pak et al., 2012; Peng et al., 2012; Petrus et al., 2012). Less common base metal oxide and carbonate minerals have also been studied (Hope et al., 2012; Hope et al., 2010; Shi et al., 2013; Wang and Liu, 2013). However, for RE minerals study, no flotation study has been conducted by other authors. Bêche has studies the Ce electronic states in Ce oxide and $\text{Ce}_x\text{Ti}_y\text{O}_z$ compound using XPS (Bêche et al., 2008). We published the XPS results for the characterization and interaction between RE compounds, minerals and the flotation reagent (Cui et al., 2012).

In this thesis, XPS data was obtained on an ESCALAB 250Xi spectrometer using monochromatised Al K_α X-rays focused to a spot size of 0.5 mm and an electron analyser pass energy of 20 eV for narrow range scans. Included in the binding energies employed for calibration were 83.96 eV for Au $4f_{7/2}$ of metallic gold and 932.6 eV for Cu $2p_{3/2}$ of Cu metal. The pressure in the analysis chamber was higher than 5×10^{-9} mbar during spectral acquisition. Because of the poor electrical conductivity of most of the minerals and compounds investigated, photoelectron spectra was obtained with the specimen under the influence of a low energy electron beam (4 V, 175 μA) from a charge-neutralisation flood gun. The observed binding energies, which were lower than the correct values due to the over-compensation of charging to achieve minimum linewidth, were usually referenced to 285.0 eV for the hydrocarbon C 1s photoelectrons. The possibility of beam damage by the low energy

electrons was monitored, and in order to minimise any damage, spectra were obtained as quickly as possible at the expense of signal-to-noise. The data were collected and processed under Thermo Scientific Avantage 4.58 and 4.54 software. For fitting the 3d spectra, in most cases a linear background was appropriate.

3.3.5 Scanning electron microscopy

3.3.5a Introduction

SEM is used for characterizing the physical nature of the surface. It is an imaging technique using a finely focused electron beam impinging on the surface of interest to generate a variety of signals. The primary electrons beam is focused and scanned across in the X and Y direction (raster scanning). The signal is synchronously received in the Z direction by the electron detector and converted into image on the monitor. SEM overcomes the focus limits of optical microscopy which is limited by the diffraction effect in both lateral and depth resolution.

During the process, the accelerated electrons collide with the sample atoms, two interactions occur: elastic interaction and inelastic interaction. Different signals are then produced including X-ray, Auger electrons, secondary electrons, backscattered electrons and sometimes longer-wavelength photos (Fig. 3.5) (Skoog et al., 2007). SEM records the backscattered electrons, secondary electrons and characteristic X-ray with different detectors. Backscattered electrons take up most of the emitted signals. After collision, the speed of some electrons (backscattered electrons) remains the same as the incident electrons, but the deflection angles are in a range from 0° to 180° . These electrons are carrying high energies from 50 eV up to the energy of the incident beam. They normally penetrate to a depth of 1.5 μm when operated with typical beam energy of 20 keV. The diameter of the backscattered electrons can reach to several μm which is much bigger

than the incident beam. A small fraction of the electrons with much lower energies (≤ 50 eV) also emitted, they are secondary electrons. The interaction volume is limited to 50 to 500 Å and the exit diameter is slightly larger than the incident beam. This type of signal is particularly useful to generate a high resolution image (Stokes, 2009). X-ray emission results from the relaxation of the excited atom arising from an inner shell vacancy. It has the highest energy level, the incident electrons penetrate to a bigger and deeper area of the solid surface. The characteristic X-ray provides the elemental analysis information of the specimen, which is referred to energy dispersive X-ray (EDX).

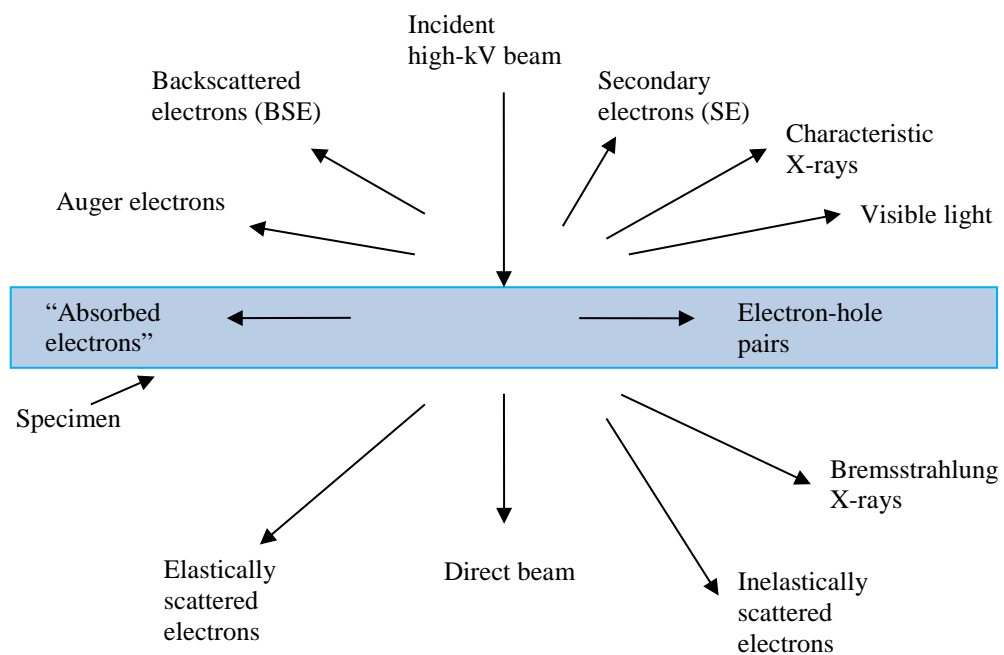


Fig. 3.5 Typical signals generated when the specimen is struck by the electrons.

3.3.5b Instrumentation

Instrumentation includes an electron source, lens and apertures, rastering coils, detectors and data processing system. Two types of electron sources are being employed:

thermionic emission source which is usually a tungsten filament and a field emission source made from a LaB₆ crystal. The latter can generate a more coherent beam with a lower energy distribution and is used for high resolution work. Stringent high vacuum conditions must be maintained when using a field emission source. Electromagnetic lens are used to reduce the spot size of the source and shape the beam size striking the surface.

Different signals are recorded by different types of detectors. Secondary electrons are often accelerated first then detected by a scintillator-photomultiplier system. Backscattered electrons are detected in a similar way but with a modified scintillator. X-ray in most SEM is analysed by a semiconductor detector (Skoog et al., 2007). The limitation for conventional SEM is that the high vacuum environment has led to a restriction for samples. Only samples that are stable to the electronic beam are suitable for investigation.

3.3.5c RE minerals research by using SEM and instrumental details in this study

RE minerals are non-conductive materials. In order to acquire a reliable image, a coating of carbon on the surface was normally required for SEM investigation. In recent years, field emission source coupled with a superconducting transition-edge sensor was developed in SEM, which allows the RE minerals to be investigated without any coating. There have been only two systems in the world before 2012, which may restrict its application (Uehara et al., 2012). Brodusch prepared a RE sample by immersing the mineral in a dilute solution of ionic liquid and then air dried prior to SEM investigation. With this approach, the author obtained a satisfactory surface image by conventional SEM without coating the sample with conductive material (Brodusch et al., 2014).

In this thesis, two different SEM systems have been used. The image for a bastnaesite ore sample was collected using a JEOL JSM 6510LV with a 10–12 mm working distance, a spot size of 0.2 μm and a beam energy of 15 kV with secondary or back scattered electron detection. Other analytical and imaging data were collected using a JEOL JSM-5600 system equipped with an Oxford X-MaxN x-ray detector. The images were acquired at a working distance of 14 mm and beam energy of 30 kV with secondary or back scattered electron detection. All the data were processed with the Ztec software.

References

- Bêche E., Charvin P., Perarnau D., Abanades S. and Flamant G., 2008, Ce 3d XPS investigation of cerium oxides and mixed cerium oxide (CexTiyOz), *Surface and Interface Analysis*, 40, 3-4, 264-267.
- Biesinger M. C., Hart B. R., Polack R., Kobe B. A. and Smart R. S. C., 2007, Analysis of mineral surface chemistry in flotation separation using imaging XPS, *Minerals Engineering*, 20, 2, 152-162.
- Brodusch N., Waters K., Demers H. and Gauvin R., 2014, Ionic liquid-based observation technique for nonconductive materials in the scanning electron microscope: Application to the characterization of a rare earth ore, *Microsc Res Tech*, 77, 3, 225-235.
- Cui J., Hope G. A. and Buckley A. N., 2012, Spectroscopic investigation of the interaction of hydroxamate with bastnaesite (cerium) and rare earth oxides, *Minerals Engineering*, 36-38, 91-99.
- Eaton P. and West P., 2010, *Atomic Force Microscopy*: Oxford University Press, Oxford, GBR, 9780191576676.
- Feng P. K. and Fernando Q., 1960, Chelates of 4-hydroxybenzothiazole with the rare earths, *Analytica Chimica Acta*, 24, 548-554.
- Frost R. L., López A., Scholz R., Xi Y. and Belotti F. M., 2013, Infrared and Raman spectroscopic characterization of the carbonate mineral huanghoite – And in comparison with selected rare earth carbonates, *Journal of Molecular Structure*, 1051, 221-225.
- Frost R. L. and Palmer S. J., 2011, Raman spectrum of decrespignyite $[(Y,REE)_4Cu(CO_3)_4Cl(OH)_5 \cdot 2H_2O]$ and its relation with those of other halogenated

- carbonates including bastnaesite, hydroxybastnaesite, parisite and northupite, Journal of Raman Spectroscopy, 42, 11, 2042-2048.
- Frost R. L., Sejkora J., Keeffe E. C., Plášil J., Čejka J. and Bahfenne S., 2009, Raman spectroscopic study of the phosphate mineral churchite-(Y) $\text{YPO}_4 \cdot 2\text{H}_2\text{O}$, Journal of Raman Spectroscopy, 41, 2, 202-206.
- Frost R. L., Weier M. L., Čejka J. and Ayoko G. A., 2006, Raman spectroscopy of uranyl rare earth carbonate kamotoite-(Y), Spectrochim Acta A Mol Biomol Spectrosc, 65, 3-4, 529-534.
- Hope G. A., Numprasanthai A., Buckley A. N., Parker G. K. and Sheldon G., 2012, Bench-scale flotation of chrysocolla with n-octanohydroxamate, Minerals Engineering, 36-38, 12-20.
- Hope G. A., Woods R., Parker G. K., Buckley A. N. and McLean J., 2010, A vibrational spectroscopy and XPS investigation of the interaction of hydroxamate reagents on copper oxide minerals, Minerals Engineering, 23, 11-13, 952-959.
- Ikumapayi F., Makitalo M., Johansson B. and Rao K. H., 2012, Recycling of process water in sulphide flotation: Effect of calcium and sulphate ions on flotation of galena, Minerals Engineering, 39, 77-88.
- Miranowicz A. and Kielich S., 1994, Advances in Chemical Physics, Modern Nonlinear Optics: Wiley, New York, USA, 531-626.
- Morse P. M. and Feshbach H., 1953, Methods of Theoretical Physics: The McGraw-Hill Book Company, New York, 52-11515. 453-471.
- Nefedov V. I., 1988, X-Ray photoelectron spectroscopy of solid surfaces, 1st edition, Brill Publishing, Leiden, The Netherlands, 1-35.
- Pak T. H., Sun T.-c., Xu C.-y. and Jo Y. H., 2012, Flotation and surface modification characteristics of galena, sphalerite and pyrite in collecting-depressing-reactivating system, Journal of Central South University, 19, 6, 1702-1710.

- Peng Y., Wang B. and Gerson A., 2012, The effect of electrochemical potential on the activation of pyrite by copper and lead ions during grinding, *International Journal of Mineral Processing*, 102-103, 141-149.
- Petrus H. T. B. M., Hirajima T., Sasaki K. and Okamoto H., 2012, Effects of sodium thiosulphate on chalcopyrite and tennantite: An insight for alternative separation technique, *International Journal of Mineral Processing*, 102-103, 116-123.
- Sherman C.-P., 1997, *Hand Book of Instrumental Techniques for Analytical Chemistry*, Settle F. A.: Prentice Hall PTR, New Jersey, USA, 0131773380.
- Shi Q., Zhang G., Feng Q. and Deng H., 2013, Effect of solution chemistry on the flotation system of smithsonite and calcite, *International Journal of Mineral Processing*, 119, 34-39.
- Silva E. N., Ayala A. P., Guedes I., Paschoal C. W. A., Moreira R. L., Loong C. K. and Boatner L. A., 2006, Vibrational spectra of monazite-type rare-earth orthophosphates, *Optical Materials*, 29, 224-230.
- Skoog D. A., Holler F. J. and Crouch S. R., 2007, *Principles of Instrumental Analysis*, 6th edition, David Harris, Belmont, USA, 9780495012016.
- Spedding F. H., 1971, The rare earths, *Historical introduction to the rare earths*, F. H. Spedding and A. H. Daane, Robert E. Krieger Publishing Co. Inc., New York, 1-3.
- Stiles P. L., Dieringer J. A., Shah N. C. and Van Duyne R. P., 2008, Surface-Enhanced Raman Spectroscopy, *Annual Review of Analytical Chemistry*, 1, 1, 601-626.
- Stokes D., 2009, *Principles and Practice of Variable Pressure : Environmental Scanning Electron Microscopy (VP-ESEM)*: Wiley, Chichester, GBR, 9780470758748.
- Uehara S., Takai Y., Shiroye Y. and Fujii Y., 2012, TEM microcalorimeter SEM-EDX system for rare-earth elements analyses, *Journal of Mineralogical and Petrological Sciences*, 107, 105-109.

- Unuma H., Kanehama T., Yamamote K., Watanabe K., Ogata T. and Sugawara M., 2003, Preparation of thin films of MnO₂ and CeO₂ by a modified chemical bath (oxidative-soak-coating) method, *Journal of Materials Science*, 38, 255-259.
- van der Heide P., 2011, *X-Ray Photoelectron Spectroscopy : An Introduction to Principles and Practices*: Wiley, Hoboken, NJ, USA, 9781118162927.
- Wang K. and Liu Q., 2013, Adsorption of phosphorylated chitosan on mineral surfaces, *Colloids and Surfaces A: Physicochemical and Engineering Aspects*, 436, 656-663.
- Zepf V., 2013, *Rare earth elements: A new approach to the nexus of supply, demand and use: exemplified along the use of neodymium in permanent Magnets*, Doctoral, the University of Augsburg, Germany.

CHAPTER 4

CHARACTERIZATION OF REOs, RARE EARTH MINERALS AND GANGUE MINERALS

4.1 Preamble

The success of mineral flotation is contingent upon the interfacial interaction between collector(s) and the mineral surface. In order to characterize and ascertain the mechanisms of flotation reagent interaction with rare earth minerals, it is necessary to determine the physical and chemical properties of the constituent components.

Rare earth oxides are the most important components of RE minerals. Each individual REO has different vibrational and electronic properties including Raman and fluorescence spectra. There have been a number of papers published for the characterization of REOs using Raman spectroscopy (Keramidas and White, 1973; Boldish and White, 1979; Weber et al., 1993; Biljan et al., 2004; Ubaldini and Carnasciali, 2008). Tucker et al. reported three REOs (Eu_2O_3 , Dy_2O_3 , and Tm_2O_3) using multiple laser sources (Tucker et al., 1984). Most of the studies, however, have used just one laser source and the identification of Raman bands from the fluorescence emissions is often ambiguous. Raman spectroscopy and fluorescent emissions are both valuable techniques for use in identifying the interactions in the RE minerals flotation system. The fundamental physics studies of REO fluorescence are not readily appreciated by mineral technologists, and there is a need for presenting the data to these investigators in a clear and unified way. Systematic investigation using multiple radiation sources has been undertaken in this study. In addition, the Raman spectroscopic studies related to crystal structural analysis were undertaken in wavenumber region between 100 cm^{-1} – 2000 cm^{-1} . The Raman spectra region for wavenumber above 3500 cm^{-1} has not been reported for Nd_2O_3 and La_2O_3 .

For this thesis, 7 REOs including La_2O_3 , CeO_2 , Nd_2O_3 , Yb_2O_3 , Er_2O_3 , Tm_2O_3 and Tb_4O_7 were investigated using Raman spectroscopy and fluorescence emission. These REOs cover the rare earth elements from light to heavy REEs. The most common RE

mineral, bastnaesite, is rich in Ce and La (Farmer, 1974; Frost and Dickfos, 2007) while Nd and Er have been widely applied in different industries. The less common Tm and Yb are also important due to the increasing interest in the heavy REEs that have not been fully investigated. Tb is a unique RE that has been reported to form mixed valence compounds with a non-stoichiometric structure (Imanaka et al., 2004). Fundamental characterization of these REOs is important for better understanding the properties of the REs as well as in the exploration of new applications. This thesis has adopted multiple radiation sources (wavelengths of 325 nm, 442 nm, 514 nm and 632.8 nm) in the wavenumber of the Raman shift ranges from 100 cm^{-1} – 5000 cm^{-1} of these excitations.

Bastnaesite and monazite have been the most commonly mined RE minerals for decades. Thus, it is imperative that these minerals be investigated in model and fundamental RE flotation studies. While, the physical and chemical properties of the REs are similar it is, nevertheless, crucial to fully characterize individual REs in order to ascertain the flotation mechanism and optimise flotation performance and selectivity. For example, how the RE compounds/complexes structures affect the interfacial properties and why the differences in structure lead to variations in flotation efficiency. Gangue minerals are also an important aspect of flotation efficiency as they can be floated or extracted along with the RE minerals, thus reducing the grade of the product. Therefore, characterization of the gangue minerals is essential for fully understanding the selectivity of the collector reagent(s).

4.2 Characterization of rare earth oxides

Most REEs (in this study Er, Nd, Tm, Yb, and La) only exhibit 3^+ oxidation states in their compounds and sesquioxides are usually observed. Ce is stable in its 4^+ oxidation state (Eu has a stable 2^+ oxidation state but it is much less abundant than Ce) while Tb oxide has been reported as a mixed valence compound (Imanaka et al., 2004). In addition, polymorphism has been observed for the sesquioxides and five different crystalized types (A, B, C, H, X) were reported (Ubal dini and Carnasciali, 2008). C type sesquioxides are formed under room temperature and would transform to other phases with different conditions (Ubal dini and Carnasciali, 2008; Atkinson, 2013). It is expected that Raman spectra with a similar band pattern would be obtained from RE sesquioxides having the same crystal structure. Fluorescence emissions with RE compounds are commonly observed overlapping the Raman spectra. Typical strong fluorescing REOs include Er and Nd. It is considered important to identify the origin of the various bands/lines presented in the Raman spectra as a possible rapid REO identification tool. Using a range of excitation energy is an effective method to distinguish the Raman bands from fluorescence emissions. Theoretical energy levels for Er, Nd and Yb were also utilized for the interpretation of fluorescence emission.

4.2.1 Cerium oxide (CeO_2)

CeO_2 has the fluorite type cubic crystal structure that exhibits only one allowed Raman mode, T_{2g} . It emanates from the Ce-O-Ce symmetric vibration (Keramidas and White, 1973; Araújo et al., 2012). In the present study, the Raman spectra from 442 nm, 514 nm and 633 nm excitation were consistent, having a single Raman band observed at a shift of 465 cm^{-1} (Fig. 4.1).

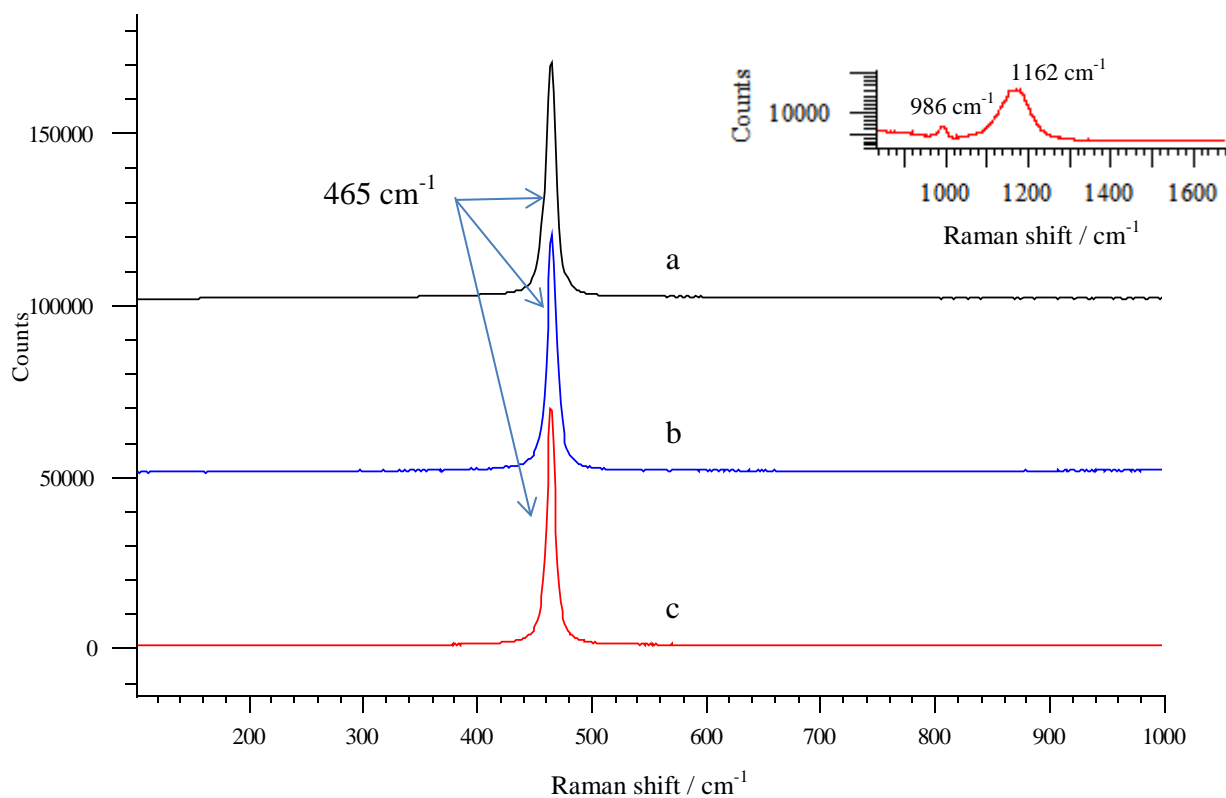


Fig. 4.1 Raman band for CeO₂ with (a) 442 nm excitation (b) 514 nm excitation and (c) 633 nm excitation.

The spectrum is consistent that reported by several authors and the band at 465 cm⁻¹ has been assigned to the first order scattering (Keramidas and White, 1973; Weber et al., 1993; Dogra et al., 2014). No fluorescence emissions were observed in the spectra (Fig. 4.2).

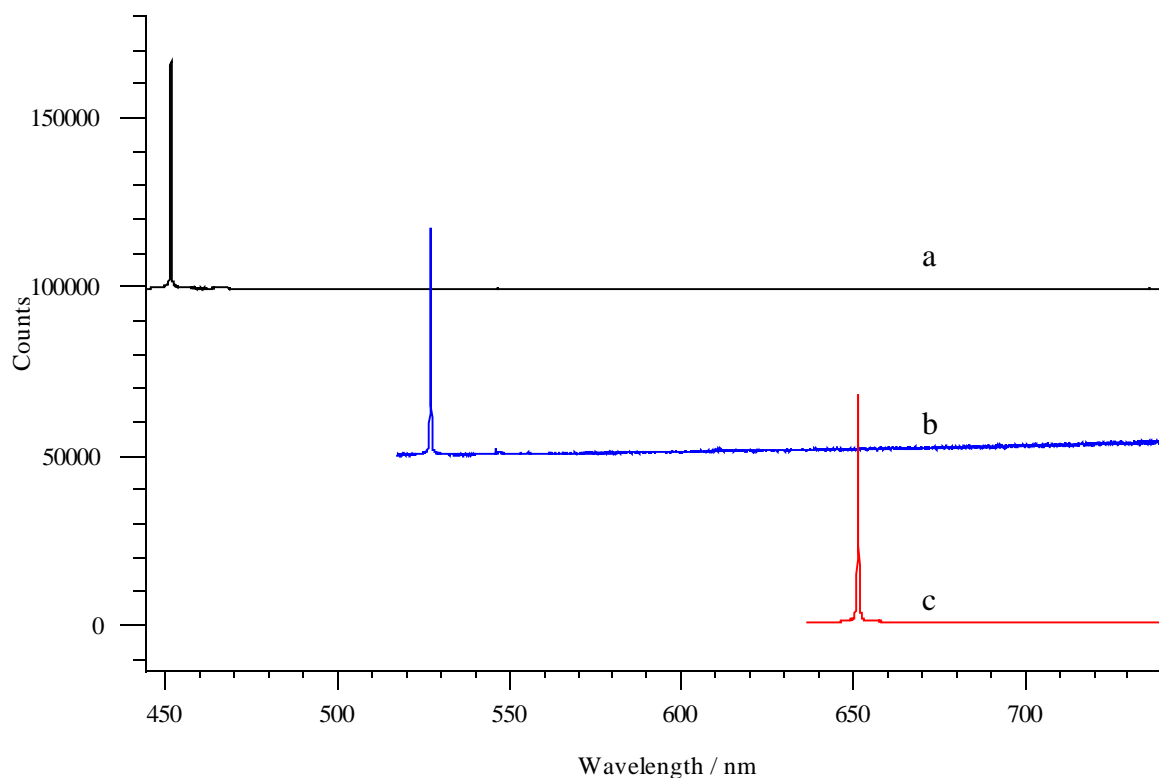


Fig. 4.2 Emission spectra for CeO₂ with (a) 442 nm excitation (b) 514 nm excitation and (c) 633 nm excitation. The emission lines observed are from the Raman band at 465 cm⁻¹ shift.

The second-order scattering bands have been reported by other authors at 983 cm⁻¹, 1030 cm⁻¹ and 1160 cm⁻¹ (Dogra et al., 2014). In this study, low intensity bands at 986 cm⁻¹ and 1162 cm⁻¹ were observed that can be attributed to this mode (Fig. 4.1, top right figure). Weber et al. have conducted a comprehensive study on the Raman second order scattering on CeO₂. The authors concluded that there were a number of bands that ranged from 264 cm⁻¹ to 1180 cm⁻¹ attributable to second order scattering. These bands resulted from different phonon symmetry modes (Weber et al., 1993). For example, the band observed at the present study at 986 cm⁻¹ emanated from the combination of the A_{1g}, E_g and F_{2g} modes. The band near 1180 cm⁻¹ (in this study, the band was observed

at 1162 cm^{-1}) was assigned to a 2LO mode rather than single critical point phonon overtone (Table 4.1).

Table 4.1 Band positions and corresponding Raman modes for REOs

BAND POSITION (CM^{-1})	RAMAN MODE	REO	REFERENCE
465	T_{2g}	CeO_2	(Keramidas and White, 1973; Ikumapayi et al., 2012)
986	$A_{1g} + E_g + F_{2g}$	CeO_2	(Weber et al., 1993)
1162	2LO	CeO_2	(Weber et al., 1993)
472	A_{2u}	Nd_2O_3	(Denning and Ross, 1972)
384	$A_g + F_g$	Tm_2O_3	(Heide, 2008; Ubaldini and Carnasciali, 2008)
365	$A_g + F_g$	Yb_2O_3	(Ubaldini and Carnasciali, 2008; Yu et al., 2014)
444	E_g	Ld_2O_3	(Denning and Ross, 1972)

The band positions (including first order and second order scattering) varied from 1 cm^{-1} to 20 cm^{-1} to those reported by previous investigators, careful calibration and

reference spectra eliminated the possibility of instrumental error. Spanier et al. proposed that a number of factors can contribute to changes of the Raman band position, including phonon confinement, strain, particle size effect and defects (Spanier et al., 2001). Raman band shifts caused by differences in particle sizes have been reported by a number of authors (Weber et al., 1993; Spanier et al., 2001; Araújo et al., 2012). Differences in particle size have led to variation in phonon relaxation, and thus caused band position shifts in the lattice area of the spectra (Spanier et al., 2001).

The intensities of the T_{2g} Raman bands are above 65,000 in counts when excited with less than 0.006 mW of power output and the CCD could easily be saturated (the same effect was observed for the three lasers used). This is an unusually strong signal for a normal Raman spectrum using the Renishaw instruments. Similar observations also have been reported with other fluorite type structure compounds; for example, Mead reported low gain settings were required for CaF_2 , BaF_2 , SrF_2 and SrCl_2 compounds due to the strong scattering effect (Mead and Wilkinson, 1977). It is suggested that the fluorite type cubic crystal structure generates intense Raman scattering.

4.2.2 Erbium oxide (Er_2O_3)

Er is commonly used as a laser source material and it has been well characterized for its fluorescence properties (Stoneman and Esterowitz, 1992; Wu et al., 2013). The Raman and emission spectra observed from Er_2O_3 are present as Fig. 4.3 and Fig. 4.4.

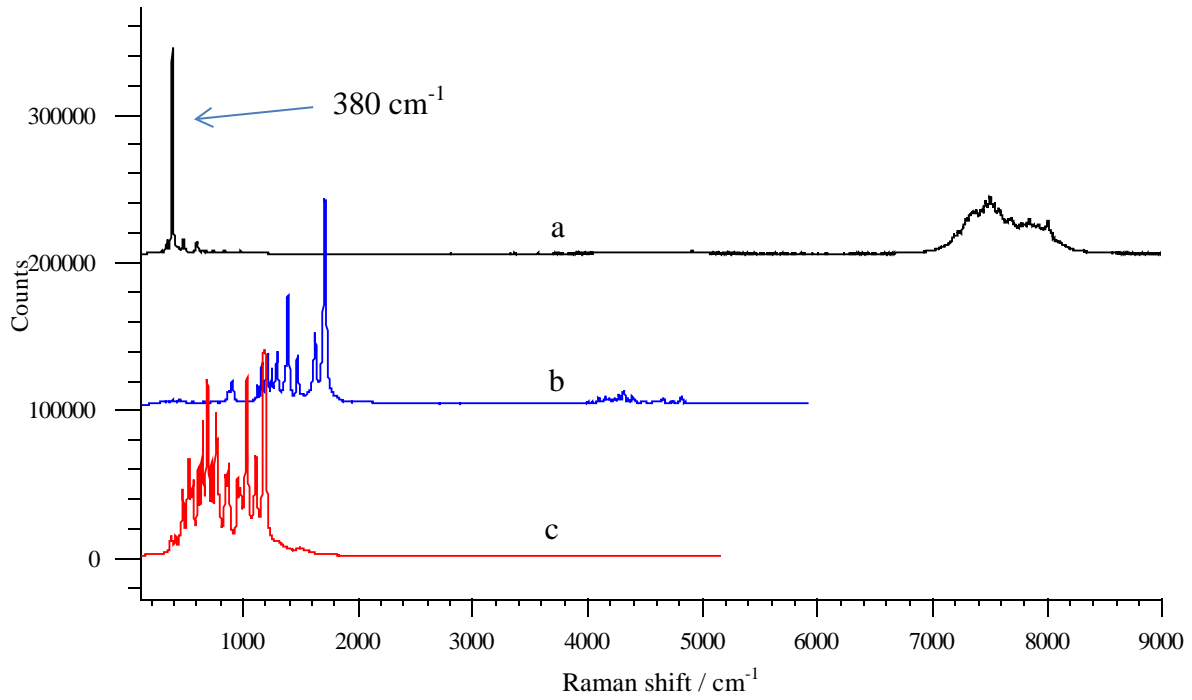


Fig. 4.3 Spectra obtained from Er_2O_3 using (a) 442 nm excitation (b) 514 nm excitation and (c) 633 nm excitation, presented as Raman shifts.

No Raman bands were observable in the three spectra (Fig. 4.3). It is probably that the Raman bands were either overlapped by the fluorescence emission or were too weak to be observed in the presence of the strong fluorescence effect. For most REOs, the Raman bands are usually present between 100 cm^{-1} to 1000 cm^{-1} . With the Er_2O_3 sample, the fluorescence lines were coincidentally shown in this area (or near this area) when the spectra were plotted as wavenumbers.

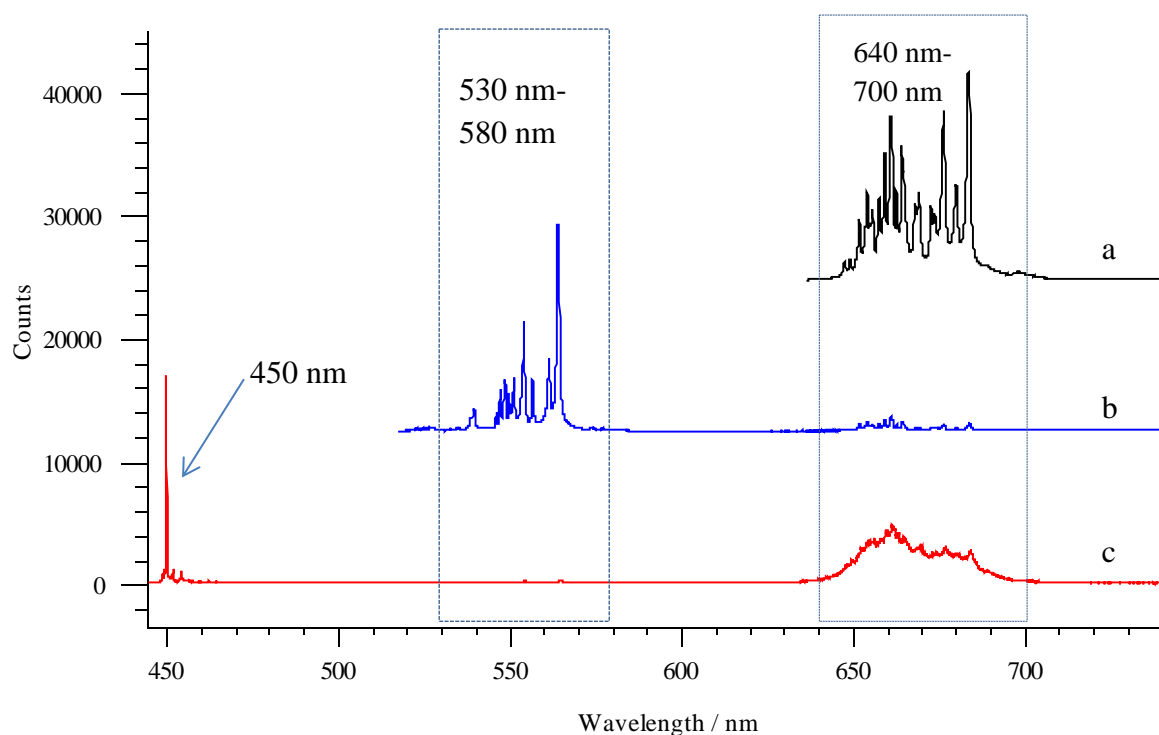


Fig. 4.4 Emission spectra from Er_2O_3 using (a) 633 nm excitation (b) 514 nm excitation and (c) 442 nm excitation.

In the emission spectra from 640 nm – 700 nm and 530 nm – 580 nm, the emission lines show good agreement in both line shapes and wavelength position between the three sets of excitations spectra (Fig. 4.4 and Fig. 4.5). The intensities vary between different excitations, due to the variation of excitation laser power. It can be confirmed that the lines are sourced from fluorescence emissions from the Er(III) (Kik, 2000). An intense band together with a number of small emissions is exhibited for the 442 nm emission spectra at 450 nm. These lines are also observed at 380 cm^{-1} in the Raman spectrum. They are assigned to fluorescence emissions.

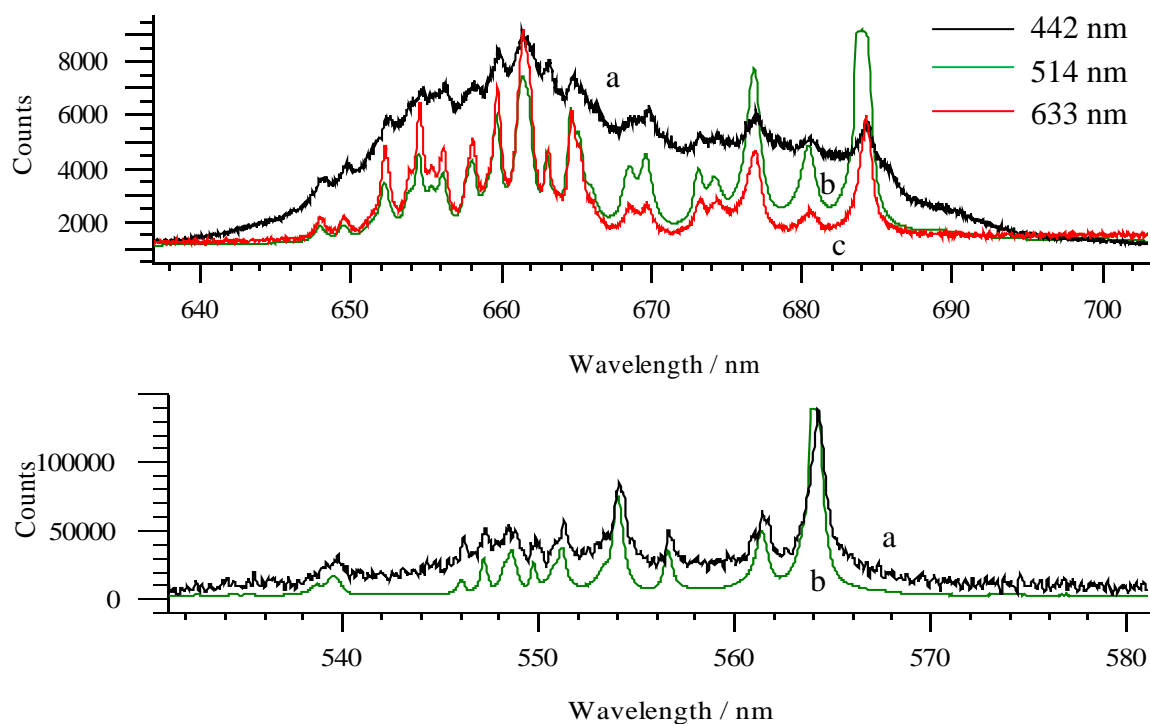


Fig. 4.5 Fluorescence emission spectra for Er_2O_3 with (a) 442 nm excitation (b) 514 nm excitation and (c) 633 nm excitation in the range of (1) 640 nm – 700 nm (2) 530 nm – 580 nm. The emission lines exhibit good agreement in emission positions for different excitation wavelengths.

Electrons can be excited to different energy levels, and they can emit photons during relaxation. A theoretical energy level diagram for Er(III) is shown in Fig. 4.6. The experimental results in the present study are consistent with the theoretical value presented by Wu, allowing for some relaxation processes (Wu et al., 2013). The transition at 650 nm is due to the electronic transition from $^4\text{F}_{9/2} \rightarrow ^4\text{I}_{15/2}$. Similarly, the emissions observed in Fig. 4.4 and Fig. 4.5 (bottom figure) from 530 nm – 580 nm are expected to result from relaxation and emission from a higher energy level excited state ($^4\text{S}_{3/2} \rightarrow ^4\text{I}_{15/2}$).

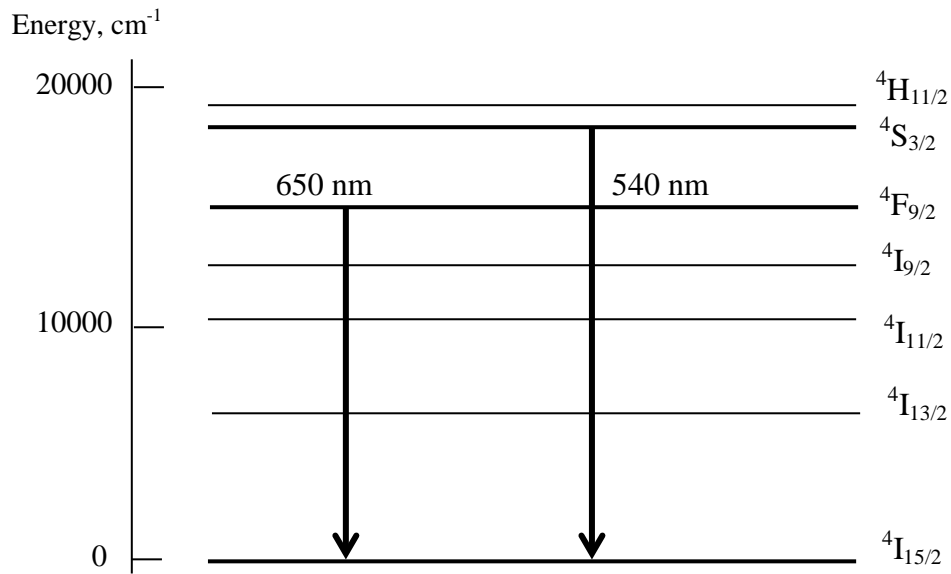


Fig. 4.6 Energy level for Er(III), data sourced from Wu et al. (Wu et al., 2013).

4.2.3 Neodymium oxide (Nd₂O₃)

A theoretical energy level diagram of Nd(III) is presented in Fig. 4.7 (Borrero-González and Nunes, 2012). A number of fluorescence emissions were expected in the emission spectra from the Raman laser excitation. For example, emissions of 592 nm and 594 nm corresponding to $^4G_{5/2}, ^2G_{7/2} \rightarrow ^4I_{9/2}$ and $^4G_{7/2}, ^2K_{13/2} \rightarrow ^4I_{11/2}$ were expected when using the 514 nm wavelength as excitation.

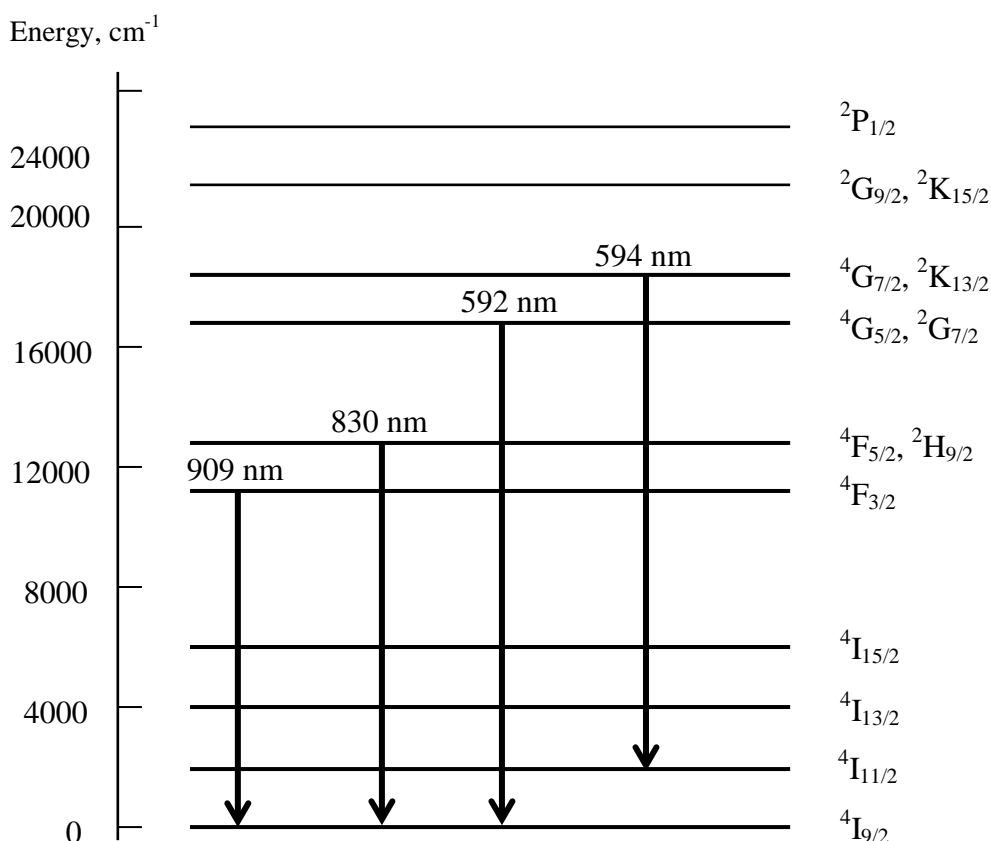


Fig. 4.7 Energy level diagram of Nd(III) (Borrero-Gonzalez and Nunes, 2012).

Fig. 4.8 presents the fluorescence emission spectra obtained using four different excitation wavelengths (325 nm, 442 nm, 514 nm and 633 nm). The emissions from 860 nm to 900 nm using the 633 nm excitation are in good agreement with the transition from $^4F_{3/2} \rightarrow ^4I_{9/2}$ and $^4F_{5/2}, ^2H_{9/2} \rightarrow ^4I_{9/2}$. The electronic transition corresponding to 592 nm and 594 nm ($^4G_{5/2}, ^2G_{7/2} \rightarrow ^4I_{9/2}$ and $^4G_{7/2}, ^2K_{13/2} \rightarrow ^4I_{11/2}$) were also displayed in spectrum where 514 nm excitation was used. When higher energy excitation was utilized (442 nm and 325 nm), no emissions were observed in the range of 580 nm – 720nm. It is likely that the electrons were excited to a much higher energy level and relaxed through a different pathway compared to when the 514 nm wavelength used, and the emission was out of the detection range of the equipment.

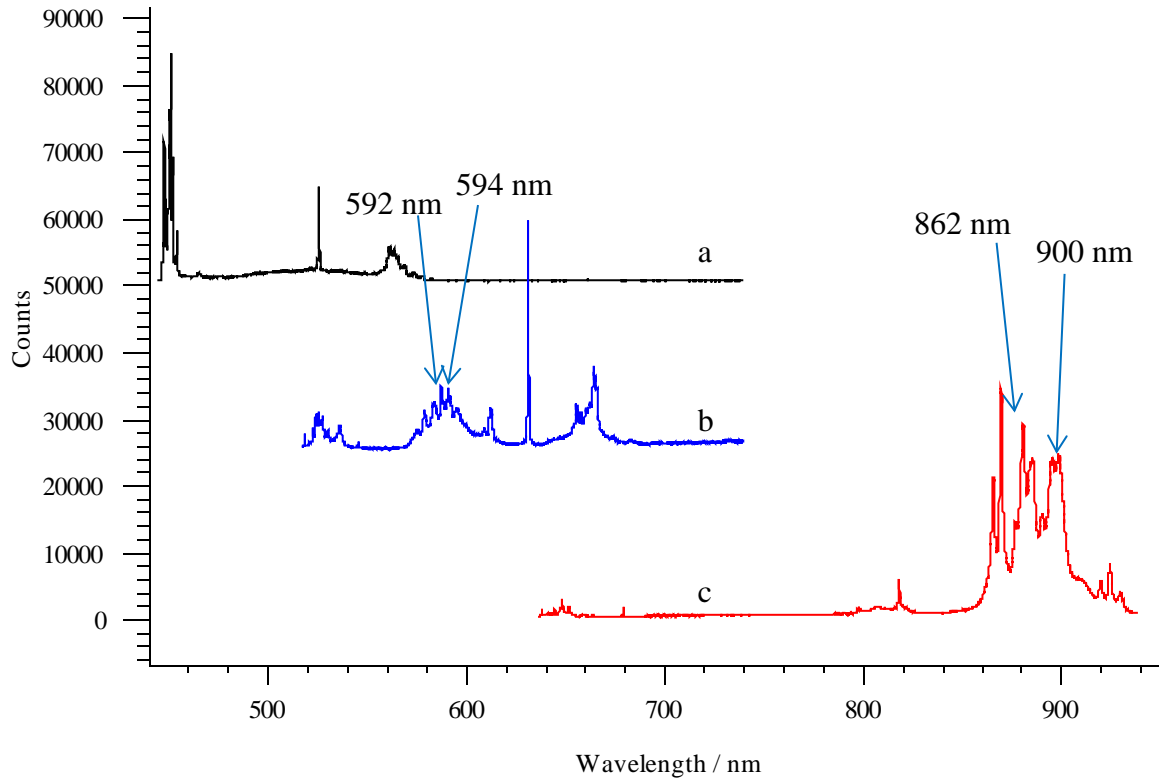


Fig. 4.8 Fluorescence emissions for Nd₂O₃ by using (a) 442nm (b) 514 nm and (c) 633 nm excitations.

Under room temperature, Nd₂O₃ powder was reported having an A type phase crystal structure, but sometimes a combination of C type phase could exist (Ubaldini and Carnasciali, 2008; Atkinson, 2013). Four phonons modes ($2A_{2u} + 2E_u$) were expected for the A type crystal (Ubaldini and Carnasciali, 2008). The irreducible representations for the C type crystal optical and acoustical modes are:

$$\Gamma_{op} = 4A_g + 4E_g + 14F_g + 5A_{2u} + 5E_u + 16F_u, \Gamma_{ac} = F_u$$

where 22 Raman bands (A_g , E_g and F_g) are predicted in the lower wavenumber area (Tucker et al., 1984; Heiba et al., 2012). However, none of the reported spectra in literature has shown all the predicted bands. Heiba attributed this to the accidental degeneracies or low Raman scattering cross-sections of the corresponding vibrations

(Heiba et al., 2012). In the present study, the Raman spectra with excitation of 442 nm and 633 nm were identical. Fluorescent emissions were observed overlapping the Raman spectrum in the lattice area with the 514 nm excitation (Fig. 4.9). Four Raman bands were observed at 296 cm^{-1} , 362 cm^{-1} , 387 cm^{-1} and 472 cm^{-1} . The band at 472 cm^{-1} has been assigned to the A_{2u} mode (Denning and Ross, 1972) (Table 4.1). Ubaldini and Carnasciali who synthesized the Nd_2O_3 powder with C type crystal structure from $\text{Nd}(\text{OH})_3$ reported a number of different bands from the current study in the lattice area (Ubaldini and Carnasciali, 2008). Two types of crystals present in the Nd_2O_3 powder used for this study could be responsible for the different observations in the two studies. In addition, the X-ray photoelectron spectroscopy has confirmed Nd carbonate and Nd hydroxide were present at the surface. The sharp band at 3598 cm^{-1} assigned to $\nu\text{O-H}$ also supports the existence of neodymium hydroxide. Surface hydroxylation and carbonation have contributed to a complicated Raman spectra and it is difficult to identify the assignments in the lattice area.

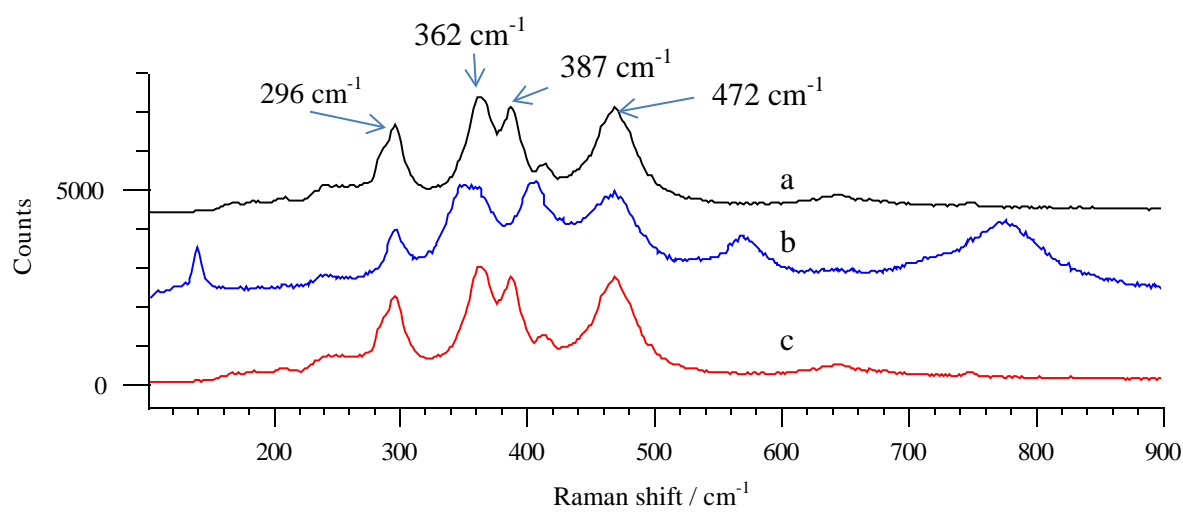
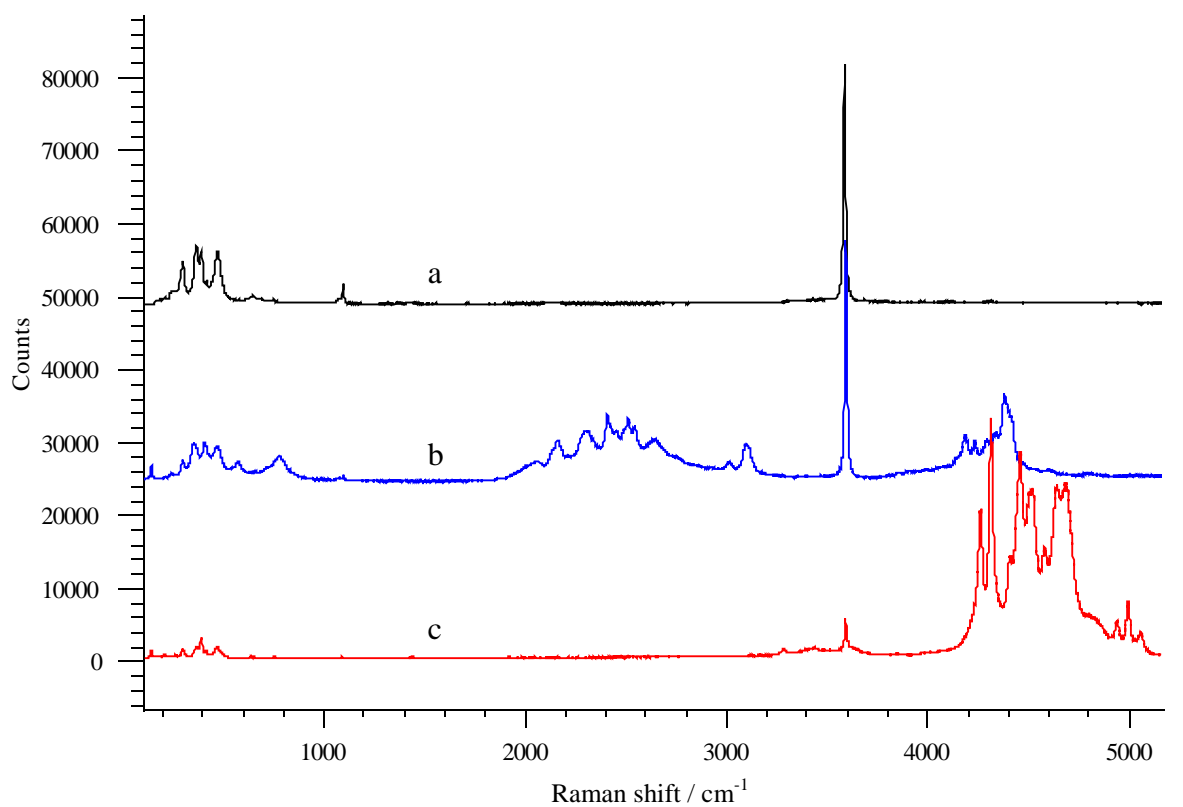


Fig. 4.9 Raman spectra for Nd_2O_3 by using (a) 442 nm (b) 514 nm and (c) 633 nm excitations.

4.2.4 Thulium oxide (Tm_2O_3)

Tm_2O_3 powder is reported having a C-type cubic structure at room temperature (Ubal dini and Carnasciali, 2008). Similar to other C-type structure REOs, not all the predicted bands were observed. In the present study, four Raman bands, 336 cm^{-1} , 384 cm^{-1} , 484 cm^{-1} and 602 cm^{-1} , were observed in the spectra obtained with the three excitations (Fig. 4.10). Comparison of the wavenumber shift and energy plots confirms these are Raman bands. Fig. 4.11 presents the emission data for three wavelengths that is consistent with the strong Raman spectra observed, with very weak (or no) fluorescence bands evident in the spectra. Using 633 nm laser excitation, Ubal dini reported the most intense Raman band was at 383 cm^{-1} while another two bands were at 482 cm^{-1} and 601 cm^{-1} (Ubal dini and Carnasciali, 2008). The spectra obtained in this study were consistent with those Ubal dini reported. The strongest band at 384 cm^{-1} has been assigned to the Ag mode or the combination mode of Ag and Fg (Ubal dini and Carnasciali, 2008; Heiba et al., 2012) (Table 4.1).

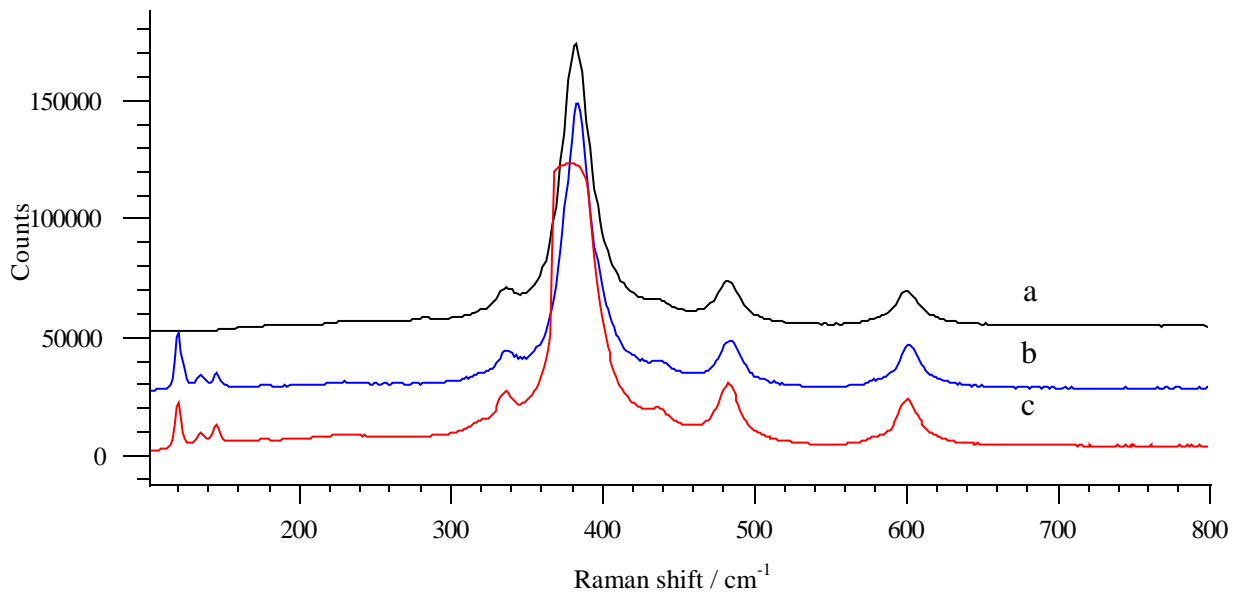


Fig. 4.10 Raman spectra for Tm_2O_3 with (a) 442 nm excitation (b) 514 nm excitation and (c) 633 nm excitation.

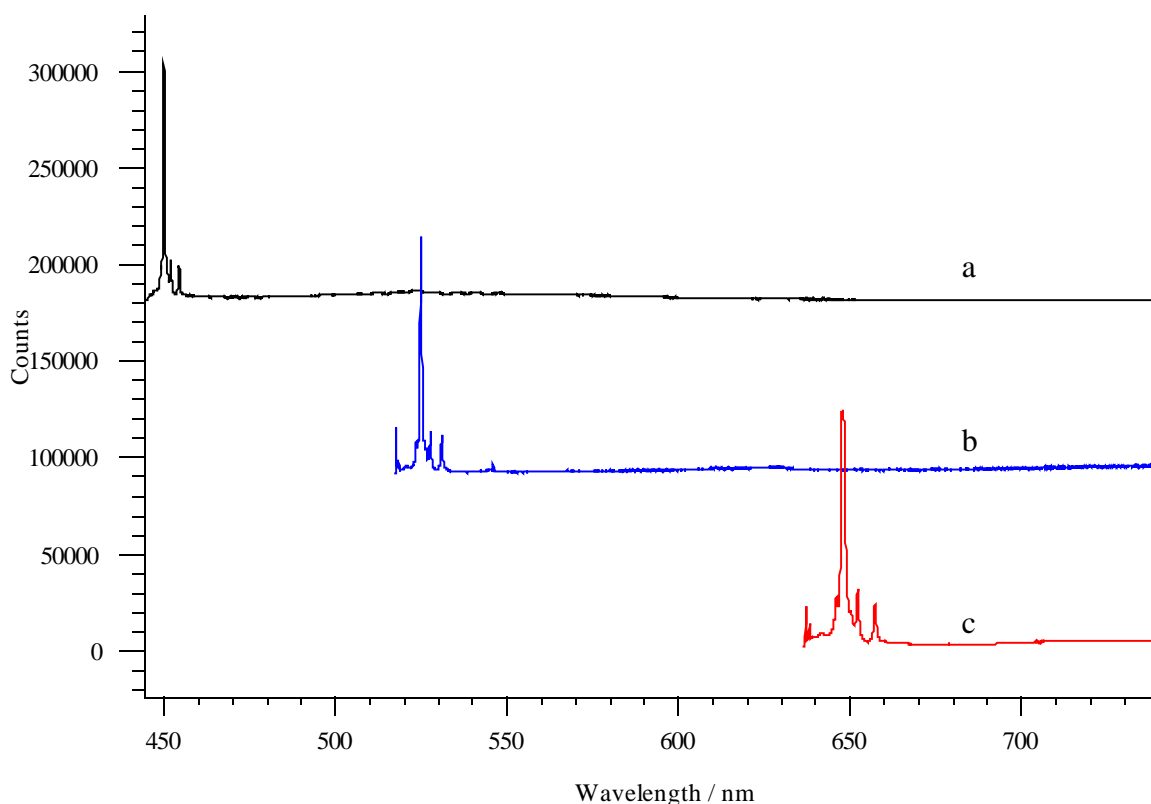


Fig. 4.11 Fluorescence emission spectra for Tm₂O₃ with (a) 442 nm excitation (b) 514 nm excitation and (c) 633 nm excitation. Raman bands, being Raman shifts appear at different wavelengths in the emission spectra.

Biljan also reported broad ranges of Raman bands from 1000 cm⁻¹ to 2000 cm⁻¹ (1090 1140, 1303, 1377, 1593, 1814 at cm⁻¹) and 3000 cm⁻¹ to 3500 cm⁻¹ (3217, 3417 at cm⁻¹) using 1064 nm excitation (Biljan et al., 2004). These bands correspond to 1190 nm to 1351 nm and 1562 nm to 1695 nm for the emission spectra when using 1064 nm excitation. These emissions are out of the detection limit in the present study. The reported 'Raman' bands were not observed with the three excitation wavelengths in the present study and it is likely that they were fluorescence bands from ³H₅ → ³H₆ and ³F₄ → ³H₆ transitions.

4.2.5 Ytterbium oxide (Yb_2O_3)

The most intense Raman band, observed at 365 cm^{-1} , was evident at all three excitations for the Yb_2O_3 sample (Fig. 4.12). This band can be attributed to the combination mode of A_g and F_g (Ubaldini and Carnasciali, 2008; Yu et al., 2014) (Table 4.1).

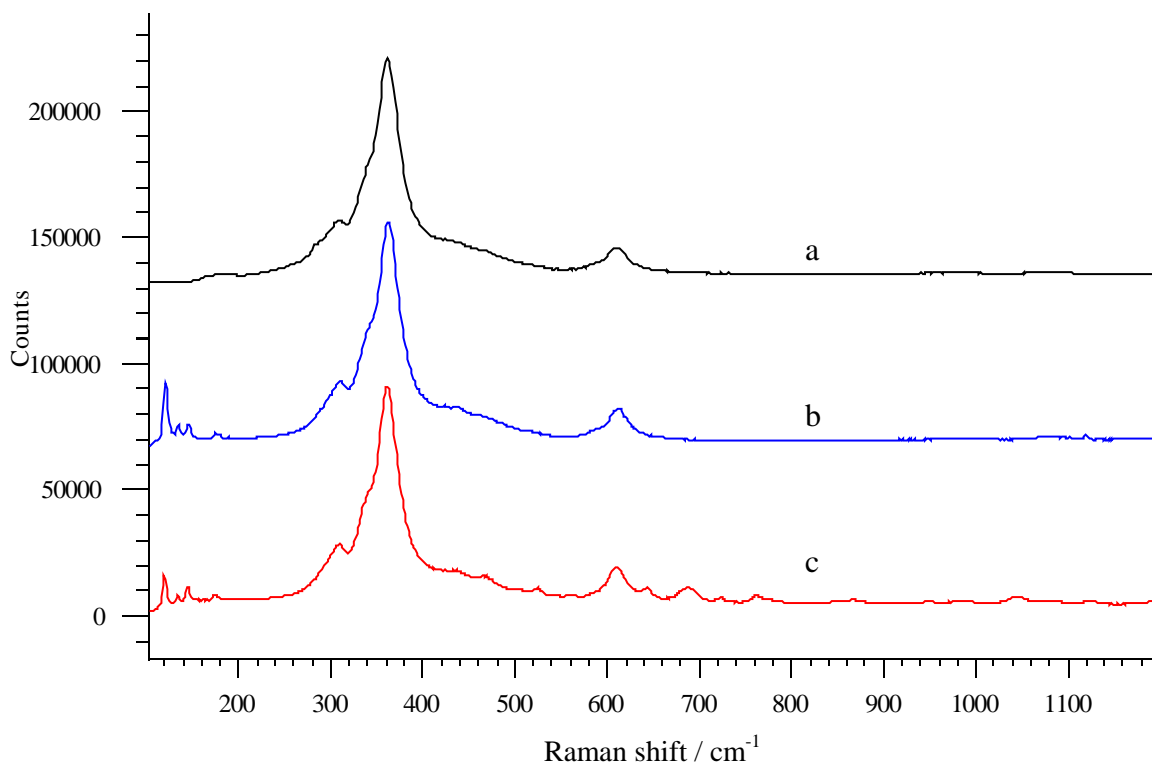


Fig. 4.12 Raman spectra for Yb_2O_3 with (a) 442 nm excitation (b) 514 nm excitation and (c) 633 nm excitation.

A number of small bands near 620 cm^{-1} were shown in the 633 nm spectrum. These bands correspond to 662 nm to 685 nm in the emission spectrum (Fig. 4.13). The emissions are in good agreement with the 514 nm excitation spectrum. It indicates that they are fluorescence lines. These emissions have not been reported in literature. The general agreement is that Yb^{3+} has a simple energy diagram consisting of three crystal field levels in the excited $2F_{5/2}$ manifold and four in the $2F_{7/2}$ ground state manifold (Krebs and Happek, 2001; Biljan et al., 2004). The transition between these two states is

corresponding to the 980 nm emission. However, the observation for the Yb_2O_3 emission spectrum does not agree with this energy level diagram, with which only transition $2F_{5/2} \rightarrow 2F_{7/2}$ is predicted. It supports that additional transition exists (even though is not strong) allowing the 662 nm - 685 nm emission to occur.

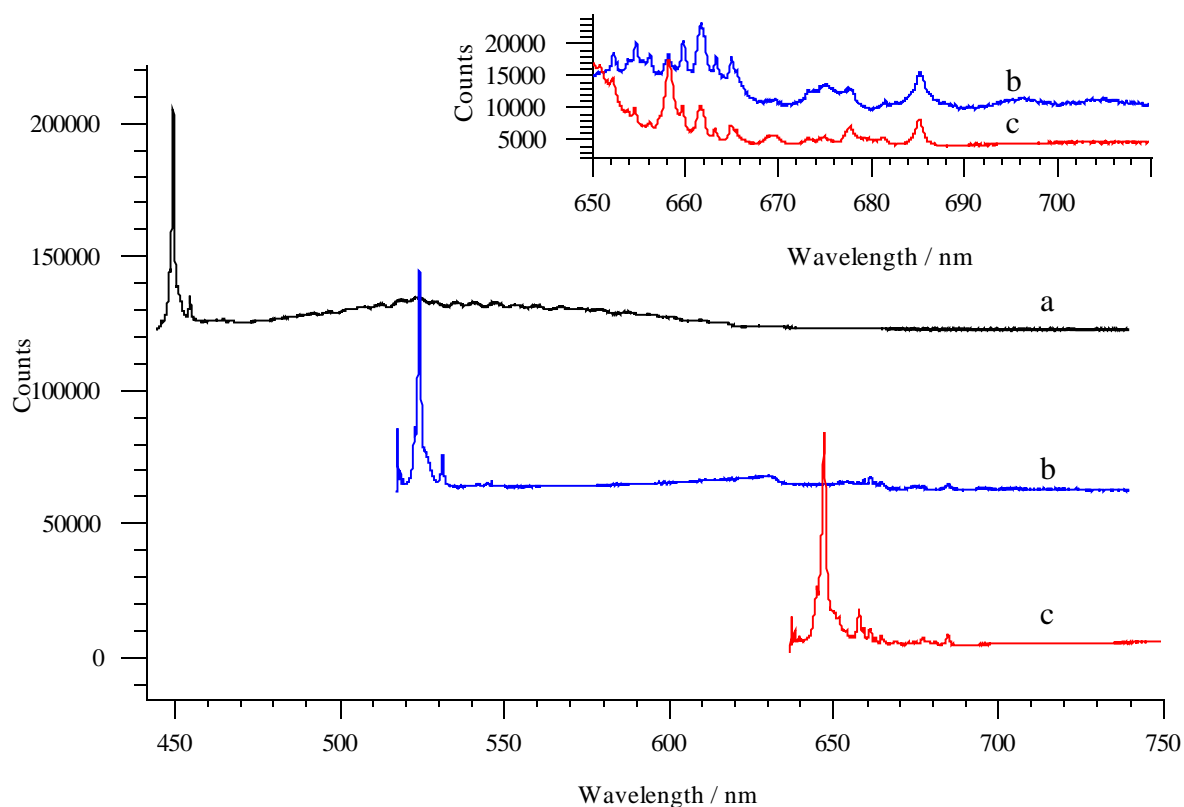


Fig. 4.13 Emissions spectra for Yb_2O_3 with (a) 442 nm excitation (b) 514 nm excitation and (c) 633 nm excitation. The 514 nm (blue) and 633 nm (red) spectra range from 650 nm to 700 nm is shown on the top right corner.

4.2.6 Lanthanum oxide (La_2O_3)

In the present study, four bands at 451 cm^{-1} , 341 cm^{-1} and 283 cm^{-1} , 271 cm^{-1} were observed at all excitations (Fig. 4.14). These bands have been identified as Raman bands. No fluorescence emissions were observed (Fig. 4.15).

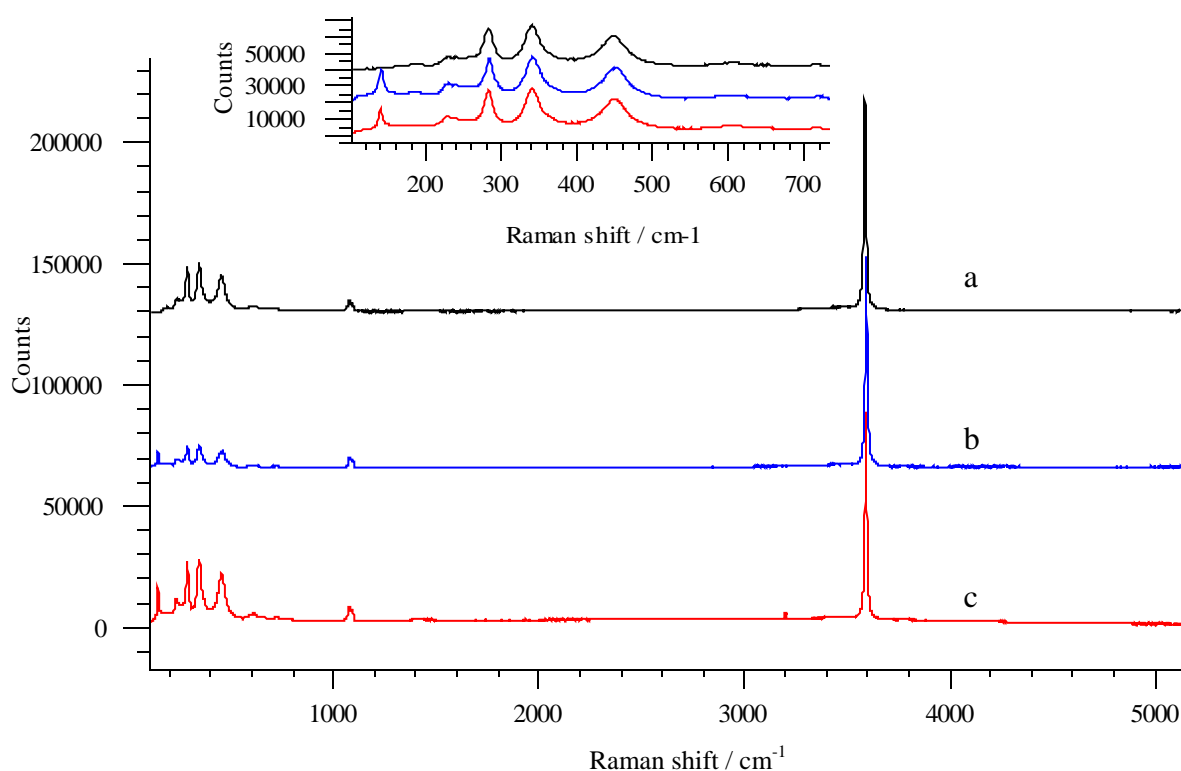


Fig. 4.14 Raman spectra for La_2O_3 with (a) 442 nm excitation (b) 514 nm excitation and (c) 633 nm excitation. The spectra ranges from 200 nm to 750 cm^{-1} are shown on the small figure. From top to bottom: 442 nm excitation, 514 nm excitation and 633 nm excitation.

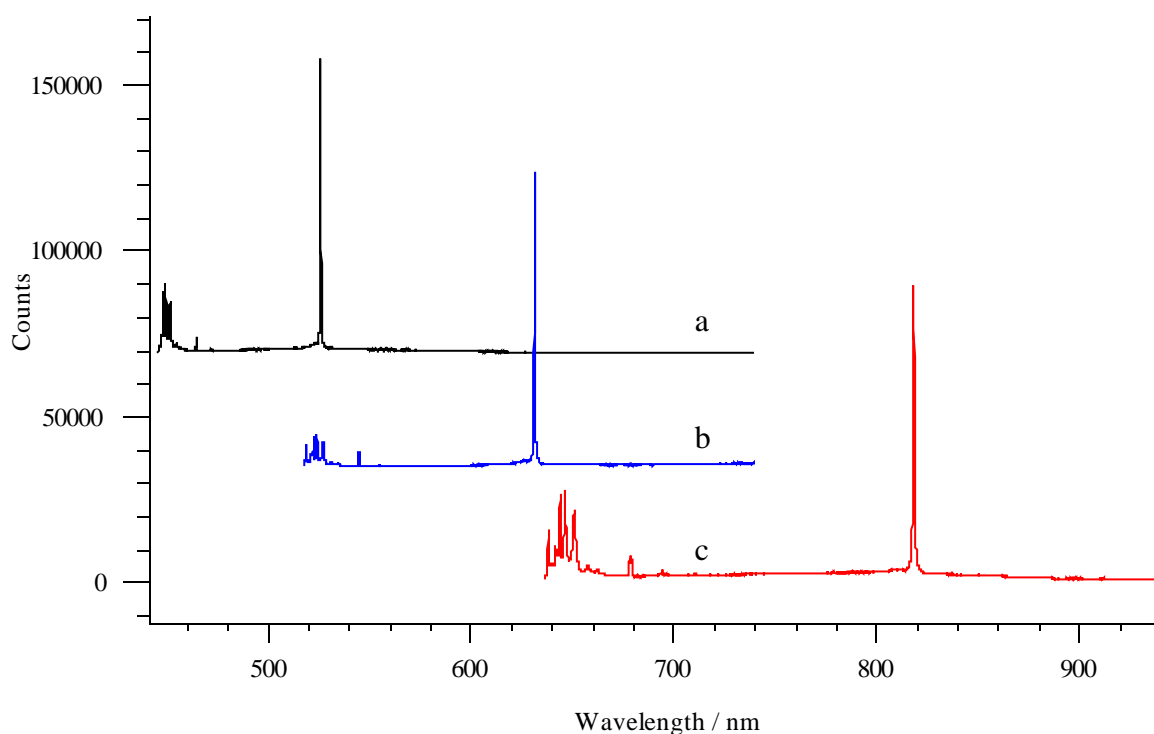


Fig. 4.15 Emission spectra for La_2O_3 with (a) 442 nm excitation (b) 514 nm excitation and (c) 633 nm excitation.

Different theoretical and experimental Raman shifts have been reported in the literature (Denning and Ross, 1972; Ubaldini and Carnasciali, 2008). The band at 451 cm^{-1} is assigned to the $E_g \nu_1$ mode and is consistent with that observed by Denning and Ross (Table 4.1). The authors also employed the FG matrix method for the theoretical band positions and predicted that the $E_g \nu_1$ mode would occur at 449 cm^{-1} (Denning and Ross, 1972). The calculation is in good agreement with the present study. Other Raman bands (341 cm^{-1} and 283 cm^{-1} , 271 cm^{-1}) observed in the present work have not previously been reported. The Raman shifts reported by Boldish and White, for their La_2O_3 sample, 410 cm^{-1} and 195 cm^{-1} were not observed in the present study (Boldish and White, 1979). Similar to Nd_2O_3 , the spectra of La_2O_3 from powder samples would include a couple of crystal orientations and would be different to single crystal spectra (Boldish and White, 1979). Surface hydroxylation and carbonation also contribute to the

differences in band position reported by different authors. The bands at 1074 cm^{-1} , 1092 cm^{-1} and 3604 cm^{-1} support carbonate and hydroxide compounds present at the surface (Fig. 4.14).

4.2.7 Terbium oxide (Tb_4O_7)

Tb_4O_7 has been reported as a mixed valence compound with non-stoichiometric structure (Imanaka et al., 2004). It undergoes phase and structural changes when exposed to an electron beam (Eick et al., 1982; Kang and Eyring, 1987). In order to avoid structural change during examination, low intensity excitation radiation was adopted for this Raman spectroscopic study. Surface damage was observed in the samples at any of the laser wavelengths studied. Fig. 4.16 shows the microscope images before and after the sample was excited using the 442 nm excitation. The surface was uniform before the laser was introduced, following exposure, a bright orange ring was observed where the laser had been focused. Two bright areas next to the ring were also observed. It is likely that a phase transformation has occurred during the examination.

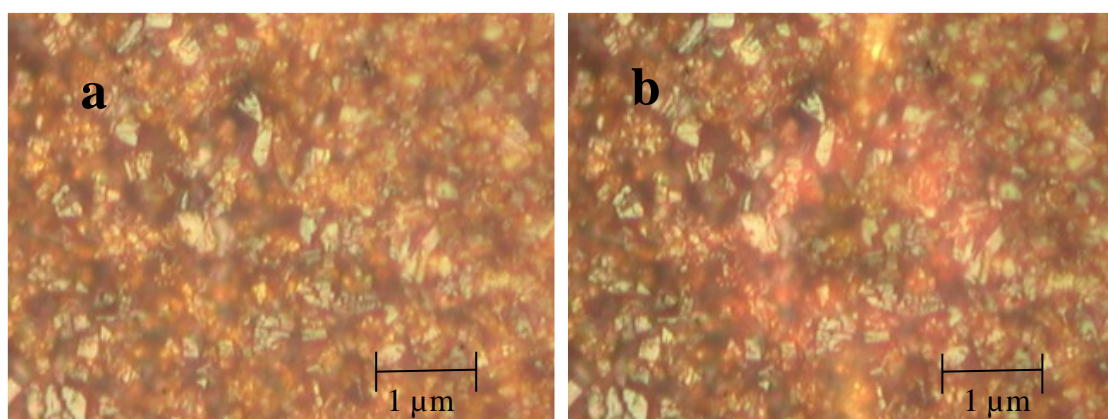


Fig. 4.16 Images for Tb_4O_7 (a) before investigation using Raman spectroscopy; (b) after investigation using Raman spectroscopy. Excitation: 442 nm laser, exposure time: 10s.

The Raman spectra from the sample changed with exposure time, as a result of the laser radiation induced changes. Fig. 4.17 shows two acquired Raman spectra on the same spot using 442 nm excitation. Both spectra were run under the same excitation conditions. The initial spectrum showed two bands at 352 cm^{-1} and 598 cm^{-1} , subsequently, these two bands broadened and shifted to 302 cm^{-1} and 502 cm^{-1} . A broad band was observed from 1800 cm^{-1} to 3000 cm^{-1} also shifted to lower wavenumbers by 200 cm^{-1} and the spectrum became exhibiting a low signal to noise ratio.

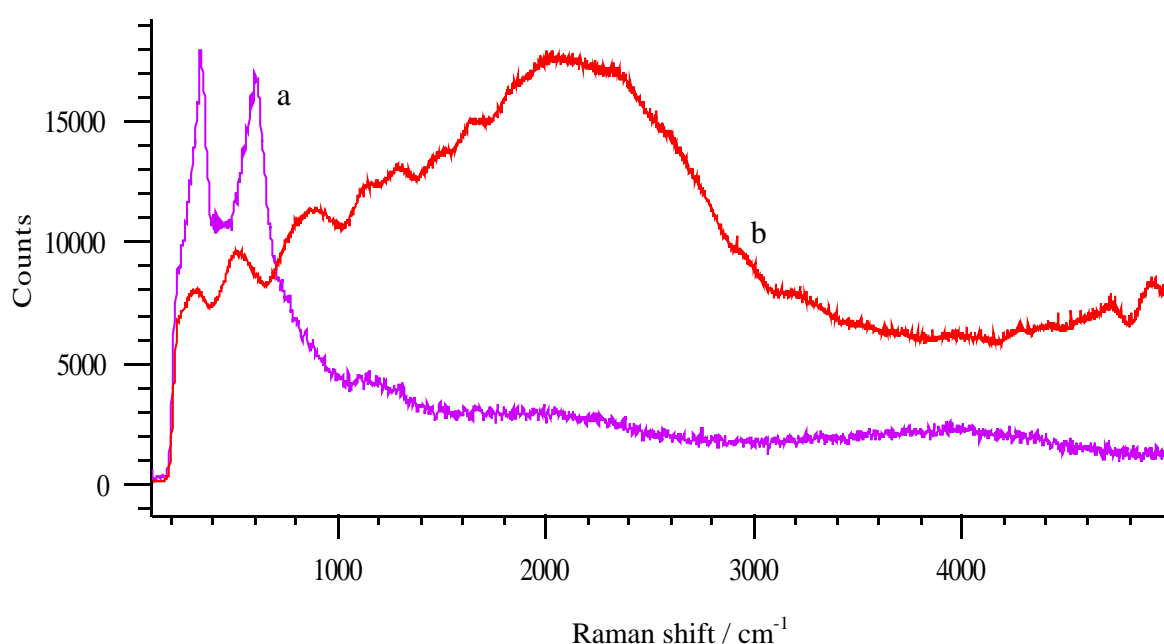


Fig. 4.17 Raman spectra on the same spot for Tb_4O_7 (a) primary spectrum and (b) consecutive spectrum (excitation wavelength was 442 nm).

4.3 Characterization of rare earth minerals

4.3.1 Bastnaesite crystal

4.3.1a Investigation using XPS

The nominal composition of bastnaesite is $(\text{Ce,Lu})\text{FCO}_3$. The photoelectron spectra from crushed crystals and abraded surfaces of Pakistan bastnaesite showed the sample contains Ce 2.1, Nd 1.7, La 0.8, F 4.1, Ca 2.9, and CO_3 9.0 at%. It is indicated that in addition to bastnaesite, Ca minerals such as $\text{Ca}(\text{Ce,Lu})_2(\text{CO}_3)_3\text{F}$ (parisite) and CaCO_3 (calcite) might be present. The Ca 2*p* and Ce 3*d* XPS images ($100 \times 100 \mu\text{m}$) on an abraded surface revealed that the Ca was in a $\sim 20 \mu\text{m}$ circular region within an $80 \mu\text{m}$ rectangular distribution of Ce. This observation supports that gangue mineral (probably calcite) occurred with the bastnaesite. The carbonate C 1*s* binding energy was observed at 289.7 eV, and the O 1*s* binding energy at 531.6 ± 0.1 eV. The result is consistent with carbonate rather than oxide.

Fig. 4.18 exhibits the REs (La, Nd and Ce) 3*d* and 4*d* XPS spectra. Two components separated by 17 eV were observed in the La 3*d* XPS spectrum. The two components resulted from the strong mixed configurations of the ground state $3d^9 4f^0$ and the final state $3d^9 4f^1 \underline{L}$. Slight differences in the structure (shape) of the two peaks were also observed that was due to multiplet coupling. The low binding energy side of the La 3*d*_{5/2} peak at 830 ± 0.2 eV was observed interfered by the F KL_{2,3} L_{2,3} Auger peak (at the equivalent binding energy of ~ 831 eV) and the Ce M_{4,5}N_{4,5}N_{4,5} Auger peak (at an equivalent binding energy of ~ 832 eV). Another component of the La 3*d*_{5/2} peak was observed at 835.6 ± 0.2 eV and it was more intense. No interference was observed for this peak.

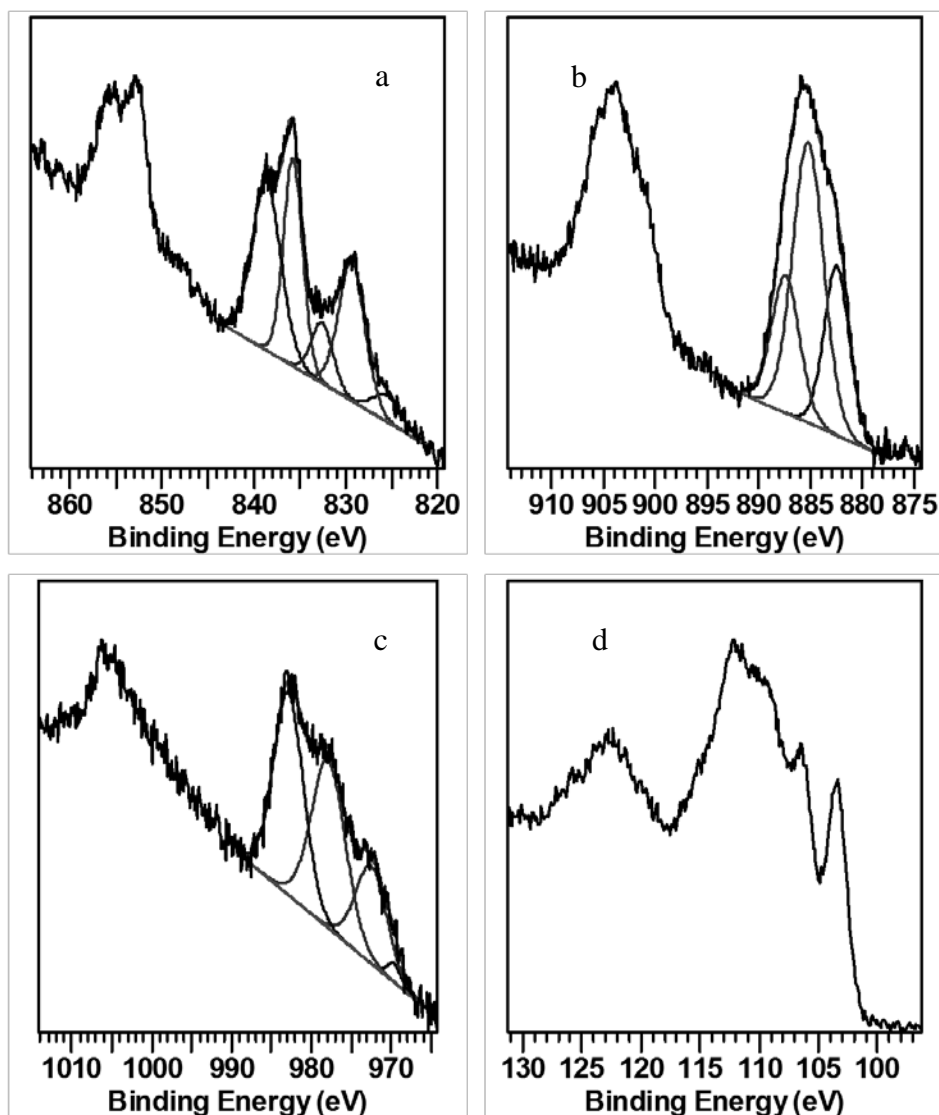


Fig. 4.18 Photoelectron spectra from an unconditioned bastnaesite surface: (a) La 3d; (b) Ce 3d; (c) Nd 3d; (d) Nd, Ce and La 4d.

Ce^0 has a $4f^2 6s^2$ electronic configuration. The spectra are similar to those of La. The lower binding energy peak of each doublet is slightly less intense as the mixing of the $3d^9 4f^1$ and $3d^9 4f^2 \underline{L}$ configurations is slightly weaker than for La. Compared to La_2O_3 , the Ce 3d spectrum (Fig. 4.18b) was more complex (Kotani and Ogasawara, 1992; Mullins et al., 1998), in that each 3d peak appeared to consist of 3 unresolved components, rather than two partially resolved ones. The separation of the outermost components was ~ 4.5 eV, which is slightly larger than for La_2O_3 . The highest binding

energy $3d_{5/2}$ component was near 887 eV, ~2 eV higher than that reported for Ce(III) oxide (Mullins et al., 1998). It is possible, but unlikely, that X-ray excited Auger peaks were superimposed on the Ce $3d$ spectrum. For example, any Ba present would have given rise to an $M_4N_{4,5}N_{4,5}$ peak at an equivalent binding energy near 889 eV and to a more intense $M_5N_{4,5}N_{4,5}$ peak near 902 eV, but a corresponding Ba $3d$ doublet at ~780 and 795 eV was barely discernible in the spectrum. Ce $3d_{5/2}$ peaks from CeO_2 have been reported at 882.3 and 888.8 eV (Teterin et al., 1998). It is more likely that Ce $3d$ peaks from a minor Ce^{IV}/O species such as CeO_2 are superimposed on those from the major Ce^{III}/O species. It is expected that the Ce(III) $3d$ spectrum would reflect the influence of the F in the structure of bastnaesite. In that structure, there are alternating $(REEF)^{+II}$ and $(CO_3)^{-II}$ sheets such that each rare earth atom has eight O and three F atoms as nearest neighbours (Hsu, 1992).

The Nd $3d$ peaks were as expected (Fig. 4.18c). The peaks were less intense than those from Nd_2O_3 and therefore more affected by interference from the X-ray excited O KLL Auger peaks. Nevertheless, the binding energy (~982.9 eV) for the principal Nd $3d_{5/2}$ component had been free of interference.

The La, Ce and Nd $4d$ region of the photoelectron spectrum are showed in Fig. 4.18d. The La $4d$ spectrum is a doublet with the $4d_{5/2}$ peak near 103 eV, while the Ce $4d$ spectrum near 111 eV contains no resolved structure due to dominant multiplet coupling. For the Nd $4d$ spectrum, a broad single peak near 123 eV is present. The $4d$ photoelectrons are less surface-sensitive than the $3d$. Therefore, the $4d$ spectra are useful for comparison with the corresponding $3d$ spectra to obtain information from the two different analysis depths.

4.3.1b Investigation using SEM-EDX

Various locations on the sample have been examined and the results revealed a consistent composition. Analysis of the X-ray output yielded of F 4.1, O 13.9, Ca 3.8, La 17.1, Ce 38.5, Pr 4.0, Nd 16.3 and Sm 2.3 at % by weight in the sample. The result is consistent with the specimen being a typical bastnaesite (Ce) crystal. The image of the sample surface, presented in Fig. 4.19, shows a number of small cubic crystals on the surface topography, ranging from 1-40 μm . Most of the remaining areas were uniform.

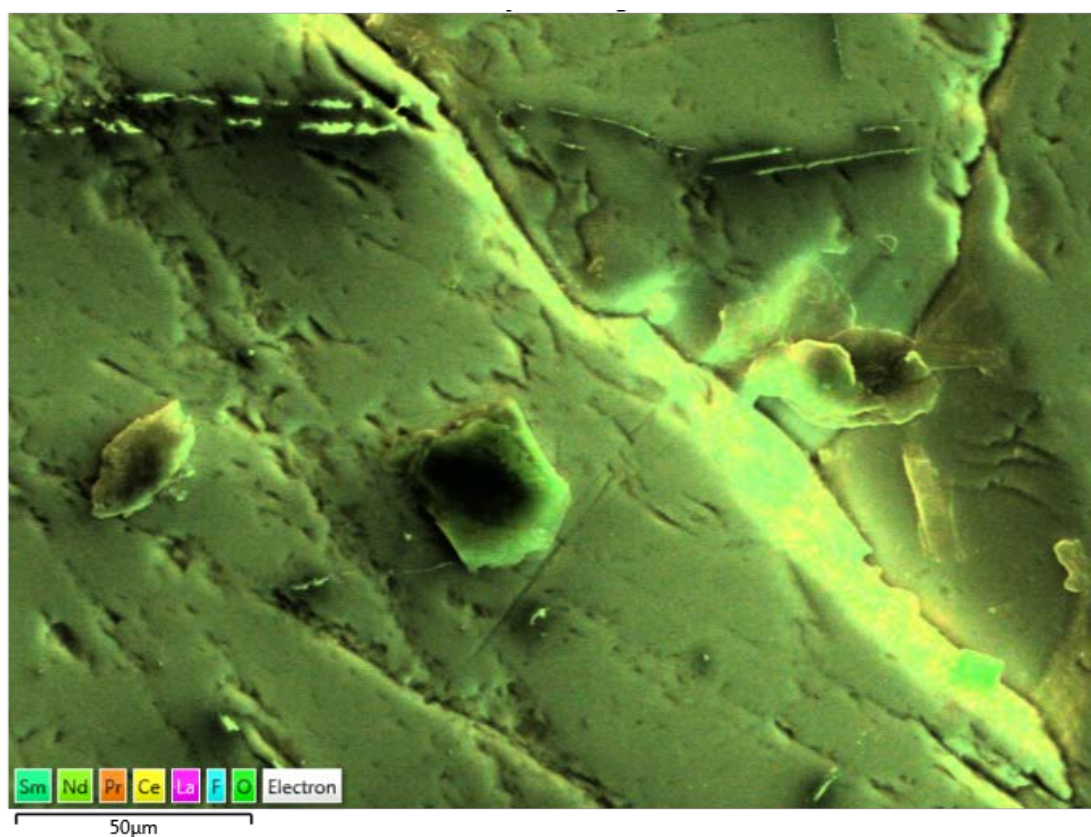


Fig. 4.19 Electron micrograph of a carbon sputtered bastnaesite crystal from Pakistan. Scanning area is 200 $\mu\text{m} \times 200 \mu\text{m}$.

The corresponding elemental mappings for the same area are shown in Fig. 4.20. Different colours represent various elements and the colour intensity represents the relative concentration of the corresponding elements. The small crystals present on the surface are O enriched while all the rare earth elements and F are surrounding these crystals. The co-occurrence of F with REs supports the sample as a rare earth fluorite mineral. Ca was present together with O on the crystal. This gangue mineral is probably calcite; the result is consistent with the XPS analysis results.

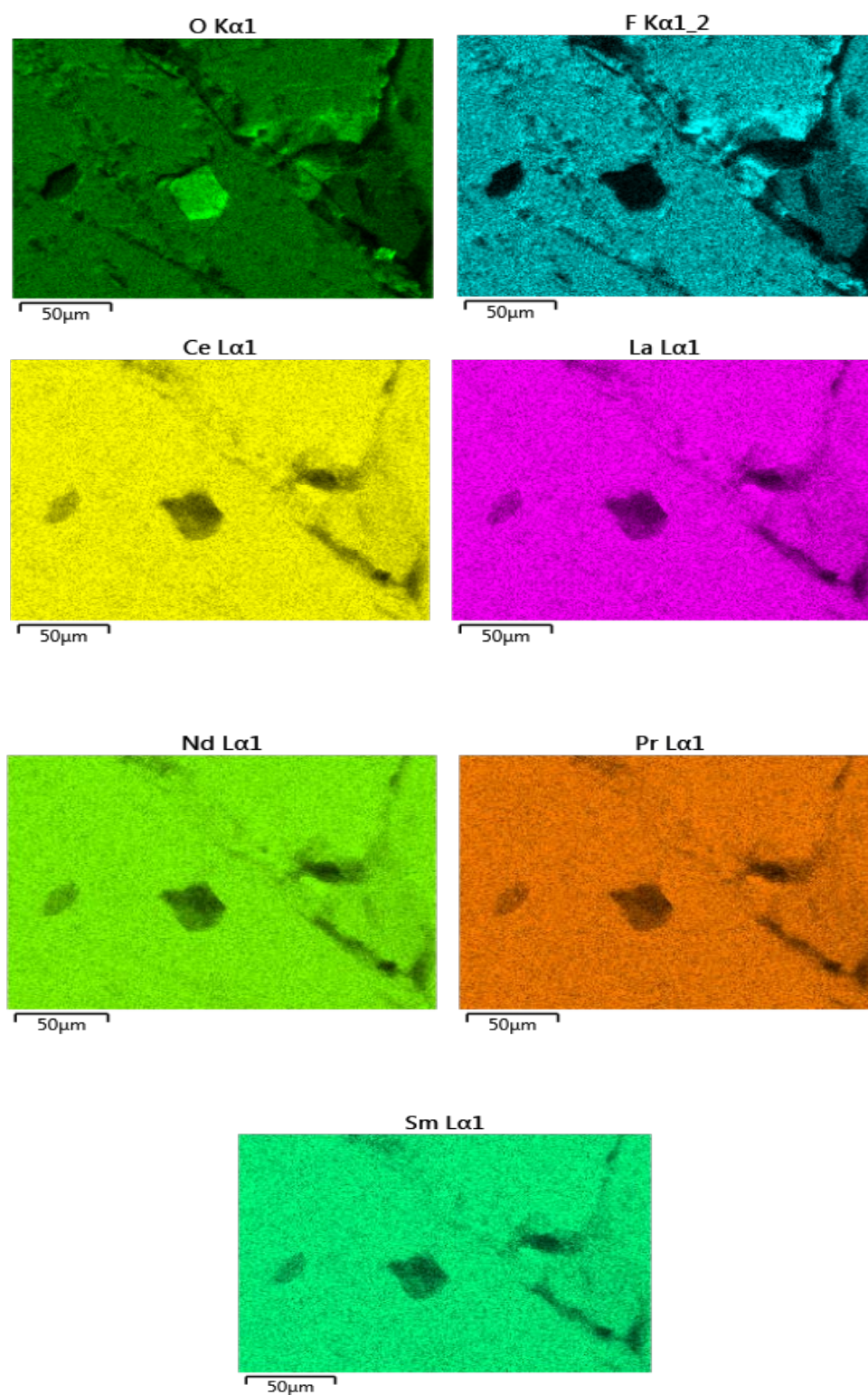


Fig. 4.20 SEM mapping on $L\alpha_1$ signal on single element of a bastnaesite crystal sample from Pakistan. The colour shades represent different concentration of the corresponding elements.

4.3.1c Investigation using Raman spectroscopy

The bastnaesite crystal was investigated using vibrational spectroscopy. Fig. 4.21 shows the Raman spectra using three different excitation wavelengths (442 nm, 514 nm and 633 nm). Three bands assigned to $(\text{CO}_3)^{2-}$ ν_1 were observed at 1083 cm^{-1} , 1094 cm^{-1} and 1096 cm^{-1} in all three spectra.

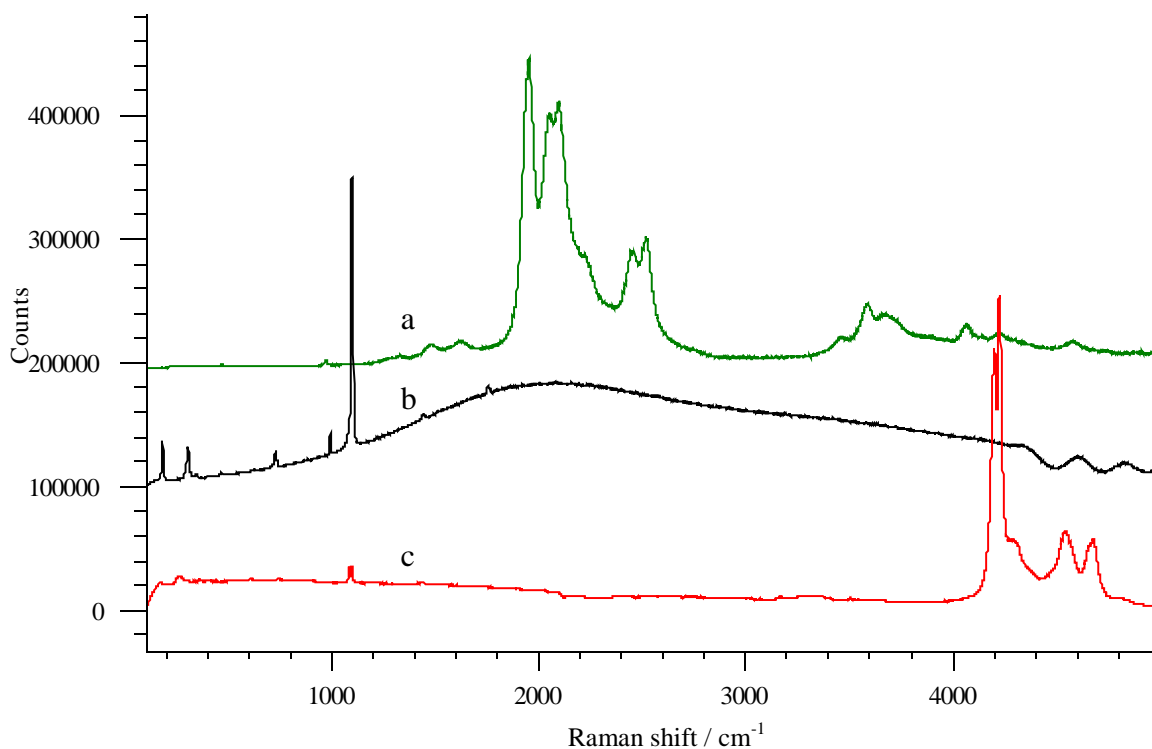


Fig. 4.21 Raman spectra of bastnaesite by using excitations of (a) 514 nm (b) 442 nm and (c) 633 nm.

Frost and Dickfos reported a single intense band for the $(\text{CO}_3)^{2-}$ ν_1 at 1096 cm^{-1} , 1085 cm^{-1} and 1097 cm^{-1} from three bastnaesite specimens sourced from different locales (Frost and Dickfos, 2007). Their results differed from the present study and could be due to different RE atoms substituting in the crystal structure in the samples investigated, leading to the non-equivalent states for the $(\text{CO}_3)^{2-}$ group (Adler and Kerr,

1963). Apart from Ce and La; Pr, Nd and Sm were detected in the sample used for the present study, while the bastnaesite crystal used by Frost and Dickfos only contained Ce and La.

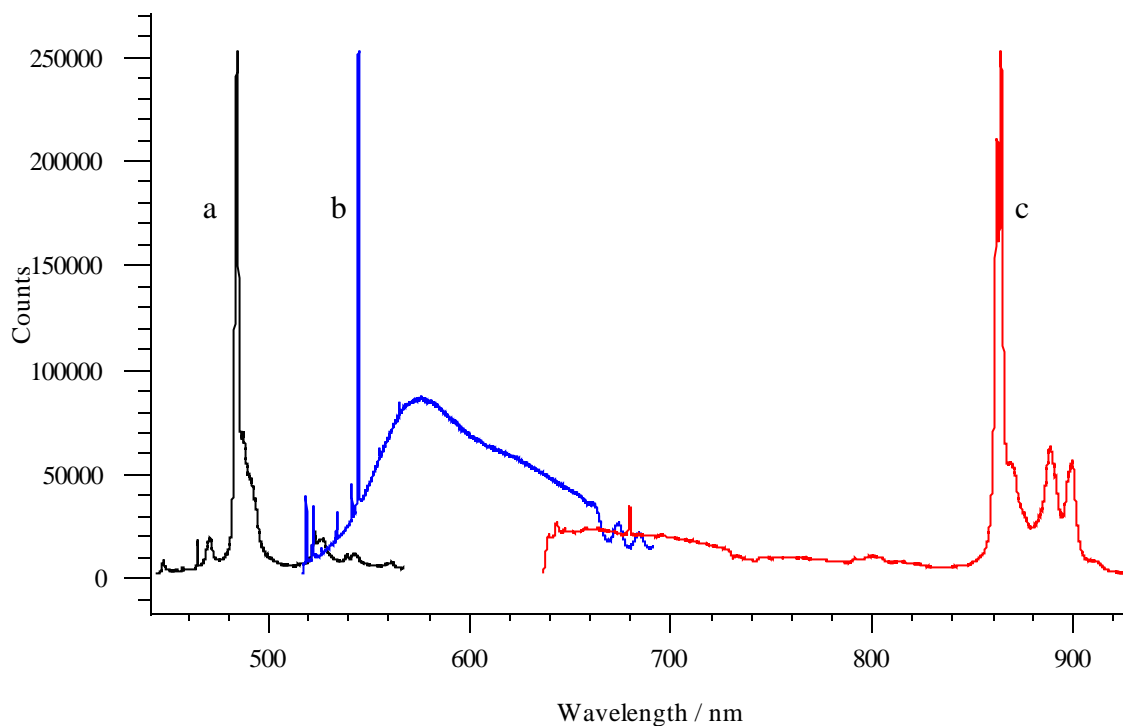


Fig. 4.22 Emission spectra of bastnaesite by using excitations of (a) 442 nm (b) 514 nm and (c) 633 nm.

Strong fluorescence lines were observed in the 633 nm and 442 nm spectra (Fig. 4.22). Emission lines were observed at 863, 865, 890, 899 and 901 nm in the 633 nm spectrum. The emission lines were similar to the fluorescence spectrum of Nd_2O_3 with 0 - 8 nm shift. The bastnaesite crystal spectrum is consistent with Nd being present in the crystal.

The intense band observed at 484 nm in the 442 nm spectrum supports Pr(III) was present in the sample. Pr was detected at 4% by weight using SEM-EDX. The energy level for Pr(III) was given in Fig. 4.23 (Zhou et al., 2012). The transition from $^3\text{P}_0$ to the

ground states corresponds to the emission of 490 nm. The emissions of 528 nm can be assigned to the transition of $^3P_0 \rightarrow ^3H_5$.

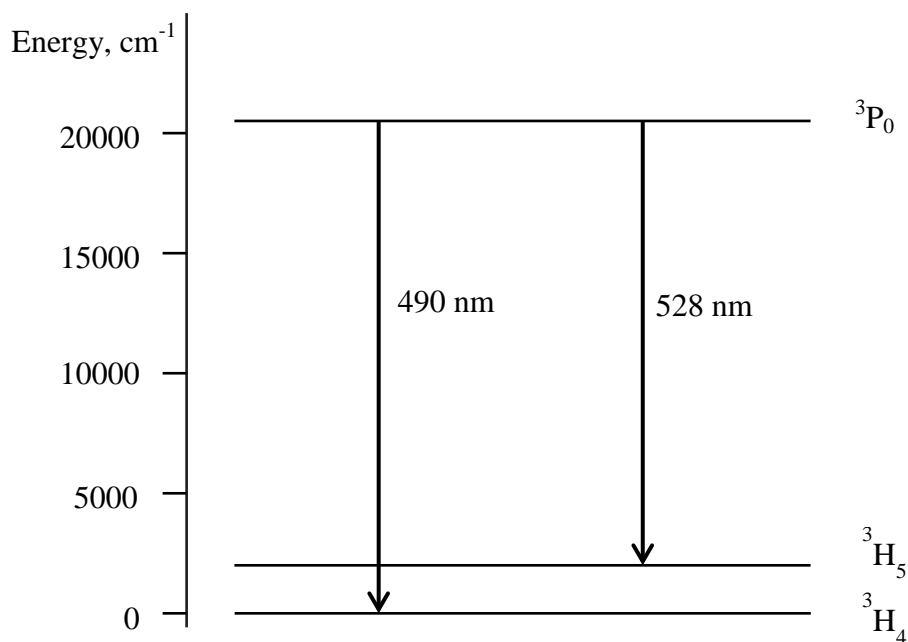


Fig. 4.23 Energy level diagram for Pr(III), data sourced from Zhou et al. (Zhou et al., 2012).

Zhou et al. have reported the absorption spectrum for a 0.5 mole% of Pr(III) fluorotellurite glass sample and the emission spectrum for Pr(III) doped fluorotellurite glass samples (doped at various concentrations). The absorption line was observed at 485 nm, while the emission lines shifted to higher wavelengths with higher concentration of Pr(III). In addition, low intensity emissions were also reported at 528 nm – 530 nm (Zhou et al., 2012). These emissions were observed in the present study at 523 nm and 527 nm with 442 nm excitation and 521 nm, 524 nm and 525 nm with the 514 nm excitation. The emissions at 484 nm and ~525 nm are in good agreement with the energy level transition of Pr(III) from $^3P_0 \rightarrow ^3H_4$ and $^3P_0 \rightarrow ^3H_5$ (Zhou et al., 2012).

4.3.1d Investigation using AFM and AFM-Raman

The grinding size for REs ore used in flotation is crucial for successful liberation of the mineral, in that it has to be achieved at an efficient grinding size. Oversized fractions would result in insufficient reagent attaching to the mineral surface and thus to decrease the collision efficiency. On the other hand, fine particles have been proven to have a low collision efficiency, and so with bubbles they are difficult to float in the process (Miettinen et al., 2010). The investigation of the surface topography can provide data on optimal grinding size for successful flotation. Fig. 4.24 exhibits an AFM image obtained from a $5\text{ }\mu\text{m} \times 5\text{ }\mu\text{m}$ area. Small regions are observed in this topographical image of the etched surface. These vary from $0.2\text{ }\mu\text{m}$ to $1\text{ }\mu\text{m}$. In the biggest operational plant, Bayan Obo, and three other major plants in China, the ores were ground to less than $74\text{ }\mu\text{m}$. Most of the particles sizes are $20\text{ }\mu\text{m} - 50\text{ }\mu\text{m}$ (Yu, 2001). If the region shown on the AFM image in Fig. 4.24 reflects areas of RE enrichment, the ore would need to be very finely ground to liberate minerals from the ore.

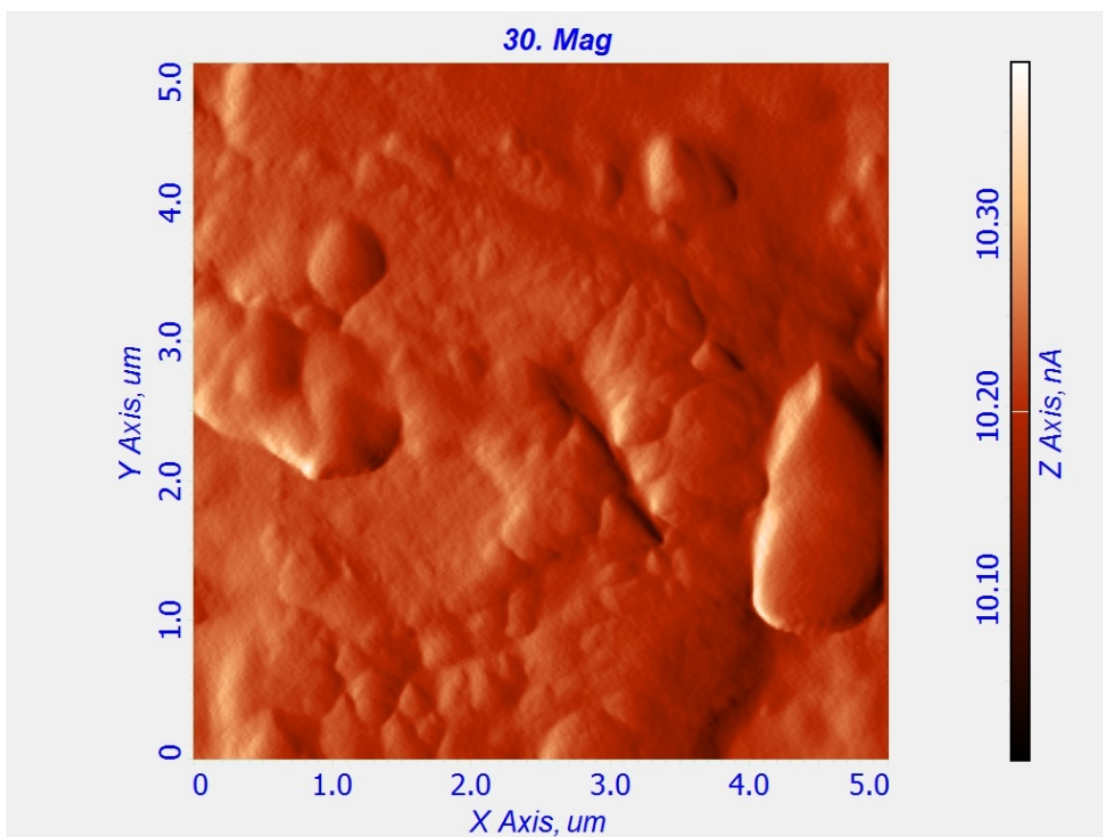
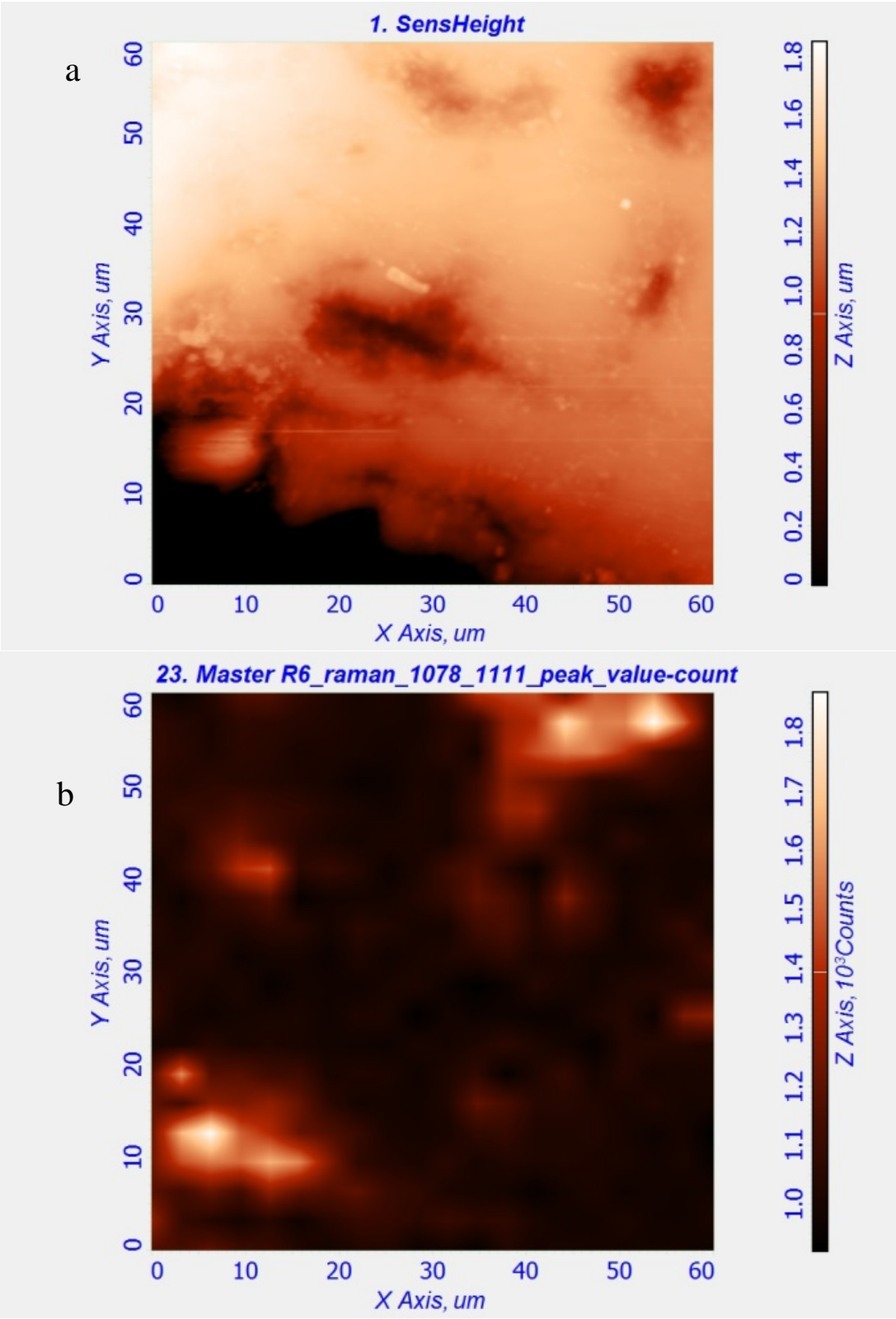


Fig. 4.24 AFM image of bastnaesite sized $5\ \mu\text{m} \times 5\ \mu\text{m}$.

Larger areas ($60\ \mu\text{m} \times 60\ \mu\text{m}$ and $20\ \mu\text{m} \times 20\ \mu\text{m}$) were also investigated by AFM and AFM-Raman. Fig.4.25a shows the surface topographic image of the specimen and Fig. 4.25b shows the Raman map simultaneously obtained for the same area. Different variations in height were present in the topographic image; when these regions were examined with Raman mapping, it was observed that the dark areas in the topographic regions corresponded to strong Raman bands between $1078\ \text{cm}^{-1}$ and $1111\ \text{cm}^{-1}$. The $1096\ \text{cm}^{-1}$ band has been assigned to a $(\text{CO}_3)^{2-}$ symmetric stretching mode. This observation is consistent with the fluorocarbonate RE mineral being concentrated in the dark areas in the AFM image. The observation is confirmed in Fig. 4.25c and Fig. 4.25d, where a smaller area was scanned. A higher count in the Raman map is present on the top right corner where a low area is observed in the AFM image. Both of the AFM and AFM-Raman images have shown that the REs are enriched in batches. The enriched

areas are observed no bigger than $10\text{ }\mu\text{m} \times 10\text{ }\mu\text{m}$, consistent with the AFM topography observation.



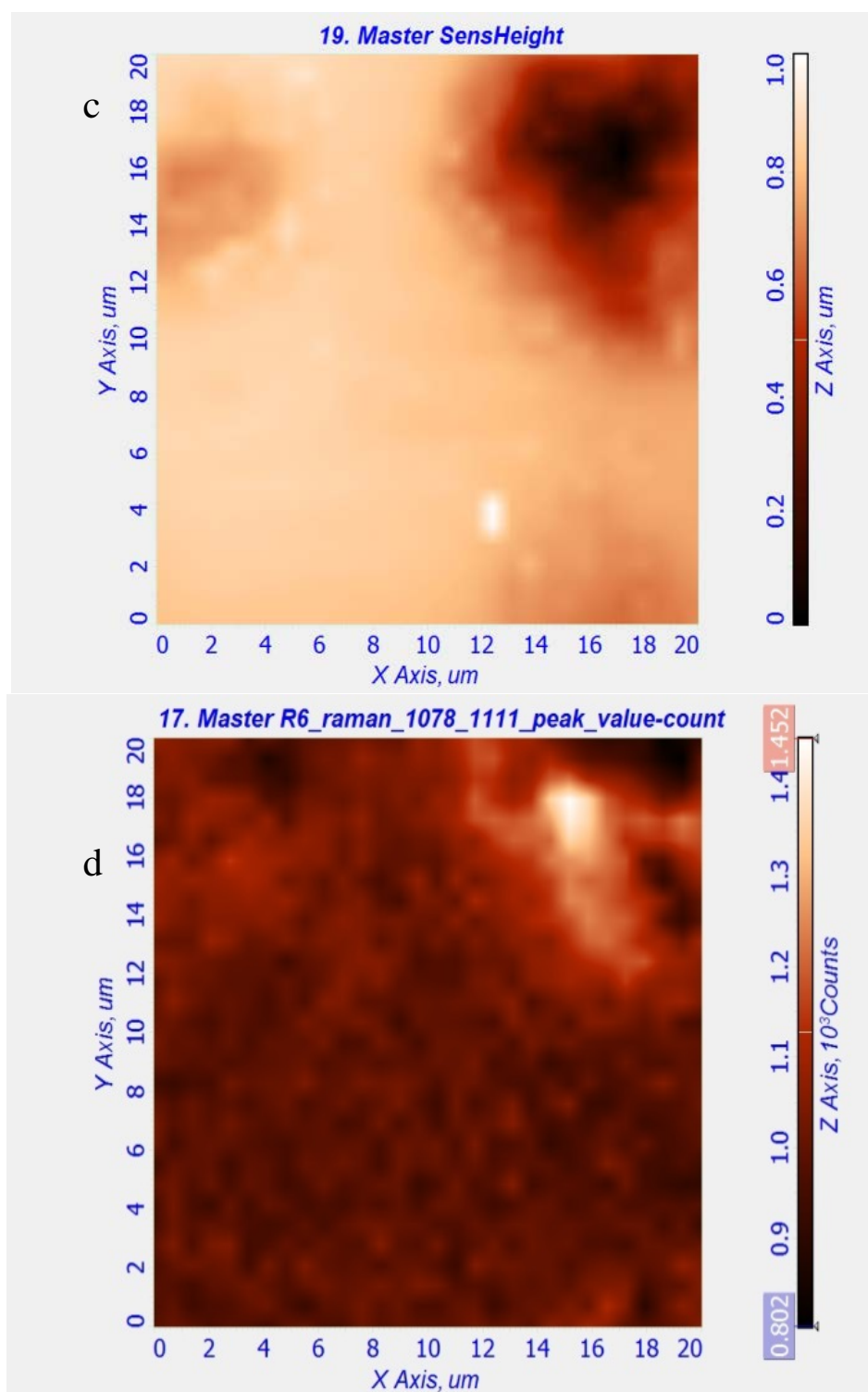


Fig. 4.25 AFM and AFM-Raman images for bastnaesite: (a), (c): Surface image, 60 μm × 60 μm and 20 μm × 20 μm, respectively; (b), (d): AFM-Raman image with a static scan centred at 1094.5 cm⁻¹, scan area: 60 μm × 60 μm and 20 μm × 20 μm, respectively. Both of the AFM and AFM-Raman images have shown that the REs are enriched in regions. The enriched area dimensions are less than 10 μm × 10 μm.

4.3.1e Investigation by Magnetic AFM

Several rare earths exhibit strong magnetic properties and this has been utilized in the manufacture of Nd high performance magnets by industry. The SEM-EDX results have shown that the composition of the bastnaesite specimen was RE elements with Ca, F and O. No other magnetic materials were present in the sample. Therefore, it would be possible to investigate the localized magnetic field using a magnetic tip on the AFM. The magnetic moment variation can be used as an indicator for enrichment locations for REs.

In order to compare the strength of the magnetic signals, a typical magnetic sample (magnetite) was measured prior to bastnaesite. Magnetite is considered as the most magnetic of the naturally occurring minerals on earth (Harrison et al., 2002). Therefore, it was chosen as a referenced sample for magnetic AFM investigation.

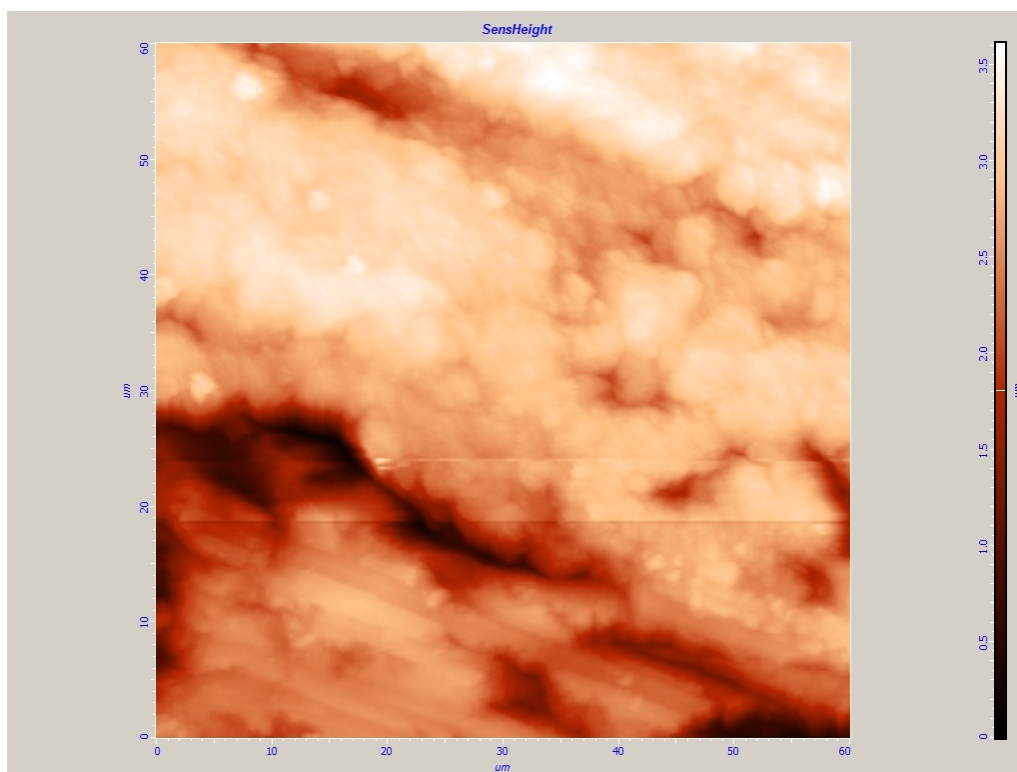


Fig. 4.26 Topography AFM image of magnetite sized 60 μm × 60 μm.

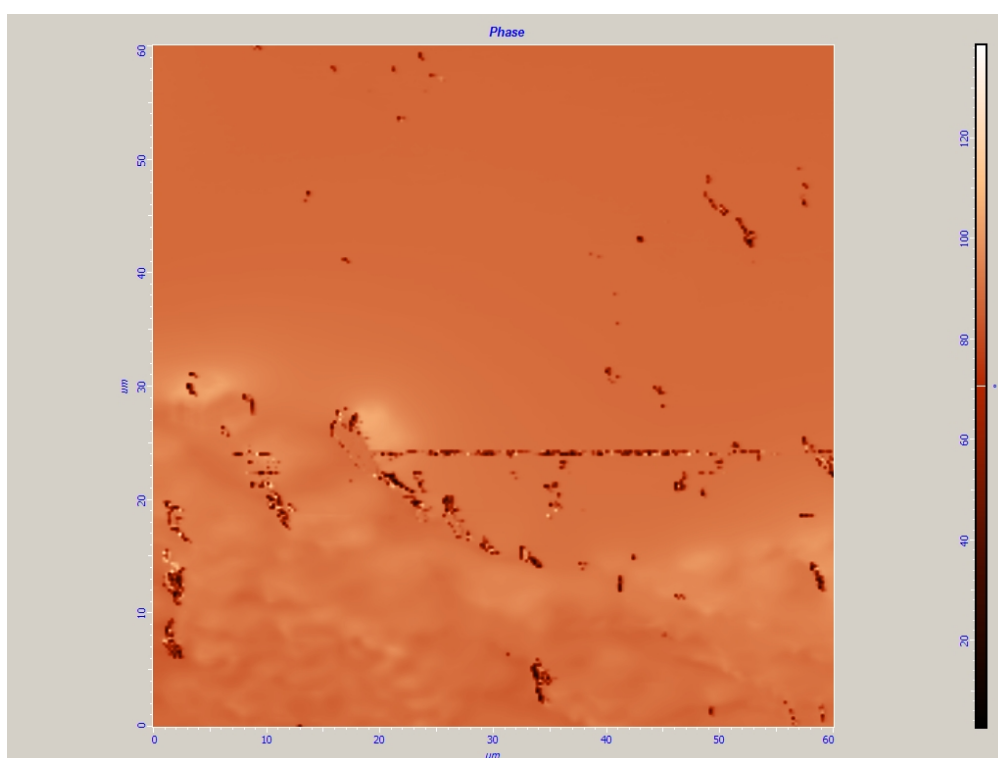
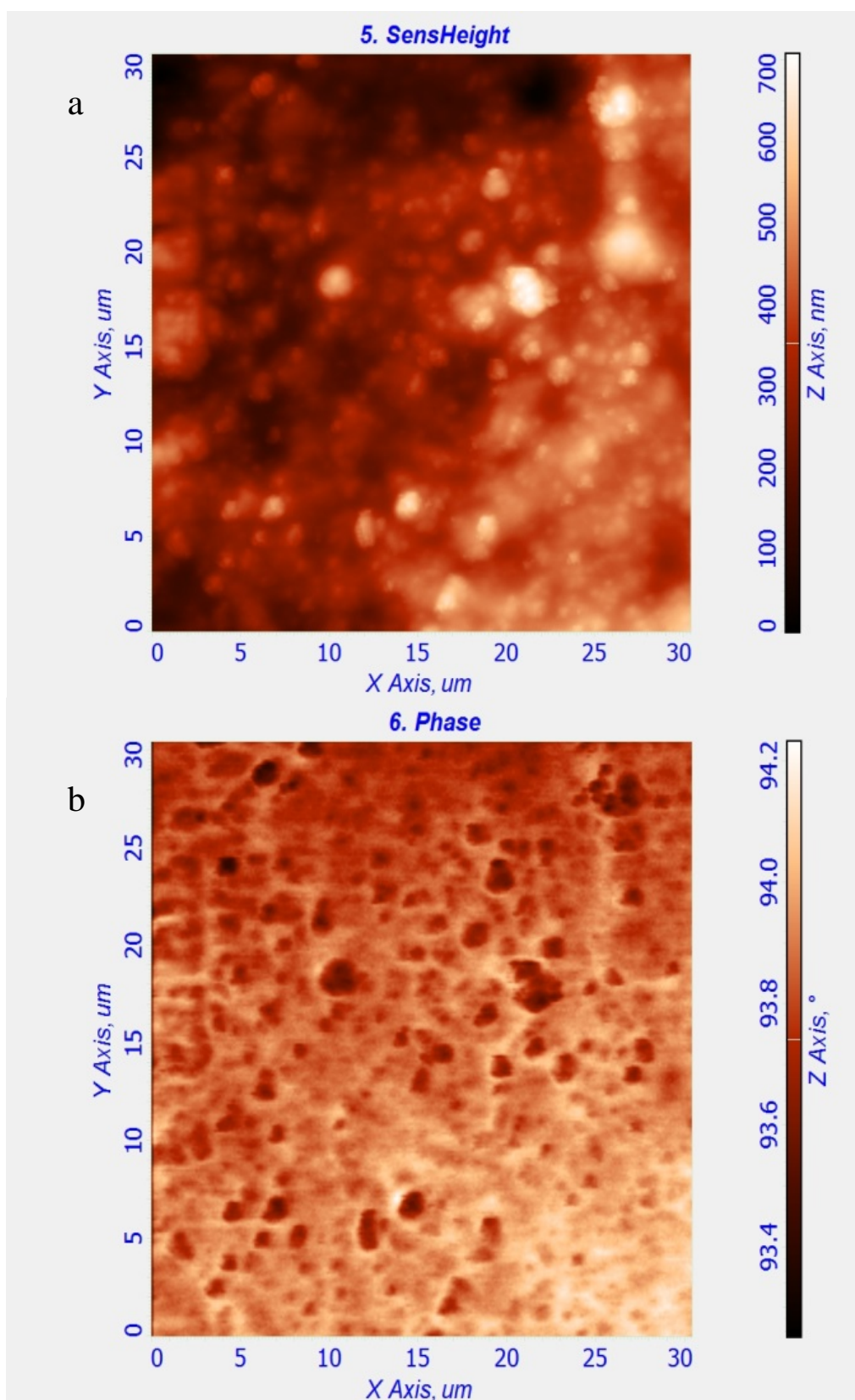


Fig. 4.27 Magnetic AFM image of magnetite corresponding to the same area as Fig. 4.26. The colour range indicates the magnetic signal strength.

Fig. 4.26 and Fig. 4.27 show the topographic and the corresponding magnetic scan image of a magnetite specimen. Small crystals ranging from 1 – 5 μm were present on the surface. A variation of 0.01- 3.5 μm in height was also observed in the AFM image. The change in magnetic moment ranged detected from 0 – 140 unit. The lower areas appear to have less magnetic signal response (Fig. 4.27). It indicates gangue mineral was present in the dark (low) area in the AFM image. Other areas where the crystals were uniform showed little variation in the magnetic scan map. It is expected these are magnetite crystals and have the same magnetic moment. This technique has established the feasibility for identification of the REs location on the sample surface using magnetic imaging scan. In addition, the strength of the signal of magnetite can also be used as a reference to compare the REs magnetic force.



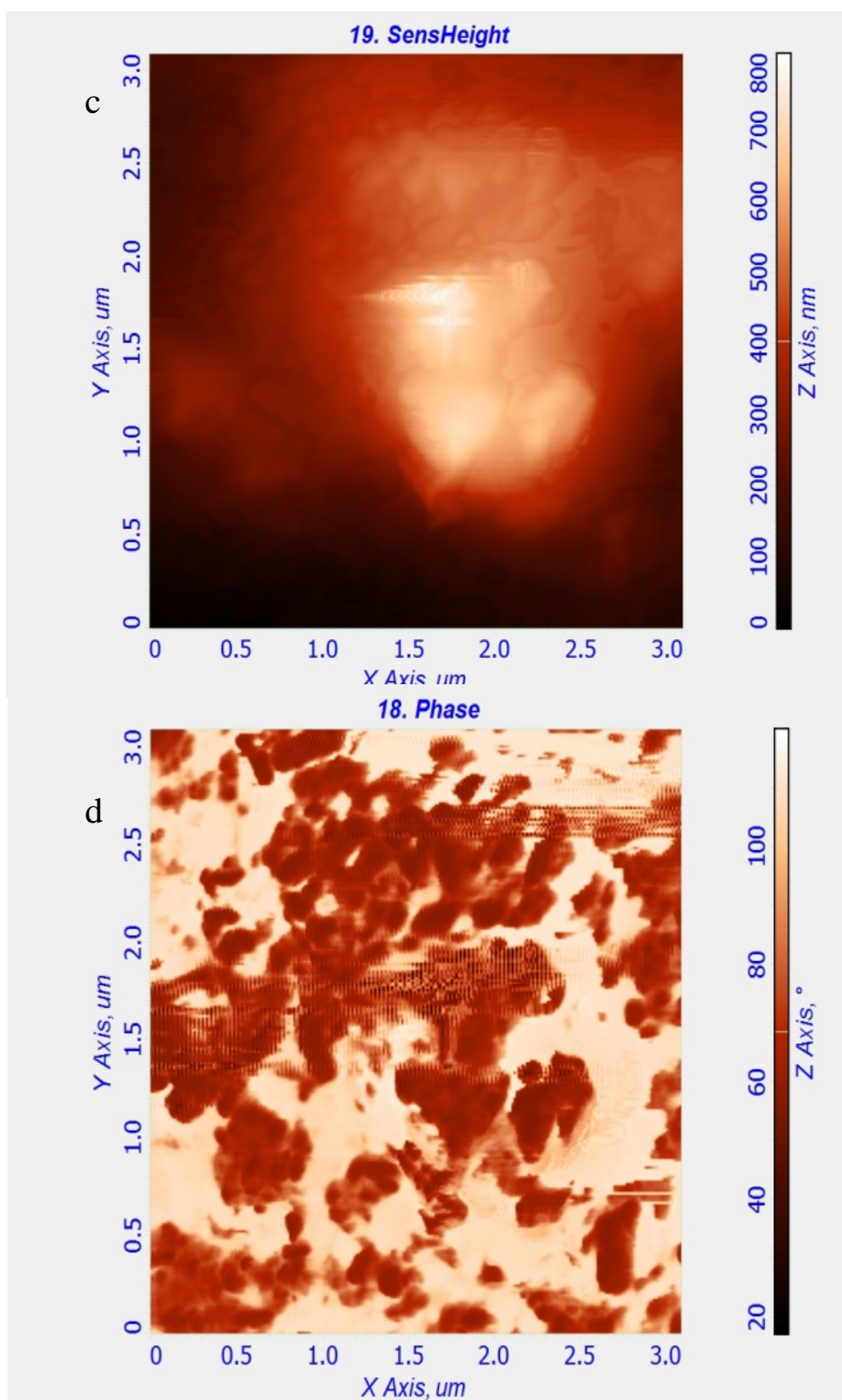


Fig. 4.28 (a) topography and (b) magnetic AFM images of bastnaesite, $30\ \mu\text{m} \times 30\ \mu\text{m}$;
 (c) topography and (d) magnetic AFM images of bastnaesite, $3\ \mu\text{m} \times 3\ \mu\text{m}$.

The bastnaesite specimen, areas of $30\text{ }\mu\text{m} \times 30\text{ }\mu\text{m}$ and $3\text{ }\mu\text{m} \times 3\text{ }\mu\text{m}$ were scanned to investigate the localized magnetic fields (Fig. 4.28). The higher count areas are expected to be attributable to REs enriched areas. The particle (crystals) sizes from $0.1\text{ }\mu\text{m} - 2\text{ }\mu\text{m}$ on the surface were observed to have less signal strength (Fig. 4.28a and 4.28b). The result was consistent with the SEM-EDX data, in which gangue minerals crystals were present on the surface and surrounded by REs. When a smaller scanning area was scanned ($3\text{ }\mu\text{m} \times 3\text{ }\mu\text{m}$, Fig. 4.28c and Fig. 4.28d), the magnetic image shows much more details. This can be conflict to the standard AFM topography, which only displays one obvious crystal in the centre of the image (Fig. 4.28c). This is attributed to the measurement of variations in the magnetic signal observed across the (relatively) featureless topographical scan. Compared to magnetite, the magnetic count for the bastnaesite was similar to that in magnetite (about 94 units for the highest count). It is feasible to identify the REs locations in minerals.

4.3.2 Monazite

4.3.2a Investigation using SEM-EDX

Monazite has the nominal composition as $\text{REE}(\text{PO}_4)$. The elemental analysis using SEM-EDX found that Ce was 15.6%, w/w with Nd 6.7%, La 6.2%, Sm 1.7% and Th 11.4% for the sample. Other metals Al, Ca and Si were present in minor amounts. It indicates a small quantity of gangue material was present in the specimen.

A SEM surface image generated from the combination of backscattered and secondary electrons ($150\text{ }\mu\text{m} \times 110\text{ }\mu\text{m}$) revealed small patches of crystals present on the sample surface that appeared to be calcite and aluminosilicate (Fig. 4.29). The rough surface was unpolished due to radioactivity constraints.

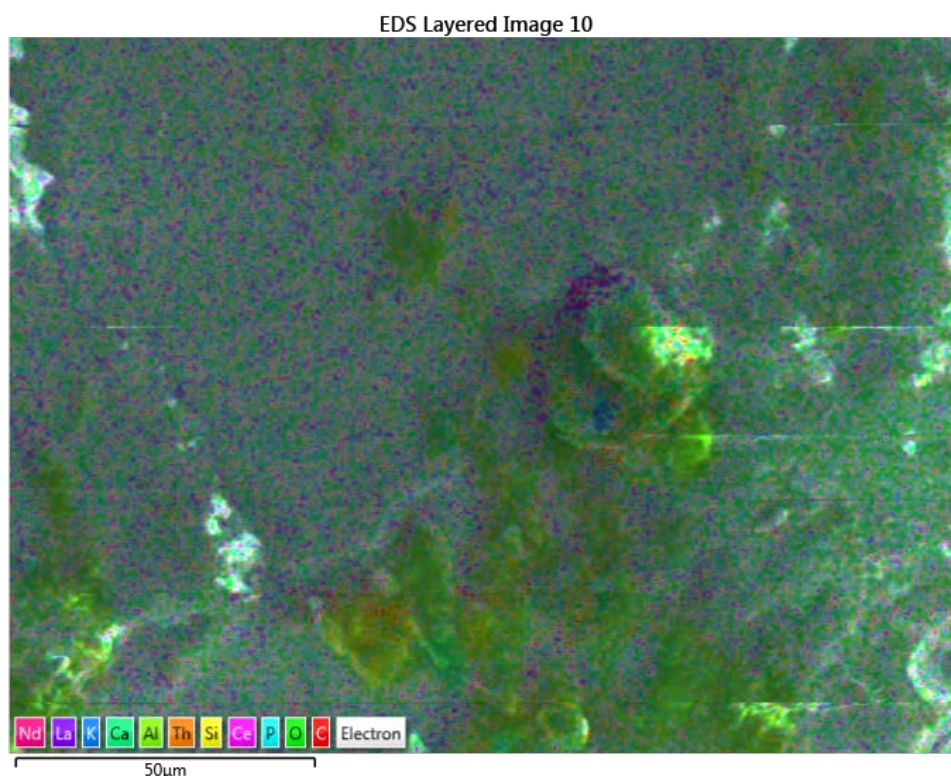
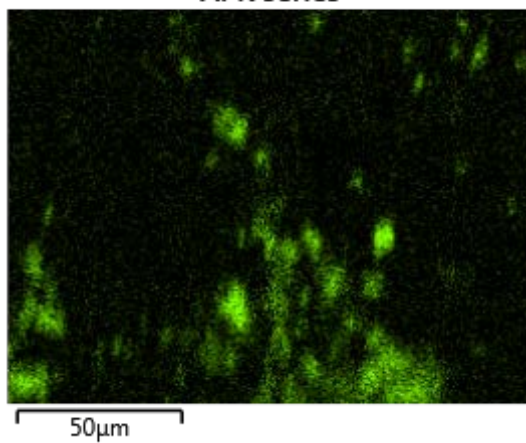


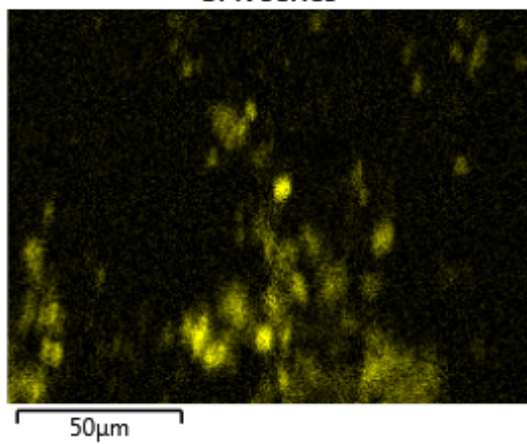
Fig. 4.29 Electron micrograph of a carbon sputtered monazite crystal.

Elemental mapping revealed that all the rare earth elements were co-located with the Th, O and P. The result is consistent with a sample comprised of rare earth phosphate. The Al and Ca were localized with the Si (Fig 4.30). Mapping of Al, Ca and Si revealed gangue crystals exposed on the fracture surface, ranging in size from 5-20 μm. Al and Si were co-located while Ca was present in different locations. O was observed in most locations. It was expected that both the REs minerals and gangue minerals would contain oxygen. It is also indicated that at least two gangue minerals were present. Typical gangue minerals include ilmenite, rutile, quartz, and zircon (Jordens et al., 2013). In the present study, quartz and calcite probably were present. The differences in gangue minerals from that of bastnaesite could require different collectors and depressors in the two flotation systems.

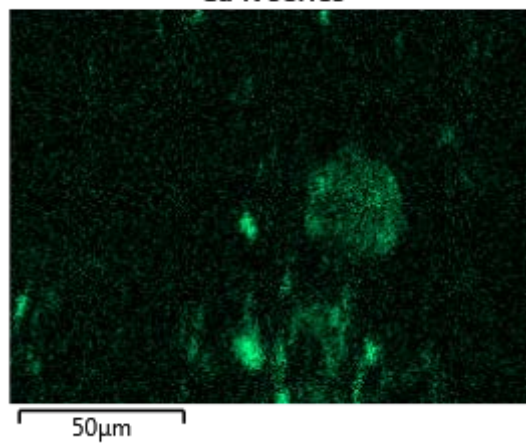
Al K series



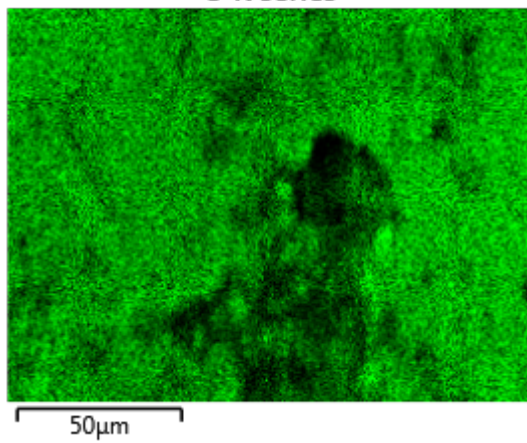
Si K series



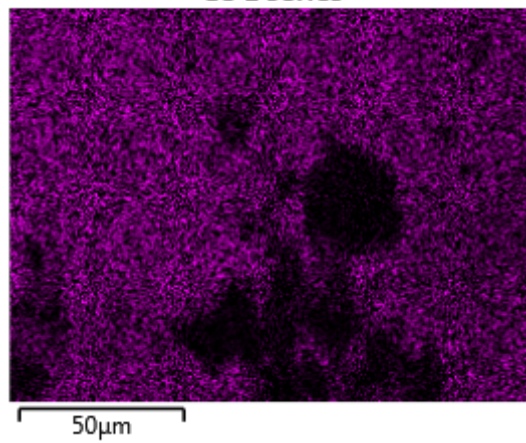
Ca K series



O K series



Ce L series



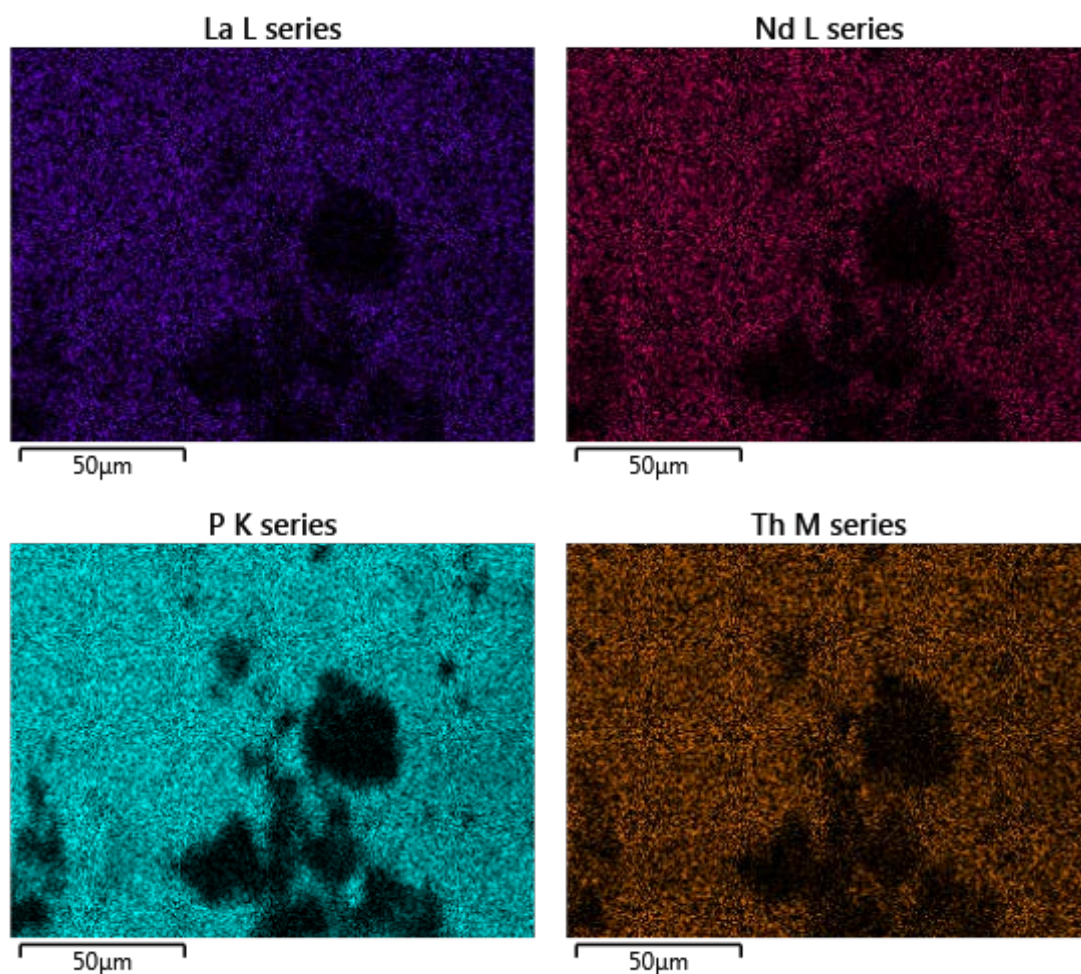


Fig. 4.30 SEM mapping on $L\alpha_1$ signal on single element of a monazite crystal sample

4.3.2b Raman Spectroscopy Investigation

The monazite crystals were placed on the sample platform and aligned using modelling clay in order to achieve a flat surface suitable for scanning purposes. The monazite crystals were examined using three different excitation sources (Fig. 4.31). A band at 975 cm^{-1} was observed with each laser source. Bands at 466 cm^{-1} , 624 cm^{-1} and 1065 cm^{-1} were also observed. These are assigned to the $(\text{PO}_4)^{3-}$ ν_2 , ν_3 , and ν_4 modes respectively.

Frost et al. reported the Raman spectra for churchite-Y with the formula of $(\text{REE})(\text{PO}_4) \cdot 2\text{H}_2\text{O}$. The author observed an intense sharp band at 975 cm^{-1} for the

$(\text{PO}_4)^{3-}$ ν_1 mode and bands at 497 cm^{-1} , 1065 cm^{-1} and 563 cm^{-1} assigned to ν_2 , ν_3 , and ν_3 modes. The Raman spectra of the monazite sample are consistent with those reported by Frost (Frost et al., 2009). Different REs can substitute in the mineral structure and thus minor shifts are expected when various sources monazite are examined. Ruschel synthesized a number of monazite structural compounds with different REs substituted (Ruschel et al., 2012). The synthesized compound $\text{Ce}_{0.62}\text{Nd}_{0.15}\text{La}_{0.12}\text{Th}_{0.08}\text{PO}_4$ has the closest composition to the sample used in this thesis. The $(\text{PO}_4)^{3-}$ ν_1 band was reported at 973.0 cm^{-1} . Another two synthesized compounds $\text{Ce}_{0.52}\text{Sm}_{0.49}\text{P}_{0.99}\text{O}_4$ and SmPO_4 were reported to have the ν_1 band at 976.3 cm^{-1} and 981.3 cm^{-1} (Ruschel et al., 2012). The present study contains 1.7% of Sm together with Ce, Nd, La and Th. The ν_1 Raman shift for $(\text{PO}_4)^{3-}$ was expected to be between 973.0 cm^{-1} and 981.3 cm^{-1} . The band observed at 975 cm^{-1} has good agreement with the expected value.

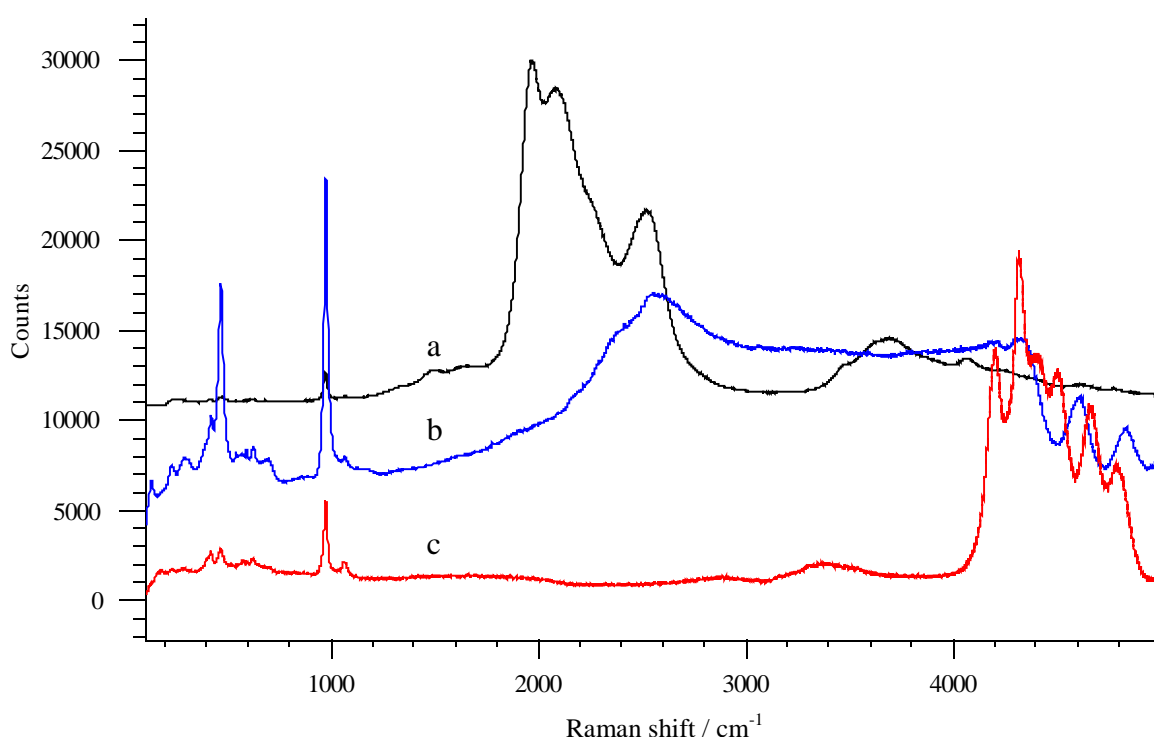


Fig. 4.31 Raman spectra of monazite using excitation sources of (a) 633 nm (b) 514 nm and (c) 442 nm, showing the wavelength dependence of the fluorescence emission.

A number of fluorescent emissions were observed to overlap the Raman spectra. The corresponding emission spectra are exhibited in Fig. 4.32. Fluorescence bands are observed in the 633 nm, 514 nm and 442 nm spectra. The fluorescent emissions at 863 - 901 nm in the 633 nm spectrum are consistent with Nd being present in the monazite sample. Fluorescence bands at 485 nm, 498 nm and 527 nm in the 442 nm excitation spectrum (527 nm with the 514 nm excitation) indicate Pr was also present (as discussed in 4.3.1c). The results appear to be inconsistent with the SEM-EDX data. It is probable that the concentration of Pr is below the detection limit of the SEM-EDX (0.3% -1.5% (w/w)) (Sessa et al., 2011). Fluorescence detection limits vary based on quantum yield, but for intensely fluorescent compounds the detection limit can be as low as 10^{-11} and 10^{-12} mol·L⁻¹ (Sherman, 1997). For Pr, a doping concentration of 0.05 mol% (0.00045%, w/w) in fluorotellurite glasses was able to produce a satisfactory fluorescence spectrum (Zhou et al., 2012). In the present study, it is suggested that the low concentration of Pr in the monazite sample fell below the detection limit of SEM-EDX, but the strong fluorescence bands was sufficient to identify the low concentrations of Pr that were present in the sample.

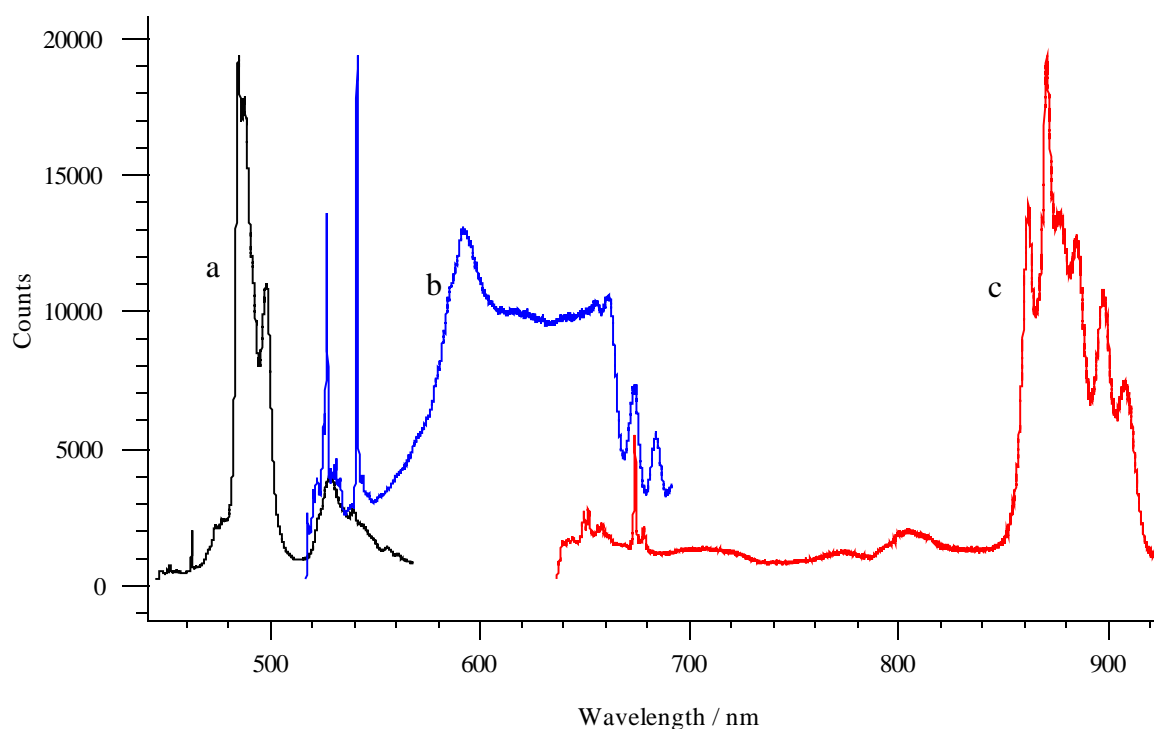


Fig. 4.32 Emission spectra from monazite with excitation by (a) 442 nm (b) 514 nm and (c) 633 nm.

4.3.2c Monazite Investigation using AFM and Magnetic AFM

Due to contamination and radiation hazard, monazite was not polished before being investigated. Substantial variations were observed on the Z axis, which resulted in a less than optimal topographic scan image and this was most apparent at smaller scale scan areas. The images for monazite, when compared to the bastnaesite sample (Fig. 4.24 and Fig. 4.25), displayed fewer features and had a lower resolution (Fig. 4.33 and Fig. 4.34). The images for bastnaesite and monazite both exhibited small crystals on the surface, with sizes ranging from 0.2 μm to 3 μm across. The topographical results are consistent with the SEM images.

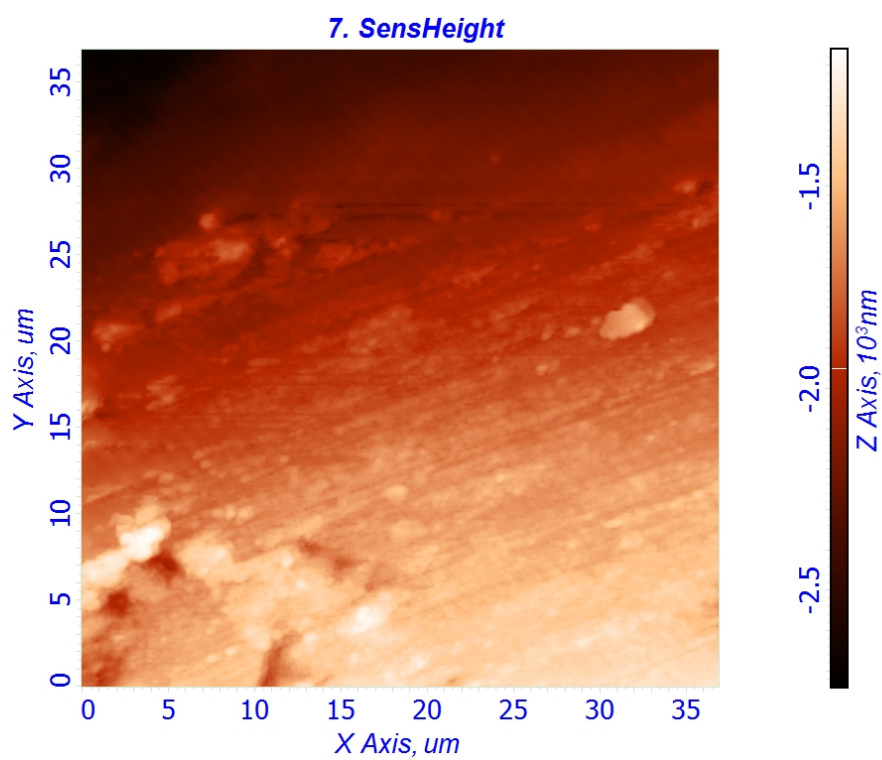


Fig. 4.33 AFM image of monazite ($35\ \mu\text{m} \times 35\ \mu\text{m}$ scan).

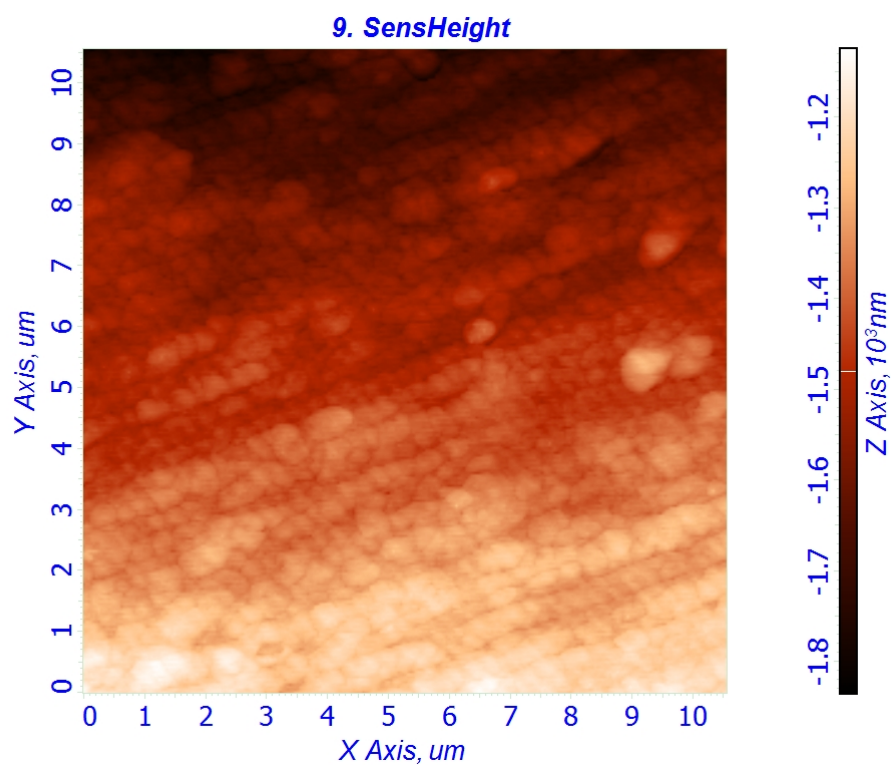


Fig. 4.34 AFM image of monazite ($10\ \mu\text{m} \times 10\ \mu\text{m}$ scan).

The presence of neodymium fluorescence in the Raman spectra was evidence for magnetic element substitution in the monazite and the possibility of micro domain formation. This was investigated using a magnetized cobalt coated AFM probe. A common area of $30\text{ }\mu\text{m} \times 30\text{ }\mu\text{m}$ was examined using an AFM topographic scan and then by a magnetic tip scan (Fig. 4.35).

The monazite surface was not polished before being investigated, and accordingly, to avoid tip damaged, the scan distance between the tip and the surface was higher than the scan undertaken for bastnaesite (0-1.6 μm in monazite scan compared to 0-0.8 μm in bastnaesite scan). The increased scanning distance and the bigger variation in height of the sample have resulted into fewer features displayed in the scans of monazite.

The magnetic scan exhibited a strong variation in the magnet signal from the monazite (Fig. 4.35). The count varied from 0 to 100. The maximum count was 20 units less than bastnaesite and 40 units less than magnetite, demonstrating a weaker interaction between the probe and the monazite under the scanning conditions. It is probable that the greater tapping distance required for the unpolished monazite surface was responsible for the low signal results. Nevertheless, the resolution is clear enough to distinguish between the magnetic REs area and gangue mineral regions. The lower regions observed on the crystal in the middle of Fig. 4.35 are non-magnetic. This is consistent with the crystal being a gangue mineral rather than monazite. The results are also consistent with the XPS-EDX data where small crystals presented as the gangue minerals.

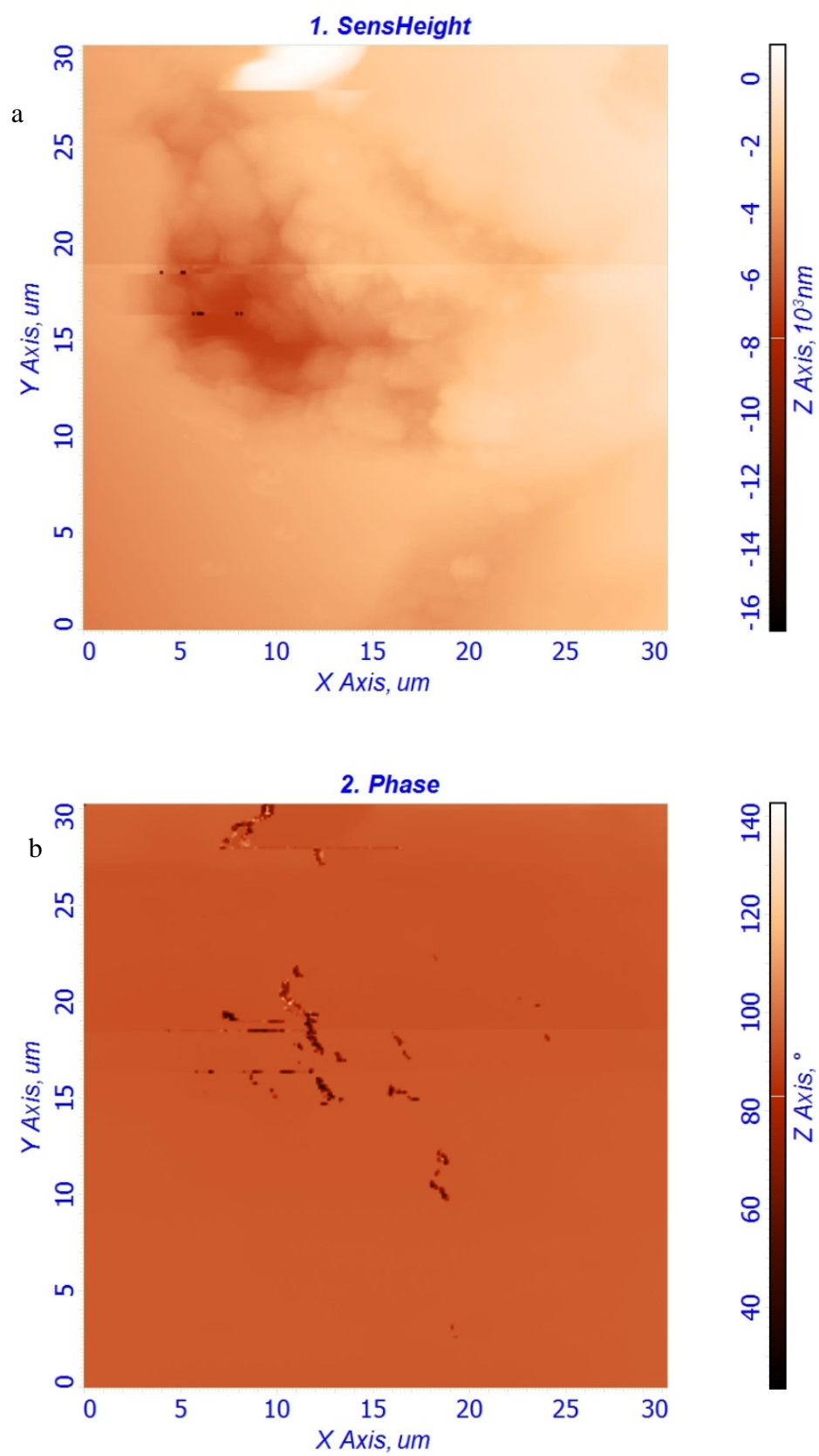
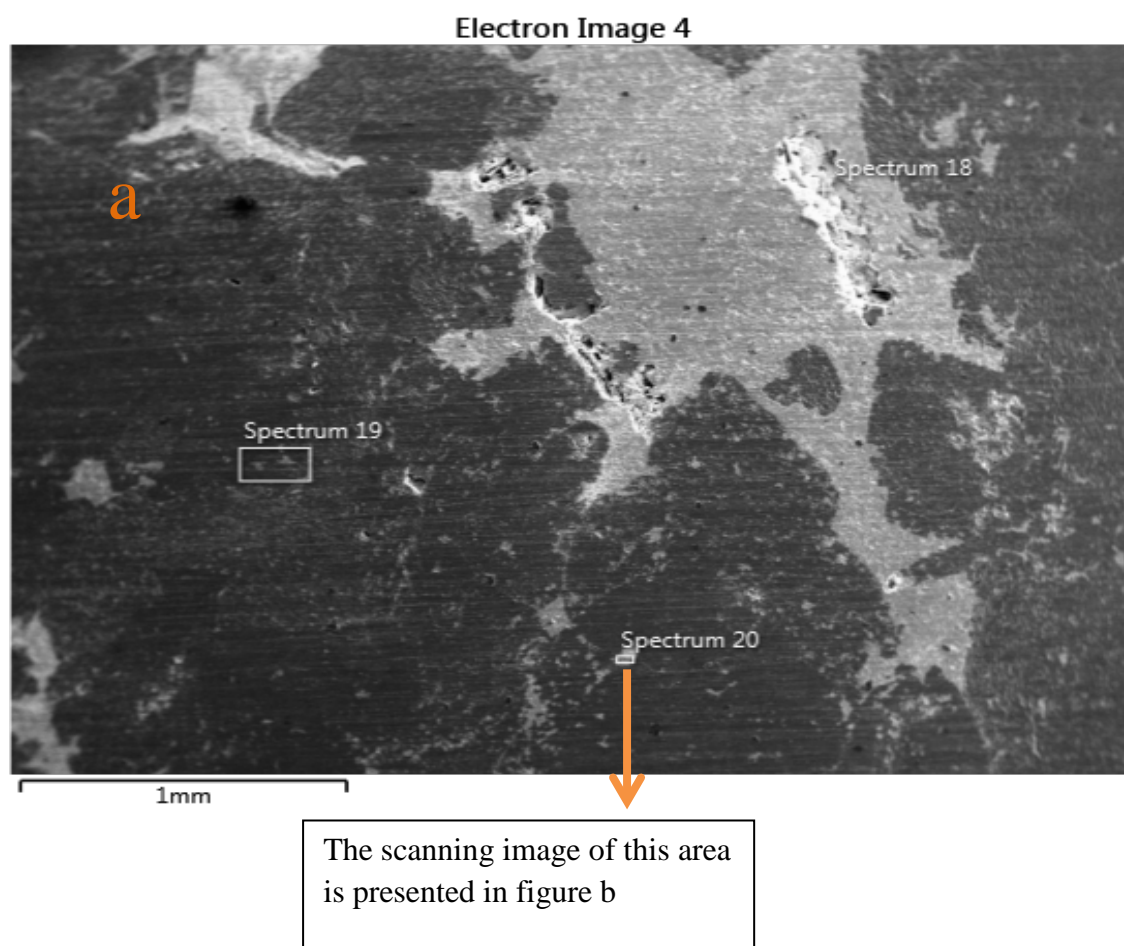


Fig. 4.35 (a) Topographic and (b) magnetic AFM images of monazite $30\ \mu\text{m} \times 30\ \mu\text{m}$.

4.4 Gangue minerals investigation

4.4.1 Investigation by SEM-EDX and XPS

A bastnaesite ore specimen was examined by SEM-EDX. The elemental analysis for an area of 3 mm × 3 mm indicates that the majority of the sample consists of gangue minerals with no REs presented. The sample mainly contained Ca, Mg, Zr with minor Fe, Mn, Ba, Na and K. The surface characterization by SEM-EDX is shown in Fig. 4.36. The image displays two distinct surface structures. A small area (250 μm × 200 μm) was found containing REE crystals. Higher resolution images of the micron-sized crystals on the sample surface are shown in Fig. 4.36b and 4.36c.



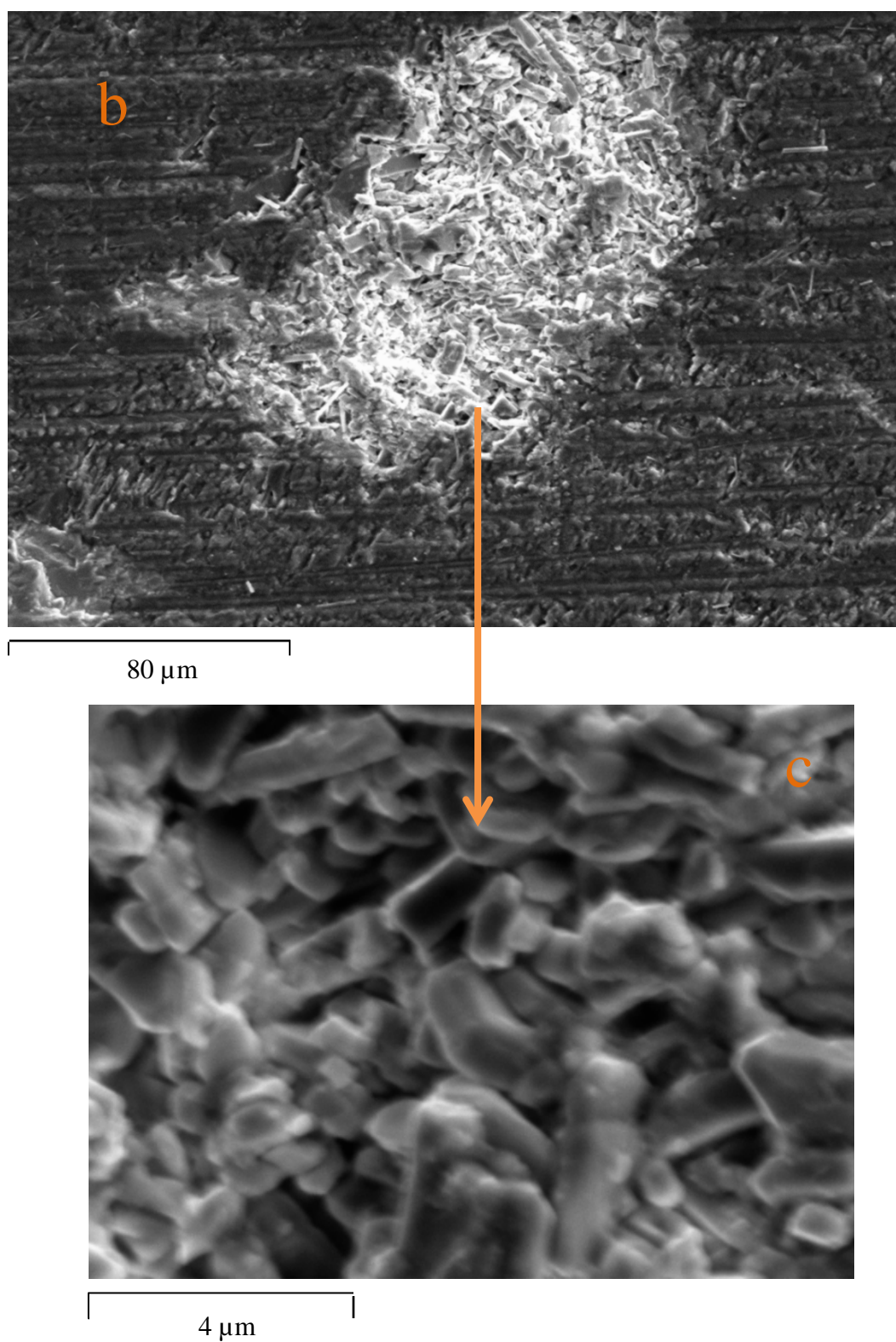
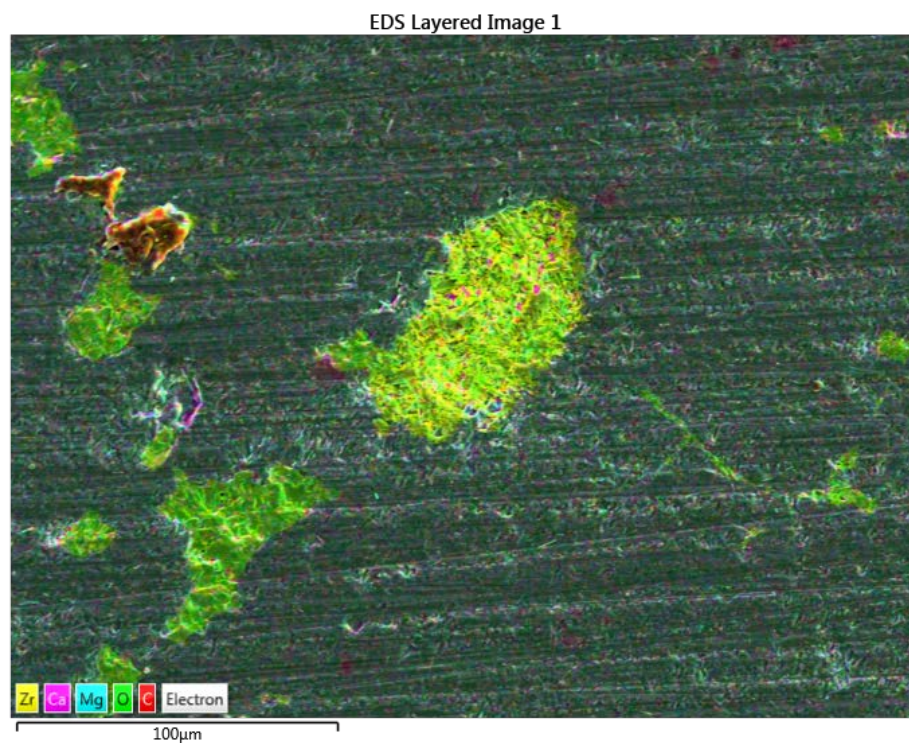
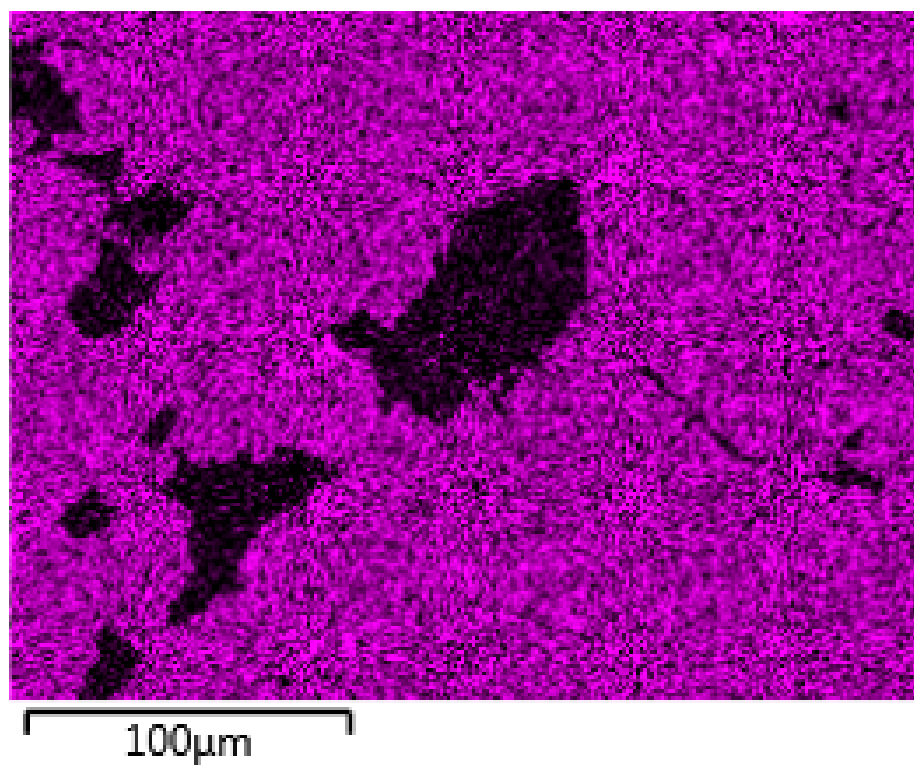


Fig. 4.36 SEM image for a bastnaesite ore specimen; (a) scanning size at 3 mm × 3 mm; (b) a 80 μm × 30 μm crystal containing REE; (c) 10 μm × 10 μm image for the crystal shown in (b).

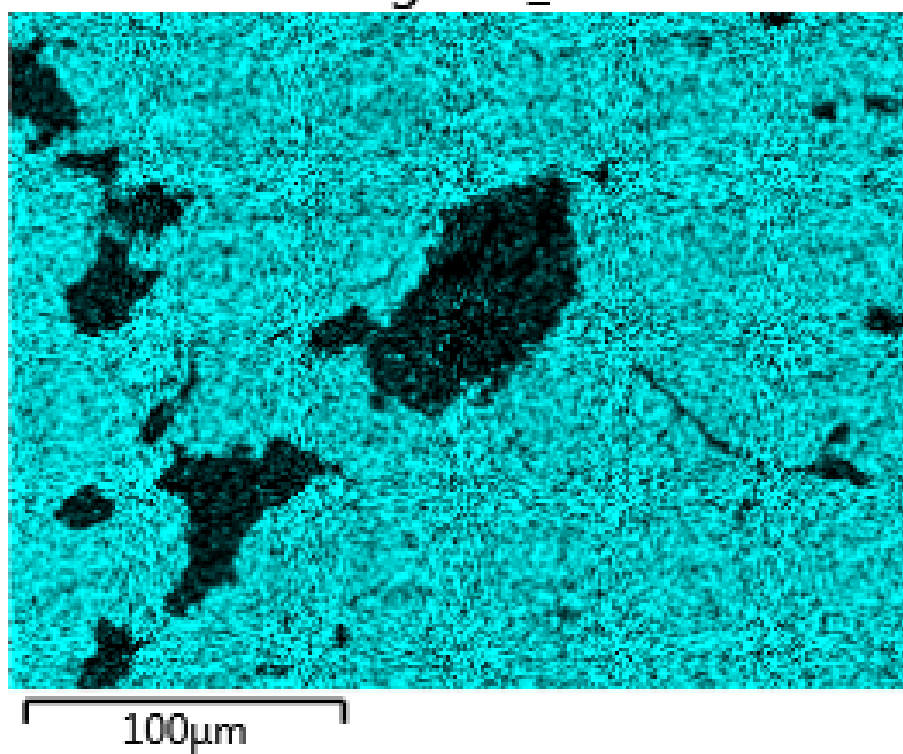
Elemental mapping was conducted over the area where the REs were present (Fig. 4.37). It was found that Ce was the major REE, along with minor Nd, La, Pr and Sm. The concentrations for the last four elements only slightly exceeded the detection limit.



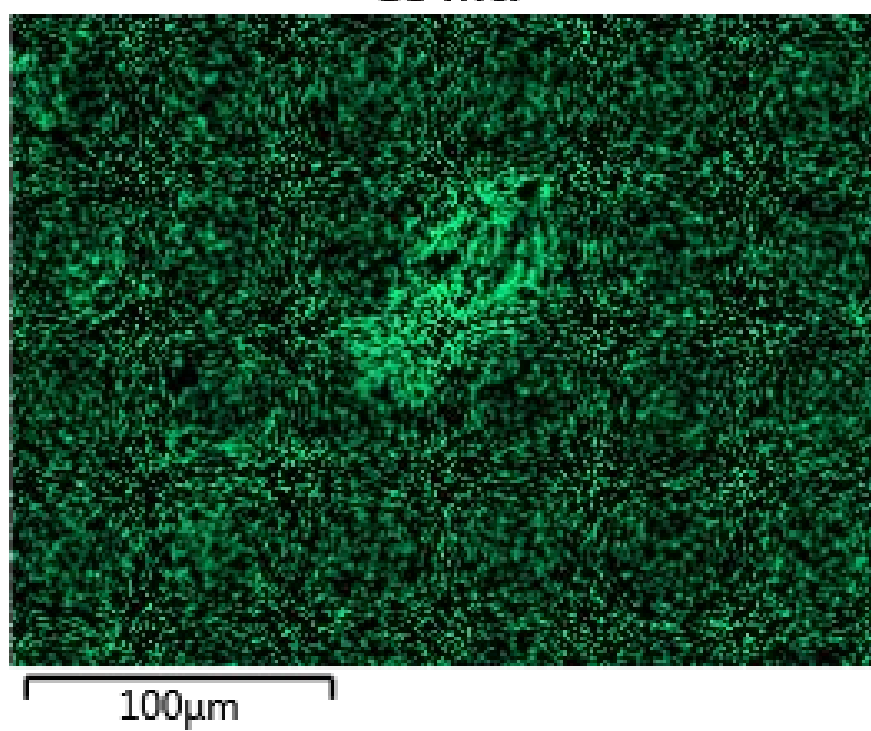
Ca K α 1



Mg K α 1_2



Ce M α



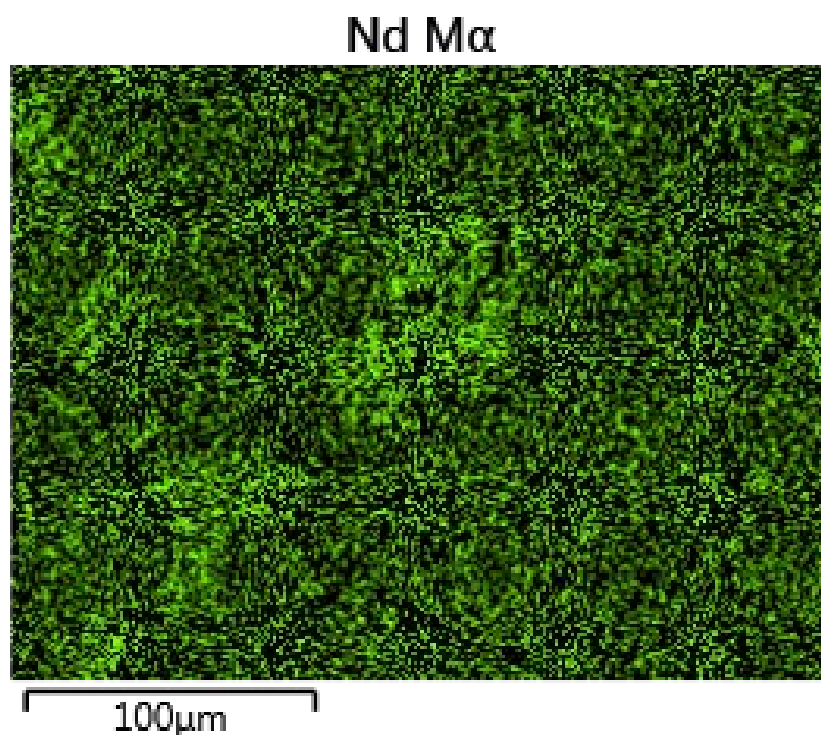


Fig. 4.37 Elemental mapping for the area where REs were present in a bastnaesite ore specimen; Collection time: 15 min.

After 15 min of collection time, it was evident that Ce enrichment occurred in the central crystal. Nd appeared to be more uniformly distributed. The concentrations for La, Pr and Sm were not sufficient for mapping. P was also present on the crystal while no F was detected (the reported SEM-EDX detection limit is 0.1 wt%). This indicates that the REs mineral is monazite other than bastnaesite. Ca and Mg were clearly not co-located with the RE minerals and it can be observed that small RE mineral patches were distributed in the gangue minerals. The specimen can be considered as a low-grade RE ore. Much smaller grinding particles are required for this type of ore for flotation.

The XPS result is consistent with the SEM-EDX data for the gangue mineral area. The XPS characterisation indicated that the ore sample containing no rare earth elements. Compared to SEM-EDX, the analysed depth for XPS was much smaller.

Therefore, this is expected that the REs enriched area was not detected. The XPS result showed the specimen consisted of minerals containing Ca, Mg and Ba, with minor Zr, Fe, Zn and Na. It is possible that there was a low concentration of Nd, but the F content was negligible, so the presence of bastnaesite has been excluded. An intense carbonate peak near 290 eV was observed in the C 1s spectrum. There was no oxide component near 530 eV in the O 1s spectrum, indicating that the minerals were carbonates (or basic carbonates) rather than oxides. No K 2p, nor Si 2p or 2s peaks were evident. The Ca $2p_{3/2}$ peak was at 347.5 eV, and the Ba $3d_{5/2}$ was at 780.55 eV.

4.4.2 Investigation by vibrational spectroscopy

A number of locations on the sample surface were examined with the Mountain Pass specimen using the 633 nm excitation. Four different spectra were obtained (Fig 4.38). The 1096 cm^{-1} band with various intensities was present in all spectra and can be assigned to the $(\text{CO}_3)^{2-}$ ν_1 mode. The band at 988 cm^{-1} , assigned to the $(\text{PO}_4)^{3-}$ ν_1 mode, was observed in spectra b, c and d. The two Raman bands indicate that both carbonate and phosphate were present in the specimen. The results are consistent with the SEM data.

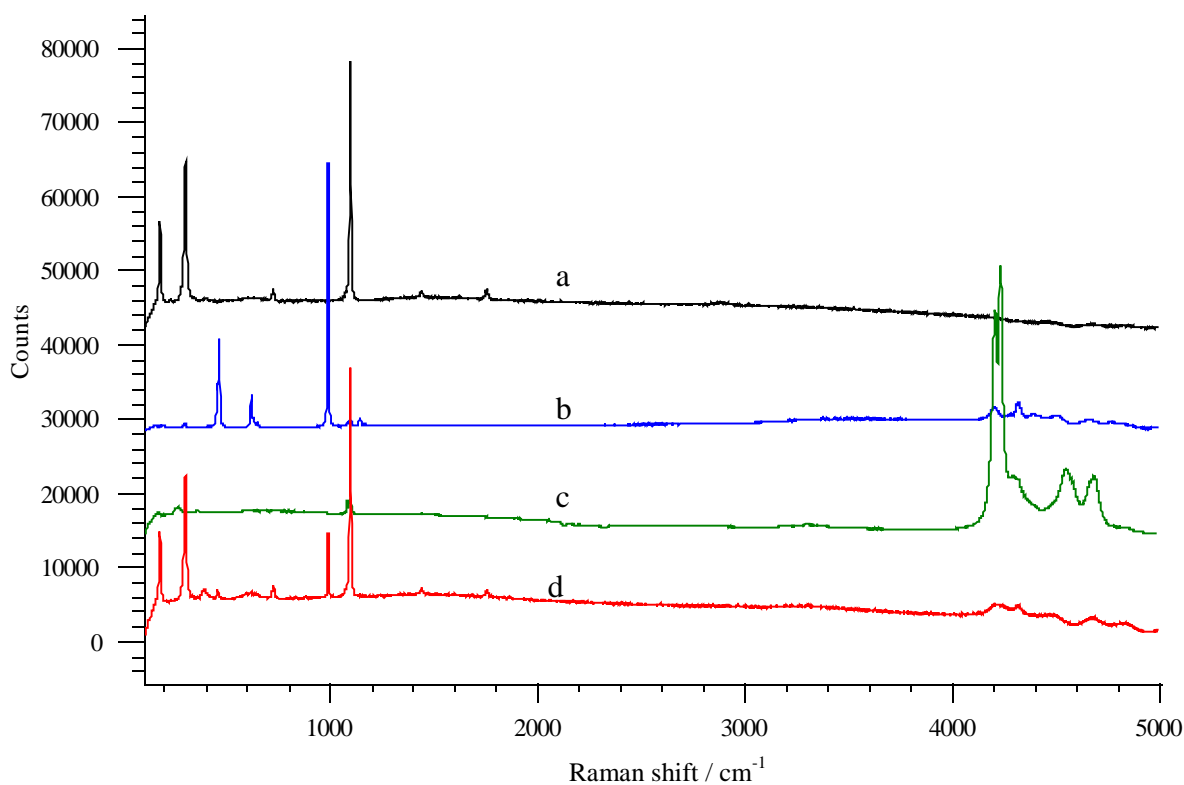


Fig. 4.38 Raman spectra of bastnaesite ore with different locations (a, b, c and d) on the surface using 633 nm of excitation.

For location a, the band at 1096 cm^{-1} indicates a carbonate mineral was present. Compared to a spectrum of pure crystalline calcite, at the lattice vibration bands at 175

cm^{-1} and 298 cm^{-1} were red-shifted $\sim 20 \text{ cm}^{-1}$. This is consistent with mainly Ca being present in the sample with minor other metal atoms. For spectrum b and d, carbonate and phosphate Raman bands were observed at 1096 cm^{-1} and 988 cm^{-1} , respectively, along with low intensity Nd fluorescence lines at 863, 872, 878, 887 and 898 nm (present in the Raman spectra as wavenumber from 4000 cm^{-1} to 4800 cm^{-1}) at sample site b, the band at 988 cm^{-1} is much more intense while the carbonate band at 1096 cm^{-1} is less intense than in spectrum d. This indicates higher concentration of phosphate was present in location b and location d has higher carbonate content. In spectrum d, the bands at 174 cm^{-1} and 297 cm^{-1} also indicate Ca was present.

At location c, strong Nd fluorescence emissions were observed, demonstrating that the Nd distribution was variable. Raman bands at 1056 cm^{-1} and 969 cm^{-1} were also observed. Farmer concluded that the $(\text{CO}_3)^{2-}$ ν_1 band shifts to lower wavenumber in carbonate minerals with an increase in cation radius, which is consistent with these observations (Farmer, 1974). The spectrum is comparable to that reported by Frost and Dickfos for a hydroxybastnaesite sample. The authors reported two bands at 1053 cm^{-1} and 965 cm^{-1} and attributed the band at 965 cm^{-1} to the OH deformation mode. The $\nu(\text{O-H})$ bands observed at 3169 cm^{-1} , 3142 cm^{-1} , 3306 cm^{-1} , 3376 cm^{-1} and 3510 cm^{-1} support the presence of a hydroxybastnaesite mineral at this location.

The sample was also examined using 442 nm excitation (Fig. 4.39). The results were similar to those obtained using 633 nm excitation. Four spectra from different locations are presented in figure 4.39.

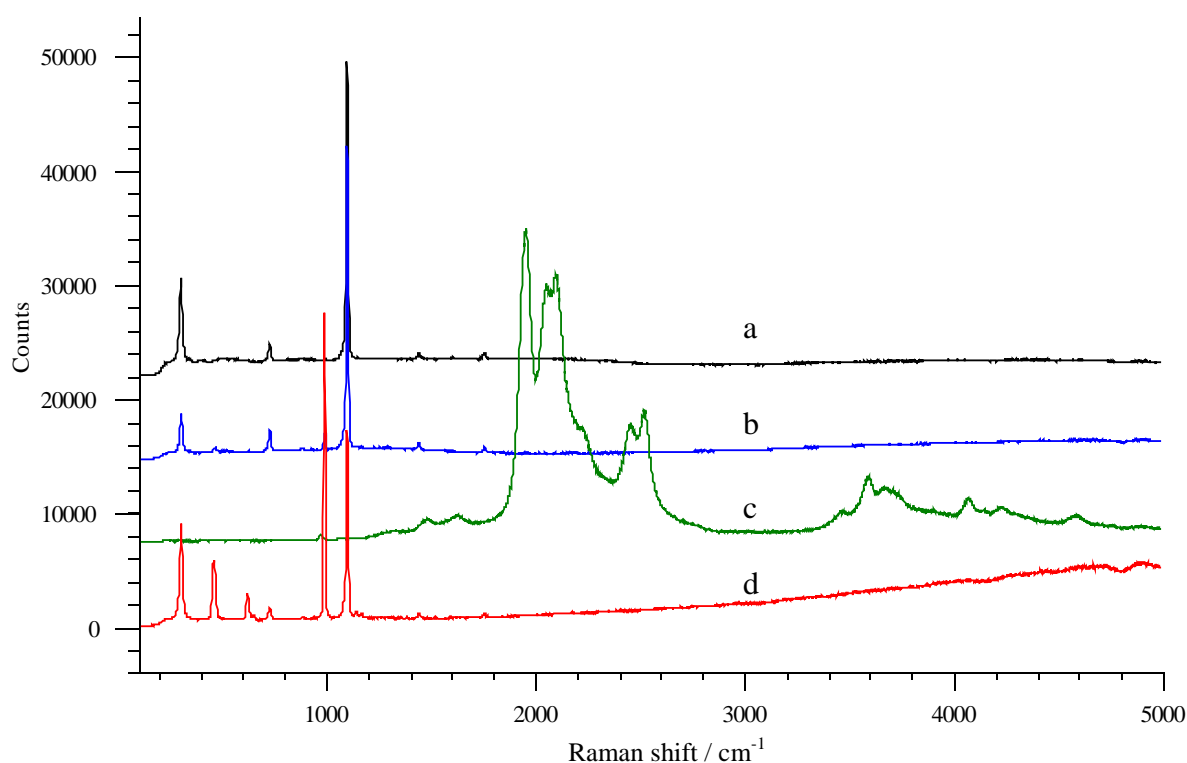


Fig. 4.39 Raman spectra of bastnaesite ore with different locations (a, b, c and d) on the surface using 442 nm of excitation.

All these Raman results were consistent with spectra a, b and d when using the 633 nm of excitations. With location d contains more phosphate, additional bands were observed at 456 cm^{-1} and 618 cm^{-1} . It is likely that REs were present in location d.

Intense fluorescence lines are shown in spectrum c at 484, 486, 487, 496 and 498 nm (present in the Raman spectra as wavenumber from 1800 cm^{-1} to 2600 cm^{-1}) using the 442 nm laser. Less intense emissions were also observed at 522, 526, 539 and 544 nm. These lines overlapped the Raman bands from 1900 cm^{-1} to 2600 cm^{-1} and 3500 cm^{-1} to 4300 cm^{-1} . The emission spectrum was consistent with Pr being present at location c. The emission spectrum shows good agreement with the energy level model of Pr(III) (Fig. 4.23). The result is also consistent with the SEM-EDX data, with which it showed the sample contains minor Pr.

Conclusion and future work

The vibrational characterizations of selected REOs support that each individual REE has distinct properties. Fluorescence emissions were observed overlapping the Raman spectra in Nd and Er. It is feasible to identify these elements using their fluorescence properties. In the flotation system, collectors are the most important reagents in concentrating RE minerals. The interaction between the flotation reagent and the REE could change the vibrational property of pure REOs. A model RE-collector compound is thus essential for the investigation of surface properties that caused by the chemical adsorption on the surface. Specifically, the bondings between molecules and change in oxidation states are critical information for understanding the mechanism of the floatation process.

The investigation for bastnaesite (including the gangue mineral) and monazite using different surface characterization techniques demonstrated that REEs concentrate in batches on the surface. A number of properties vary in natural RE minerals including particle sizes, REE ions substitution and impurities containing different gangue minerals. It is difficult to ascertain the surface interaction mechanism with the flotation reagent using natural RE minerals. A model mineral with known components is imperative for the surface adsorption investigation.

A range of RE hydroxamate compounds and a cerium carbonate thin film on calcite have been synthesized. The model system investigations are present in the next chapter.

References

- Adler H. H. and Kerr P. F., 1963, Infrared spectra, symmetry, and structure relations of some carbonate minerals, *American Mineralogist*, 48, 893.
- Araújo V. D., Avansi W., de Carvalho H. B., Moreira M. L., Longo E., Ribeiro C. and Bernardi M. I. B., 2012, CeO₂ nanoparticles synthesized by a microwave-assisted hydrothermal method: evolution from nanospheres to nanorods, *CrystEngComm*, 14, 1150.
- Atkinson S. C., 2013, Crystal structures and phase transition in the rare earth oxides, Doctor of Philosophy University of Salford, Salford.
- Biljan T., Rončević S., Meić Z. and Kovač K., 2004, Non-vibrational features in NIR FT-Raman spectra of lanthanide sesquioxides, *Chemical Physics Letters*, 395, 246-252.
- Boldish S. I. and White W. B., 1979, Vibrational spectra of crystals with the A-type rare earth oxide structure - I. La₂O₃ and Nd₂O₃, *Spectrochimica Acta*, 35A, 1235-1242.
- Borrero-González L. J. and Nunes L. A. O., 2012, Near-infrared quantum cutting through a three-step energy transfer process in Nd³⁺-Yb³⁺ co-doped fluorindogallate glasses, *Journal of Physics: Condensed Matter*, 24, 385501.
- Denning J. H. and Ross S. D., 1972, The vibrational spectra and structures of rare earth oxides in the A. modification, *Journal of Physics C: Solid State Physics*, 5, 1123-1133.
- Dogra S., Singh J., Sharma N. D., Samanta K., Poswal H. K., Sharma S. M. and Bandyopadhyay A. K., 2014, Phase progression via phonon modes in lanthanide dioxides under pressure, *Vibrational Spectroscopy*, 70, 193-199.

- Eick H. A., Eyring L., Summerville E. and Tuenge R. T., 1982, Electron beam-induced reduction of higher oxides of the rare earths: a high-resolution electron microscopic study, *Journal of Solid State Chemistry*, 42, 47-74.
- Farmer V. C., 1974, *The Infrared Spectra of Minerals*, Mineralogical Society, London,
- Frost R. L. and Dickfos M. J., 2007, Raman spectroscopy of halogen containing carbonates, *Journal of Raman Spectroscopy*, 38, 11, 1516-1522.
- Frost R. L., Sejkora J., Keeffe E. C., Plášil J., Čejka J. and Bahfenne S., 2009, Raman spectroscopic study of the phosphate mineral churchite-(Y) $\text{YPO}_4 \cdot 2\text{H}_2\text{O}$, *Journal of Raman Spectroscopy*, 41, 2, 202-206.
- Harrison R. J., Dunin-Borkowski R. E. and Putnis A., 2002, Direct imaging of nanoscale magnetic interactions in minerals, *Proceedings of the National Academy of Sciences*, 99, 26, 16556-16561.
- Heiba Z. K., Mohamed M. B. and Fuess H., 2012, XRD, IR, and Raman investigations of structural properties of $\text{Dy}_{2-x}\text{Ho}_x\text{O}_3$ prepared by sol gel procedure, *Crystal Research and Technology*, 47, 535-540.
- Heide S., 2008, *Biological Low-Voltage Scanning Electron Microscopy*, Springer, New York, NY, USA,
- Hsu L. C., 1992, Synthesis and stability of bastnaesites in a part of the system (Ce, La)–F–H–C–O, *Mineralogy and Petrology*, 47, 87-101.
- Ikumapayi F., Makitalo M., Johansson B. and Rao K. H., 2012, Recycling of process water in sulphide flotation: Effect of calcium and sulphate ions on flotation of galena, *Minerals Engineering*, 39, 77-88.
- Imanaka N., Masui T. and Kim Y. W., 2004, First electrochemical growth of $\text{Tb}_{16}\text{O}_{30}$ single crystal, *Journal of Solid State Chemistry*, 177, 3839-3842.

- Jordens A., Cheng Y. P. and Waters K. E., 2013, A review of the beneficiation of rare earth element bearing minerals, *Minerals Engineering*, 41, 97-114.
- Kang Z. C. and Eyring L., 1987, Dynamic edge and surface processes in terbium oxide, *Ultramicroscopy*, 22, 71-80.
- Keramidas V. G. and White W. B., 1973, Raman spectra of oxides with the fluorite structure, *The Journal of Chemical Physics*, 59, 1561.
- Kik P. G., 2000, Energy transfer in erbium doped optical waveguides based on silicon, *Institute for Atomic and Molecular Physics*, 1-14.
- Kotani A. and Ogasawara H., 1992, Theory of core-level spectroscopy of rare-earth oxides, *Journal of Electron Spectroscopy and Related Phenomena*, 60, 257-299.
- Krebs J. K. and Happek U., 2001, Yb^{3+} energy levels in $\alpha\text{-Al}_2\text{O}_3$, *Journal of Luminescence*, 94, 65-68.
- Mead D. G. and Wilkinson G. R., 1977, The temperature dependence of the Raman spectra of some alkaline earth crystals with the fluorite structure, *Journal of Physics C: Solid State Physics*, 10, 1063-1072.
- Miettinen T., Ralston J. and Fornasiero D., 2010, The limits of fine particle flotation, *Minerals Engineering*, 23, 5, 420-437.
- Mullins D. R., Overbury S. H. and Huntley D. R., 1998, Electron spectroscopy of single crystal and polycrystalline cerium oxide surfaces, *Surface Science*, 409, 307-319.
- Ruschel K., Nasdala L., Kronz A., Hancher J. M., Többens D. M., Škoda R., Finger F. and Möller A., 2012, A Raman spectroscopic study on the structural disorder of monazite-(Ce), *Mineralogy and Petrology*, 105, 1-2, 41-55.

- Sessa C., Vila A. and JF. G., 2011, Determination of detection limits for SEM-EDS and m-FTIR analysis of artwork, *Analytical and Bioanalytical Chemistry*, 400, 2241-2251.
- Sherman C.-P., 1997, *Hand Book of Instrumental Techniques for Analytical Chemistry*, Prentice Hall PTR, New Jersey, USA, 260-261.
- Spanier J. E., Robinson R. D., Zhang F., Chan S.-W. and Herman I. P., 2001, Size-dependent properties of CeO_{2-y} nanoparticles as studied by Raman scattering, *Physical Review B: Condensed Matter and Materials Physics*, 64, 1-8.
- Stoneman R. C. and Esterowitz L., 1992, Efficient resonantly pumped 2.8-um Er^{3+} : GSGG laser, *Optical Letter*, 17, 816-818.
- Teterin Y. A., Teterin A. Y., Lebedev A. M. and Utkin I. O., 1998, The XPS spectra of cerium compounds containing oxygen, *Journal of Electron Spectroscopy and Related Phenomena*, 89-91, 275-279.
- Tucker L. A., Carney F. J., McMillan P., Lin S. H. and Eyring L., 1984, Raman and resonance Raman spectroscopy of selected rare-earth sesquioxides, *Applied Spectroscopy*, 38, 857-860
- Ubal dini A. and Carnasciali M. M., 2008, Raman characterisation of powder of cubic RE_2O_3 (RE=Nd, Gd, Dy, Tm, and Lu), Sc_2O_3 and Y_2O_3 , *Journal of Alloys and Compounds*, 454, 374-378.
- Weber W. H., Hass K. C. and McBride J. R., 1993, Raman study of CeO_2 : Second-order scattering, lattice dynamics, and particle-size effects, *Physical Review B*, 48, 178-185.

- Wu Z. H., Sun D. L., Wang S. Z., Luo J. Q., Li X. L., Huang L., Hu A. L., Tang Y. Q. and Guo Q., 2013, Performance of a 967 nm CW diode end-pumped Er:GSGG laser at 2.79 μm , *Laser Physics*, 23, 055801.
- Yu J., Cui L., He H., Yan S., Hu Y. and Wu H., 2014, Raman spectra of RE_2O_3 (RE=Eu, Gd, Dy, Ho, Er, Tm, Yb, Lu, Sc and Y): laser-excited luminescence and trace impurity analysis, *Journal of Rare Earths*, 32, 1-4.
- Yu Y., 2001, Dressing technology of REO ore and its development in China, *Journal of China University of Mining & Technology*, 30, 534-542.
- Zhou B., Tao L., Tsang Y. H., Jin W. and Pun E. Y.-B., 2012, Superbroadband near-IR photoluminescence from Pr^{3+} -doped fluorotellurite glasses, *Optics Express*, 20, 3803-3813.

CHAPTER 5

MODEL SYSTEMS INVESTIGATION FOR

RARE EARTH HYDROXAMATE

COMPOUNDS AND BASTNAESITE (Ce)

5.1 Preamble

Mineral flotation depends on surface hydrophobicity; a property that may be controlled by reagent adsorption or by surface compound formation. It is important that surface interaction characterisation be able to identify the nature of the bonding between the flotation reagent and the target or gangue minerals. In particular, the lanthanide elements have closely related chemical properties and this means that careful spectral characterization of the lanthanide compounds is required if it is to be feasible to observe individual lanthanide – hydroxamate interactions. REE hydroxamate compounds were synthesized to enable the measurement of the spectral properties of pure compounds. In addition, a model mineral compound is crucial for undertaking interaction studies due to the structural variations in the RE minerals and associated difficulties in fully characterizing the natural samples. Cerium carbonate on a calcite crystal surface was synthesized for this purpose as a model sample resembling bastnaesite for interaction studies.

5.2 Synthesis and characterization of REE hydroxamate compounds

5.2.1 Neodymium hydroxamate

5.2.1a Gravimetric analysis

The stoichiometry of the neodymium hydroxamate was confirmed as being close to $\text{Nd}(\text{C}_8\text{O}_2\text{N})_3$ by gravimetric analysis. In the procedure, a known mass of the compound that had been vacuum dried for 48 h was combusted in air for 2 h in a muffle furnace at 1000°C , and the mass loss determined. The stoichiometry of the compound was calculated as $\text{Nd}(\text{C}_8\text{O}_2\text{N})_{3.16}$ on the assumption that Nd_2O_3 was the product following heat treatment.

5.2.1b Characterization by XPS

The expected elemental composition (excluding H) of neodymium hydroxamate would be $\text{Nd}(\text{C}_8\text{O}_2\text{N})_3$ and the corresponding bulk atomic concentrations would be; Nd 2.9, C 70.6, O 17.6 and N 8.8 at%. The atomic composition of the sample surface is expected to be slightly higher in C and O because of surface contamination. The measured elemental compositions of three batches of neodymium hydroxamate (synthesized either from potassium hydroxamate or hydroxamic acid) were broadly similar and close to $\text{Nd}(\text{C}_8\text{O}_2\text{N})_{3.9}$. The result was consistent with the gravimetric analysis (minor C and O from surface contamination may be ignored). The prepared complexes had a slightly lower than expected calculated surface Nd content, probably due to the accuracy of the Nd sensitivity factors used in the data analysis is not known (detailed discussion for the Nd sensitivity factor see Chapter 4). The main component in the Nd $3d_{5/2}$ peak occurred at a binding energy of 982.4 ± 0.2 eV, slightly lower than for air-exposed neodymium oxide, but with a similar separation of ~ 3.5 eV between the major and minor components. The O KLL Auger peak at an equivalent binding

energy of ~ 976 eV was taken into account when determining the intensity of the Nd $3d_{5/2}$ peak and this Auger peak did not interfere with the determination of the main $3d_{5/2}$ binding energy. No extraneous elements (including K) were detected, and the C $1s$ and O $1s$ spectra were similar to those reported for other n-octanohydroxamate complexes (Hope et al., 2010).

The N $1s$ spectrum consisted of two partially-resolved components (Fig. 5.1). It could be fitted with a more intense component at 400.9 ± 0.1 eV, which was assigned to a protonated hydroxamate N. The other component at 398.9 ± 0.1 eV is attributed to a deprotonated hydroxamate N, or the N of a hydroxamate decomposition product.

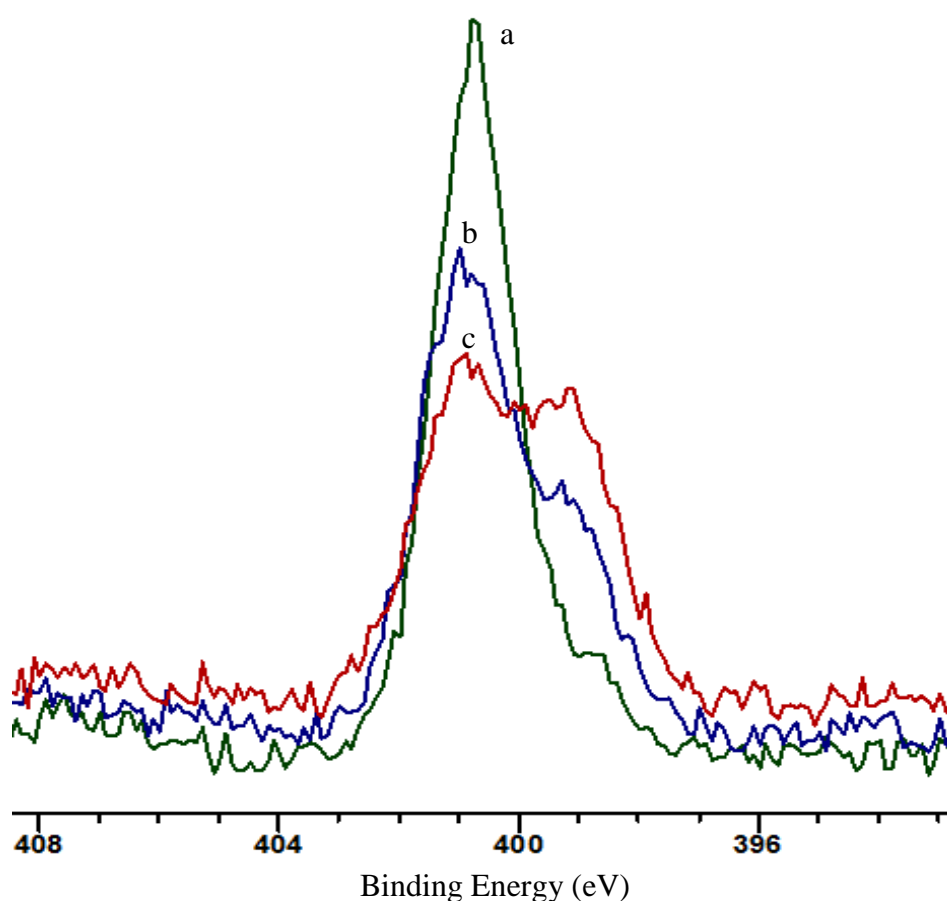
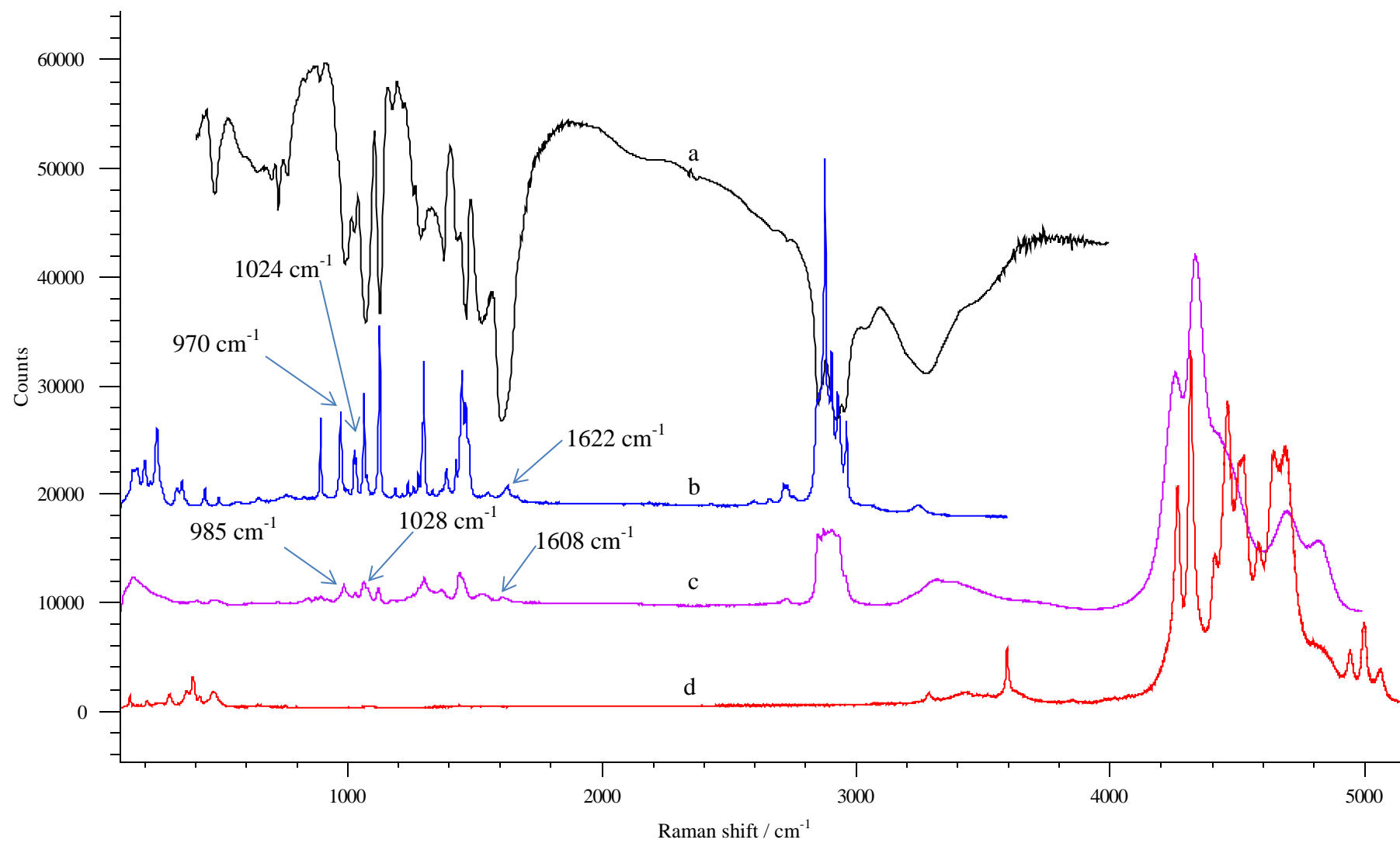


Fig. 5.1 N $1s$ spectra from Nd hydroxamate obtained at different stages in the spectral suite: (a) at the outset; (b) mid-suite; (c) at the end.

The component near 401 eV was much more intense in the N 1s spectrum determined at the outset compared to that recorded at the end of the spectral suite. This was consistent with a lower binding energy component that was produced by damage caused by either the secondary electrons or by the low energy electrons from the flood gun. The 401 eV component accounted for more than 90% of the N 1s intensity at the outset, but less than 55% at the end, demonstrating that the Nd hydroxamate was susceptible to beam damage. For the neodymium hydroxamate prepared from hydroxamic acid, a minor N 1s component at 406.9 eV, which would have arisen from an impurity N/O species, was also observed. The intensity of this component became lower with increasing beam time. The La n-octanohydroxamate prepared by Belkasem et al. was reported to be $\text{La}(\text{C}_8\text{H}_{16}\text{NO}_2)_3 \cdot 6\text{H}_2\text{O}$ (Belkasem et al., 2010). In this thesis, there was no evidence in the O 1s spectrum for water of crystallisation in the neodymium hydroxamate.

5.2.1c Vibrational investigation

Neodymium hydraxamate complex was observed to precipitate at pH 5.5. The collected complex was characterized using Raman and infrared spectroscopy. Fig. 5.2 presents the Raman spectra of Nd_2O_3 , n-octanohydroxamic acid and neodymium hydroxamate as well as the FT-IR spectrum of neodymium hydroxamate.



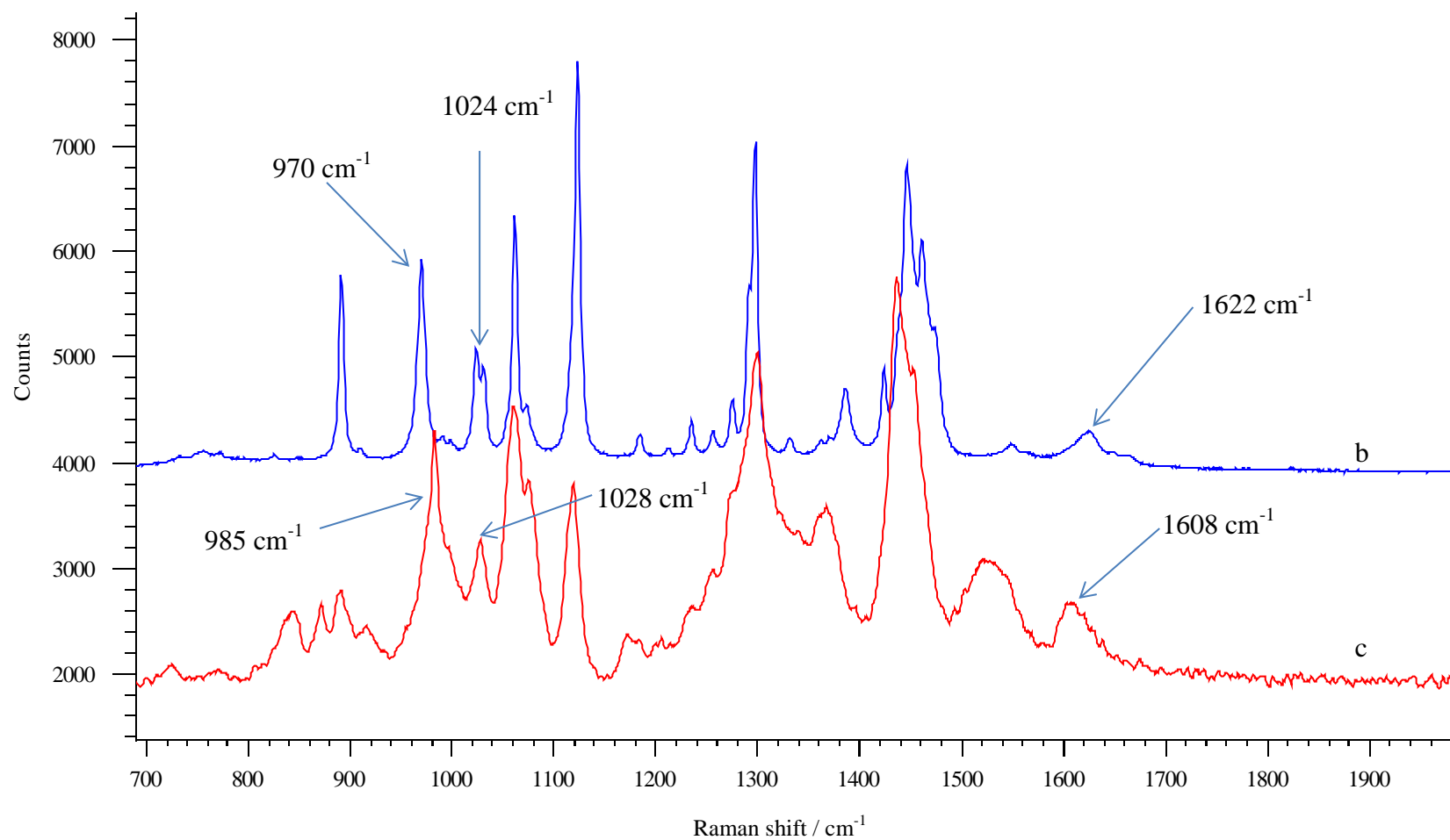


Fig. 5.2 Vibrational spectra of: (a) FT-IR of neodymium hydroxamate, (b) Raman spectra of n-octanohydroxamic acid, (c) neodymium hydroxamate and (d) Nd_2O_3 .

The crystal structure of Fe^{III} tris acetohydroxamate has shown that the ligand coordination comprises three bidentate hydroxamate ligands in an octahedral configuration, with coordination occurring through the N-O and C=O oxygen atoms of the hydroxamate (Failes and Hambley, 2000; Alagha et al., 2011). This forms a five membered coordination ring. While the lanthanide cations may be able to coordinate a larger number of ligands, it is probable that all the lanthanides will be coordinated by 3 bidentate hydroxamate ligands. The vibrational spectra of the lanthanide complexes are expected to exhibit features that are generated by this bonding. The spectral regions of particular interest are those that are derived from bonds directly involved with the coordination of the hydroxamate with the lanthanide cations. The Raman band assignments for n-octanohydroxamic acid have been published (Hope et al., 2010). The Raman spectrum for the neodymium hydroxamate exhibits a shift compared to that of the acid; in particular, C=O at 1622 cm^{-1} is shifted to lower wavenumber by 14 cm^{-1} . In contrast, C-N (1024 cm^{-1}) and N-O (970 cm^{-1}) are shifted to higher wavenumber by 4 and 15 cm^{-1} in the spectrum of Nd hydroxamate, respectively. The infrared spectrum also shows similar bonding shifts; in particular, C=O shifts from 1625 to 1603 cm^{-1} while N-O shifts from 1273 to 1288 cm^{-1} and C-N 970 to 996 cm^{-1} . This spectral change is consistent with bonding between Nd and n-octanohydroxamate involving an N-O as a part of the coordination.

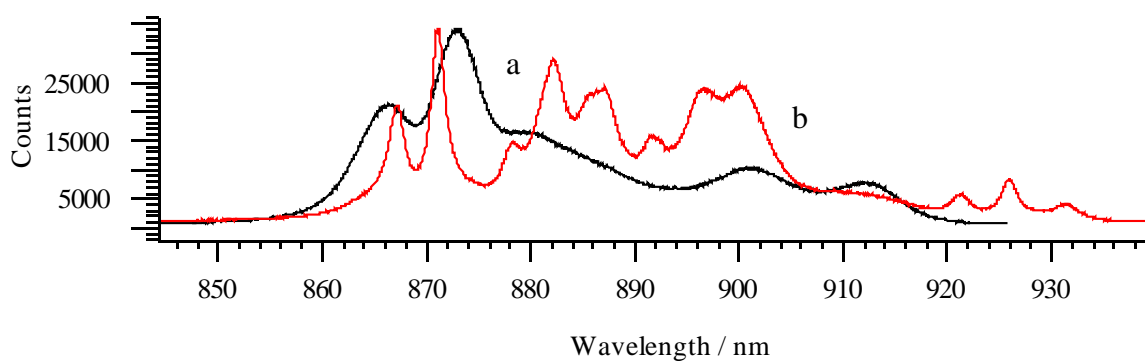


Fig. 5.3 Emission spectra of: (a) neodymium hydroxamate and (b) Nd_2O_3 . The fluorescence peaks observed for the neodymium oxide differ in intensity and energy from those for the neodymium hydroxamate.

Fluorescence emissions from Nd were observed from 850 nm – 930 nm in the oxide spectrum. The fluorescence peaks observed for the oxide differ in intensity and energy from those for the neodymium hydroxamate compound (Fig. 5.3). This is consistent with Nd electron energy level changes that result from the bonding of the Nd atom to oxygen of n-octanohydroxamate.

5.2.2 Cerium hydroxamate

A white precipitate was observed immediately without pH adjusting when $\text{Ce}(\text{NO}_3)_3 \cdot 6\text{H}_2\text{O}$ was added to hydroxamate. A colour change occurred from white to dark brown when the sample was washed with water and vacuum filtered in air. A similar effect was observed when the sample was exposed in air for 2 h after filtration without vacuum assistance. The synthesized product was insoluble in organic solvents including ethanol, methanol, acetone, diethyl ether, chloroform, ethyl acetate, n-pentane and furan. Agrawal and John reported the colour for a number of Ce(IV) hydroxamate complexes. The authors observed reddish brown colour for the compounds and the Ce to ligand ratio was determined of 1:4. The present study used Ce(III) to form a complex with hydroxamate. Ce has been reported to undergo a valence change under pressure

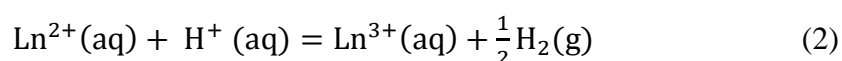
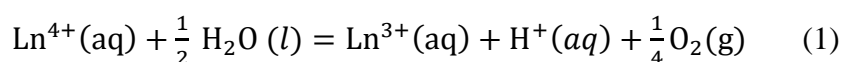
accompanied with a phase change (Adroja, 1991). It is probable that a portion of Ce(III) was oxidised to Ce(IV) in air which led to colour changed. The final product was examined by XPS, Raman and infrared spectroscopy for further investigations.

5.2.2a Characterization by XPS

The XPS data taken from a sample prepared in nitrogen showed that the spectra were consistent with Ce(III) hydroxamate being the major component (95%). There was no residual K, and an N 1s peak was observed near 407 eV. Approximately 5% Ce(IV) was evident at the start of the spectral suite, but the first Ce 3d spectrum was obtained after the initial N 1s spectrum. It is likely that some of the Ce(IV) was produced by beam damage. The initial N 1s spectrum has a major single peak at 401 eV and a peak at 399 eV with less than 10% of the intensity. At the end of the spectral suite, the overall N 1s intensity had decreased by about 10% (probably due to electron stimulated desorption), but the intensity of the 399 eV component had increased by 30%. The O 1s spectrum was a single peak at ~531.4 eV; there were no components from oxide or physisorbed water. It is probable that the cerium hydroxamate sample was a mixed valence compound. The specimen was stored in a glass container for 7 d before investigated by XPS. Observation of the colour change on air exposure would support a sample was pure Ce(III) hydroxamate when was freshly prepared and some Ce(III) slowly oxidized to Ce(IV) hydroxamate over time.

A number of researches have preferred explanations for a mechanism of valence fluctuation in Ce. Cerium has unique electronic and chemical properties. Where nearly all the REs exhibit a +3 oxidation state in solutions with different solvents, Ce is the only REE element that has been observed to have a stable +4 oxidation state in aqueous solution and Eu can exhibit a +2 oxidation state in solution (Moeller, 1975). These occurrences can be explained by their respective electronic configurations, the cations

of Ce^{4+} and Eu^{2+} have empty and half-filled electrons in the $4f$, respectively, which stabilizes their cations. Gschneidner and Eyring also have concluded that the ground-state energy of these two configurations is very close to each other in solid phase, which leads to a strong valence fluctuation of the $4f$ charge (Gschneidner and Eyring, 1993). Moeller provided another explanation for the REs with the +3 state (Moeller, 1975). The author described the different oxidation states are determined by the free energy changes (ΔG^0) in the following reactions:



If reaction (1) and (2) spontaneously happened, the Ln^{3+} would be stable in the system. A similar calculation was given for the solid RE compounds.

5.2.2b Vibrational investigation

Fig 5.4 presents the Raman and infrared spectra of cerium hydroxamate as well as the Raman spectrum of hydroxamic acid and $\text{Ce}(\text{NO}_3)_3 \cdot 6\text{H}_2\text{O}$. For cerium hydroxamate, 1599 cm^{-1} , 1031 cm^{-1} and 986 cm^{-1} were observed in the Raman spectrum while 1594 cm^{-1} , 1027 cm^{-1} and 994 cm^{-1} were observed in the IR spectrum. These bands are assigned to the C=O, C-N and N-O functional groups in the cerium hydroxamate compound, respectively.

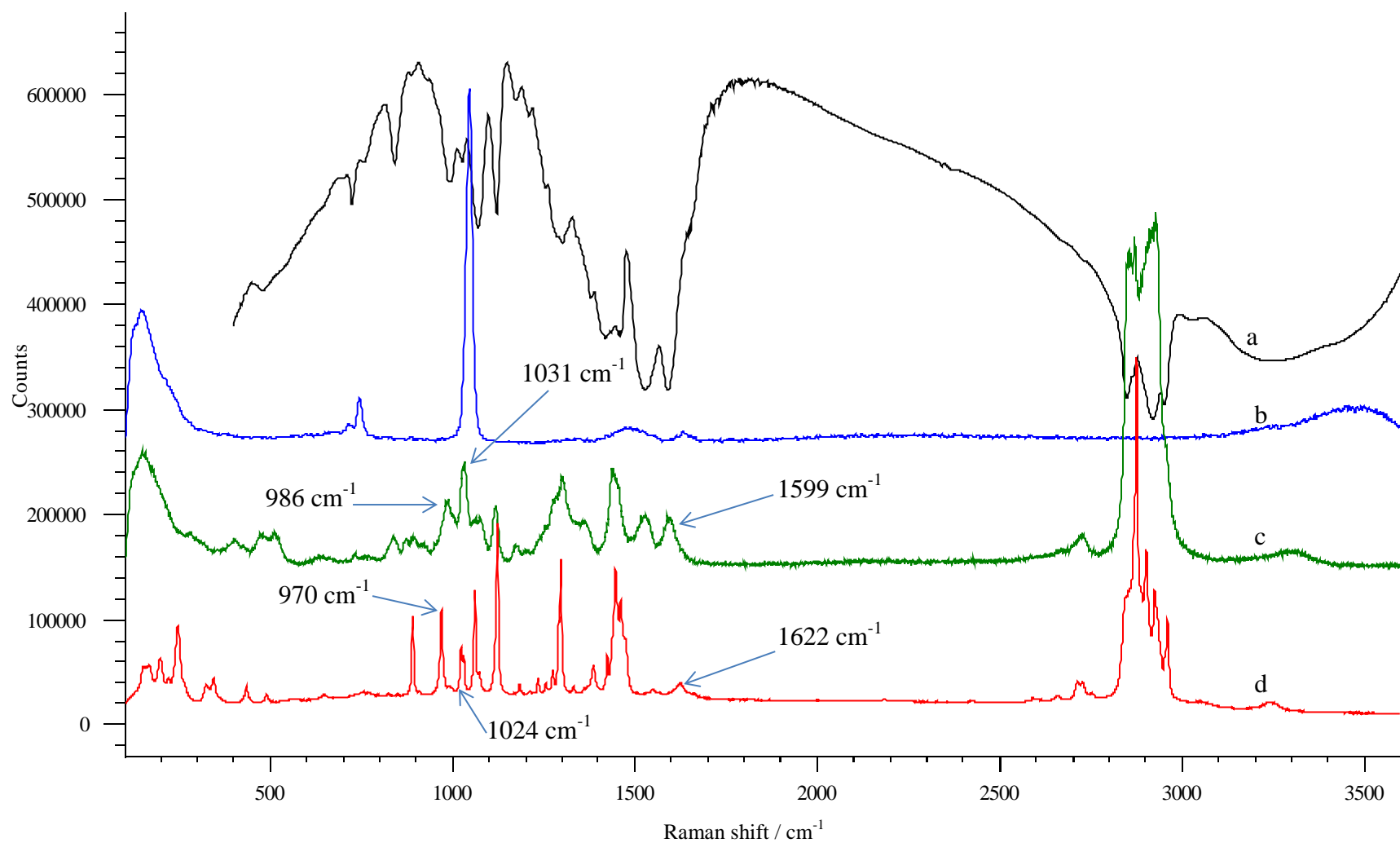


Fig. 5.4 Vibrational spectra of: (a) FT-IR of cerium hydroxamate, (b) $\text{Ce}(\text{NO}_3)_3 \cdot 6\text{H}_2\text{O}$, (c) cerium hydroxamate and (d) Raman spectra of n-octanohydroxamic acid.

Compared to the hydroxamic acid spectrum, the $\nu\text{C=O}$ shifted to lower wavenumber by 23 cm^{-1} ; $\nu\text{C-N}$ and $\nu\text{N-O}$ shifted to higher wavenumber by 7 cm^{-1} and 16 cm^{-1} , respectively (Fig. 5.5). Similar observation was obtained for the IR spectrum, 24 cm^{-1} to 71 cm^{-1} of IR shifts was exhibited for the three bondings described above (C=O, C-N and N-O). By comparing the differences of the vibrational spectra, it is reasonable to conclude that a cerium hydroxamate complex was formed through the functional groups of C=O, C-N and N-O.

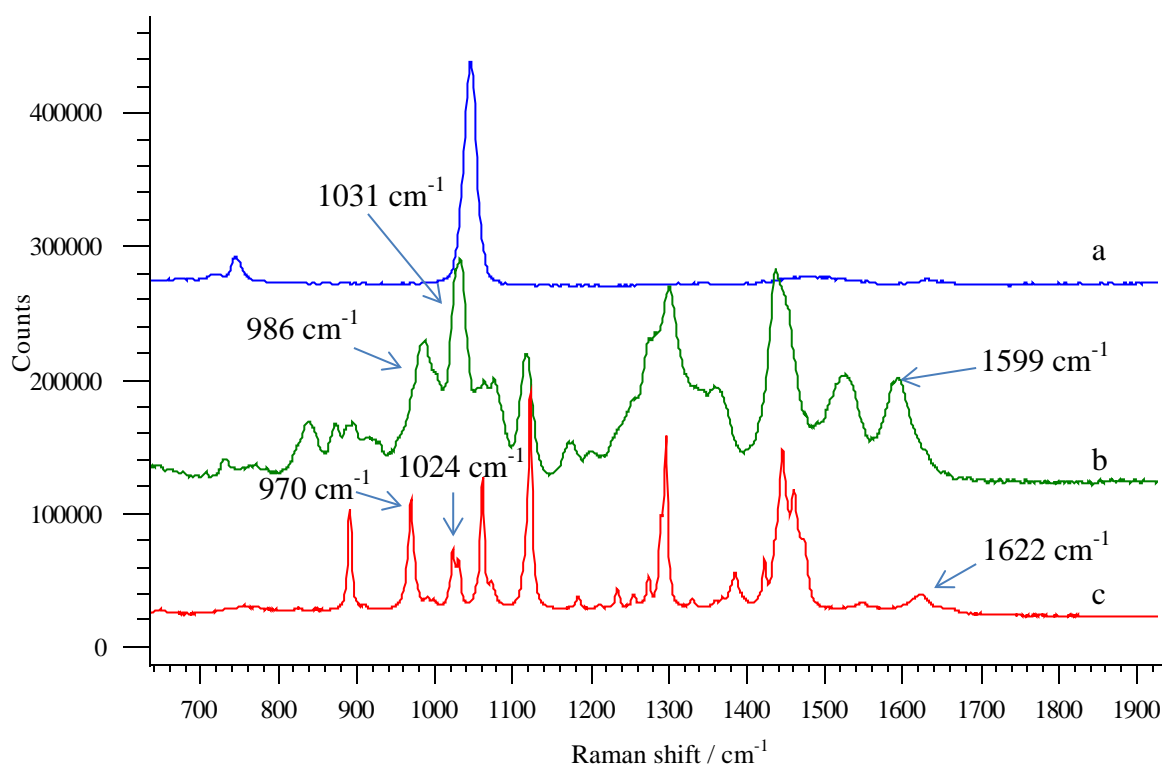


Fig. 5.5 Raman spectra of: (a) $\text{Ce}(\text{NO}_3)_3 \cdot 6\text{H}_2\text{O}$ (b) cerium hydroxamate and (c) n-octanohydroxamic acid, in the range of 800 cm^{-1} to 1700 cm^{-1} .

The XPS analysis had revealed that two oxidation states for Ce were present in the cerium hydroxamate compound. It is expected that Raman spectrum would be different between Ce(III) hydroxamate and Ce(IV) hydroxamate. For this purpose, another Ce compound was also synthesized from cerium ammonium nitrate, with which the

oxidation states for Ce is 4+. It is expected the final cerium hydroxamate product would be Ce(IV) hydroxamate.

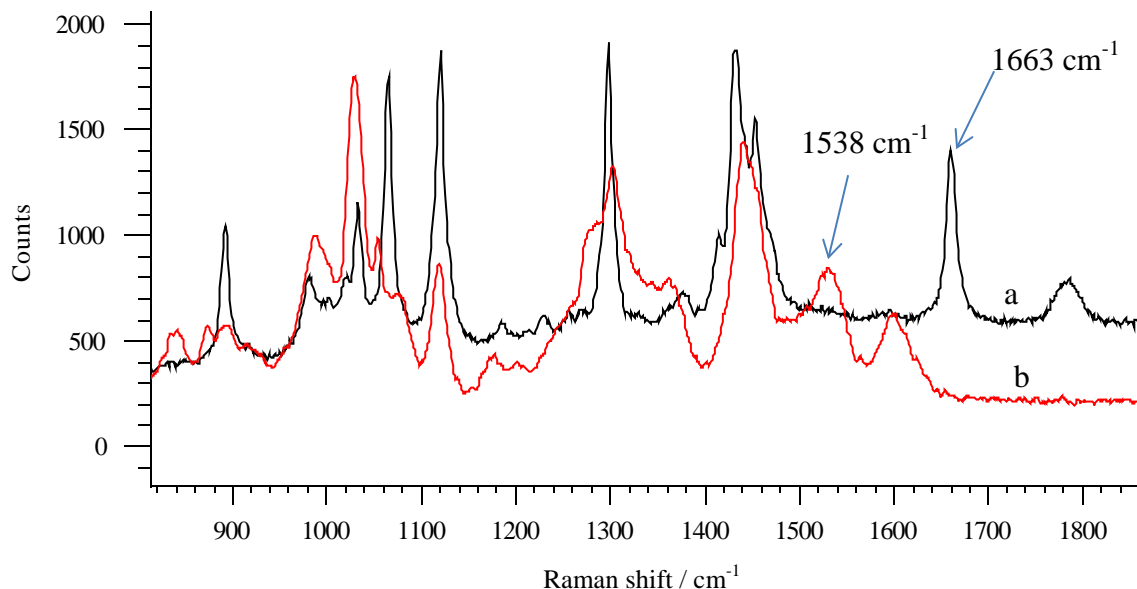


Fig. 5.6 Raman spectra of: (a) Ce(IV) hydroxamate prepared from cerium ammonium nitrate (b) Ce(III) hydroxamate prepared from $\text{Ce}(\text{NO}_3)_3 \cdot 6\text{H}_2\text{O}$ in the range of 800 cm^{-1} to 1700 cm^{-1} .

Fig. 5.6 shows the Ce(IV) hydroxamate prepared from cerium ammonium nitrate and Ce(III) hydroxamate prepared from $\text{Ce}(\text{NO}_3)_3 \cdot 6\text{H}_2\text{O}$. The band for $\nu\text{C}=\text{O}$ are a distinguishing feature for the two compounds. For Ce(IV) hydroxamate, the band shifts to higher wavenumber by 63 cm^{-1} at 1663 cm^{-1} . A band observed at 1538 cm^{-1} for Ce(III) hydroxamate and probably assigned to an N-H bend was not observed for Ce(IV) (Hope et al., 2010). For the $\nu\text{N}-\text{O}$, a 9 cm^{-1} difference was observed in the two compounds. A low intensive band at 981 cm^{-1} assigned to $\nu\text{C}-\text{N}$ presented in the spectrum of Ce(IV) hydroxamate compared to 986 cm^{-1} for Ce(III) hydroxamate. It is suggested that the polarizable electron density increased for the Ce(IV) hydroxamate, mainly through greater coordination with the $\text{C}=\text{O}$ functional group. This has resulted into the biggest

change in the $\nu\text{C=O}$ band position. The results are also consistent with Ce(IV) hydroxamate having 8 coordination while 6 for Ce(III) hydroxamate.

To investigate the valence change phenomenon, the Ce(III) hydroxamate sample was exposed to air for 4 d before investigated by Raman spectroscopy. Fig. 5.7 presents the two Raman spectra.

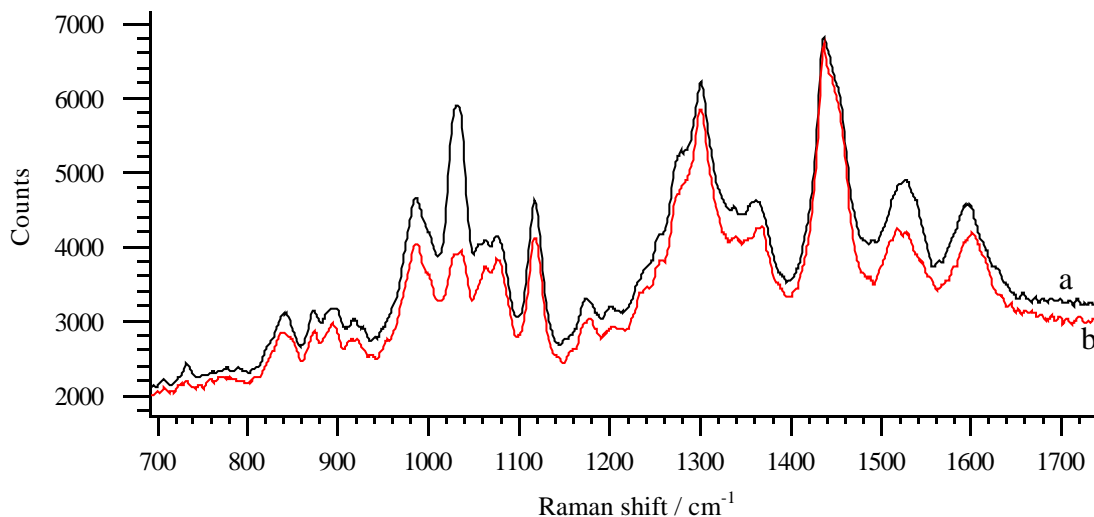


Fig. 5.7 Raman spectra in the range of 800 cm^{-1} to 1700 cm^{-1} for: (a) Ce (III) hydroxamate and (b) Ce (III) hydroxamate exposed to air for 4 d.

Following exposure to air, the $\nu\text{C=O}$ shifted to higher wavenumbers by 4 cm^{-1} . An attempt was made to calculate the oxidation percentage, based on the band positions of Ce(III) and Ce(IV) hydroxamate. According to Fig. 5.6, 63 cm^{-1} of Raman shifts corresponded to 100% of oxidation. Assuming the oxidation rate is a linear function in the form of $y = kx$, the oxidation percentage is given as:

$$\text{OT} = 0.01587 \times (A - A_o) \times 100\%$$

(OT - Oxidation percentage; A - Raman shifts for air exposed sample, A_o – Raman shift for initial sample)

Therefore, the oxidation percentage for the 4 d exposed sample would be:

$$OT = 0.01587 \times (1604 - 1600) \times 100\% = 6.3 \%$$

The XPS data indicated that about 5% of the sample contained Ce(IV) that was 7 d after being prepared. The calculated oxidation percentage for Ce(IV) is in surprisingly good agreement with the XPS data.

5.2.3 Other RE hydroxamate compounds (Ho, Gd, Dy and Er)

In a flotation system, the REEs are expected to interact similarly with the collector, and consequently, given the similarities in their chemical properties we would anticipate similar Raman spectra. However, fine details in the spectra are also expected to be apparent due to differences in the atomic radius and valence electron distributions of the REEs. To further investigate these properties, four more REE hydroxamate compounds were also investigated.

In Fig. 5.8, the fluorescence emissions observed in the range from 850 nm – 950 nm for neodymium and 640 nm – 660 nm for holmium are presented. These fluorescent lines do not overlap the respective Raman bands that provide the bonding information of the REEs with the collector. These fluorescent emissions provide a unique and sensitive method for the identification of Ho and Nd.

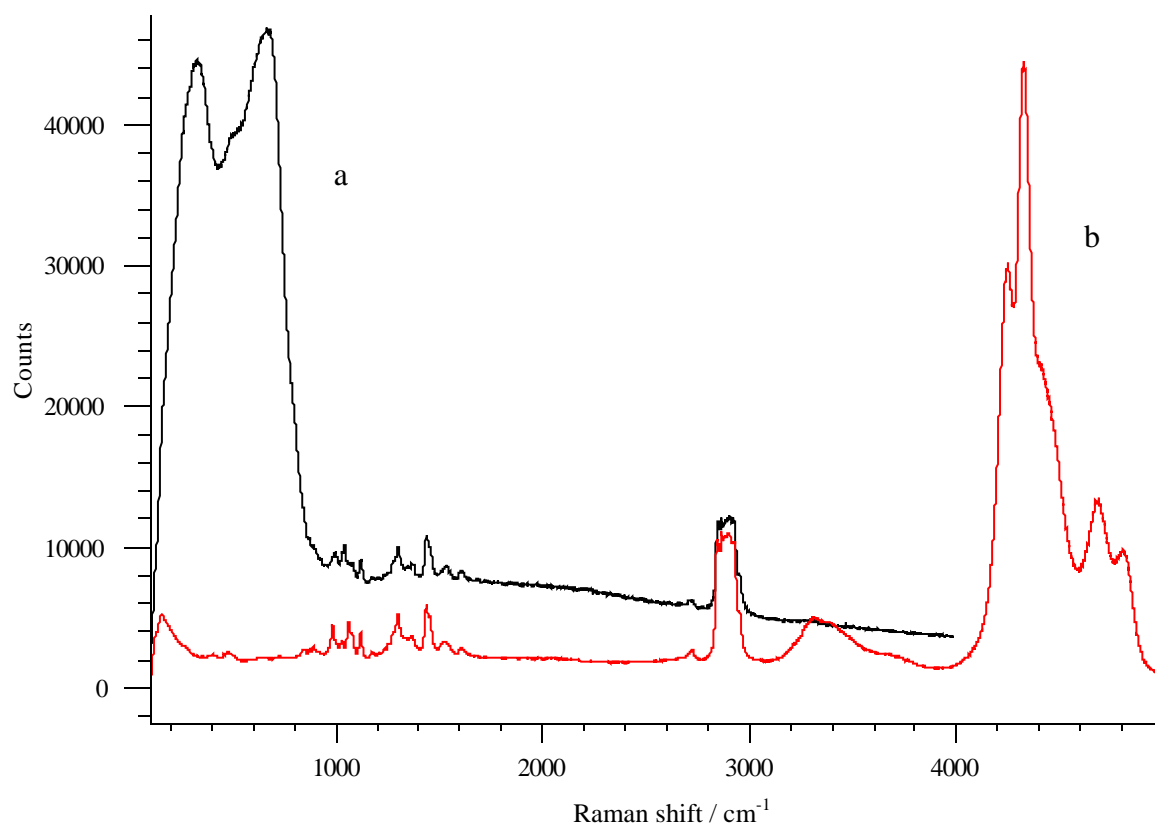


Fig. 5.8 Emission spectra of: (a) holmium hydroxamate and (b) neodymium hydroxamate.

Fig. 5.9 presents the Raman spectra for four REE hydroxamate compounds (Ho, Gd, Dy and Er) together with neodymium hydroxamate. For the expected bonding regions, the other four REE hydroxamate complexes (Ho, Gd, Dy and Er) exhibit similar Raman spectra to that observed for neodymium hydroxamate.

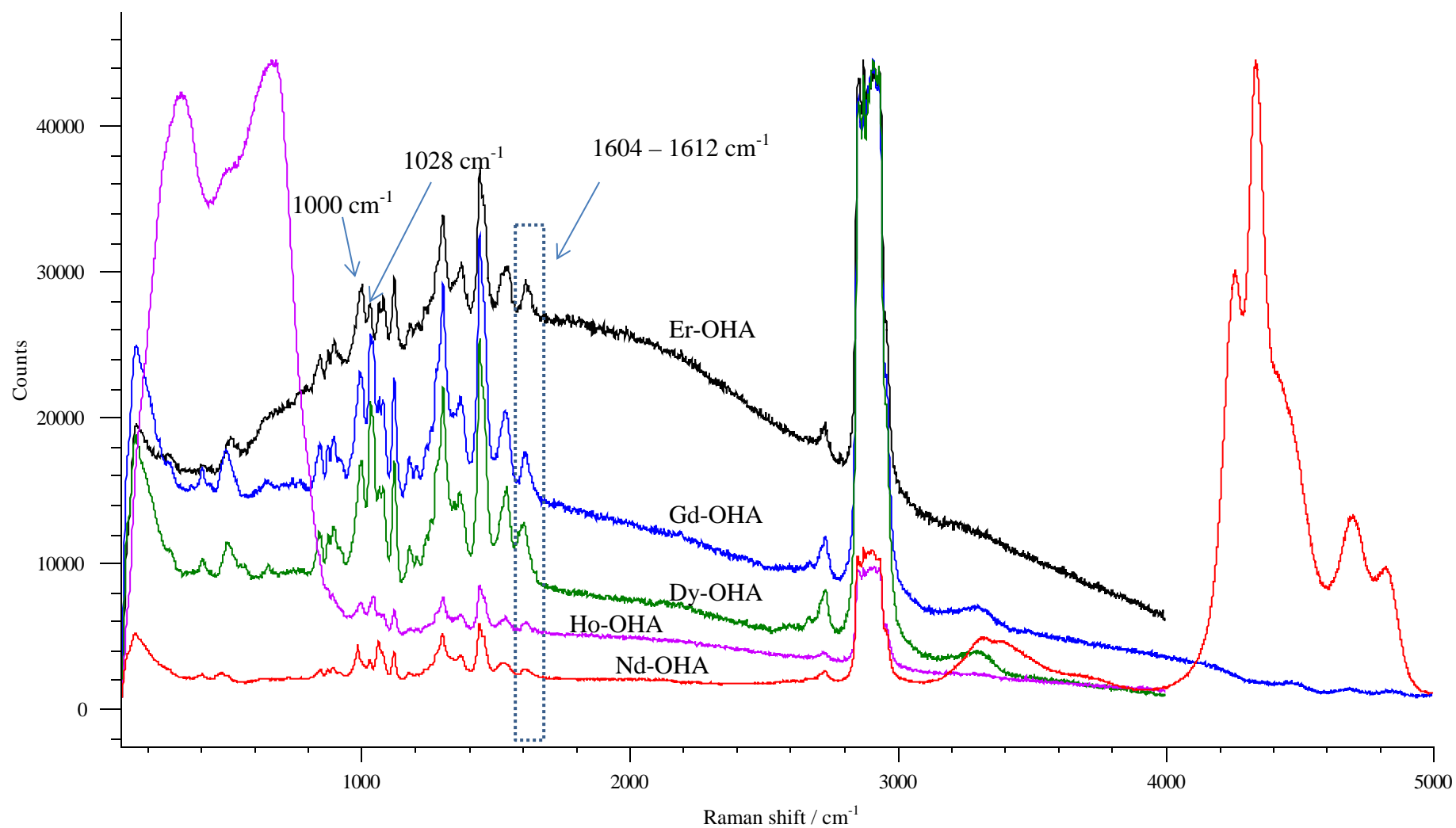


Fig. 5.9 Raman spectra from hydroxamates of Er, Gd, Dy, Ho and Nd, from top to bottom.

An average shift between 11 (1604-1612 cm^{-1}) and 9 (1028-1041 cm^{-1}) cm^{-1} is observed in the C=O and C-N bands whereas a shift to higher wavenumber of 24 cm^{-1} occurred for the N-O band (Table 5.1). These differences in the Raman band positions are attributed to the small differences in the physical and chemical properties exhibited by the REEs. It is feasible to distinguish between the REE compounds by the precise positions of the Raman bands. Damage from the 632.8 nm laser beam was not evident in the Raman spectra of the hydroxamate complexes investigated.

Table 5.1 Vibrational band positions for REE hydroxamates, and n-octanohydroxamic acid

compound	Raman cm^{-1}			FT-IR cm^{-1}		
	$\nu_{\text{C=O}}$	$\nu_{\text{C-N}}$	$\nu_{\text{N-O}}$	$\nu_{\text{C=O}}$	$\nu_{\text{C-N}}$	$\nu_{\text{N-O}}$
Nd-OHA	1608	1028	988	1603	1288	996
Gd-OHA	1612	1031	991	1606	1297	997
Ho-OHA	1611	1041	994	1610	1306	998
Dy-OHA	1604	1032	998	1608	1299	998
Er-OHA	1611	1028	1000	1606	1288	997
n-octanohydroxamic acid	1622 ^a	1024 ^a	970 ^a	1665 ^a	1273 ^a	970 ^a

^a Data sourced from Hope et al., 2010.

Infrared spectra were also measured for the five REE hydroxamate complexes synthesized. This data show that a similarity of spectral properties was also found in FT-IR spectra (Fig. 5.10). The band for C=O shifted to lower wavenumber while the C-N and N-O shifted to higher wavenumber (Table 5.1). Huang et al. prepared 30 coordination compounds of the lanthanides and recorded their IR spectra (Huang et al.,

1991). Their study showed a similar trend for the C=O band ($\sim 1606\text{ cm}^{-1}$) and N-O (997 cm^{-1}) for the five REE hydroxamate compounds prepared in their work. In the case of the C-N band, the five compounds were reported to be slightly higher than 1300 cm^{-1} whereas this investigation has found that only the holmium hydroxamate C-N was observed to occur above 1300 cm^{-1} .

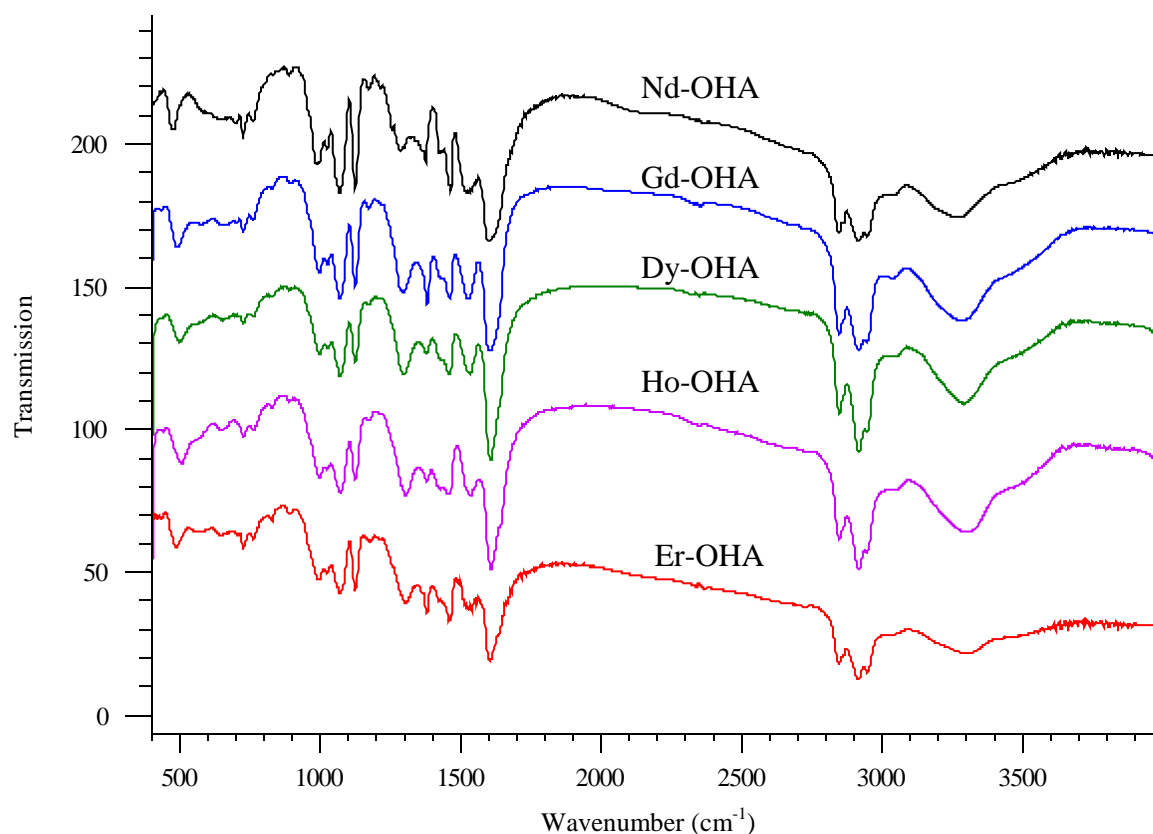


Fig. 5.10 FT-IR spectra from hydroxamates of Nd, Gd, Dy, Ho and Er from top to bottom.

5.3 Model system investigation for bastnaesite (Ce)

A model system is essential to investigate the interaction between the mineral and the collector due to the composition variation in natural RE minerals. Bastnaesite (Ce) is the most important RE mineral that has been the dominant RE source since 1960s (Jordens et al., 2013). Pradip et al. synthesized a cerium bastnaesite sample with the formula of CeFCO_3 (Pradip et al., 2013). The final product was in a powder form which is difficult for surface investigation. In this thesis, attempt has been made to synthesize a cerium carbonate thin film on a substrate that is suitable for surface interaction investigation. Calcite was chosen as the substrate due to the cleavage properties of the crystal structure that provides a natural flat surface. It is also one of the most common gangue minerals occurring with RE minerals.

5.3.1 Preparation and characterization of cerium carbonate thin film on calcite

5.3.1a Synthesis of cerium carbonate on calcite

A white thin film was formed on the surface of the calcite crystal (Fig. 5.11). The thin film was uniform and it was slightly thinner on the edge. The product film grown on the calcite was amenable to stripping as an unsupported layer that could be transferred to a flat microscope slide. This indicated that only weak interactions between the calcite and thin film were maintained. If a glass slide was used as a growing substrate, a coherent film was not formed. The discovery of rare earths minerals commonly occurring with carbonates in mineral deposits probably reflects the importance of the interactions between calcite surfaces and the rare earth deposits.

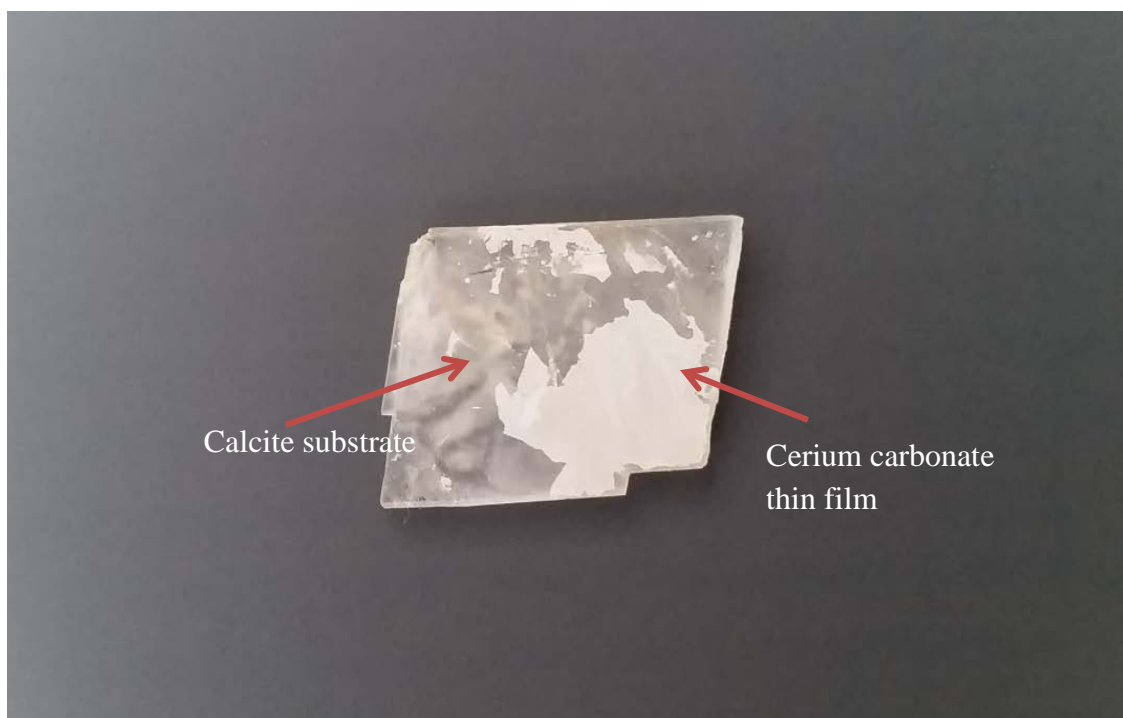


Fig. 5.11 Image for synthesized cerium carbonate on calcite.

5.3.1b Characterization of cerium carbonate thin film on calcite by Raman spectroscopy

In order to avoid signal interference from the calcite base, a portion of the cerium carbonate thin film was separated from the calcite substrate and transferred to a glass slide before investigated by Raman spectroscopy. Fig. 5.12 presents the Raman spectra for the cerium carbonate and calcite.

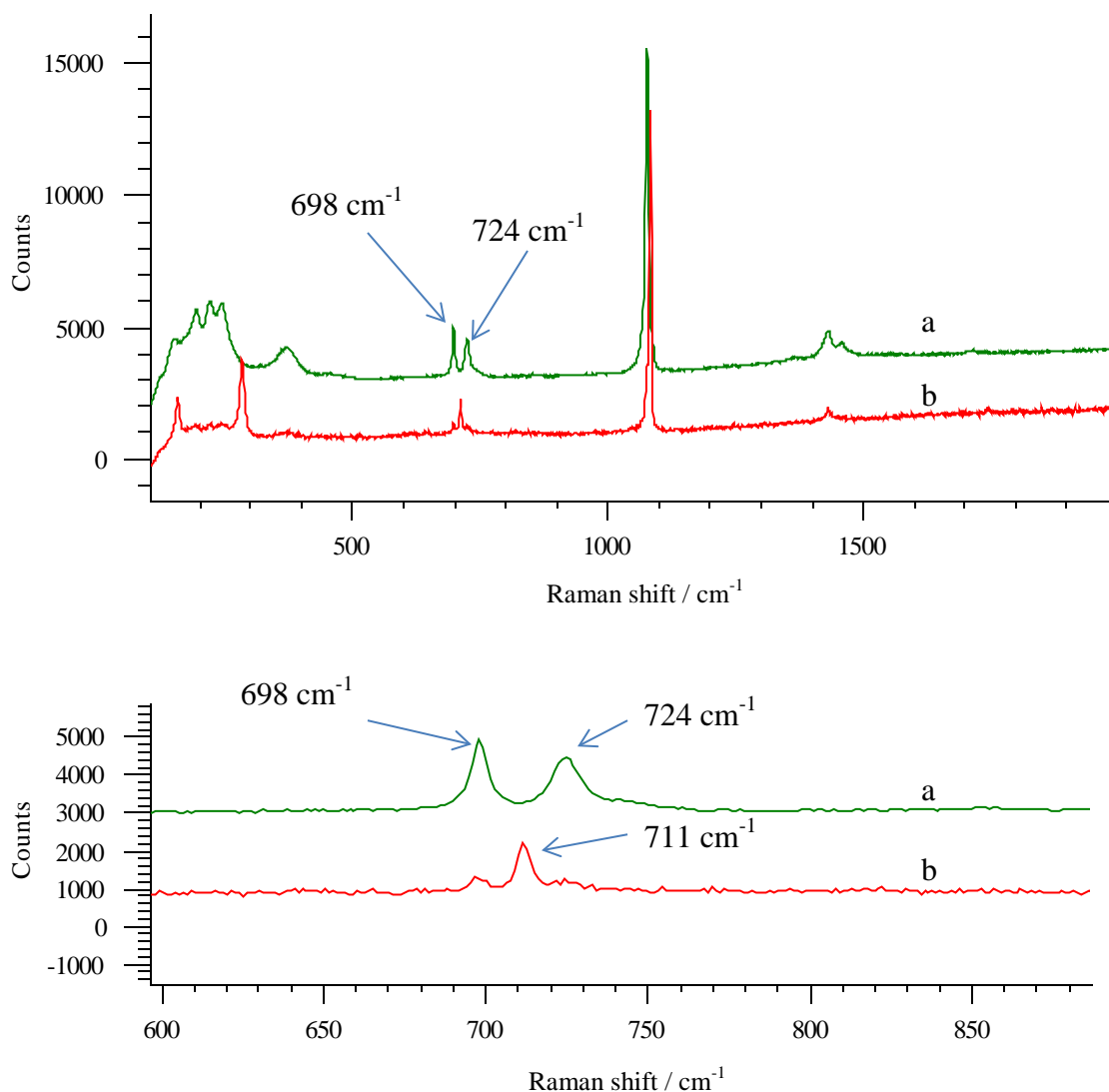


Fig. 5.12 Raman spectra for (a) synthesized cerium carbonate thin film and (b) calcite in different ranges.

A number of differences in band position were observed in the two spectra. The $(\text{CO}_3)^{2-}$ ν_1 band in the spectrum of cerium carbonate was observed at 1079 cm^{-1} where as in the calcite spectrum it occurred at 1086 cm^{-1} . Other differences between the two spectra include less intensive bands exhibited at 698 cm^{-1} and 724 cm^{-1} for the thin film sample while calcite has a Raman band at 711 cm^{-1} and a very low insensitive band at 698 cm^{-1} . The band at 711 cm^{-1} has been agreed by various authors assigning to an

external Eg mode that corresponding to in-plane bending ν_4 (Rutt and Nicola, 1974; Urmos et al., 1991; Gunasekaran and Anbalagan, 2007). The band at 698 cm^{-1} presents in the calcite sample spectrum is probable from the impurity of cerium carbonate. In the lattice vibrational region from 100 cm^{-1} to 400 cm^{-1} , significant differences were observed in both band positions and band shape. Different lattice dynamics in these two compounds are responsible for the differences in Raman shifts.

An *in-situ* investigation was also conducted. Raman spectra were collected for the thin film on calcite. Different locations were investigated and two different spectra were obtained (Fig. 5.13).

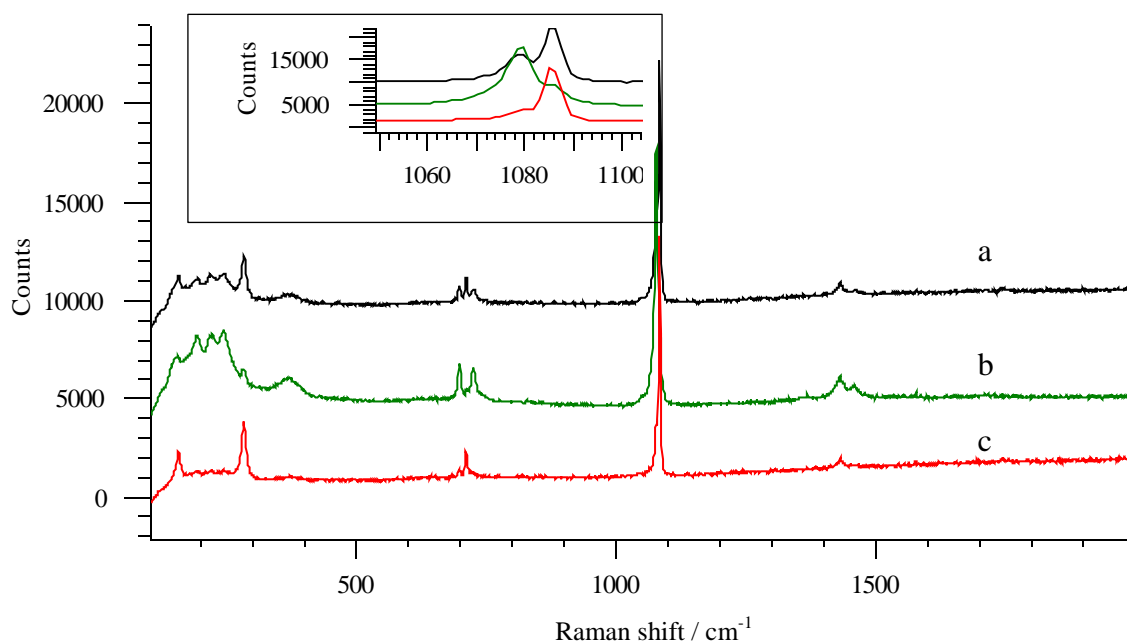


Fig. 5.13 Raman spectra for different spots of synthesized cerium carbonate thin film (a and b) and calcite (c). Spectrum A was collected near the edge of the thin film. Spectrum B was collected in the middle area of the sample.

Compared to the cerium carbonate and calcite spectra, spectrum A has the Raman bands featured from both samples. For example, the $(\text{CO}_3)^{2-}$ ν_1 bands were observed at 1079

cm⁻¹ and 1086 cm⁻¹ which are emanated from cerium carbonate and calcite, respectively (spectra shown on the top left corner in Fig. 5.13). Spectrum A was collected near the edge of the thin film. The edge area of the cerium carbonate film was thin, so that data was collected for both the surface film and the base (calcite), occurred given the penetration depth of the Raman collection. For spectrum B where data was collected in the middle area of the sample, the (CO₃)²⁻ v1 band was observed shifted to the lower wavenumber at 1079 cm⁻¹. Other featured bands including the lattice area and the (CO₃)²⁻ v4 area at around 700 cm⁻¹ (Frost and Dickfos, 2007) are consistent as a pure cerium carbonate compound present. These observations are consistent with the thickness of the sample reducing from the middle area to the edge. Due to the nature of the thin film, the *in-situ* adsorption investigation with hydroxamate was conducted in the middle area where the substrate would not interfere the result.

Raman mapping was conducted over the edge area of cerium carbonate and calcite (Fig. 5.14). The Raman bands at 1079 cm⁻¹ and 1086 cm⁻¹ were used for the fitting as indication for cerium carbonate and calcite.

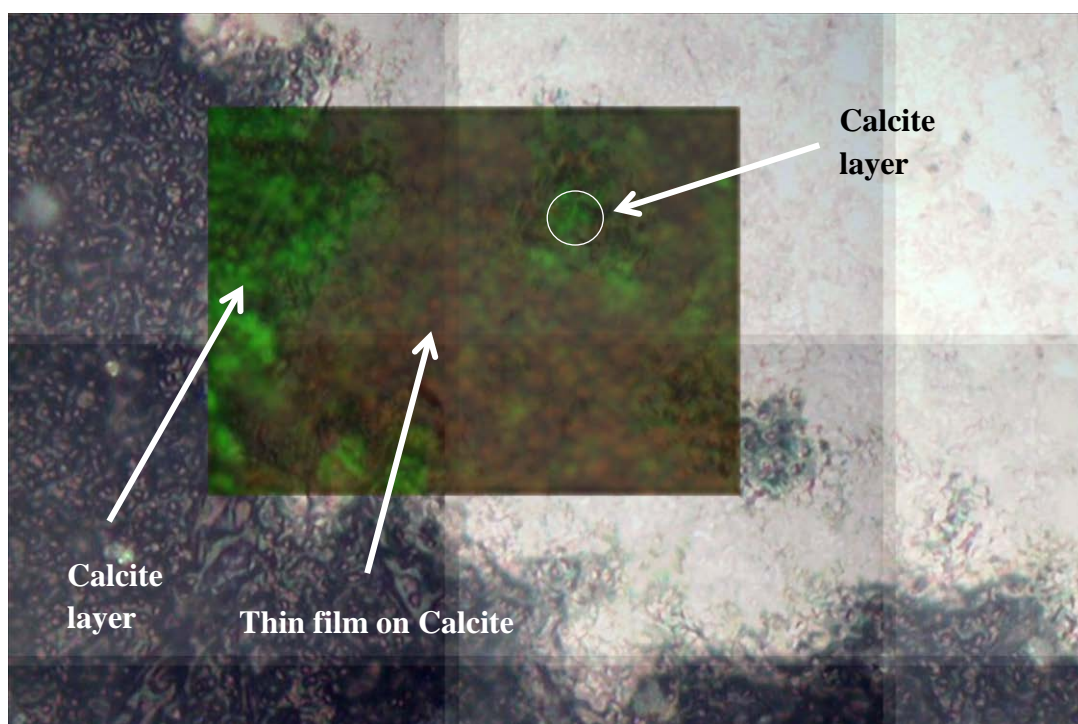


Fig. 5.14 Raman mapping over the edge of synthesized cerium carbonate thin film and calcite using 633 nm laser. The Raman bands at 1079 cm^{-1} and 1086 cm^{-1} were used for fitting where red represents cerium carbonate and green represents calcite. The microscopy image is shown in the background. $25\text{ }\mu\text{m} \times 20\text{ }\mu\text{m}$.

The surface of the cerium carbonate thin film is mostly uniform. Some areas near the edge are thinner as calcite is evident in the spectra. The green colour represents calcite and red represents cerium carbonate. In the red area, recognizable green colour is shown in the background. It is indicated that the film is thin (less than $1\text{ }\mu\text{m}$ due to the depth resolution for Raman spectroscopy is 5 nm to $1\text{ }\mu\text{m}$), so that the signal from calcite was also collected. The Raman map is consistent with a cerium carbonate thin film deposited on the calcite mineral.

5.3.1c Characterization of cerium carbonate thin film on calcite by AFM and magnetic AFM

The feasibility to identify REs using magnetic AFM scanning in the minerals (magnetite, bastnaesite and monazite, see Chapter 4) has been established. For the sample prepared for this investigation, cerium is the only element with magnetic properties. Therefore, magnetic AFM was suitable for the cerium carbonate particle characterization. Fig. 5.15 displays the topography image and the magnetic mapping for the thin film sample with a scanning size of $50\text{ }\mu\text{m} \times 50\text{ }\mu\text{m}$.

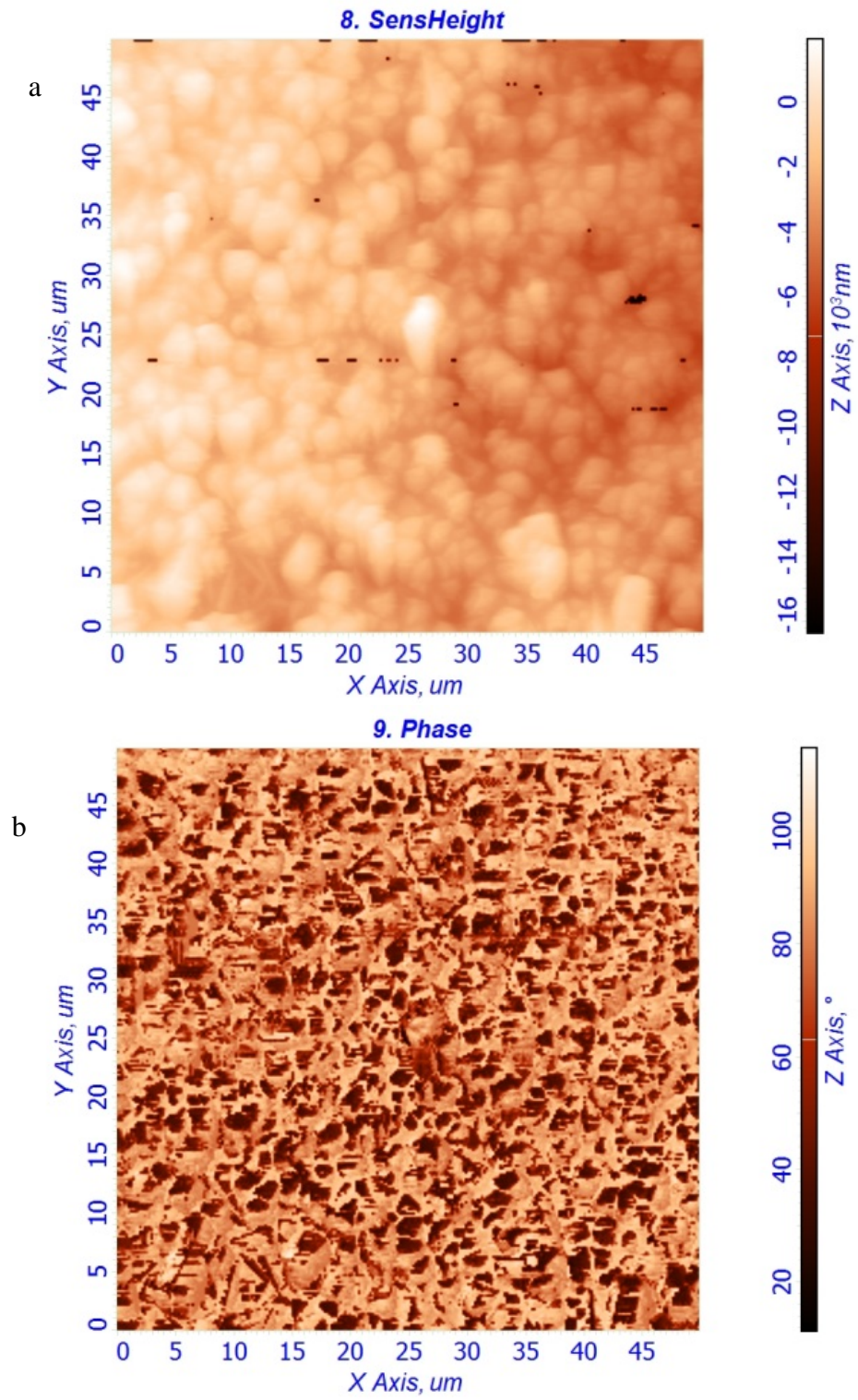


Fig. 5.15 (a) AFM image for cerium carbonate thin film on calcite and (b) AFM magnetic scan for the corresponding area; Scan size: 50 $\mu\text{m} \times 50 \mu\text{m}$.

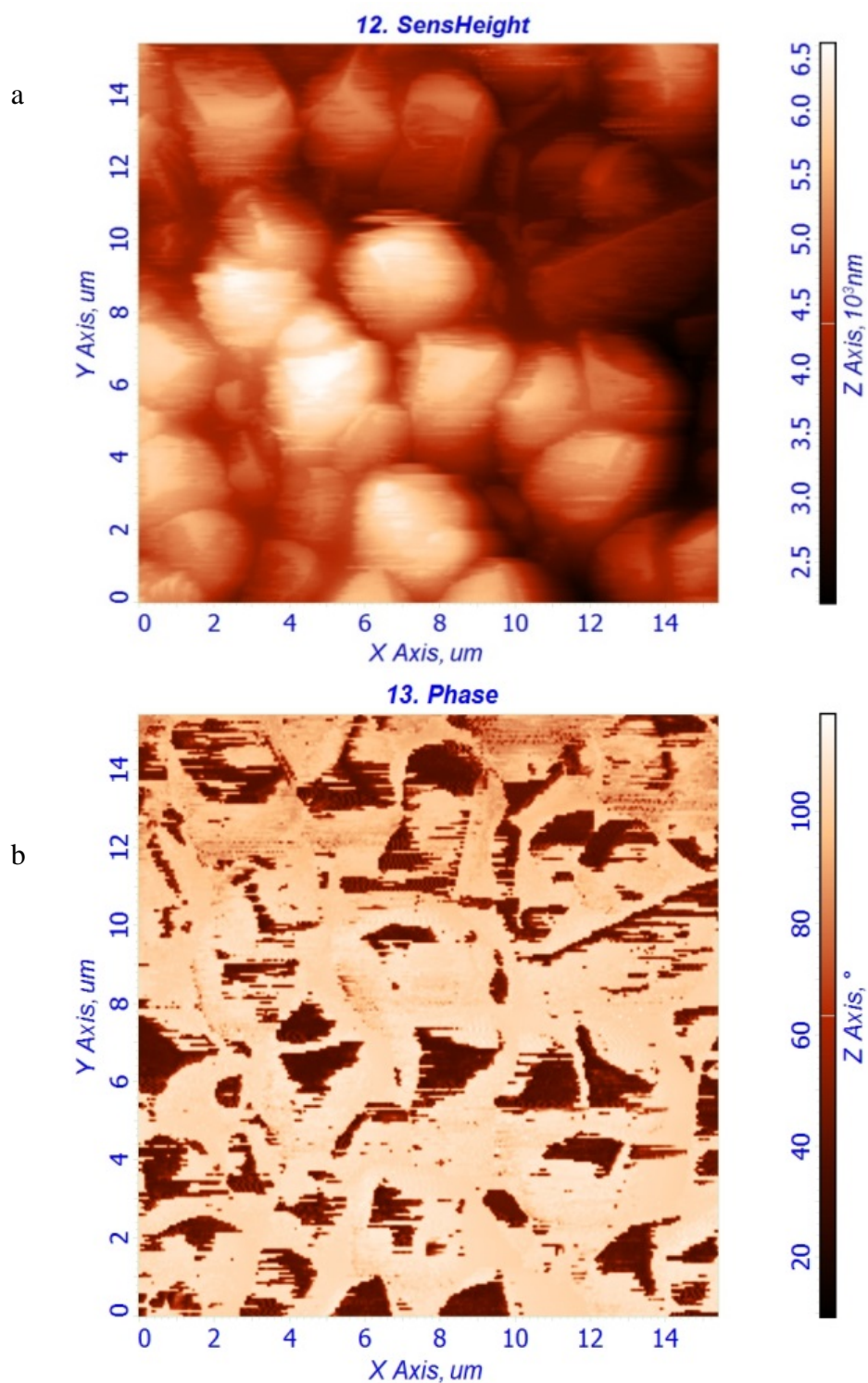


Fig. 5.16 (a) AFM image for cerium carbonate thin film on calcite and (b) AFM magnetic scan for the corresponding area; Scan size: $15\ \mu\text{m} \times 15\ \mu\text{m}$. Cerium carbonate formed triangle shaped particles sized from $0.5\ \mu\text{m} \times 0.5\ \mu\text{m} \times 0.5\ \mu\text{m}$ to $1\ \mu\text{m} \times 1\ \mu\text{m} \times 1\ \mu\text{m}$ on calcite.

The diameters for the particles shown on the topography image are from 1 μm - 5 μm . Most of the particles are within 2 μm - 3 μm . Compared to the topography image, the magnetic scan gives more detail on the surface structures and properties. Strong variations for the magnetic signal were observed for the magnetic scan. The dark areas are assigned to Ce rich region and the sizes observed are about 1-2 μm . The particle sizes for the cerium carbonate are consistent with the REs enriched components found in the natural mineral. The synthesized cerium carbonate specimen is suitable as a model compound for interaction investigation.

A smaller area was scanned for the same specimen. Fig. 5.16 displays a 15 μm \times 15 μm area for both the topography image and the magnetic map. With smaller scan areas, clearer images were obtained. The topography image shows triangular crystals ranging from 0.5 μm^3 to 2 μm^3 formed on the surface. The variations in height are from 0 to 650 nm. Triangle particles are also observed in the magnetic map. The magnetic signals are as strong as the large scale scanning. The dark areas where Ce presented are consistent with the topography image.

5.3.2 Absorption study for cerium carbonate thin film on calcite with hydroxamate

Fig. 5.17 displays the Raman spectra for the conditioned cerium carbonate thin film for 1 h, 5 h, 24 h and 72 h as well as the 72 h for conditioned calcite. After the first hour of conditioning, the Raman spectrum was consistent that the cerium carbonate thin film without hydroxamate absorbed on the surface. For the spectra of 5 h and 24 h of conditioning, the band at 2810 cm^{-1} to 2940 cm^{-1} became more apparent but still weak. This band is assigned to the $\nu\text{C-H}$ emanated from hydroxamate. Bands for important functional groups such as C=O , N-O , C-N were absent in the spectra. It is probable that the absorption is either physical and/or too thin for these to be detected with normal Raman spectroscopy. After 72 h of conditioning, the band for $\nu\text{C-H}$ at 2820 cm^{-1} to 2960 cm^{-1} were evident. Bands for $\nu\text{C=O}$, $\nu\text{C-N}$ and $\nu\text{N-O}$ at 1555 cm^{-1} , 1032 cm^{-1} and 986 cm^{-1} were also observed, consistent with the growth of bulk cerium hydroxamate.

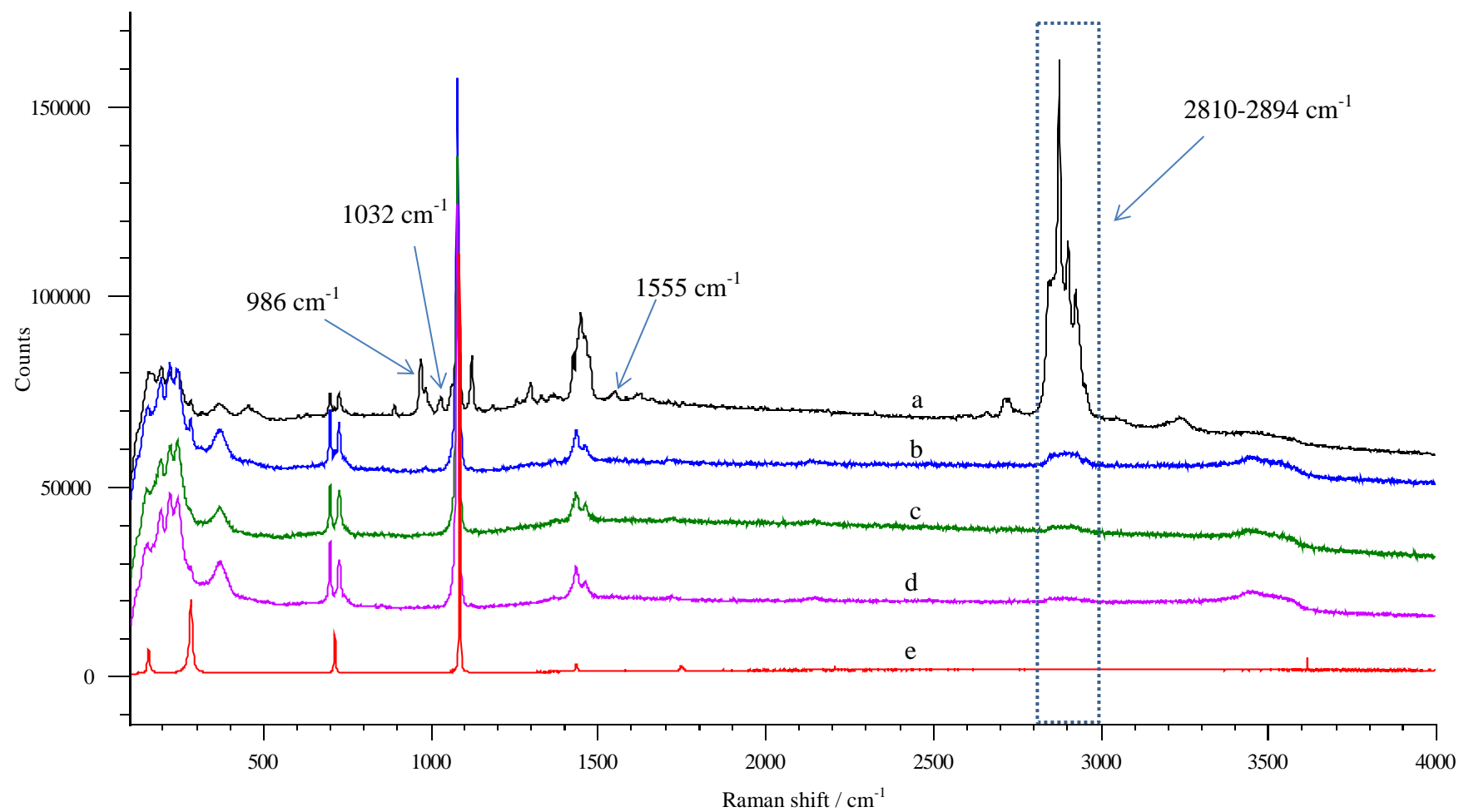


Fig. 5.17 Raman spectra of conditioned cerium carbonate thin film with $\text{KH}(\text{OHA})_2$, (a)-(d): 72 h, 24 h, 5 h, 1 h; (e): calcite conditioned with $\text{KH}(\text{OHA})_2$ for 72 h.

It is probable that chemical absorption occurred between the cerium carbonate thin film and hydroxamate. The absorption study was undertaken using normal Raman. Therefore a thick multilayer must have been present to be observable. On the other hand, no additional bands were observed for calcite over the entire conditioned period. This indicates hydroxamate is selective to Ce compared to Ca. During the process of flotation, it is expected that hydroxamate would preferably collect REs minerals when gangue mineral calcite is present.

Conclusion

Six rare earth hydroxamate compounds (Nd, Ce, Er, Ho, Dy, Gd hydroxamate) have been synthesized and investigated by XPS and vibrational spectroscopy. Chemical adsorptions through oxygen and nitrogen atoms of hydroxamate bonding to the REE atoms were observed. It has demonstrated that critical vibrational bands including $\nu\text{C=O}$, $\nu\text{N-O}$ and $\nu\text{C-N}$ can be used as surface adsorption indicators between minerals and collectors.

A cerium carbonate thin film has been synthesized on the calcite substrate. It was investigated as a model system for the surface study between REs and hydroxamate. The study established the utility of using AFM-Raman to investigate and mineral surface interaction *in-situ*. The adsorption studies for cerium carbonate and calcite demonstrated that hydroxamate is selective to Ce over Ca.

The investigations of RE hydroxamate compounds and the cerium carbonate thin film on calcite provide the feasibility and fundamental information for the surface study for natural compounds and minerals. In practice, it is also important to understand the selectivity of individual REs and minerals to hydroxamate as well as the localization of adsorption area of natural RE and gangue minerals. Next chapter presents the results for REOs and RE minerals adsorption studies with hydroxamate.

References

- Adroja D. T., 1991, Valence fluctuation and heavy fermion behaviour in rare earth and actinide based compounds, *Journal of Magnetism and Magnetic Materials*, 100, 126-138.
- Alagha A., Parthasarathi L., Gaynor D., Muller-Bunz H., Starikova Z. A., Farkas E., Brien E. C. O., Gil M.-J. and Nolan K. B., 2011, Metal complexes of cyclic hydroxamates. Synthesis and crystal structures of 3-hydroxy-2-methyl-3H-quinazolin-4-one (ChaH) and of its Fe (III), Co (II), Ni (II), Cu (II) and Zn (II) complexes, *Inorganica Chimica Acta*, 368, 58-66.
- Belkasem H. A., Benghuzi S. A. and Desouky O. A. M., 2010, Preparation and characterization of N-substituted octanohydroxamic acids metal complexes, *Journal of Agricultural Chemistry and Biotechnology*, Mansoura University, 12, 629-638.
- Failes T. W. and Hambley T. W., 2000, Crystal structures of tris (hydroxamate) complexes of iron (III), *Australian Journal of Chemistry*, 53, 879-881.
- Frost R. L. and Dickfos M. J., 2007, Raman spectroscopy of halogen containing carbonates, *Journal of Raman Spectroscopy*, 38, 1516-1522.
- Gschneidner J. K. A. and Eyring L., 1993, *Handbook on the Physics and Chemistry of Rare Earths*, Amsterdam: North-Holland, 0444897828.
- Gunasekaran S. and Anbalagan G., 2007, Spectroscopic characterization of natural calcite minerals, *Spectrochimica Acta Part A*, 68, 3, 656-664.
- Hope G. A., Woods R., Buckley A. N., White J. M. and McLean J., 2010, Spectroscopic characterisation of n-octanohydroxamic acid and potassium hydrogen n-octanohydroxamate, *Inorganica Chimica Acta*, 363, 5, 935-943.

- Huang Y., Jiang Q. and Gu Y., 1991, Preparation and properties of rare earths coordination compounds with benzohydroxamic acid and octahydroxamic acid, Chinese Journal of Inorganic Chemistry, 7, 296-300 (无机化学学报).
- Jordens A., Cheng Y. P. and Waters K. E., 2013, A review of the beneficiation of rare earth element bearing minerals, Minerals Engineering, 41, 97-114.
- Moeller T., 1965, The Chemistry of the Lanthanides, Chapman & Hall Ltd, London, 35-66.
- Pradip, Li C. C. H. and Fuerstenau D. W., 2013, The synthesis and characterization of rare-earth fluocarbonates, KONA Powder and Particle Journal, 30, 193-200.
- Rutt H. N. and Nicola J. H., 1974, Raman spectra of carbonates of calcite structure, Journal of Physics C: Solid State Physics, 7, 4522-4528.
- Urmos J., Sharma S. K. and Mackenzie F. T., 1991, Characterization of some biogenic carbonates with Raman spectroscopy, American Mineralogist, 76, 641-646.

CHAPTER 6

INTERFACIAL INTERACTION STUDIES USING *IN-SITU* AND *EX-SITU* TECHNIQUES – RARE EARTH OXIDES, RARE EARTH MINERALS AND GANGUE MINERALS

6.1 Preamble

Natural RE minerals usually contain a number of REEs and the selectivity of hydroxamate for individual REs could be different. This can potentially affect the recovery rate of different REs. To understand and optimise on-site flotation processes, it is necessary to undertake adsorption studies with individual natural RE compound minerals. In addition, even though hydroxamate has been reported as a high efficiency collector for RE minerals (Fuerstenau and Pradip, 1984), the selectivity for different RE minerals (mainly bastnaesite and monazite) has not been investigated. Natural monazite normally contains proportional thorium and can be a radiation hazard. It is of interest to investigate the feasibility for the separation of monazite and bastnaesite using a highly selective collector to improve radiation control in ore processing.

The investigation of the synthesized RE hydroxamate compounds has identified the chemical bonding of RE metals with hydroxamate. The Raman bands of the critical bonding were used as indicators for the adsorption in this study. AFM-Raman and SEM are used for identifying the localization of the surface adsorption. A referencing method based on referring positions on a computer controlled microscope stage was used for revisiting the same sample points before and after conditioning with hydroxamate.

6.2 Adsorption studies between REOs and potassium hydrogen n-octanohydroxamate

6.2.1 Conditioned cerium oxide

CeO₂ was examined at conditioning times of 1 h and 18 h. The spectral acquisitions started from 800 cm⁻¹ to 4000 cm⁻¹ due to the strong Raman band at 465 cm⁻¹ which could saturate the detector at high power output. After 1 h of conditioning, three absorption bands assigned to ν C=O, ν C-N and ν N-O were observed at 1602 cm⁻¹, 1031 cm⁻¹ and 992 cm⁻¹. The evident adsorption bands indicate the adsorption rate was very rapid and that the collector accumulated in thick layers on the surface. After 18 h of conditioning, the bands for ν C-N and ν N-O shifted to 1032 cm⁻¹ and 986 cm⁻¹ while the ν C=O band remained at the same position (Fig. 6.1). The Raman spectrum for the 18 h of conditioned sample is more consistent with spectrum of the model cerium hydroxamate compound, for which bands for the ν C=O, ν C-N and ν N-O are at 1599 cm⁻¹, 1031 cm⁻¹ and 986 cm⁻¹. It is indicated a bulk multilayer of > 500 nm was formed. The Raman shifts in the longer conditioned sample spectrum may also indicate the adsorption structure changed over time.

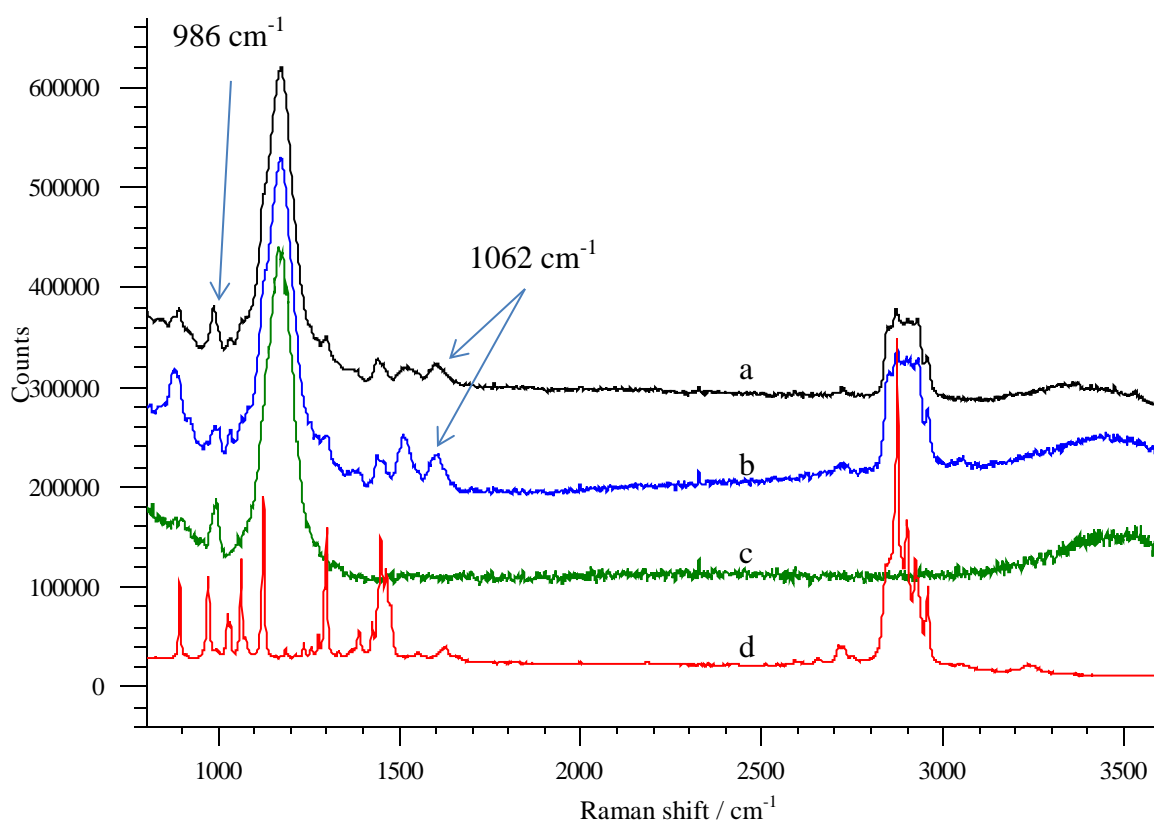


Fig. 6.1 Raman spectra of (a) conditioned CeO_2 with $\text{KH}(\text{OHA})_2$ for 18 h (b) conditioned CeO_2 with $\text{KH}(\text{OHA})_2$ for 1 h (c) CeO_2 (d) $\text{KH}(\text{OHA})_2$.

6.2.2 Conditioned neodymium oxide

Fig. 6.2 shows the Raman spectra of Nd_2O_3 , $\text{KH}(\text{OHA})_2$ and $\text{KH}(\text{OHA})_2$ conditioned (saturated) Nd_2O_3 for various conditioning times. For the critical functional groups C-N, N-O and C=O, all treated samples exhibit no apparent spectral features in the Raman spectra. Only hydroxamate bands at 2840 cm^{-1} to 2940 cm^{-1} , that are attributable to $\nu\text{C-H}$, were evident after 5 h of conditioning. These bands became more intense after the sample was conditioned for 18 h and the intensity reduced by more than 50% after 48 h. The same effect was observed in the mineral lattice vibrational region.

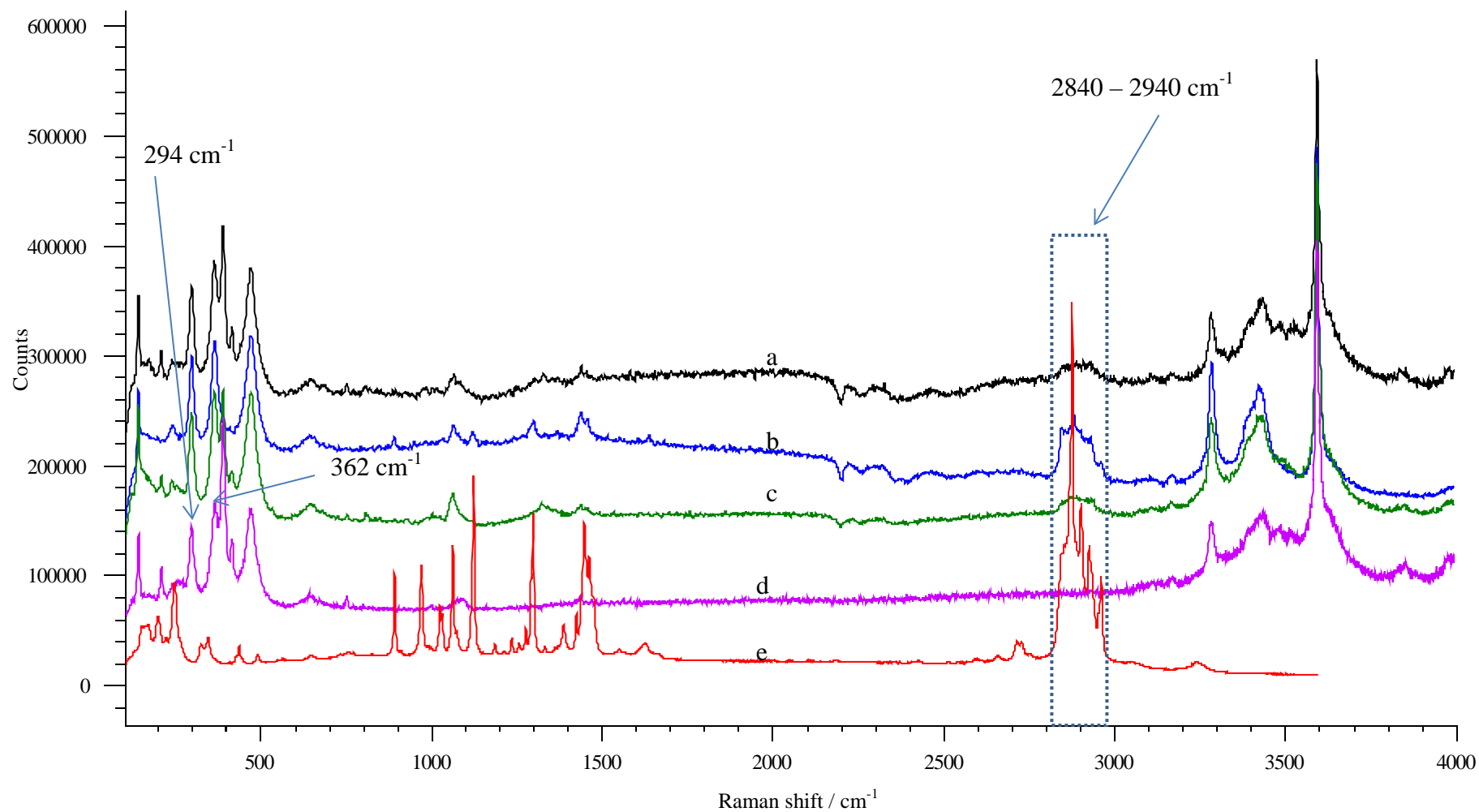


Fig. 6.2 Raman spectra of (a) conditioned Nd_2O_3 with $\text{KH}(\text{OHA})_2$ in water for 48 h (b) conditioned Nd_2O_3 with $\text{KH}(\text{OHA})_2$ in water for 18 h (c) conditioned Nd_2O_3 with $\text{KH}(\text{OHA})_2$ in water for 5 h; (d) Nd_2O_3 ; (e) $\text{KH}(\text{OHA})_2$.

At 294 cm^{-1} and 362 cm^{-1} , the Raman bands for the 18 h of conditioned sample shifted the most by 2 cm^{-1} to 3 cm^{-1} compared to the spectrum of Nd_2O_3 . The 18 h spectrum is also distinguished from the other spectra, including Nd_2O_3 , in the emission region. No lines were observed in three areas centred at 879 nm, 887 nm and 892 nm (Fig. 6.3). After 48 h of conditioning, the emission lines exhibit the same features as in the spectrum of Nd_2O_3 . The result is consistent with the Raman spectroscopic data and can be explained by the dissociation of hydroxamate on the surface.

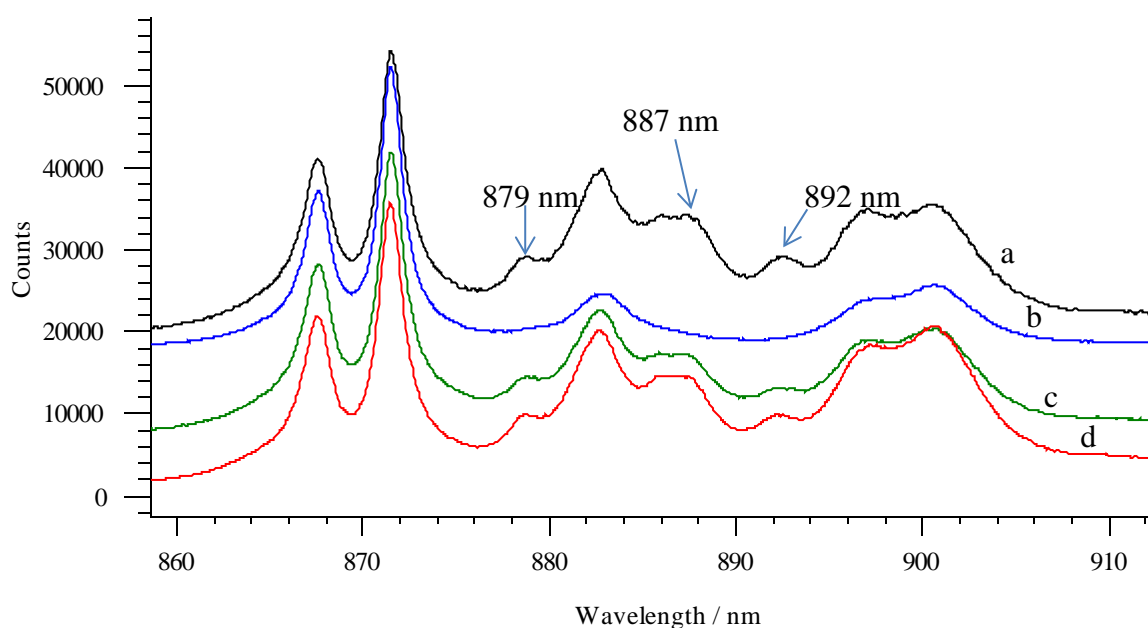


Fig. 6.3 Fluorescent spectra in the range of 860 nm – 940 nm for (a) conditioned Nd_2O_3 with for $\text{KH}(\text{OHA})_2$ in water for 48 h (b) conditioned Nd_2O_3 with $\text{KH}(\text{OHA})_2$ in water for 18 h (c) conditioned Nd_2O_3 with $\text{KH}(\text{OHA})_2$ in water for 5 h; (d) Nd_2O_3 .

Both the Raman and the fluorescent spectra indicate the interaction between hydroxamate and Nd_2O_3 had caused the energy change on the surface. However, the interfacial interaction was very weak and no multilayer was formed on the surface. It is also indicated that desorption occurred during the conditioning time. The maximum adsorption rate occurred at the 18 h of conditioning time.

Nd_2O_3 was selected as the model compound for solvent dependence investigation because neodymium oxide has the strong fluorescent emissions accessible for observation in a spectral region that does not overlap the Raman bands. Ethanol was added as the solvent for hydroxamate and the specimen was conditioned in the solution of mixed ethanol and water. With 50% ethanol/water, the solubility of n-octanohydroxamate significantly increases than using pure water as solvent. This could potentially increase the adsorption converge on the surface. Other experimental conditions were the same amount as the adsorption investigation with water.

Fig. 6.4 shows the Raman spectra of Nd_2O_3 , $\text{KH}(\text{OHA})_2$ and the $\text{KH}(\text{OHA})_2$ treated Nd_2O_3 for up to 48 h in 1:1 ethanol and water. The treated sample exhibits all the expected spectral features from Nd_2O_3 with a 2 cm^{-1} shift observed in the carbonate band (1096 cm^{-1}). Additionally, from all the treated sample in the region of $800\text{-}1700\text{ cm}^{-1}$, bands that would be attributable to the potassium hydrogen n-octanohydroxamate are absent while bands at 943 and 1636 cm^{-1} are evident and are assigned to a hydroxamate complex (the assignments for neodymium n-octanohydroxamate see chapter 5).

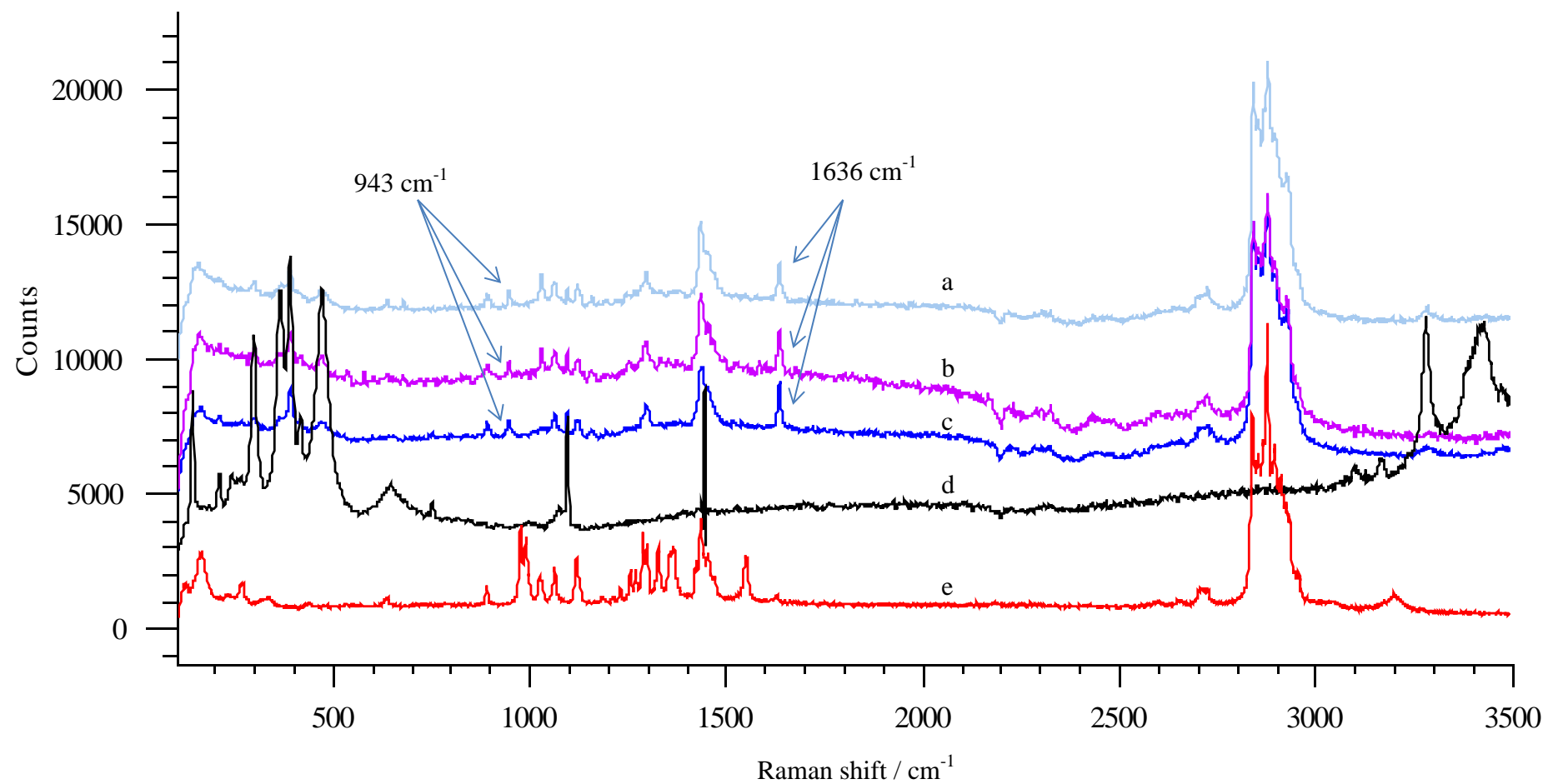


Fig. 6.4 Raman spectra of (a) conditioned Nd_2O_3 with $\text{KH}(\text{OHA})_2$ in 1:1 ethanol and water for 48 h (b) conditioned Nd_2O_3 with $\text{KH}(\text{OHA})_2$ in 1:1 ethanol and water for 18 h (c) conditioned Nd_2O_3 with $\text{KH}(\text{OHA})_2$ in 1:1 ethanol and water for 5 h; (d) Nd_2O_3 ; (e) $\text{KH}(\text{OHA})_2$.

Two bands at 1032 cm^{-1} that can be assigned to the $\nu\text{C-N}$ were observed in the spectra of 18 and 48 h of conditioning. This band was not showed when the specimen was treated for 5 h. It is suggested that chemical adsorption occurred on the surface and bonds formed between the collector and Nd_2O_3 after 18 h of conditioning. The bonds were strong and probably is the reason why desorption was not observed during the conditioned time. In addition, the model compound neodymium n-octanohydroxamate is sparsely soluble in most of the organic solvent including ethanol. This also contribute to a lower dissociate in the solution and thus higher concentration of the complex formed on the surface.

For the emission spectra, all treated specimens exhibited similar adsorption pattern of the Raman spectra (Fig. 6.5). Compared to the spectrum of Nd_2O_3 , the lines shape changed in the region of 895 nm to 905 nm and lines position shifts were observed from 878 nm to 893 nm.

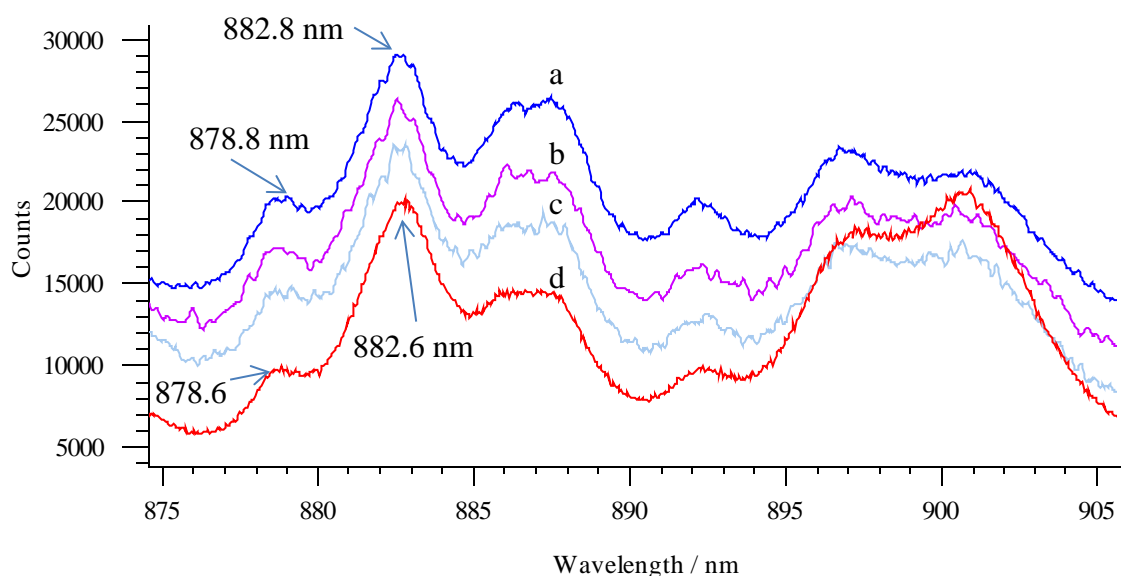


Fig. 6.5 Fluorescent spectra in the range of 875 nm – 905 nm for (a) conditioned Nd_2O_3 with $\text{KH}(\text{OHA})_2$ in 1:1 ethanol and water for 48 h; (b) conditioned Nd_2O_3 with

KH(OHA)₂ in 1:1 ethanol and water for 18 h; (c) conditioned Nd₂O₃ with KH(OHA)₂ in 1:1 ethanol and water for 5 h; (d) Nd₂O₃.

Specifically, all the spectra for the treated samples exhibit 0.2 nm shifts at 882.6 nm and 878.6 nm compared to 882.8 nm and 878.8 nm for Nd₂O₃. The emission spectra did not change with the conditioning time. This indicates the adsorption reached its equilibrium point after 5 h of conditioning and no desorption occurred thereafter.

The solvent dependant study gives evidence that ethanol contributes to increase the adsorption rate. In the flotation system, it is beneficial to add ethanol to increase the recovery rate if the strategy is allowed from the economic view.

6.2.3 Conditioned erbium oxide

Fluorescent emissions overlapped the Raman vibrations in the range of 350 cm⁻¹ to 1200 cm⁻¹ for Er₂O₃. However, the fluorescent lines do not affect the observation of the hydroxamate Raman bands (N-O, C-N and C=O). In the model erbium n-octanohydroxamate compound, bands at 1000 cm⁻¹, 1028 cm⁻¹ and 1611 cm⁻¹ assigned to $\nu(\text{N-O})$, $\nu(\text{C-N})$ and $\nu(\text{C=O})$, respectively, were observed. In all the conditioned Er₂O₃ specimen spectra, no hydroxamate bands were observed (Fig. 6.6).

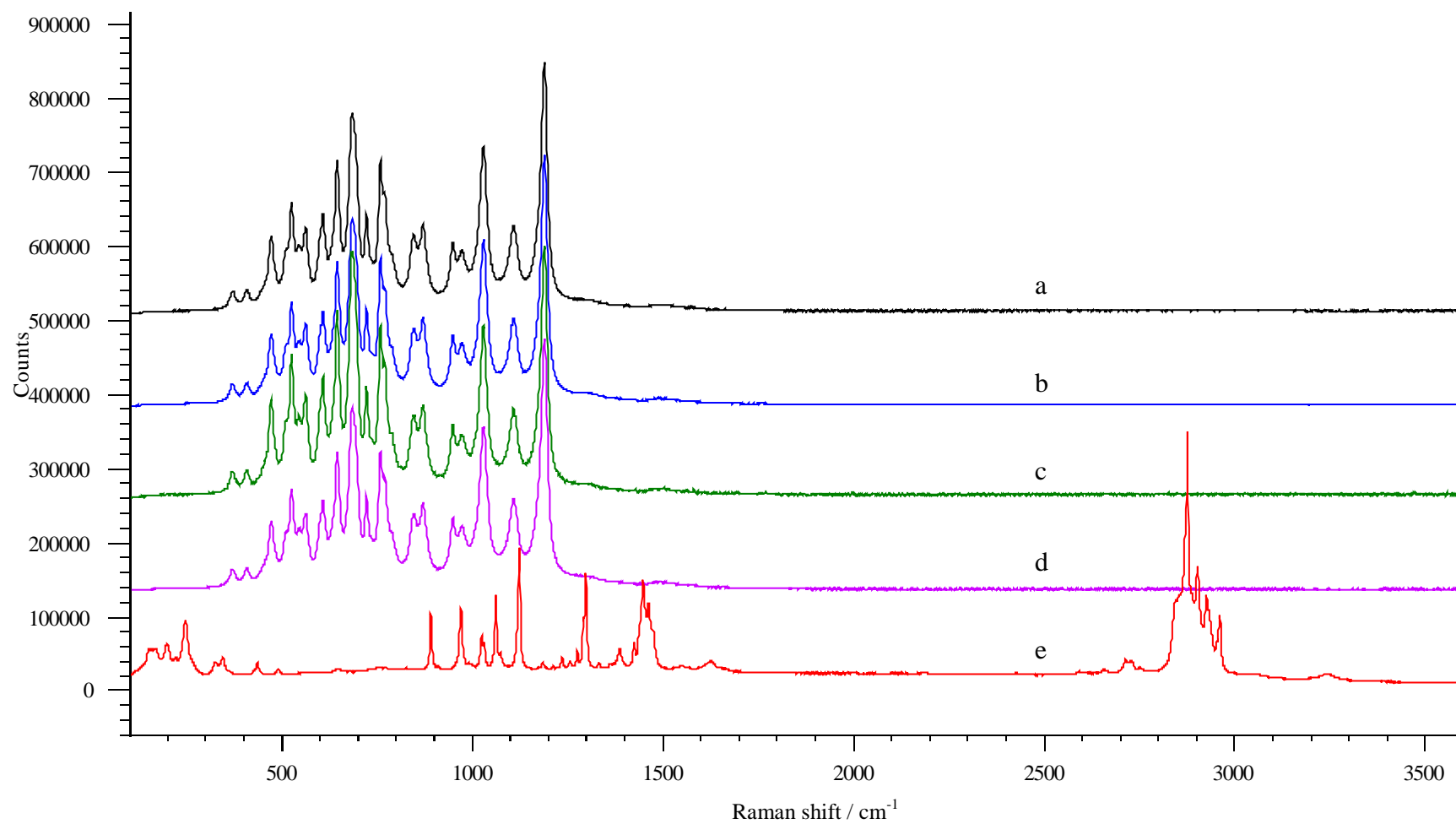


Fig. 6.6 Raman spectra of (a) conditioned Er_2O_3 with $\text{KH}(\text{OHA})_2$ for 18 h; (b) conditioned Er_2O_3 with $\text{KH}(\text{OHA})_2$ for 5 h; (c) conditioned Er_2O_3 with $\text{KH}(\text{OHA})_2$ for 1 h; (d) Er_2O_3 ; (e) $\text{KH}(\text{OHA})_2$.

In the emission spectra from 300 cm^{-1} to 1350 cm^{-1} , the fluorescent bands are identical with pure Er_2O_3 (Fig. 4.7). It is indicated that there was no energy change on the surface and it is expected that no adsorption occurred during the conditioned time. The emission studies are consistent with the vibrational spectroscopic investigations.

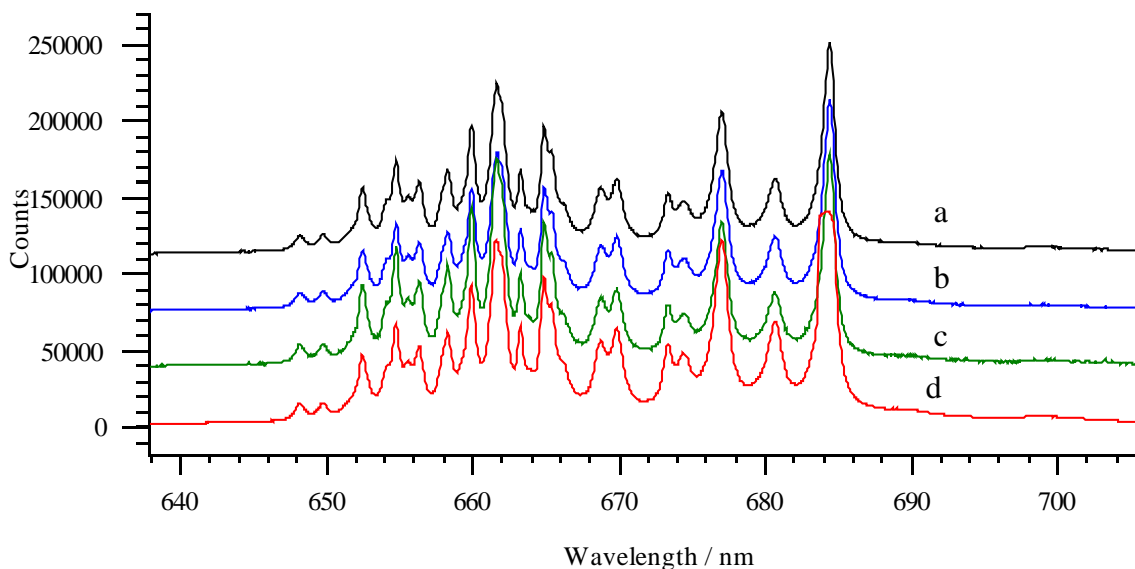


Fig. 6.7 Fluorescent emission spectra of (a) conditioned Er_2O_3 with $\text{KH}(\text{OHA})_2$ for 18 h; (b) conditioned Er_2O_3 with $\text{KH}(\text{OHA})_2$ for 5 h; (c) conditioned Er_2O_3 with $\text{KH}(\text{OHA})_2$ for 1 h; (d) Er_2O_3 .

Both of the studies indicate that the collector hydroxamate is not selective for Er_2O_3 . Er minerals are unlikely to be collected during flotation by using this type of reagent. However, the floatation conditions (pH, temperature, ions factor, etc.) vary in the industrial environment. Further bench-scale experiment and investigation are required to verify this result.

6.2.4 Conditioned thulium oxide

Fig. 6.8 shows the spectra for conditioned Tm_2O_3 at different times and compared to the spectra of Tm_2O_3 and potassium hydrogen n-octanohydroxamate. The spectrum for the 1 h conditioned Tm_2O_3 exhibits low intensity bands at 1001 cm^{-1} , 1034 cm^{-1} , 1582 cm^{-1} and 1601 cm^{-1} that differ from the spectra of Tm_2O_3 and hydroxamate. By comparing with other model RE hydroxamate compounds, the bands at 1001 cm^{-1} , 1034 cm^{-1} and 1601 cm^{-1} can be assigned to the $\nu\text{N-O}$, $\nu\text{C-N}$ and $\nu\text{C=O}$ vibrational modes (detailed discussion in Chapter 5).

After 5 h of conditioning, all the bands became evident with 2 cm^{-1} shifts compared to thulium n-octanohydroxamate. The band at 1034 cm^{-1} shifted to lower wavenumber to 1032 cm^{-1} . Both bands at 1582 cm^{-1} and 1601 cm^{-1} shifted to higher wavenumber by 2 cm^{-1} . The absorption bands in the 18 h conditioned spectrum are the most intensive compared to the other two treated sample spectra. No further shift was observed with the 18 h spectrum. The band at 1001 cm^{-1} was broader but remained at the same position. The spectra were consistent with multilayer chemical adsorption. It is also suggested that more rare earth atoms bonded through the nitrogen and oxygen atoms as the conditioning time increased. Hydroxamate can be considered as an effective collector for thulium.

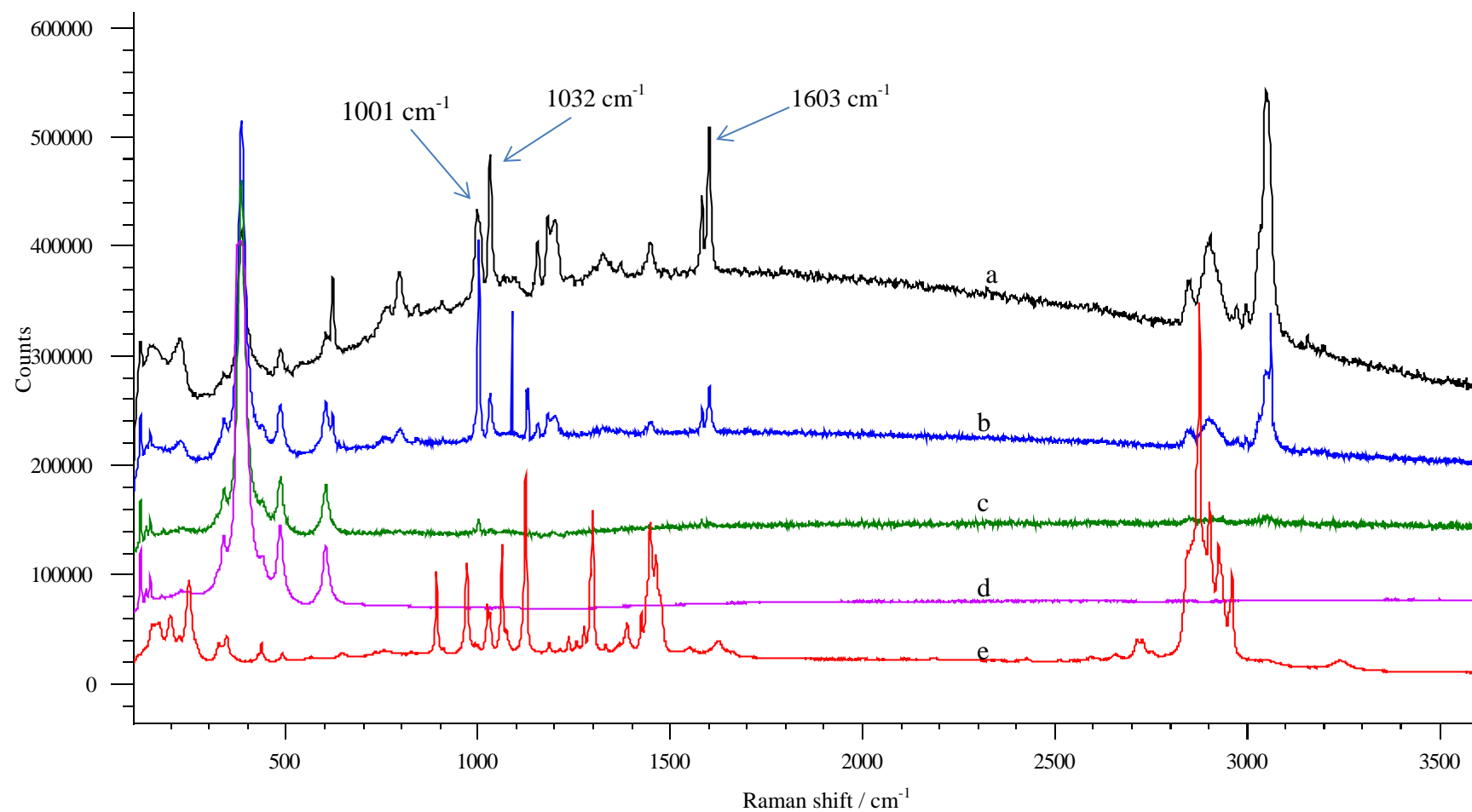


Fig. 6.8 Raman spectra of (a) conditioned Tm_2O_3 with $\text{KH}(\text{OHA})_2$ for 18 h; (b) conditioned Tm_2O_3 with $\text{KH}(\text{OHA})_2$ for 5 h; (c) conditioned Tm_2O_3 with $\text{KH}(\text{OHA})_2$ for 1 h; (d) Tm_2O_3 ; (e) $\text{KH}(\text{OHA})_2$.

6.2.5 Conditioned ytterbium oxide

For Yb_2O_3 , critical bands at 1002 cm^{-1} assigned to $\nu\text{N-O}$ were observed after 1 h of conditioning and intensified at longer conditioning times. The important bonding for C=O at around 1600 cm^{-1} were not observed for all the conditioned samples spectra (Fig. 6.9). For $\nu\text{C-N}$, a very low intensive band was observed at 1032 cm^{-1} in the 5 h of conditioning spectrum. This indicates the bonding on the surface was very weak and the adsorption layer must have been thin.

In the region of 2800 cm^{-1} to 3200 cm^{-1} , the spectra from all the treated samples are consistent with the region at around 1000 cm^{-1} . Low intensity bands assigned to $\nu\text{C-H}$ were observed in the three conditioned samples. This band in the 5 h of conditioned sample spectrum was slightly more intensive than the other two spectra. Compared to CeO_2 , Nd_2O_3 and Tm_2O_3 , the results exhibit poor selectivity of hydroxamate for Yb_2O_3 .

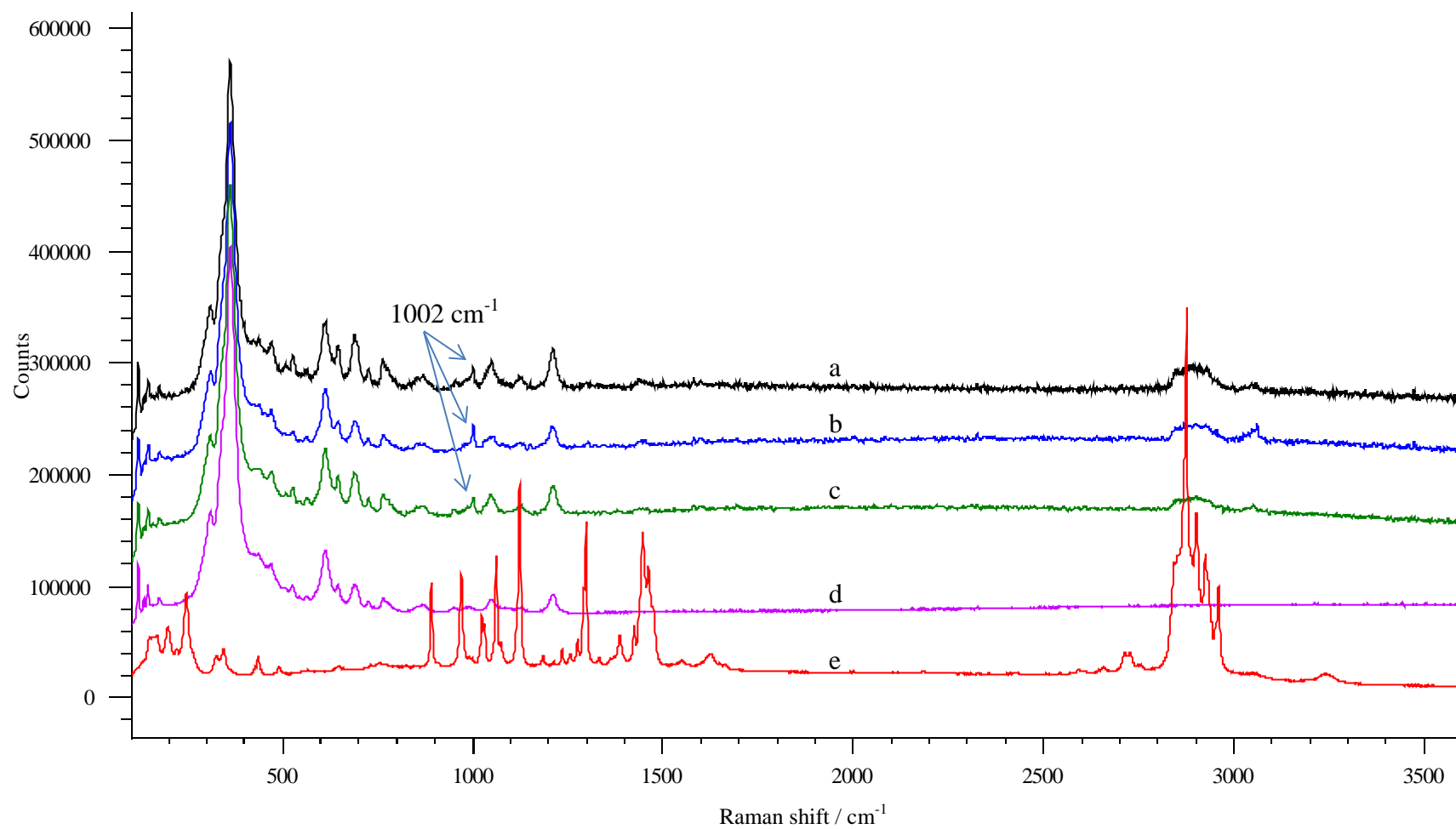


Fig. 6.9 Raman spectra of (a) conditioned Yb_2O_3 with $\text{KH}(\text{OHA})_2$ for 18 h; (b) conditioned Yb_2O_3 with $\text{KH}(\text{OHA})_2$ for 5 h; (c) conditioned Yb_2O_3 with $\text{KH}(\text{OHA})_2$ for 1 h; (d) Yb_2O_3 ; (e) $\text{KH}(\text{OHA})_2$.

6.2.6 Conditioned lanthanum oxide

Fig. 6.10 shows the spectra of La_2O_3 conditioned with hydroxamate for different times and compared with the spectra of La_2O_3 and hydroxamate. The 1 h spectrum exhibits bands at 1002 cm^{-1} , 1032 cm^{-1} and 1602 cm^{-1} assigned to the $\nu\text{N-O}$, $\nu\text{C-N}$ and $\nu\text{C=O}$ vibrations of hydroxamate, respectively. The intensity of these bands rose when the conditioning time increased. The 18 h conditioned sample spectrum displayed a very strong sharp band at 1002 cm^{-1} .

The same observation was made in the region assigned to $\nu\text{C-H}$ from 2800 cm^{-1} to 3200 cm^{-1} . The intensity counts at 3060 cm^{-1} was at the ratio of 37: 12: 7 corresponding to the 18 h, 5 h and 1 h spectrum. The result indicated multilayer adsorption occurred between La_2O_3 and hydroxamate as conditioned time increased.

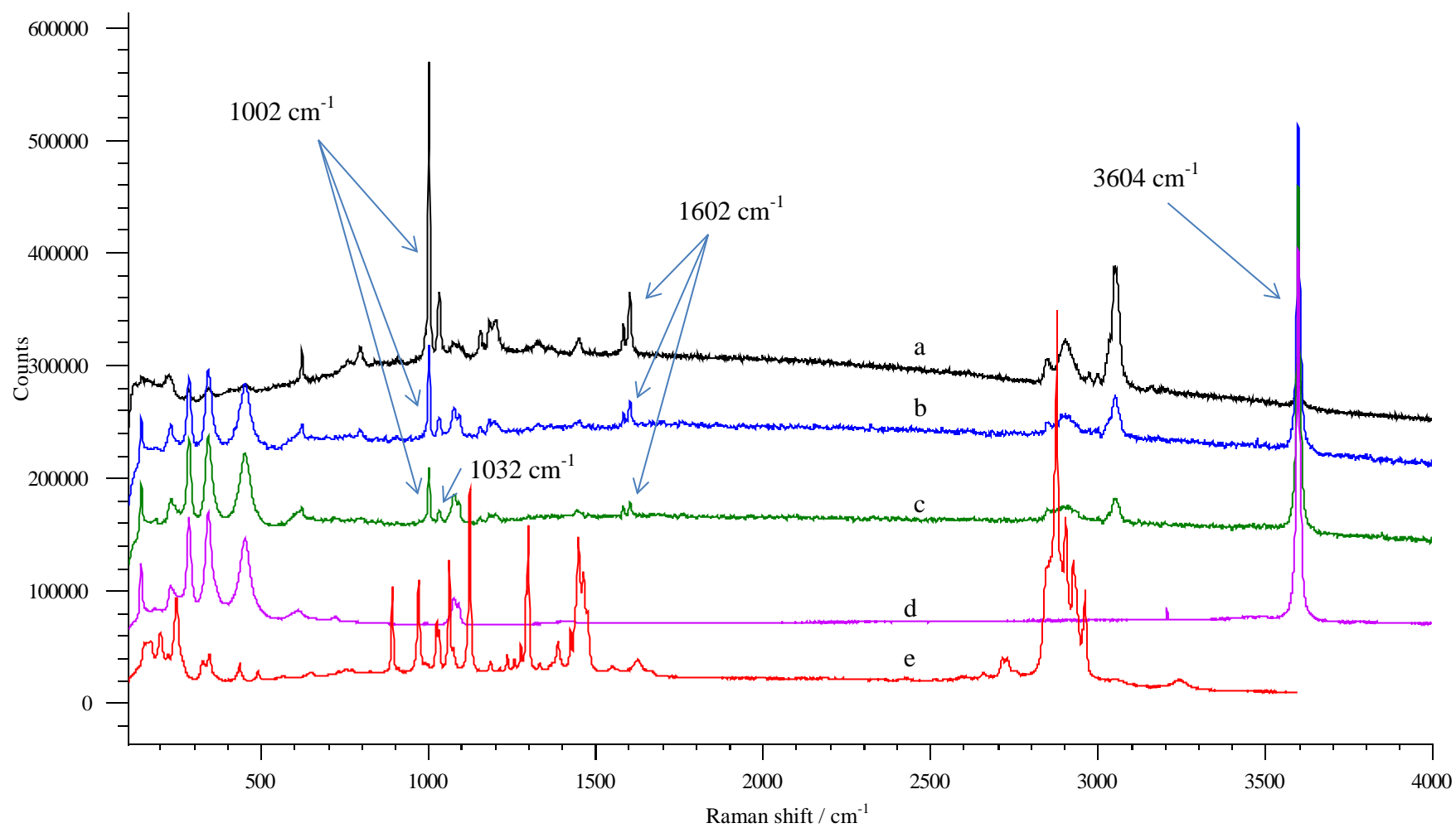


Fig. 6.10 Raman spectra of (a) conditioned La_2O_3 with $\text{KH}(\text{OHA})_2$ for 18 h; (b) conditioned La_2O_3 with $\text{KH}(\text{OHA})_2$ for 5 h; (c) conditioned La_2O_3 with $\text{KH}(\text{OHA})_2$ for 1 h; (d) La_2O_3 ; (e) $\text{KH}(\text{OHA})_2$.

The Raman band at 3604 cm^{-1} showed the least intensive in the 18 h of conditioned spectrum. The three bands in the lattice area at 283 cm^{-1} , 341 cm^{-1} and 451 cm^{-1} were displayed initially in the La_2O_3 , 1 h and 5 h treated samples spectra but the intensity decreased by 80% after 18 h of conditioning. The band at 228 cm^{-1} also shifted by 4 cm^{-1} to 224 cm^{-1} in the 18 h conditioned spectrum. It is indicated that different adsorption mechanism could occur in La_2O_3 (not just the thickness of the adsorption layer increased). Surface hydroxylation has been confirmed for the sample used in this thesis and the band at 3604 cm^{-1} is assign to the O-H in the $\text{La}(\text{OH})_3$ compound. This band can be used as an indication for surface hydroxylation. The 18 h conditioned sample spectrum had a significant reduction in intensity for this band. This indicate the concentration of $\text{La}(\text{OH})_3$ on the surface has decreased, probably due to ligands competition during the conditioned time (hydroxamate substituted the O-H). It also can explain the reason why the intensities decreased dramatically at 283 cm^{-1} , 341 cm^{-1} and 451 cm^{-1} and shifted for the band at 228 cm^{-1} . The substitutions have led to vibrational energy changes on the surface and thus cause bands shift in the lattice area of the spectra.

6.2.7 Summary and discussion for the adsorption studies for REOs

La_2O_3 exhibited the most intense Raman bands during the conditioning time. The increased intensities in critical bands (bonding with hydroxamate through O) and the weak intensities and Raman shifts for the La-O (in La_2O_3) bands are consistent with multilayer chemisorption having occurred on the La_2O_3 surface. Hydroxamate is expected to collect La prior to other REs (Ce, Nd, Er, Yb, Tm) during flotation. For CeO_2 , Raman spectra revealed that evident adsorption was observed through the functional groups of C=O and C-N after 1 h of conditioning and the band for N-O was consistent with the model cerium hydroxamate compound after 18 h of conditioning. This indicates that Ce also has strong interaction with n-octanohydroxamate. Apparent adsorption occurred for Tm_2O_3 after 5 h of conditioning while low intensities of the $\nu\text{N-O}$ and $\nu\text{C-N}$ were observed with the absence of $\nu\text{C=O}$ during the conditioning time for Yb_2O_3 . No adsorption evidence was observed for Er with n-octanohydroxamate. Spectral features for the adsorption functional groups were not observed for the Nd_2O_3 sample. It is suggested that only physical adsorption occurred on the surface and Nd exhibited weak interaction with n-octanohydroxamate. The addition of ethanol as solvent was observed to assist the adsorption process for the Nd_2O_3 adsorption investigation. It can be concluded that hydroxamate is selective to La_2O_3 over CeO_2 , followed by Tm_2O_3 , Yb_2O_3 , Nd_2O_3 and Er_2O_3 when water is used as solvent.

Fuerstenau and Pradip reported the stability constants for a number of metal hydroxamate compounds including Ce, La, and Yb that have been investigated in this study (Fuerstenau and Pradip, 1984). It appears that the adsorption rate on the RE oxide is not consistent with the stability constant for corresponding RE hydroxamate complex. For example, the $\log K_1$ for La and Ce are 5.16 and 5.45, hydroxamate exhibited better coverage on La than Ce. Yb is reported having higher $\log K_1$ (6.61) compared to La and

Ce, however n-octanohydroxamate had poor selectivity over Yb. It can be concluded that the stability of the RE compounds does not reflect the selectivity of hydroxamate.

6.3 Adsorption studies between RE minerals and hydroxamate

6.3.1 Bastnaesite conditioned with hydroxamate

6.3.1a Investigation using XPS

The XPS spectra showed that carbonate C (3.4 at%) remained evident in the C 1s spectrum and the hydrocarbon C concentration was about 65 at%. It is indicated that the adsorbate layer was either thin if uniform, or thicker if in patches. The intensity of the F 1s peak reduced to the same extent as the carbonate peak, supporting the conclusion that the adsorbed layer was either thin or thicker if in patches. No K 2p peak was observed and this indicated no residual K from the collector remained at the surface.

The carbonate component was relatively narrow (1.4 eV), whereas the hydrocarbon component consisted of several unresolved components. Therefore, binding energies for the conditioned bastnaesite spectra were referenced to carbonate C 1s, F 1s and Ca 2p_{3/2} due to their consistency.

It is expected that most of the N in hydroxamate would be adsorbed to La, Ce, Nd and Ca at the mineral surface; consequently the N 1s and C 1s spectra were expected to be complex. The XPS data indicated the surface N concentration was 3.8 at%. The N 1s spectrum was asymmetric and two components at 398.6 and 400.8 eV could be fitted. The more intense component was observed at the lower binding energy of 398.6 eV in the spectrum that was obtained at the outset. This component could be attributed to deprotonated hydroxamate N, but this assignment requires further investigation before it can be confirmed.

The Nd 3*d*, La, Ce and Nd 4*d*, and Ca 2*p* spectra were all similar to those from the unconditioned bastnaesite. No significant differences were observed in the metal 3*d* or 2*p* binding energies from the corresponding carbonates or fluoro-carbonates. The results indicate that no adsorption between the metals and hydroxamate has occurred. In addition, the intensities in the La, Ce and Nd 4*d* spectral region remained the same after conditioning as before. This indicated that there had no significant concentration of one metal hydroxamate (in patches) on the conditioned surface. The relative intensity of the F KL_{2,3}L_{2,3} Auger peak near the La 3*d* spectrum was unchanged. It supported that La hydroxamate (in patches) was not present. All these observations indicate that no more than one molecular layer of metal hydroxamates could have been retained at the rinsed bastnaesite surface.

6.3.1b Investigation using Raman spectroscopy

A bastnaesite crystal was conditioned with saturated hydroxamate in water for 40 min before investigation. Fig. 6.11 shows the Raman spectrum for the KH(OHA)₂ treated bastnaesite crystal which is compared with the spectra from the crystal sample and KH(OHA)₂.

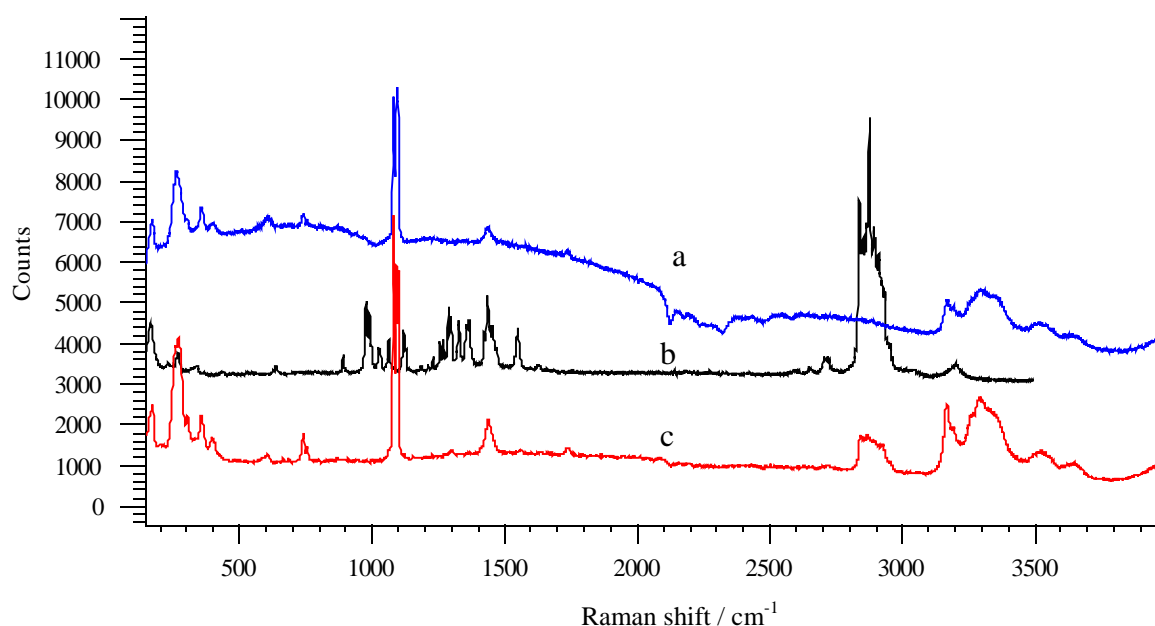


Fig. 6.11 Raman spectra for (a) bastnaesite crystal (b) $\text{KH}(\text{OHA})_2$ (c) treated bastnaesite crystal. The bastnaesite crystal sourced from Pakistan.

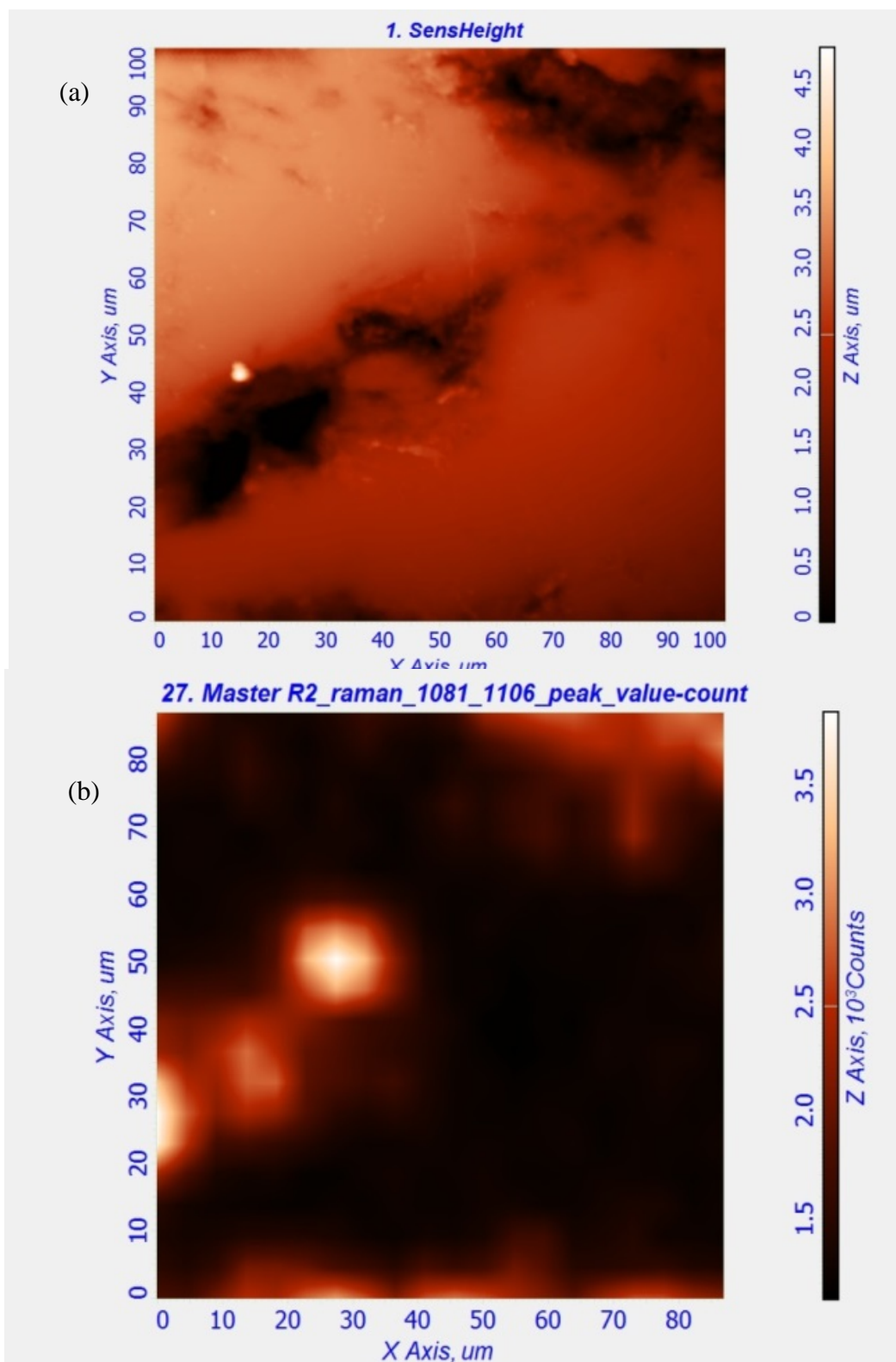
Hydroxamate bands at 2846-2966 ($\nu\text{C-H}$ broad) are apparent in the spectrum from the treated crystal (spectrum c). In addition, the band at 1094 cm^{-1} that is assigned to the carbonate symmetric mode shifted to 1092 cm^{-1} in the treated sample spectrum. In the lattice area, the band at 252 cm^{-1} became broader in the conditioned sample spectrum. The results indicate vibrational energy has changed during conditioning and is consistent with formation of bulk hydroxamate on the surface of the mineral. This result might appear to be inconsistent with the XPS data however the conditioning time was substantially longer in the Raman study (10 min for the XPS investigation and 40 min when the sample was examined using Raman spectroscopy).

On the other hand, the bands for C-N, N-O and C=O stretches were not observed in the treated sample spectrum. This could be due to the concentration of REs that were present on the surface and lead to an absorption layer was too thin to give observable normal Raman signal. It also could be the adsorption was in patches where REs are enriched.

6.3.1c Investigation using AFM - Raman

AFM-Raman mapping has the advantage over normal Raman mapping that the surface focus is consistent and optimal. For polished mineral samples, the height variation of the surface is usually 1-2 μm . Off focus on some areas could happen when mapping with traditional Raman sampling stage and result in poor resolution that might not reflect the adsorption. It is therefore most efficient to use AFM-Raman to identify the interfacial interaction areas. Therefore, AFM-Raman mapping was adopted for the same conditioned bastnaesite sample previously investigated by Raman spectroscopy.

Fig. 6.12 shows three AFM-Raman maps with spectral scanning centred at 1093.5 cm^{-1} , 985 cm^{-1} and 3169 cm^{-1} together with the corresponding AFM topographic image. The Raman bands in these regions are primarily derived from the bonding vibrations of C-O from carbonate, N-O and C-H from hydroxamate, respectively. These signals provide information for the location of bastnaesite and the presence of hydroxamate on the surface.



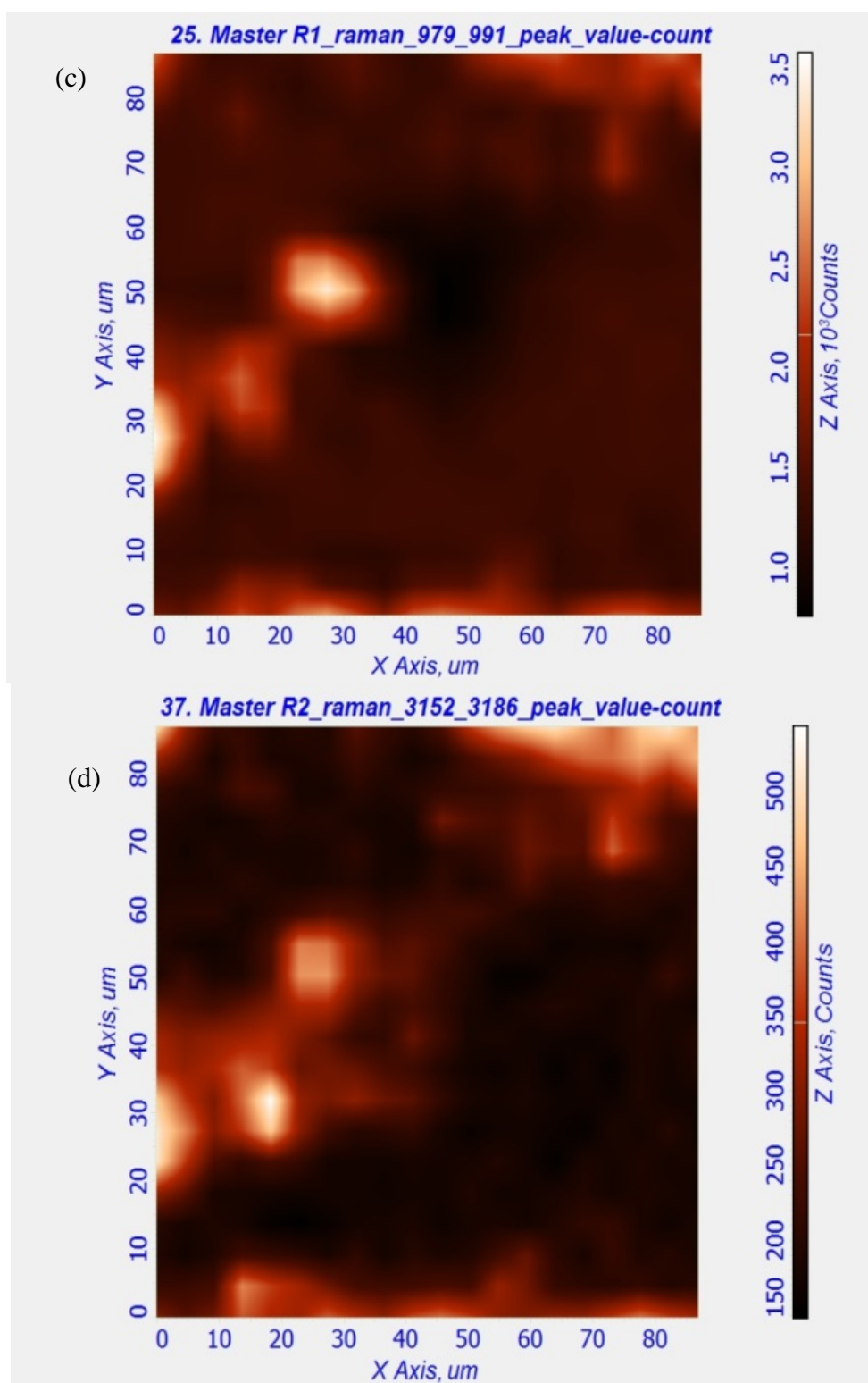


Fig. 6.12 AFM and AFM-Raman images for conditioned bastnaesite: (a) surface image of bastnaesite, $100 \times 100 \mu\text{m}$; (b), (c), (d): AFM-Raman images on the same area with static scans centred at 1093.5 cm^{-1} , 985 cm^{-1} and 3169 cm^{-1} , respectively.

In Fig. 6.12a, two dark areas are shown in the bottom left and top right corners. Strongest Raman signals of the three wavenumbers are found on these two dark areas. The signal at 1093.5 cm^{-1} indicates bastnaesite is present in batches (Fig. 6.12b) and the result is consistent with previous AFM and magnetic AFM data (see Chapter 4). Strong signals responsible for hydroxamate (Fig. 6.12c and 6.12d) were observed in the same location where bastnaesite presented. This adsorption study is consistent with the RE elements being enriched in patches on the sample crystal.

6.3.2 Monazite crystal conditioned with hydroxamate

Monazite crystals were conditioned in a saturated hydroxamate solution (water as solvent) for up to 48 h. Fig 6.13 displays the conditioned spectra for 2 h and 48 h with potassium hydrogen n-octanohydroxamate and monazite crystal spectrum.

In the region from 800 cm^{-1} to 1600 cm^{-1} , the expected adsorption bands for C-O, N-O and C=O are not present in both treated samples. A slight shift of 2 cm^{-1} is observed at 1065 cm^{-1} that is assigned to the $(\text{PO}_4)^{3-}$ ν_3 mode for the 48 h of conditioned sample. This band was not observed in the 2 h conditioned specimen spectrum. It is indicated that surface binding energy may have changed during the conditioning time; however, the energy is not sufficient to cause physical and chemical adsorption on the surface.

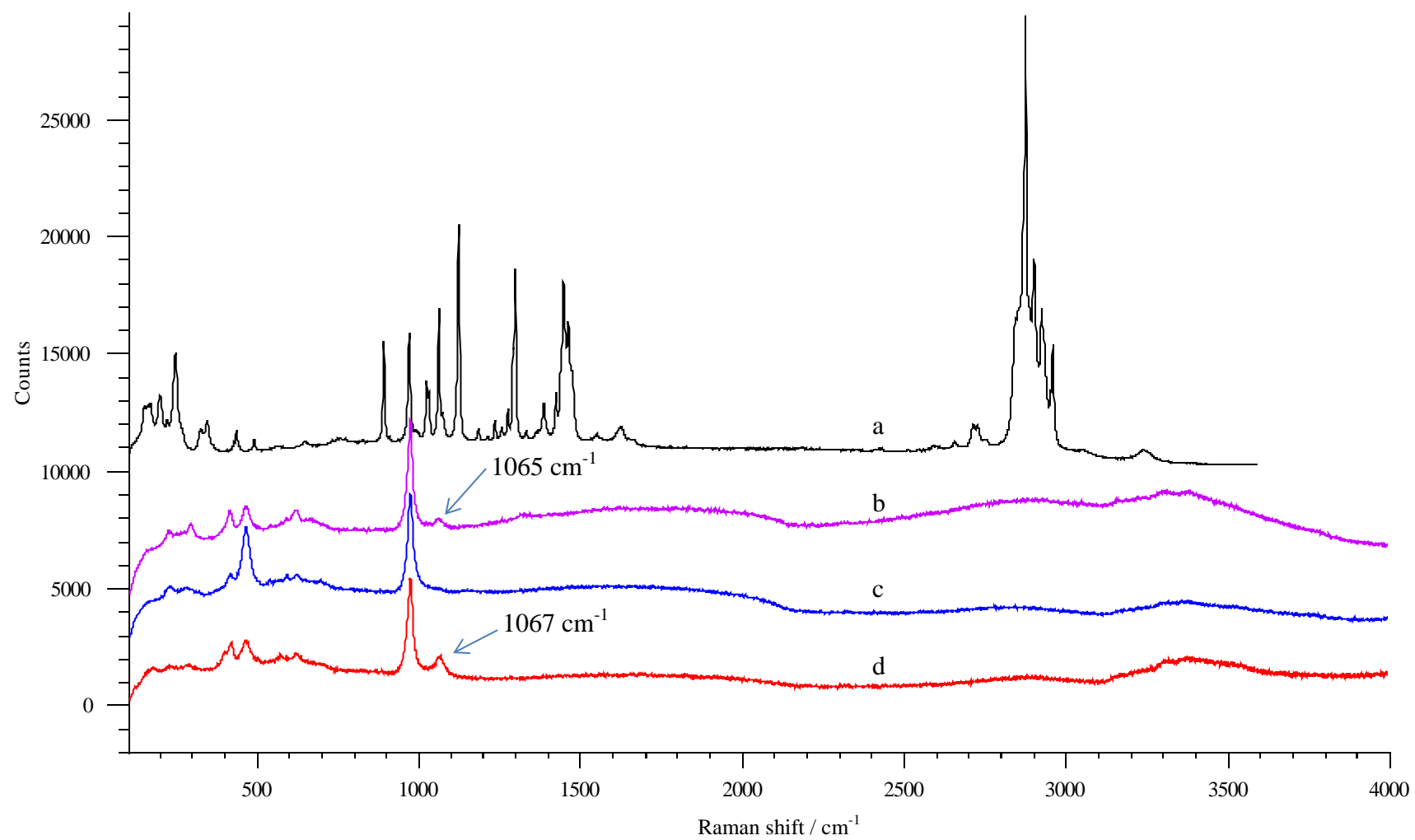


Fig. 6.13 Raman spectra for (a) $\text{KH}(\text{OHA})_2$; (b) $\text{KH}(\text{OHA})_2$ treated monazite crystal for 48 h; (c) $\text{KH}(\text{OHA})_2$ treated monazite crystal for 2 h and (d) monazite crystal.

Previous model system investigation showed that bands from 2800 cm^{-1} to 3000 cm^{-1} that are assigned to C-H are usually observed in the conditioned sample. It was used as one of the indications for adsorption of hydroxamate. In this case, very small but recognizable broad bands from 2820 cm^{-1} to 2980 cm^{-1} were present in the treated monazite spectra. Compared to the untreated monazite crystal spectrum, the treated samples spectra display similar band shape and intensities in this area. It can be concluded that this band emanates from monazite rather than $\text{KH}(\text{OHA})_2$ and no evidence was shown $\text{KH}(\text{OHA})_2$ was adsorbed on the surface after 48 h of conditioning.

Fig. 6.14 displays the fluorescent emission spectra for the treated monazite samples (2 h and 48 h) and the monazite crystal. The three spectra exhibit highly similar patterns in the emission line shape and position. Only 0.4 nm shifts were observed at 909.5 nm in the 2 h and 48 h of conditioned samples spectra. In addition, the 2 h sample spectrum exhibits much less intensities at 879 nm and 886 nm. The fluorescence investigation is consistent with the Raman spectroscopy study. No evidence was shown multilayers adsorption occurred on the surface during the conditioning time.

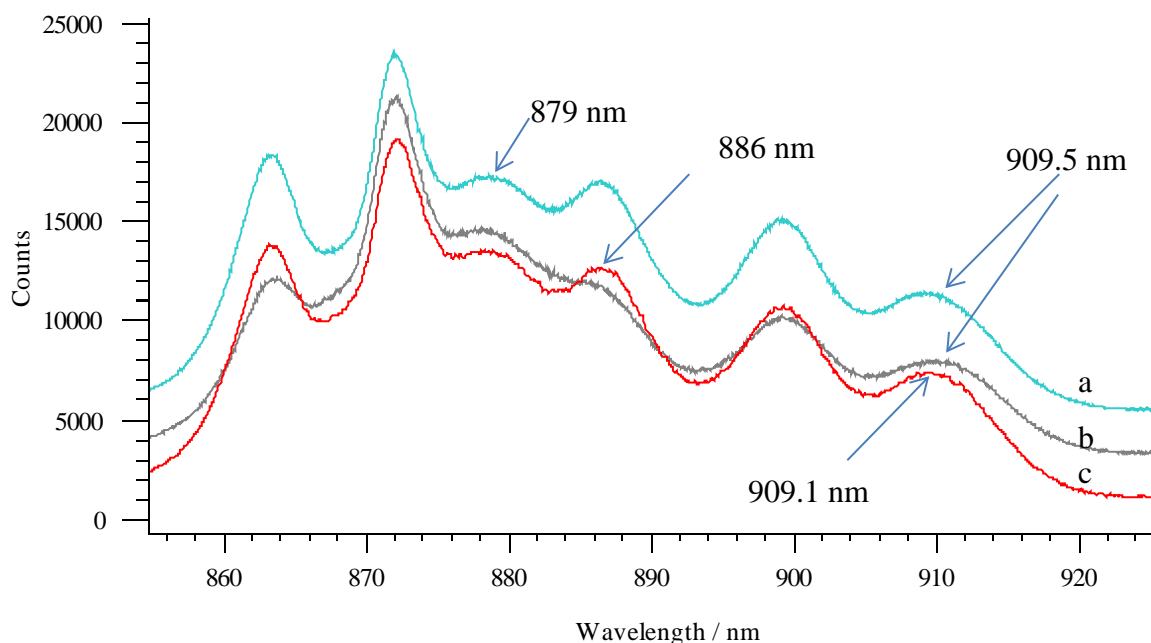


Fig. 6.14 Emission spectra for (a) $\text{KH}(\text{OHA})_2$ treated monazite crystal for 48 h (b) $\text{KH}(\text{OHA})_2$ treated monazite crystal for 2 h (c) monazite crystal. No significant shifts were observed in both treated samples compared to the untreated monazite spectrum.

Both the Raman and fluorescent investigations demonstrate hydroxamate is not selective to monazite compared to bastnaesite. Hydroxamate bands were displayed in the spectrum of the conditioned bastnaesite specimen after 40 min while no evident hydroxamate bands were observed in the 48 h conditioned monazite spectrum. Bastnaesite and monazite are commonly discovered together in the RE ores and monazite normally contains radioactive element thorium, it is possible that the collector can be applied to separate these two minerals during flotation.

6.4 Gangue minerals

6.4.1 Gangue mineral conditioned in hydroxamate

A sample purporting to be bastnaesite ore from Mountain Pass was characterized and found consists entirely of gangue mineral. Therefore, it was used for interaction study with hydroxamate.

6.4.1a Investigation by XPS

The same sample characterized by XPS was conditioned for 25 min in saturated hydroxamate solution. The result showed that carbonate C remained represented on the surface at 6%, indicating that any adsorbate layer must have been thin. The presence of 4% N indicated that some adsorption of hydroxamate had occurred, possibly to Ca (5 %) and/or to Ba (~1%) due to no RE was detected with the sample. The N 1s spectrum determined at the outset appeared to comprise at least two components. It could be fitted with a major component at 401 eV (75%) and a minor component at 399.4 eV (25%). At the end of the spectral suite, the fitted components were at the same binding energies, but the major component only accounted for 60% of the total N 1s intensity. The increase in intensity of the lower binding energy component indicates that some deprotonation of adsorbed hydroxamate had occurred as a result of beam damage. The width (1.75 eV) of the two fitted components was sufficiently large; it is possible a third component near 400.5 eV could be fitted. A better fit could be obtained on this basis, but the fit would not have been unique. The component near 401 eV remained the most intense.

A component between 400.0 and 400.6 eV might correspond to hydroxamate chemisorbed to Ca or Ba. The component near 401 eV was consistent with fully protonated N in an adsorbed metal hydroxamate. Neither the Ca 2p nor Ba 3d

spectrum was noticeably changed by the hydroxamate conditioning. However, it was not necessarily preclude the presence of monolayer Ca or Ba hydroxamate.

The XPS data exhibits that there have been adsorbed metal hydroxamate formed on the gangue mineral surface. The adsorption of hydroxamate at pH 9.5 at the surface of a gangue mineral might potentially be an ore associate of bastnaesite. In the presence of rare earth minerals, hydroxamate would be expected to preferentially adsorb on, or react with, the trivalent rare earth cations rather than the divalent alkaline earth cations.

6.4.1b Investigation by Raman spectroscopy

The conditioned sample from Mountain Pass was also investigated by Raman spectroscopy. The sample was conditioned in hydroxamate solution for 40 min before investigated.

Previous characterization for this sample has confirmed four different compositions were present on the surface. To investigate the absorption with the four specific locations, referencing of the same sample points were made for revisiting after conditioned with hydroxamate. The housing polyresin was radiated by the 442 nm laser at an appropriate distance from the mineral to obtain a reference point grid. The coordination for the surface location can be established by using the digital microscopy stage software. With this method, it allowed the same location to be revisited after the sample was conditioned.

Fig. 6.15 shows the spectra of the conditioned sample at location A. Compared to spectrum for the same location before conditioned, no Raman shift or additional bands were observed. Critical bondings such as C-O, N-O and C=O were not evident in the conditioned sample spectrum. It is indicated no chemisorption occurred on the surface

or the absorption would be thin. The characterization (Chapter 4) for location A indicated the cations in the mineral were mainly Ca. It is suggested that hydroxamate was not selective for Ca. In the RE floatation processing, Ca is not expected to affect the flotation efficiency.

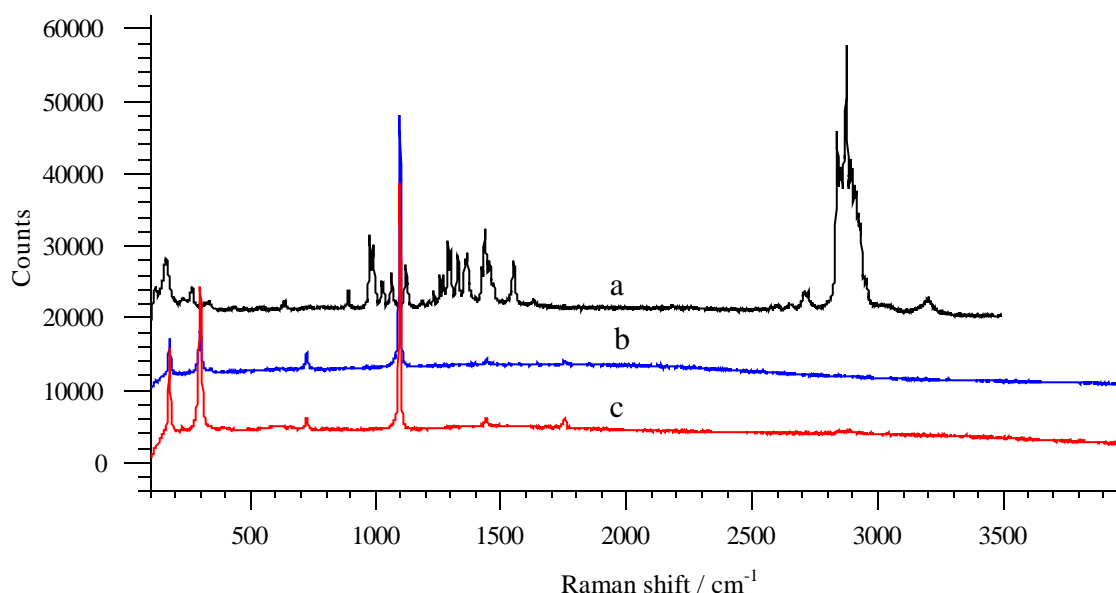


Fig. 6.15 Raman spectra for (a) KH(OHA)_2 (b) KH(OHA)_2 treated bastnaesite ore at location A and (c) bastnaesite ore at the same location.

For location B, the same observation was obtained as at location A. No noticeable change was observed with the conditioned sample spectrum compared to the spectrum of the same location (Fig. 6.16). The composition was different from that at location A. Low intensity emission lines of Nd has been observed with higher concentration of phosphate present (988 cm^{-1}). It is expected location B contains mainly monazite for RE minerals. Ca, Mg, Zr, Fe, Mn, Ba, Na and K may present at location B based on the XPS and SEM data. No chemisorption was evident between the metals and hydroxamate. The result is consistent with the monazite adsorption investigation that hydroxamate is not selective to monazite.

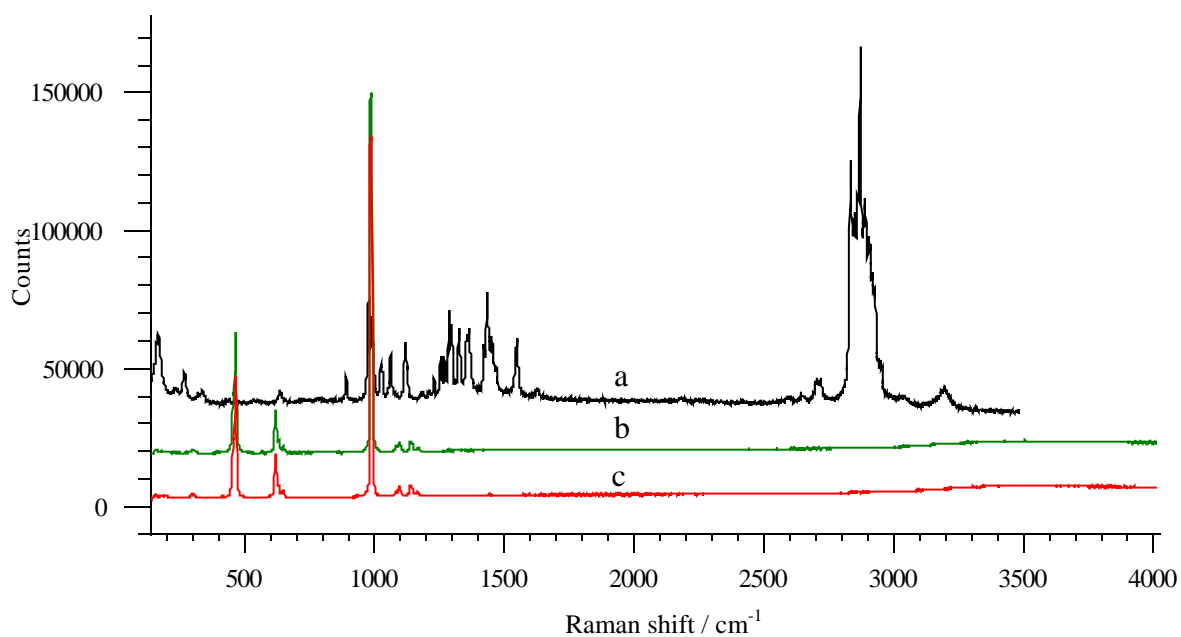


Fig. 6.16 Raman spectra for (a) $\text{KH}(\text{OHA})_2$ (b) $\text{KH}(\text{OHA})_2$ treated bastnaesite ore at location B and (c) bastnaesite ore at the same location. No significant change was observed with the conditioned sample spectrum compared to the spectrum of the same location.

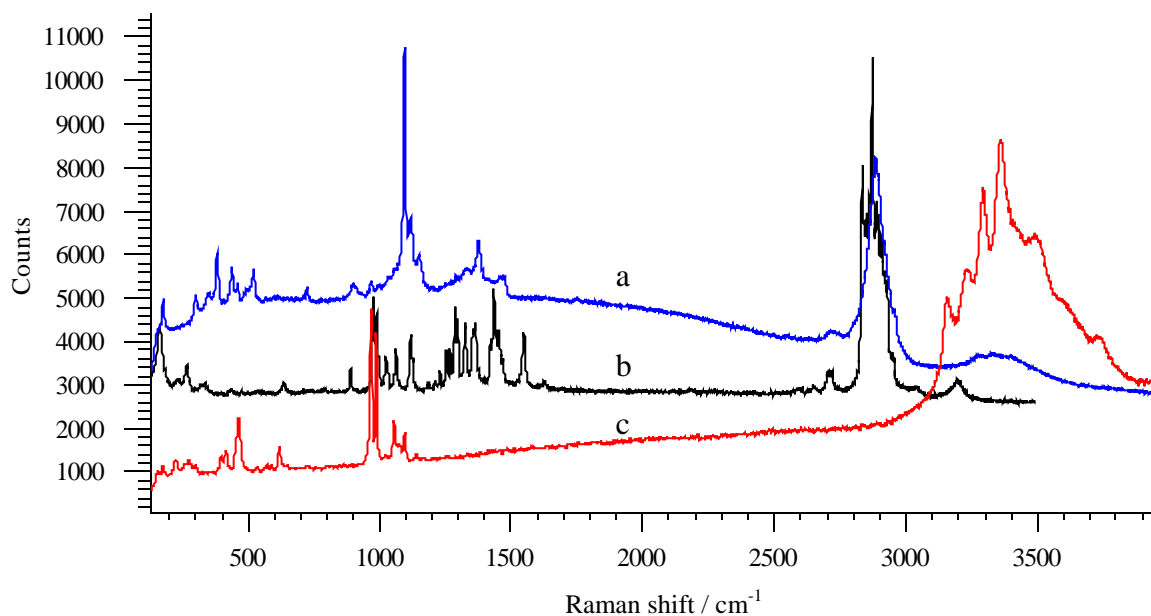


Fig. 6.17 Raman spectra for (a) $\text{KH}(\text{OHA})_2$ treated bastnaesite ore at location C (b) $\text{KH}(\text{OHA})_2$ and (c) bastnaesite ore at the same location.

Location C contains at least two REs including neodymium and praseodymium (see Chapter 4). A single band at 2895 cm^{-1} presented in the $\text{KH}(\text{OHA})_2$ treated bastnaesite ore; that band, which also featured in the spectrum from $\text{KH}(\text{OHA})_2$ (Fig. 6.17), was consistent with hydroxamate compound formation on the ore surface. The carbonate band at 1096 cm^{-1} shifted to lower wavenumber by 1 cm^{-1} . This indicated the surface energy has changed due to the chemisorption between the mineral and hydroxamate. A number of bands from hydroxamate were exhibited in the range of 1360 cm^{-1} to 1480 cm^{-1} and 385 cm^{-1} to 585 cm^{-1} . The assignments for these bands are unknown. The results support that chemisorption occurred on the surface and indicated hydroxamate was selective for REs over other base metals.

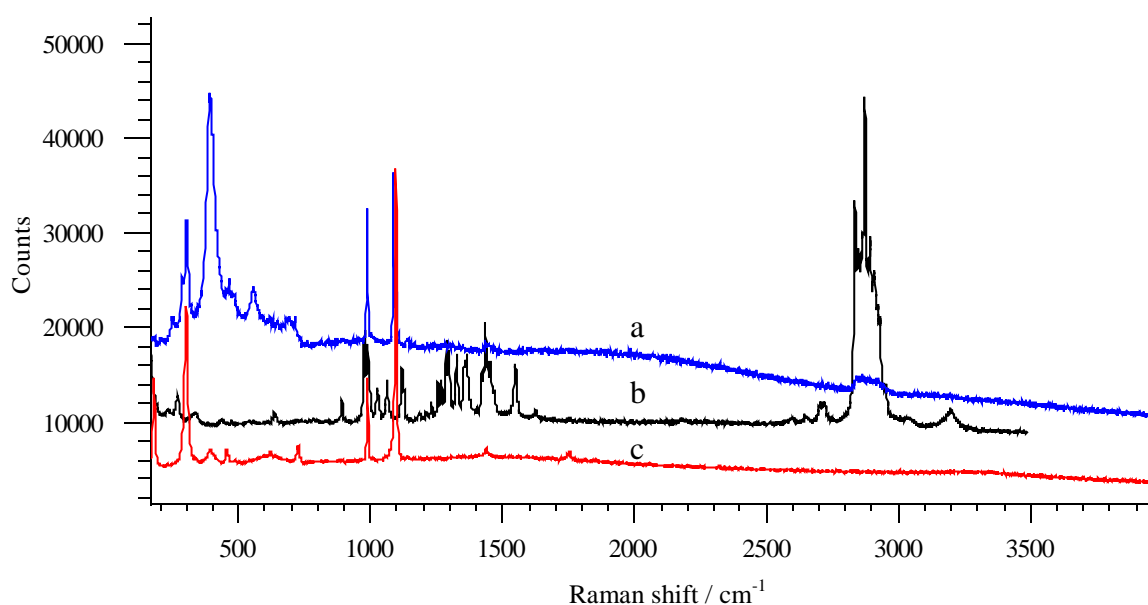


Fig. 6.18 Raman spectra for (a) $\text{KH}(\text{OHA})_2$ treated bastnaesite ore at location D (b) $\text{KH}(\text{OHA})_2$ and (c) bastnaesite ore at the same location.

Fig. 6.18 displays the conditioned spectrum at location D where phosphate and carbonate were both present. The intensity of carbonate band is stronger than the phosphate band. Low intensity of emission line 863, 872, 878, 887 and 898 nm (present

in the Raman spectra as wavenumber from 4000 cm^{-1} to 4800 cm^{-1}) supports the presence of Nd with low concentration. It is expected that higher concentration of bastnaesite was present compared to monazite. After conditioning, a very small broad band from 2800 cm^{-1} to 2950 cm^{-1} was observed in the conditioned sample spectrum. This indicates a monolayer of hydroxamate could present on the surface. However, the surface energy change is not sufficient to cause chemisorption with the collector. The result is consistent with the RE oxide interaction studies, with which hydroxamate exhibited low coverage on the surface of Nd_2O_3 . It is also suggested that bastnaesite has much stronger interaction with hydroxamate than monazite.

Conclusion

The interaction study on RE oxides surface with hydroxamate demonstrated that different REs has different adsorption rates. La_2O_3 exhibits the strongest interaction with hydroxamate followed by CeO_2 , Tm_2O_3 and Yb_2O_3 . Nd_2O_3 showed little response while no adsorption evidence was observed for Er_2O_3 . In the flotation system, conditioned time is expected to be sufficiently long to ensure the maximum adsorption. Different adsorption performances were also observed for bastnaesite and monazite. Hydroxamate exhibited stronger interaction to bastnaesite compared to monazite. It is possible that using hydroxamate to separate these two RE minerals during flotation. Gangue minerals adsorption investigation showed that hydroxamate was preferentially absorbed onto REs rather than other metals.

References

Fuerstenau D. W. and Pradip, 1984, Mineral flotation with hydroxamate collectors, Institute of mining and metallurgy, London, UK, 61–168.

CHAPTER 7

CONCLUSION

7.1 Summary of results

This thesis has described fundamental studies of the interaction between RE minerals and n-octanohydroxamate under solution conditions typical for the mineral flotation process. The results include three classes of experiment: the characterization of REO, RE minerals and gangue minerals; the investigation of a model system; and, an adsorption study of the RE compounds and for minerals with hydroxamate. Different surface characterization techniques have been utilized for these investigations. The traditional techniques of XPS, Raman spectroscopy and SEM-EDX have been demonstrated to be well suited for the surface investigation of RE compounds and minerals, whereas AFM and AFM tandem Raman spectroscopy have been used for a novel method of mineral surface characterization.

7.2 Characterization of REOs, RE minerals and gangue minerals

Systematic investigation using multiple radiation sources has been undertaken for 7 REOs including La_2O_3 , CeO_2 , Nd_2O_3 , Yb_2O_3 , Er_2O_3 , Tm_2O_3 and Tb_4O_7 . Each individual REE exhibited different vibrational and electronic property. It has been demonstrated that it is feasible to identify Nd and Er using the fluorescence emissions that do not overlap with the Raman spectra. Tb_4O_7 was observed undergoing laser induced changes during examination.

The characterization of bastnaesite and monazite showed evidence for RE enrichment in batches within the minerals. The scanning measurements from AFM and magnetic AFM confirmed that the particles are smaller than the present grinding sizes utilized in the flotation process. The RE particles sizes reported can provide guidance for the grinding operation, and a finer grind size might be advantageous, in practice, to liberate more mineral particles from the ores.

7.3 Model RE-hydroxamate compounds

REE hydroxamate compounds (Nd, Ce, Er, Ho, Gd and Dy) were synthesized for the measurement of the spectral properties of pure compounds. The n-octanohydroxamate molecule coordinated to the REE through both the nitrogen and oxygen atoms. The important functional groups likely to be involved in complex formation include C=O, N-O and C-N. Similar vibrational spectra were observed for the 6 synthesized RE hydroxamate compounds, however subtle variations in bands enable them to be distinguished between. The vibrational bands of individual RE compound for the critical bondings have been identified and used as indications for the surface interactions of hydroxamate with the natural minerals.

Nd and Ho hydroxamate compounds also can be identified through the RE(III) fluorescence emissions. The fluorescence lines of Er(III) overlap its Raman bands in the critical regions and this has resulted into difficulty of identification. Ce(III) hydroxamate was observed to undergo a colour change from white to reddish brown during preparation. The XPS and Raman data both support oxidation of the Ce(III) to Ce(IV). Results reveal that about 5% of the sample was Ce(IV), oxidized from Ce(III), after 7 days exposure to air.

7.4 Model system for surface interaction of RE minerals

A Ce carbonate thin film has been synthesized as a model bastnaesite mineral on a calcite substrate. The film was found to comprise particles, with sizes observed from 1-3 μm in diameter. The AFM data obtained from the natural bastnaesite and monazite exhibited a similar crystal size range. This established the possibility that using AFM-Raman to investigate the mineral surface interaction *in-situ*. These *in-situ* adsorption

studies for Ce carbonate and calcite demonstrated that hydroxamate is selective to Ce over Ca.

7.5 Adsorption study on the REOs surface

N-octanohydroxamate exhibited different selectivity to the 6 REOs (La, Ce, Nd, Er, Yb and Tm oxide) in the adsorption study. La_2O_3 exhibited the most intense Raman bands during the conditioning time, consistent with a greater quantity of hydroxamate present at the surface, followed by CeO_2 , Tm_2O_3 and Yb_2O_3 . Nd_2O_3 exhibited only a weak interaction while no adsorption was observed for Er_2O_3 with hydroxamate under all conditions investigated. In the flotation process, conditioning time has to be sufficiently long to ensure sufficient adsorption for hydrophobic surface formation. For those REs where hydroxamate exhibits poor adsorption, such as Nd and Er, a combination of different types of collector would be required for the flotation process. By comparing the reported stability constants of different RE hydroxamates, it is suggested that the stability of the RE compounds do not reflect the selectivity of hydroxamate.

7.6 Adsorption study on the surface of RE minerals

Bastnaesite and monazite were used for the adsorption studies with hydroxamate. Localized adsorption was observed on surface for both samples. The adsorption locations were consistent with the REs enrichment areas.

Different adsorption performances were also observed for bastnaesite and monazite with hydroxamate. Bastnaesite exhibited much stronger interaction compared to monazite. It is possible that hydroxamate could be used to separate these RE minerals during flotation of ores where both are present.

7.7 Adsorption study on the surface of a gangue mineral specimen

The SEM characterization of our bastnaesite ore specimen has confirmed that the sample contains mainly gangue minerals and was low in values (scanning size $3\text{ mm} \times 3\text{ mm}$). In a region of no more than $80\text{ }\mu\text{m} \times 30\text{ }\mu\text{m}$, only a small amount of REEs were detected by EDX. Four different Raman spectra were obtained corresponding to gangue mineral (calcite), bastnaesite and monazite crystals as well as one crystal where both RE minerals were present. The four locations were conditioned with hydroxamate and revisited using a reference point sample location technique with the computerized sample stage. This experiment revealed that bastnaesite exhibited the most intense Raman bands for adsorbed hydroxamate, followed by the crystal with both bastnaesite and monazite composition. Only a low intensity Raman signal for hydroxamate was observed on the monazite surface. No chemisorption evidence was observed in the gangue mineral region when it was conditioned for the same length of time as RE minerals. This study confirmed that bastnaesite has much stronger interaction with hydroxamate than monazite and hydroxamate is a selective collector for bastnaesite over gangue minerals.

7.8 Future work

The characterizations and the adsorption study of REOs and RE minerals have demonstrated that individual REE reacts differently to the collector hydroxamate despite their similarities in chemical and physical properties. It is likely the radioactive element thorium, that is commonly found in monazite, also has a distinguished interaction with hydroxamate. It would be prudent to investigate the properties of thorium minerals and the surface chemistry between hydroxamate and a monazite sample that contains thorium. That research would open up the possibility of using collector to separate thorium (and remove it) from other RE minerals.

A number of results (SEM, AFM and magnetic AFM) have shown that the REs enrichment regions are much smaller than the typical grinding sizes obtained in practice. Oversized fractions would result in insufficient reagent attaching to the mineral surface and thus to decrease the collection efficiency. On the other hand, fine particles (slimes) have been shown to have low bubble collision efficiency, and so they are difficult to float in the standard process (Miettinen et al., 2010). It would be of interest to investigate the optimal grinding size to maximise the liberation of REs.

This thesis has established a systematic approach for surface interaction study of major RE minerals. The method can be extended to other types of minerals. For example, the AFM has been demonstrated to be well suited for minerals surface characterization and AFM-Raman are useful techniques for localization of adsorption areas. The research approach is also suited for investigation and prediction for the performance of different types of collector.

7.9 Concluding remarks

Until now, bench-scale flotation studies have been normally undertaken to investigate the interaction of hydroxamates with rare earth minerals. Optimised site-specific flotation conditions were determined post flotation, by using extensive flotation testing regimes in which factors such as reagent type, concentration, depressant and other factors (temperature, pH etc.) were varied and tested. Systematic surface research has been absent; and mechanistic understanding of the interaction of hydroxamates with RE minerals has been deficient.

This thesis has provided such fundamental studies, these, potentially, can reduce the requirement for extensive site-specific testing programs that make limited innovations in REs processing. The fundamental study of REs flotation has been investigated in a clear and unified way that can be readily appreciated by mineral technologists and investigators. Adsorption studies for individual rare earth oxides, model compounds and minerals with hydroxamate allow for the mechanisms of interaction for each of the components to be ascertained and, in turn, facilitate the prediction of adsorption efficiency of hydroxamate with different mineral assemblages.

References

Miettinen T., Ralston J. and Fornasiero D., 2010, The limits of fine particle flotation, Minerals Engineering, 23, 5, 420-437.